The Gulf of Cadiz as a natural laboratory for the validation and exploitation of coastal altimetry and model data

PhD Thesis

Ana Isabel Aldarias Martos

Puerto Real, 2022

Università
degli Studi
di Ferrara

DOTTORATO DI RICERCA IN
"EARTH AND MARINE SCIENCES - EMAS"

CICLO XXXIV

COORDINATRICE/COORDINATORE Prof. (Cognome e Nome)
Maximo Coltorti

THE GULF OF CADIZ AS A NATURAL LABORATORY FOR THE VALIDATION AND EXPLOITATION OF COASTAL ALTIMETRY AND MODEL DATA

Settore Scientifico Disciplinare Marine Sciences/Physical Oceanography

Dottoranda/o	**Tutore**
Dott.	Profs.
Aldarias Martos, Ana Isabel	Gómez Enri, Jesús
	Laiz Alonso, Irene

Anni 2018/2022

UNIVERSIDAD DE CÁDIZ
FACULTAD DE CIENCIAS DEL MAR Y AMBIENTALES
DEPARTAMENTO DE FÍSICA APLICADA

THE GULF OF CADIZ AS A NATURAL LABORATORY FOR THE VALIDATION AND EXPLOITATION OF COASTAL ALTIMETRY AND MODEL DATA

Memoria presentada por **Ana Isabel Aldarias Martos** para optar al grado de Doctor en Ciencias y Tecnologías Marinas – EMAS

Puerto Real, Febrero 2022

D. JESÚS GÓMEZ ENRI, Profesor Titular del Departamento de Física Aplicada de la Universidad de Cádiz y Dª. IRENE LAIZ ALONSO, Profesora Contratada Doctora del Departamento de Física Aplicada de la Universidad de Cádiz, como sus directores HACEN CONSTAR:

Que esta memoria, titulada **“The Gulf of Cadiz as a natural laboratory for the validation and exploitation of coastal altimetry and model data”**, presentada por Dª. Ana Isabel Aldarias Martos, resume su trabajo de Tesis y, considerando que reúne todos los requisitos legales, autorizan su presentación y defensa para optar al grado de Doctor por la Universidad de Cádiz.

Puerto Real, Febrero 2022

Lo importante es saber a mar.

A mi persona favorita de este y de todos los mundos,
Dulce.

Agradecimientos

Siendo yo de interior, el mar ha sido siempre un imprescindible, una necesidad en mi vida. El mar me trajo a Cádiz y fue entonces que me enamoré de Cádiz y de la carrera que estaba estudiando, Ciencias del Mar. Empecé a trabajar en el laboratorio, a embarcar, a construir una cámara bentónica, etc. Todo ello me llevaba por un camino que de pronto giró 180º, pero todo pasa por algo en la vida. Ya lo decía el principito "caminando en línea recta no puede uno llegar muy lejos". Y si no fuera por cada paso y cada una de las decisiones que tomé hoy no estaría aquí escribiendo esto.

En primer lugar quiero dar las gracias a mis directores, Jesús e Irene. Gracias por la confianza, por los consejos, por las discusiones científicas, por los toques de atención cuando han hecho falta, y por vuestro apoyo a lo largo de todo el proceso, con pandemia incluida de por medio. Gracias porque al final todo ha tenido sentido, altimetría y modelo, modelo y altimetría.

Gracias a mis instituciones y supervisores de acogida. Gracias a Marcello y los compañeros del DGFI-TUM. Gracias por las charlas magistrales, por la ayuda y orientación, por intentar que sacara el máximo provecho de mi estancia con vosotros. Y gracias por comprenderme y apoyarme durante el tramo final de mi tesis, que nunca es fácil. Gracias a Álex, por acogerme y enseñarme los entresijos del Delft3D. Y gracias a Manuel, porque como decía al principio las cosas siempre pasan por algo y esos seis meses de estancia pre-doctoral en el CEAMA fueron solo la antesala de lo que vino después. Gracias por llevarme a tus clases, por aconsejarme, y por ayudarme a entender la dinámica del estuario del Guadalquivir.

Gracias a mis compañeros y compañeras del departamento por todo vuestro apoyo estos años. En especial gracias a mis compis de doctorado, los que ya terminaron, los que recién empezaron y los que han hecho el camino conmigo. A Marina, gracias por ser un ejemplo a seguir, por mostrar a todos tu pasión por la ciencia, por tu apoyo en mis inicios en la docencia universitaria y por todas las actividades de divulgación que hemos hecho juntas. Porque si la ciencia no llega a todas las personas, deja de ser útil. Roberto, gracias por tu apoyo especialmente estos últimos meses, por confiar en mis capacidades más que yo misma, y por contestar siempre con un "claro, cuenta conmigo". Gracias al equipo Quifis,

porque mis inicios fueron con vosotros y los inicios siempre marcan. Gracias Ana, no sabes lo importante que eres para mí, culpa mía que igual no te lo digo lo suficiente. Eres mi referente con mayúsculas, una guerrera y curranta, mi compañera durante todo este viaje (y lo que queda por venir), mi squaro, lo más cerca que he tenido a una hermana. Gracias por tirar conmigo para delante, por ayudarme en todo lo que estaba en tu mano y por recordarme que cuando acabas la tesis el mundo se ve de otro color. Gracias Jairo, por tu apoyo este último año, por tu sinceridad, por tu ayuda, y por estar ahí al final del día esperándome con una cerveza fresquita. A los dos gracias por cada desayuno en el CASEM, por sacarme siempre una risa antes de volver a casa y por todos los planes B que hemos tramado juntos por si esto de la investigación se pone complicado.

Gracias a mi gente de Cádiz, a Fran, Lucía, Laura, Juande, Nahuel, María, Luis, a todos, gracias por los ratos de risas y desconexión, las rutitas, los guitarreos, los tardeos y las cervecitas. Gracias por ayudarme a creer que era posible terminar la tesis. A Mar, David y Sam, los que habéis estado conmigo desde el primer día que puse un pie en la Universidad de Cádiz. Aunque la vida nos está llevando por caminos separados sé que vais a estar ahí siempre, yo siempre voy a estar. Sam, no hay palabras suficientes para agradecerte lo mucho que has trabajado conmigo estos últimos meses, eres la mejor "correctora" que ha podido tener esta tesis.

Gracias a los de siempre. Baezanos, un poco desperdigados por el país pero siempre juntos para las buenas y las malas. Gracias por estar ahí sin necesidad de estar en contacto todos los días, porque a nosotros nos basta una ligá para ponernos al día de volao. Gracias por estar siempre.

Gracias a mi equipo de monitores, sois más que amigos, sois familia. Todo lo que necesito para recargar mis pilas es una semana al año con vosotros, riendo y soñando, haciendo soñar y reír. Qué pena el tiempo perdido estos dos últimos veranos. Gracias también a mis compis de Ecologistas en Acción, sois mi punto de conexión a tierra, con vosotros soñar con otro mundo se hace más posible y menos utópico.

Gracias a mi familia, a todos, pero permitidme alguna mención especial. Tito Antonio, compi, gracias por abrirme el camino y hacer entender un poco a todos que es esto de hacer una tesis doctoral. Gracias tito José María por mostrarme que siempre merece la pena luchar hasta el final. A mi familia gaditana, en especial a mis cuñis, gracias por hacerme sentir una más desde el minuto uno, por las risas, las tardes en la playa y los domingos en El Torno. A mis abuelos, los que están y los que estuvieron y siguen estando, gracias por vivir mi pasión conmigo, por tratar de entender todo lo que os cuento sobre mi investigación, por leeros cada cosa que publico en español aunque igualmente lo entendáis tanto como en inglés, por el apoyo, los abrazos, la emoción, el amor. Madrinita gracias por tantos años y tantas cosas compartidas y gracias por hacerme el regalo más bonito que me han hecho en mi vida, mi pequeña Rocío, mi ahijada. Primi, gracias por esta portada tan increíble y maravillosa, eres el artista de la familia y que orgullo. Tato, Andrés, gracias por tus consejos, por ayudarme a entenderme a mí misma, por retarme a ser un buen ejemplo a seguir para ti, aunque a veces no tengo claro quién hace de hermano/a mayor. Mamá, papá, gracias por apoyarme en cada una de las decisiones que he tomado en mi vida, estuvierais más o menos de acuerdo, siempre habéis dejado que mis aciertos fueran míos y mis errores también. Os debo la vida y mucho más, os quiero.

Por último y no menos importante, gracias Juan Carlos porque a pesar de todo el caos (bendito caos), una pandemia y una tesis después aquí sigues a mi lado. Contigo siempre es todo fácil, y es que si se quiere bien es fácil.

Acknowledgments

The altimetry data used in this thesis were obtained from the ESA-GPOD web page. The author would like to thank Salvatore Dinardo from CLS (Collecte Localisation Satellites) for his technical support in the use of the GPOD service, as well as all the GPOD team members. Besides, altimetry data provided by Frithjof Ehlers from the Technical University of Delft, Michele Scagliola from Aresys, and Marcello Passaro and Florian Schlembach from the DGFI-Technical University of Munich were used in Chapter 6. The author is also grateful for the provision of the prototype Fully-Focused Sentinel-3. The radar tide gauge data, as well as tidal harmonic data, were provided by the Spanish Puertos del Estado. The model calibration and validation in Chapter 5 were carried out using in-situ data provided by Gabriel Navarro, Manuel Díez Minguito, Begoña Tejedor, and Óscar Álvarez. Finally, the author would like to thank Martin Saraceno and Manuel Díez Minguito for being the referees of this thesis.

This thesis is supported by the PhD program "Earth and Marine Science" of the University of Cadiz (Spain) and the University of Ferrara (Italy).

Summary

Hydrodynamic models and satellite altimetry can be complementary tools for the study of sea level variations. Nowadays, users of these tools demand high quality products in coastal zones. In this sense, this doctoral dissertation focusses on the validation of innovative products that entail an advance in the understanding of sea level variation in coastal areas. The study was carried out in the Gulf of Cadiz (GoC), an important region that connects the Atlantic Ocean and the Mediterranean Sea, although other study areas were also used to strengthen the analysis. The research was performed using: in-situ data, sea level altimetry measurements from Sentinel-3 SRAL, and observations from a hydrodynamic model implemented in the main study area. The in-situ data were used to validate the altimetry measurements, as well as to calibrate and validate the numerical model.

Different specific objectives were proposed. The first was to determine the quality of altimetric data in coastal areas from the new Sentinel-3 space mission. Altimetry data of Sentinel-3A SRAL (S3A) were validated at the sampling frequency of 80 Hz. The data were obtained from the European Space Agency (ESA) Grid Processing On Demand (GPOD) service over three coastal sites in Spain: Huelva (GoC), Barcelona (Western Mediterranean Sea), and Bilbao (Bay of Biscay). Two tracks were selected at each site: one ascending and one descending. Data were validated using in-situ tide gauge (TG) data provided by the Spanish Puertos del Estado. The altimetry Sea Level Anomaly (SLA) time series were obtained using the corrections available in GPOD. The validation was performed using two statistical parameters, the Pearson correlation coefficient (r) and the root mean square error (rmse). In the 5–20 km segment with respect to the coastline, the results obtained were 6–8 cm (rmse) and 0.7–0.8 (r) for all of the tracks. The 0–5 km segment was also analysed in detail to study the effect of land on the quality of altimetry data. Results showed that the track orientation, the angle of intersection with the coast, and the land topography concur to determine the nearest distance to the coast at which the data retain a similar level of accuracy than in the 5–20 km segment. This 'distance of good quality' to shore reaches a minimum of 3 km for the tracks at Huelva and the descending track at Barcelona.

In addition, altimetry sea level data of Sentinel-3A and Sentinel-3B SRAL (S3A and S3B) were also validated at the sampling frequency of 80 Hz. Two tracks of S3A and two of S3B were selected at seven different coasts around the Iberian Peninsula. The altimetry SLA time series obtained were compared with TG in-situ data using the standard deviation of

the difference (sdd) and the normalized sdd (sdd_n). Two tidal models were used: TPXO8 and TPXO9. They were previously validated with in-situ data and then used in the S3 assessment. Contrary to expectations, a more current version of the tide model did not always lead to improvements for all of the coasts studied. The same data availability and accuracy results (mean sdd <9cm) were obtained for both satellites, as the radar altimeter on-board S3A and S3B are identical instruments. The sdd_n results were generally ranged between 0.1 and 0.25 cm, higher values were obtained in coastal areas with a complex hydrodynamic.

The second specific objective was to implement the Delft3D model in the estuary of the Guadalquivir River and part of the GoC continental shelf with the aim of studying the influence of its discharges on the sea level variability. Details of the Delft3D FLOW module implementation are given in the manuscript. The model was calibrated and validated along the river estuary comparing the output with in-situ observations of water level and current velocities during normal and high-discharge events. In order to obtain the best possible adjustment, the friction coefficient and bathymetry were used as adjustment parameters. The determination coefficients attained mean values of $R^2= 0.9$ and $R^2=0.8$, for calibration and validation, respectively. Moreover, the model was calibrated for the continental shelf during normal discharge conditions using data from three current meters, obtaining good correlation results (rmse= 3.0 $cm \cdot s^{-1}$ and $R^2=0.7$, on average). The model simulations were able to reproduce the low salinity plume-induced over-elevations at the mouth of the estuary and its adjacent inner shelf during periods of high river discharge from the head dam (> 400 $m^3 \cdot s^{-1}$). These over-elevations were also identified in a qualitative comparison with altimetry data. Despite the good results obtained, there are some improvements that could be made for future work: including wind, coupling the wave module, updating the bathymetry, etc.

The aim of the last section was to apply the new Fully Focused SAR (FF SAR) processing technique for the Sentinel-3 altimetry signal. The accuracy and precision of this novel product were analysed in order to provide the best quality product close to the coast (0-5 km track segment). FF SAR processing is similar to SAR altimetry, but with an unprecedented high along-track resolution which goes up to the theoretical limit equal to half the antenna length (~0.5 m). Two FF SAR algorithms still in development were used in this work: FF SAR Back Projection (BP) (S3 prototype version of Kleinherenbrink et al.,

2020), and FF SAR Omega-Kappa (WK) (Guccione et al., 2018), as well as different retracking algorithms. Two tracks from Sentinel-3A and two from Sentinel-3B were processed, at 80 Hz. The products were validated by comparing time series of SLA with those obtained from a tide gauge in the Gulf of Cadiz. The accuracy was analysed using the Percentage of Cycles for High Correlation (PCHC) and the standard deviation of the difference (sdd); and the precision was determined by calculating the along-track noise. FF SAR and unfocused SAR products were compared. The results showed improvements using Adaptative Leading Edge Subwaveform (ALES+) retracker for unfocused SAR, although FF SAR BP with ALES+ was the most precise product for all the tracks. In addition, highly accurate SLA measurements were also obtained with FF SAR products. The greatest advantage of FF SAR is that it produces good quality data closer to the coast (1-2 km) than unfocused SAR (3-4 km).

Finally, the obtained results highlight the potential of the implementation of validated altimetry data and hydrodynamic models in sea level studies. Furthermore, the methodology described can be useful to validate altimetry data, as well as to implement the Delft3D model in other coastal areas.

Keywords: coastal altimetry, synthetic aperture radar (SAR) data, high posting rate, Sentinel-3, sea level anomaly, Fully Focused SAR altimetry, Gulf of Cadiz, Delft3D model, calibration, validation, Guadalquivir River estuary, fluvial discharge, water levels, altimetry-model comparison.

Resumen

Los modelos hidrodinámicos y la altimetría satelital pueden ser herramientas complementarias para el estudio de las variaciones del nivel del mar. Actualmente, los usuarios de estas herramientas demandan productos de alta calidad en las zonas costeras. En este sentido, esta tesis doctoral se centra en la validación de productos innovadores que permitan avanzar en el conocimiento de la variación del nivel del mar en zonas costeras. El estudio se llevó a cabo en el golfo de Cádiz (GoC, por sus siglas en inglés), una importante región que conecta el Océano Atlántico y el Mar Mediterráneo, aunque también se utilizaron otras áreas de estudio para reforzar los análisis. La investigación se llevó a cabo utilizando datos in-situ, datos altimétricos del nivel del mar del satélite Sentinel-3 SRAL y observaciones de un modelo hidrodinámico implementado en la principal zona de estudio. Los datos in-situ se utilizaron para validar las mediciones altimétricas, así como para calibrar y validar el modelo.

Se propusieron diferentes objetivos específicos. El primero fue determinar la calidad de los datos altimétricos en las zonas costeras procedentes de la nueva misión espacial Sentinel-3. Se validaron los datos altimétricos de Sentinel-3A SRAL (S3A) con una frecuencia de muestreo de 80 Hz. Los datos se obtuvieron del servicio “Grid Processing On Demand” (GPOD) de la Agencia Espacial Europea (ESA, por sus siglas en inglés) en tres lugares costeros de España: Huelva (en el GoC), Barcelona (Mar Mediterráneo Occidental), y Bilbao (Golfo de Vizcaya). Se seleccionaron dos trazas en cada sitio: una ascendente y otra descendente. Los datos se validaron con datos de mareógrafos proporcionados por Puertos del Estado. Las series temporales de la Anomalía del Nivel del Mar (SLA, por sus siglas en inglés) para el altímetro se obtuvieron utilizando las correcciones disponibles en GPOD. La validación se realizó mediante dos parámetros estadísticos, el coeficiente de correlación de Pearson (r) y el error cuadrático medio (rmse). En el segmento de 5-20 km con respecto a la línea de costa, los resultados fueron de 6-8 cm (rmse) y de 0,7-0,8 (r) para todas las trazas. El segmento de 0-5 km también se analizó en detalle para estudiar el efecto de la contaminación por tierra en la calidad de los datos altimétricos. Los resultados mostraron que la orientación de la traza, el ángulo de intersección con la costa y la topografía del terreno influyen en la determinación de la distancia más cercana a la costa en la que los datos conservan un nivel de exactitud similar al obtenido en el segmento de 5-20 km. Esta "distancia de buena calidad" a la costa alcanza un mínimo de 3 km para las trazas de Huelva y la traza descendente de Barcelona.

Además, datos altimétricos de nivel del mar de los satélites Sentinel-3A y Sentinel-3B SRAL (S3A y S3B) fueron también validados a una frecuencia de muestreo de 80 Hz. Dos trazas de cada uno de los satélites se seleccionaron en siete costas diferentes situadas alrededor de la península Ibérica. Las series temporales de SLA de los altímetros se compararon con datos in-situ de mareógrafos usando la desviación estándar de la diferencia (sdd, por sus siglas en inglés) y su valor normalizado (sdd_n). Dos modelos de marea fueron utilizados en este estudio: TPXO8 y TPXO9. Ambos fueron previamente validados con datos in-situ y usados después en la validación de Sentinel-3. Al contrario de lo esperado, la versión más actual del modelo de marea no siempre mostró mejoras para todas las costas estudiadas. La disponibilidad de datos y la calidad de los resultados (sdd medio < 9cm) fueron la misma para los dos satélites, dado que los altímetros radar a bordo de S3A y S3B son idénticos. En general, los resultados de la sdd_n variaron entre 0,1 y 0,25 cm, siendo mayores los valores obtenidos en zonas costeras con una hidrodinámica compleja.

El segundo objetivo específico fue implementar el modelo Delft3D en el estuario del río Guadalquivir y parte de la plataforma continental del GoC, con el fin de estudiar la influencia de sus descargas en la variabilidad del nivel del mar del GoC. Los detalles de la implementación del módulo FLOW del modelo Delft3D se recogen en este trabajo. El modelo fue calibrado y validado a lo largo del estuario del río comparando los resultados del modelo con los datos in situ de niveles y velocidades de corriente durante eventos normales y de alta descarga. Para obtener el mejor ajuste posible, se utilizó el coeficiente de fricción y la batimetría como parámetros de ajuste. Los coeficientes de determinación alcanzaron valores medios de R^2= 0,9 y R^2=0,8, para la calibración y la validación. Además, se calibró el modelo en la plataforma continental en condiciones normales de descarga utilizando datos de tres correntímetros, obteniendo buenos resultados de correlación (rmse= 3,0 $cm \cdot s^{-1}$ y R^2=0,7, en promedio). Las simulaciones del modelo fueron capaces de reproducir fielmente las sobreelevaciones inducidas por la pluma de baja salinidad en la desembocadura del estuario y su plataforma interior adyacente, durante los períodos de alta descarga del río desde la presa, situada en la cabecera (> 400 $m3 \cdot s^{-1}$). Estas sobreelevaciones también se identificaron en una comparación cualitativa con datos altimétricos. A pesar de los buenos resultados obtenidos, hay algunas mejoras que podrían realizarse pensando en futuros trabajos: incluir el viento, acoplar el módulo de oleaje, actualizar la batimetría, etc.

El objetivo de la última parte de esta tesis fue aplicar la nueva técnica de procesamiento *Fully Focused* SAR (FF SAR, por sus siglas en inglés) para la señal altimétrica de Sentinel-3. Se analizó la exactitud y precisión de este novedoso producto con el fin de encontrar el producto de mejor calidad cerca de la costa (segmento de traza 0-5 km). El procesamiento del FF SAR es similar al de la altimetría SAR pero con una alta resolución, sin precedentes, a lo largo de la traza, que aumenta hasta el límite teórico, equivalente a la mitad de la longitud de la antena (~0,5 m). En este trabajo se utilizaron dos algoritmos de FF SAR aún en desarrollo: FF SAR Back Projection (BP) (versión prototipo S3 de Kleinherenbrink et al., 2020), y FF SAR Omega-Kappa (WK) (Guccione et al., 2018); además se utilizaron diferentes algoritmos de retracking. Se procesaron dos trazas de Sentinel-3A y dos de Sentinel-3B, a 80 Hz. Los productos se validaron comparando las series temporales de SLA con las obtenidas por el mareógrafo en el golfo de Cádiz. La exactitud se analizó utilizando el Porcentaje de Ciclos de Alta Correlación (PCHC, por sus siglas en inglés) y la desviación estándar de la diferencia (sdd); y la precisión se analizó a partir del ruido calculado a lo largo de la traza. Se compararon los productos FF SAR y SAR no enfocado. Los resultados mostraron mejoras utilizando ALES+ para el SAR no enfocado, aunque el producto FF SAR BP con ALES+ fue el más preciso en todas las trazas. Además, también se obtuvieron mediciones de SLA más exactas con los productos FF SAR. La mayor ventaja del SAR FF es que produce datos de buena calidad más cerca de la costa (1-2 km) que el SAR desenfocado (3-4 km).

Finalmente, los resultados obtenidos en esta Tesis ponen de manifiesto el potencial de los datos altimétricos validados y del modelo hidrodinámico implementado para los estudios del nivel del mar. Además, la metodología aquí descrita puede ser útil para validar los datos altimétricos, así como para implementar el modelo Delft3D en otras zonas costeras.

Palabras clave: altimetría costera, altimetría de radar de apertura sintética, Sentinel-3, anomalía del nivel del mar, altimetría SAR totalmente enfocada, golfo de Cádiz, modelo Delft3D, calibración, validación, estuario del río Guadalquivir, descarga fluvial, niveles de agua, comparación altimetría-modelo.

Riassunto

I modelli idrodinamici e l'altimetria satellitare possono essere strumenti complementari per lo studio delle variazioni del livello del mare. Al giorno d'oggi, gli utenti di questi strumenti richiedono prodotti di alta qualità nelle zone costiere. Con questo scopo, questa tesi di dottorato verte sulla validazione di prodotti innovativi che comportano un progresso nella comprensione della variazione del livello del mare nelle zone costiere. Lo studio è stato condotto nel Golfo di Cadice (GoC), un'importante regione che collega l'Oceano Atlantico e il Mar Mediterraneo, sebbene siano state utilizzate anche altre aree di studio per validare l'analisi. La ricerca è stata svolta utilizzando: dati in situ, misure altimetriche del livello del mare da Sentinel-3 SRAL e osservazioni da un modello idrodinamico implementato nella principale area di studio. I dati in situ sono stati utilizzati per convalidare le misure altimetriche, così come per calibrare e convalidare il modello numerico.

Sono stati proposti diversi obiettivi specifici. Il primo era quello di determinare la qualità dei dati altimetrici nelle aree costiere dalla nuova missione spaziale Sentinel-3. I dati altimetrici di Sentinel-3A SRAL (S3A) sono stati validati alla frequenza di campionamento di 80 Hz. I dati sono stati ottenuti dal servizio Grid Processing On Demand (GPOD) dell'Agenzia Spaziale Europea (ESA) su tre siti costieri in Spagna: Huelva (GoC), Barcellona (Mar Mediterraneo occidentale), e Bilbao (Golfo di Biscaglia). Sono state selezionate due tracce in ogni sito: una ascendente e una discendente. I dati sono stati convalidati utilizzando i dati dei mareografi (TG) in situ forniti dai Puertos del Estado spagnoli. Le serie temporali dell'altimetria *Sea Level Anomaly* (SLA) sono state ottenute utilizzando le correzioni disponibili in GPOD. La validazione è stata svolta utilizzando due parametri statistici, il coefficiente di correlazione di Pearson (r) e l'errore quadratico medio (rmse). Nel segmento 5-20 km rispetto alla linea di costa, è stato ottenuto un rmse di 6-8 cm e un r di 0,7-0,8 per tutte le tracce. Anche il segmento 0-5 km è stato analizzato in dettaglio per studiare l'effetto della terra sulla qualità dei dati altimetrici. I risultati hanno mostrato che l'orientamento della traccia, l'angolo di intersezione con la costa e la topografia del terreno concorrono a determinare la distanza più vicina alla costa alla quale i dati mantengono un livello di precisione simile a quello del segmento 5-20 km. Questa "distanza di buona qualità" dalla costa raggiunge un minimo di 3 km per le tracce a Huelva e la traccia discendente a Barcellona.

Inoltre, i dati altimetrici del livello del mare di Sentinel-3A e Sentinel-3B SRAL (S3A e S3B) sono stati convalidati alla frequenza di campionamento di 80 Hz. Due tracce di S3A e due di S3B sono state selezionate in sette diverse coste intorno alla penisola iberica. Le serie temporali SLA altimetriche ottenute sono state confrontate con i dati TG in situ utilizzando la deviazione standard della differenza (sdd) e la sdd normalizzata (sdd_n). Sono stati utilizzati due modelli di marea: TPXO8 e TPXO9. Sono stati precedentemente convalidati con dati in situ e poi utilizzati nella valutazione S3. Contrariamente alle aspettative, una versione più attuale del modello di marea non ha sempre portato a miglioramenti per tutte le coste studiate. La stessa disponibilità di dati e gli stessi risultati di precisione (sdd media <9cm) sono stati ottenuti per entrambi i satelliti, poiché gli altimetri radar a bordo di S3A e S3B sono strumenti identici. I risultati sdd_n sono stati generalmente compresi tra 0,1 e 0,25 cm, valori più alti sono stati ottenuti in aree costiere con un idrodinamico complesso.

Il secondo obiettivo specifico è stato quello di implementare il modello Delft3D nell'estuario del fiume Guadalquivir e parte della piattaforma continentale del GoC con lo scopo di studiare l'influenza dei suoi scarichi sulla variabilità del livello del mare. I dettagli dell'implementazione del modulo Delft3D FLOW sono forniti nel manoscritto. Il modello è stato calibrato e validato lungo l'estuario del fiume confrontando l'output con le osservazioni in situ del livello dell'acqua e delle velocità della corrente durante gli eventi di piena normali ed eventi elevati. Al fine di ottenere la migliore regolazione possibile, sono stati utilizzati come parametri di riferimento il coefficiente di attrito e la batimetria . I coefficienti di determinazione hanno raggiunto valori medi di R2= 0,9 e R2=0,8, rispettivamente per la calibrazione e la validazione. Inoltre, il modello è stato calibrato per la piattaforma continentale durante le condizioni di piena normali utilizzando i dati di tre misuratori di corrente, ottenendo buoni risultati di correlazione (rmse= 3,0 cm-s-1 e R2=0,7, in media). Le simulazioni del modello sono state in grado di riprodurre le sovraelevazioni indotte dalla bassa salinità alla bocca dell'estuario e alla piattaforma interna adiacente durante i periodi di alta portata del fiume dalla diga di testa (> 400 m3-s-1). Queste sopraelevazioni sono state identificate anche in un confronto qualitativo con i dati altimetrici. Nonostante i buoni risultati ottenuti, ci sono alcuni miglioramenti che potrebbero essere fatti per il lavoro futuro: includere il vento, accoppiare il modulo delle onde, aggiornare la batimetria, ecc.

Lo scopo dell'ultima sezione di questa tesi è stato quello di applicare la nuova tecnica di elaborazione Fully Focused SAR (FF SAR) per il segnale altimetrico di Sentinel-3. L'accuratezza e la precisione di questo nuovo prodotto sono state analizzate al fine di fornire il miglior prodotto di qualità vicino alla costa (segmento di traccia 0-5 km). L'elaborazione FF SAR è simile all'altimetria SAR, ma con un'alta risoluzione lungo la traccia senza precedenti che arriva fino al limite teorico pari alla metà della lunghezza dell'antenna (~0,5 m). In questo lavoro sono stati utilizzati due algoritmi FF SAR ancora in fase di sviluppo: FF SAR Back Projection (BP) (versione prototipo S3 di Kleinherenbrink et al., 2020), e FF SAR Omega-Kappa (WK) (Guccione et al., 2018), così come diversi algoritmi di retracking. Sono state elaborate due tracce da Sentinel-3A e due da Sentinel-3B, a 80 Hz. I prodotti sono stati validati confrontando le serie temporali di SLA con quelle ottenute da un mareografo nel Golfo di Cadice. L'accuratezza è stata analizzata utilizzando la Percentuale di Cicli per Alta Correlazione (PCHC) e la deviazione standard della differenza (sdd); e la precisione è stata determinata calcolando il rumore lungo traccia. Sono stati confrontati i prodotti FF SAR e SAR non focalizzati. I risultati hanno mostrato miglioramenti utilizzando il retracker *Adaptative Leading Edge Subwaveform* (ALES+) per il SAR non focalizzato, anche se il FF SAR BP con ALES+ è stato il prodotto più preciso per tutte le tracce. Inoltre, sono state ottenute misure SLA molto accurate anche con i prodotti FF SAR. Il maggior vantaggio del FF SAR è che produce dati di buona qualità più vicini alla costa (1-2 km) rispetto al SAR non focalizzato (3-4 km).

Infine, questi risultati evidenziano il potenziale dell'implementazione di dati altimetrici validati e modelli idrodinamici negli studi sul livello del mare. Inoltre, la metodologia qui descritta può essere utile per convalidare i dati altimetrici, così come per implementare il modello Delft3D in altre aree costiere.

Parole chiave: altimetria costiera, altimetria radar ad apertura sintetica, Sentinel-3, anomalia del livello del mare, altimetria SAR completamente focalizzata, Golfo di Cadice, modello Delft3D, calibrazione, validazione, estuario del fiume Guadalquivir, scarico fluviale, livelli d'acqua, confronto altimetria-modello.

Table of Contents

Chapter 6. Sentinel-3 Fully Focused SAR: precision and accuracy in the Gulf of Cadiz

List of figures

List of Tables

Acronyms

ADCP	Acoustic Doppler Current Profiler
ADT	Absolute Dynamic Topography
ALES	Adaptative Leading Edge Subwaveform
BA	Barcelona
BI	Bilbao
BP	Back Projection
CCC	Coastal countercurrent
CLS	Collecte Localisation Satellites
CNES	Centre National d'Etudes Spatiales
CS2	CryoSat-2
DAC	Dynamic Atmospheric Correction
DD	Delay-Doppler
EC	European Commission
ECMWF	European Centre for Medium-range Weather Forecasts
EIGEN	European Improved Gravity model of the Earth by New techniques
EMODnet	European Marine Observation and Data Network
ENL	Effective Number of Looks
ESA	European Space Agency
EUMETSAT	European Organisation for the Exploitation of Meteorological Satellites
FBR	Full Bit Rate
FF	Fully Focused
GI	Gijon
GIM	Global Ionospheric Maps
GLOSS	Global Sea Level Observing System
GNSS	Global Navigation Satellite System
GoC	Gulf of Cadiz
GPOD	Grid Processing On Demand
GRE	Guadalquivir River Estuary
HU	Huelva
IEO	Instituto Español de Oceanografía
LO	Land to Ocean

MO	Motril
MSS	Mean Sea Surface
OET	Ocean Equilibrium Tide
OL	Ocean to Land
PCHC	Percentage of Cycle for High Correlation
PLRM	Pseudo Low Resolution Mode
PRF	Pulse Repetition Frequency
PSMSL	Permanent Service for Mean Sea Level
PTR	Point Target Response
REDMAR	Red de Mareógrafos
S3A	Sentinel-3A
S3B	Sentinl-3B
SA	Santander
SAIH	Sistemas Automáticos de Información Hidrológica
SAMOSA	SAR Altimetry MOde Studies and Applications
SAR	Synthetic Aperture Radar
SARAL	Satellite with ARgos and ALtiKa
SARvatore	SAR versatile altimetric toolkit for ocean research and exploitation
SLA	Sea Level Anomaly
SRAL	Synthetic aperture Radar Altimeter
SRTM	Shuttle Radar Topography Mission
SSB	Sea State Bias correction
SSE	Sea Surface Elevation
SSH	Sea Surface Height
SWH	Significant Wave Height
TA	Tarifa
TG	Tide Gauge
TPXO	Topex Poseidon Global Inverse Solution
VD	Valid Data
WK	Omega (ω) Kappa

CHAPTER 1

General Introduction

This first chapter includes the introduction (Section 1.1), the aims of this thesis (Section 1.2), and the thesis outline that describes the structure followed in this manuscript (Section 1.3).

1.1. Introduction

The oceans cover approximately 71% of the Earth's surface, and are the equivalent of 97% of the available water on Earth (Hoegh-Guldberg et al., 2014). They play a fundamental role in climate regulation, since ocean circulation allows for the distribution of stored heat, carbon, nutrients, etc. The study of ocean circulation dynamics is fundamental at different scales: at large scale for climate studies, and at mesoscale or submesoscale for regional studies of, for example, coastal processes. The coastal zone is one of the most active areas of the planet, despite being only 7% of the ocean's surface (Wollast, 1998). A total of approximately 3 billion people occupied the first 200 km of the coastal strip, and this is expected to double by 2025 (Creel, 2003). For this reason, coastal zones are the main focus of many research studies on hydrodynamic circulation, flooding risk, dispersion of contaminants, etc. (Baawain et al., 2015). The spatiotemporal variability of coastal processes is very high, which makes their study more complex. Thanks to advances in the development of sampling techniques, instrumentation, models, and new technologies, the scientific community could soon have access to more information about the interactions that take place in the open ocean and coastal zones. Some of these important advances for coastal areas are the development of satellite coastal altimetry (Vignudelli et al., 2011), as well as high-resolution hydrodynamic models (Sutherland, 2004).

On one hand, satellite radar altimetry is an established science that has demonstrated its ability to provide high quality global data in open oceans (Cazenave et al., 2018). In coastal areas, great progress has been recently made (Benveniste et al., 2019) but there is still potential for improvement (Vignudelli et al., 2019). Nevertheless, satellite altimetry provides a better spatial coverage than in-situ data (tige gauges, high-frequency radar, etc.). One of the main advantages of coastal altimetry is that it is supported by a large scientific community (https://coastalt.eu/community) as well as space agencies such as the European Space Agency (ESA) and the European Organisation for the Exploitation of Meteorological Satellites (EUMETSAT). In the last decade, several initiatives, both national and international, have highlighted the need to re-process altimetric data near the coast in order to reach a level of quality of the same order of magnitude as that achieved in the open ocean. At the international level, some of the most important projects are ALBICOCCA (ALtimeter-Based Investigations in COrsica, Capraia and Contiguous Areas) (Vignudelli et al., 2015); ALTICORE (ALTImetry for COastal Regions);

ReCoSeTo (Regional Coastal Sea Level Change and Sea Surface Topography in Europe), PISTACH (Prototype Innovant of Système de Traitement pour les Applications Côtières et l'Hydrologie), COASTALT (development of radar altimetry data processing in the coastal zone), Baltic SEAL (created and validated novel multi-mission sea level product for the Baltic Sea), among many others; and at national level a noteworthy project is ALCOVA (Altimetry Coastal Validation) which focuses on the validation with in-situ measurements and product application for the study of the dynamics off the Iberian Peninsula south-western coast (Gómez-Enri et al., 2014, 2016a).

Other advantages of altimetric products are their high accuracy, repeatability and stability (Vignudelli et al., 2011), the availability of long time series for different products and variables (Figure 1.1), and publicly accessible data; for example, the Grid Processing On Demand service from the ESA (GPOD, https://gpod.eo.esa.int/), Copernicus Open Access Hub from the European Commission (https://scihub.copernicus.eu/), or Open Altimeter Data Base from the Deutsches Geodätisches Forschungsinstitut of the Technical University of Munich (OpenADB, https://openadb.dgfi.tum.de/).

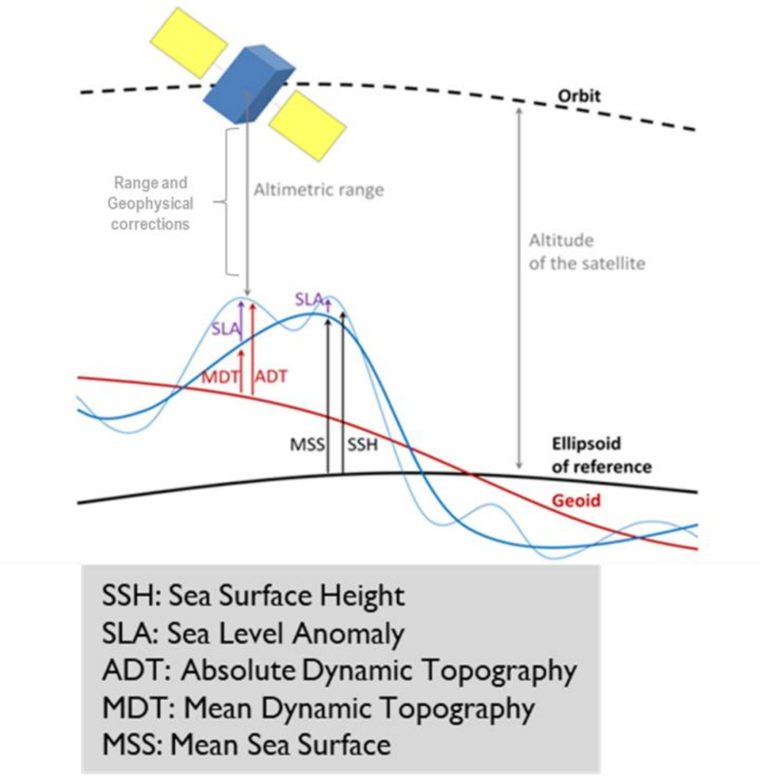

Figure 1.1. Different sea level variables used in altimetry. (Source: CNES/CLS).

Some of the most recent advances in coastal altimetry will be detailed throughout this manuscript: the development of Synthetic-Aperture Radar altimetry (SAR) (Raney, 1998), the progressive improvements in geophysical corrections (Fernandes et al. 2014; Handoko et al., 2017; Rieu et al., 2021), the implementation of coastal specific retrackers (Dinardo et al., 2018; Gommenginger et al., 2011; Passaro et al. 2014, 2020; Peng and Deng, 2018), the availability of accuracy products at high posting rate (Birol and Delebecque, 2014; Dinardo et al. 2018; Fenoglio-Marc et al., 2015; Gómez-Enri et al., 2017; Passaro et al., 2016), and the creation of new algorithms to process the satellite radar signal (Egido and Smith, 2017; Guccione et al., 2018). Nevertheless, there are also disadvantages, and improvements to be made, in relation to land contamination of the altimetry footprint close to the coast, as there are still some uncertainties in the range and geophysical corrections in coastal areas, and the spatiotemporal resolution is limited (Vignudelli et al., 2011). Regarding the corrections, satellite altimetry operates by transmitting a radiation pulse towards the sea surface and measuring the elapsed time needed by the signal to return to the altimeter, which is then used to estimate the range. The range is the measured distance between the instrument and the sea surface; however, some corrections should be applied to obtain the sea surface height (SSH) (Figures 1.1). Firstly, the range corrections, which include the wet and dry tropospheric correction, and the ionospheric correction. Secondly, the geophysical corrections, that should be applied to adjust the SSH by removing the effect of tides, atmospheric dynamics, and the sea state bias due to wind and wave conditions. For this reason, to continue improving the quality of the range and geophysical corrections, it is essential to obtain accurate SSH measurements in coastal areas (Vignudelli et al., 2011). With regards to the resolution, a good approximation in the absence of spatial-temporal coverage could be the multi-mission sea level product (e.g. Passaro et al., 2021) or the gridded maps generated by an optimal interpolation of along-track data (e.g. Gómez-Enri et al., 2015). Finally, in the case of the land contamination, more factors, analysed in this manuscript, are involved: the track orientation, the transition direction, and the angle of the track with respect to the coast (Vignudelli et al., 2011).

On the other hand, numerical modelling has become a useful and common tool to understand hydrodynamics at different scales. Over the 20th century, hydrodynamic models have evolved from simple one-dimensional analytical models to coastal profile, shoreline, and multi-line models (Lesser et al., 2004). In the last decades, the first two-dimensional models, initially depth-averaged, were developed as a tool for river engineering studies (Struiksma, 1985). Later, these models became a common tool in coastal areas for the analysis of dynamics and circulation patterns, as well as to study currents, return flows, the effects of bed slope, and the effects of wave asymmetry (Bos et al., 1996; Chesher et al., 1993; Nicholson et al. 1997; Tsimplis et al., 1995; Vriend et al. 1993; Watanabe et al., 1986). However, although two-dimensional models are a good approximation, e.g. for modelling large estuaries (Sandbach et al., 2018), they are not always enough to simulate small disturbances or interactions. For this reason, different 3D models have been developed and have been successfully applied in different coastal and estuarine environments (Bellafiore and Umgiesser, 2010; Chao and Boicourt, 1986; Cugier and Le Hir, 2002; Gessler et al. 1999; Lazure and Dumas, 2008; Reffray et al. 2004; Shchepetkin and McWilliams, 2005; among others). Nowadays, continuous improvements in computational capabilities allow for simulations of years and even decades (e.g. Roelvink et al., 2001; Steijn et al., 1998). Nevertheless, complex systems sometimes require the use of numerical models or model systems, more computationally intensive (Sutherland, 2004), that are able to simulate different combinations of processes, such as the Delft3D model used in this manuscript (Del-Rosal-Salido et al., 2019; Des et al., 2019; Elias et al., 2012; Khanarmuei et al., 2020; Lesser 2004, 2009; Martyr-Koller et al., 2017; Mendes et al., 2021; Pratama et al., 2020; Ruiz-Reina and López-Ruiz, 2021; Sandbach et al., 2018).

Hydrodynamic models present great advantages in comparison with in-situ measurements since they are cheaper than the field campaigns, and can simulate high spatiotemporal variations (Pratama, 2020). In addition, models allow for the recreation of different conditions to study how processes relate to each other. However, hydrodynamic models are a simplification of complex environments, so are commonly associated with systematic and random errors, which cause discrepancies between model results and in-situ measurements (Khanarmuei, 2020). In addition, the development of more complex models leads to an increase in the complexity of their results. For the implementation of useful models to study coastal zones, it is necessary to understand and quantify the uncertainties of the simulations (Allen et al., 2007). Model errors can be due to inaccuracies in process descriptions, parameterisation, initial conditions and forcings, or even because of the model solution algorithms used and the assumptions taken to simplify the model equations (Allen et al., 2007; Liu and Gupta, 2007; Loucks and van Beek 2017; Thompson et al., 2008). According to Thompson et al. (2008) special attention has to be paid to uncertainties introduced by external inputs in: geometry of the model grid, bathymetry, boundary condition data, initial conditions (e.g., salinity, wind, sediment), and model parameters (roughness and eddy viscosity, mainly). These uncertainties may be due to errors in the in-situ data collection, lack of replication, etc. (Allen et al., 2007).

In general, the discrepancy between model and in-situ observations can be reduced by a process of model calibration to modify the model parameters and structure (List et al. 1997). The choice of error statistics is also essential for the calibration and validation (Thompson et al., 2008). In this sense, Roelvink et al. (2009) proposed the use of the correlation coefficient, relative bias, scatter index, and the Brier Skill Score to quantify these differences. The availability of spatially distributed data is also important to reduce uncertainties and improve calibration results of hydrodynamic models (Straatsma and Huthoff, 2011). Remote sensing can be a particularly suitable tool to provide spatial information about the study area (Mertes, 2002). In fact, model results are regularly calibrated using altimetric data (Schumann et al., 2009), which could be a suitable complement to help reduce the overall uncertainty of model parameters (Berry et al., 2005; Jarihani et al., 2013) and predictions (Straatsma and Huthoff, 2011). In the same way, since the spatiotemporal resolution is a limiting factor in altimetry for monitoring the mesoscale variability in coasts, estuaries, or rivers (Vignudelli et al., 2011), hydrodynamic models can also be a good complementary tool for such studies.

There are numerous published works that show the complementarity of models and satellites, as well as their advantages. For example, some authors used satellite data to calibrate water level (Domeneghetti et al. 2015; Jiang et al., 2019; Liu et al. 2015; Paiva et al. 2013; Schneider et al., 2018; Shen et al. 2020), roughness (Liu et al. 2015; Schneider et al. 2018; Yan et al. 2014), discharges (Liu et al. 2015; Paiva et al. 2013; Paris et al. 2016) or bathymetry (Brêda et al., 2019; Jiang et al., 2019) in hydrodynamic models. In the case of Jiang et al. (2019), they used altimetry measurements to calibrate spatially distributed roughness coefficients and bathymetry simultaneously. They demonstrated the capacity of altimetry data for resolving uncertainties in model calibration. Also, Brêda et al. (2019) developed a methodology for obtaining accurate bathymetric data from altimeters, to be used in hydrodynamic models where bathymetry is often a source of error. In general, they obtained better calibration results with a higher spatial resolution satellite (e.g.

CryoSat-2). In this sense, Shen et al. (2020) highlighted the importance of designing future satellite altimetry missions by thinking of the hydrological applications. Moreover, altimetry data can also be used to validate the models, as done by Dhote et al. (2021). The authors used SARAL/AltiKa altimetry water level data to validate a hydrodynamic model (MIKE 11) implemented in the Brahmaputra River (India). Before the comparison, the authors calculated and corrected the bias between the datasets which was caused by their different reference systems. They obtained low rmse values (15-42 cm) comparing both datasets, proving the potential of both tools.

In summary, the wide availability of satellite altimetry data, new missions, hydrodynamic models development, and new methods to combine both data sources contribute to the capacity for monitoring coastal zones (Calmant et al., 2009). However, it is necessary to calibrate the models and the sensors on board the satellites and to validate the results obtained, which is the main focus of this thesis.

1.2. Aims of this study

Nowadays, more and more tools (instruments, models, technology, algorithms, etc.) are becoming available to study the processes that take place in the ocean and how they affect sea level variations. However, these same tools cannot always be used for the study of coastal zones, or not with the same quality or accuracy of results. The general aim of this thesis is to generate high quality products that advance our knowledge on sea level variation in coastal areas, using the most innovative tools available. For this purpose, the Gulf of Cadiz will be used as a natural laboratory for the validation and exploitation of coastal altimetry and model data. As previously mentioned, models and altimetry can be good complementary tools.

In order to achieve this main objective, the following specific objectives have been proposed:

(1) To determine the quality of altimetric data in coastal areas from the new Sentinel-3 space mission.

(2) To implement the Delft3D model in the Guadalquivir river estuary and part of the Gulf of Cadiz continental shelf with the aim of understanding the effect of the river's discharges on the sea level variability.

(3) To apply new processing techniques to the altimetry signal that will allow us to provide the best quality product for the study of sea level variations within the Gulf of Cadiz.

1.3. Thesis outline

This thesis is organized in 7 chapters. Each chapter includes its own section describing the data and methodology used, as these vary substantially by chapter. As a result, all chapters are organised as an article and the final structure of the thesis is as follows:

- The current chapter, **Chapter 1**, includes a general introduction that describes the two tools used in this thesis, altimetry and hydrodynamic models. It also details their main advantages and disadvantages in the study of sea level variability in coastal areas. Finally, the objectives of this thesis are described, along with the thesis outline.

- In **Chapter 2,** a detailed description of the study areas is presented. The chapter is divided into three sections; the first focuses on the main study area, the Gulf of Cadiz, the second details the characteristics of the Guadalquivir river estuary, and the third one summarises the other study areas used for the Sentinel-3 validation in Chapters 3 and 4.

- **Chapter 3** responds to the first objective of this thesis. For this purpose, Sentinel-3A is validated at locations on three different coasts of Spain. The results for Huelva, in the Gulf of Cadiz, are compared with the other study areas.

- As an addition to Chapter 3, **Chapter 4** includes the validation of the two Sentinel-3 satellites in orbit, Sentinel-3A and Sentinel-3B, in seven coasts around the Iberian Peninsula. Besides the comparison of both satellites, a comparison between different tidal models available is done in order to obtain the best product for each study area.

- **Chapter 5** is dedicated to the second objective. A description of the Delf3D model implementation in the study area is presented, as well as the model calibration and validation. This chapter also includes the results of a qualitative comparison with altimetry data.

- In order to fulfil the third objective of this thesis, **Chapter 6** presents the application of one of the most novel concepts in coastal altimetry, the Fully Focused SAR. This processing technique is used for Sentinel-3 altimetry in the Gulf of Cadiz. The validation results are compared with those obtained with unfocused SAR altimetry.

- The lasts chapters, **Chapter 7 and 8**, summarise the general conclusions and introduce some ideas about the future continuity of the work carried out in this thesis.

- Finally, the list of References cited along the manuscript is presented together with the Annexes. For ease of reading, the lists of figures, tables and acronyms used in the text are included at the beginning of this manuscript.

CHAPTER 2

Study Areas

This chapter is organized in three sections. A description of the Gulf of Cadiz is presented in Section 2.1. Section 2.2 gives more details about its main tributary, the Guadalquivir River, and the influence of its discharges on the Gulf of Cadiz continental shelf. Finally, Section 2.3 describes other study areas used in the altimetry products validation.

The target study area in this thesis is the Gulf of Cadiz and its principal tributary, the Guadalquivir River, which will be described in Section 2.1 and Section 2.2 respectively. Moreover other study areas around the Iberian Peninsula (Figure 2.1) were used in the works presented in Chapters 3 and 4, with the aim to validate the altimetry data under different hydrodynamic and tidal conditions (Section 2.3).

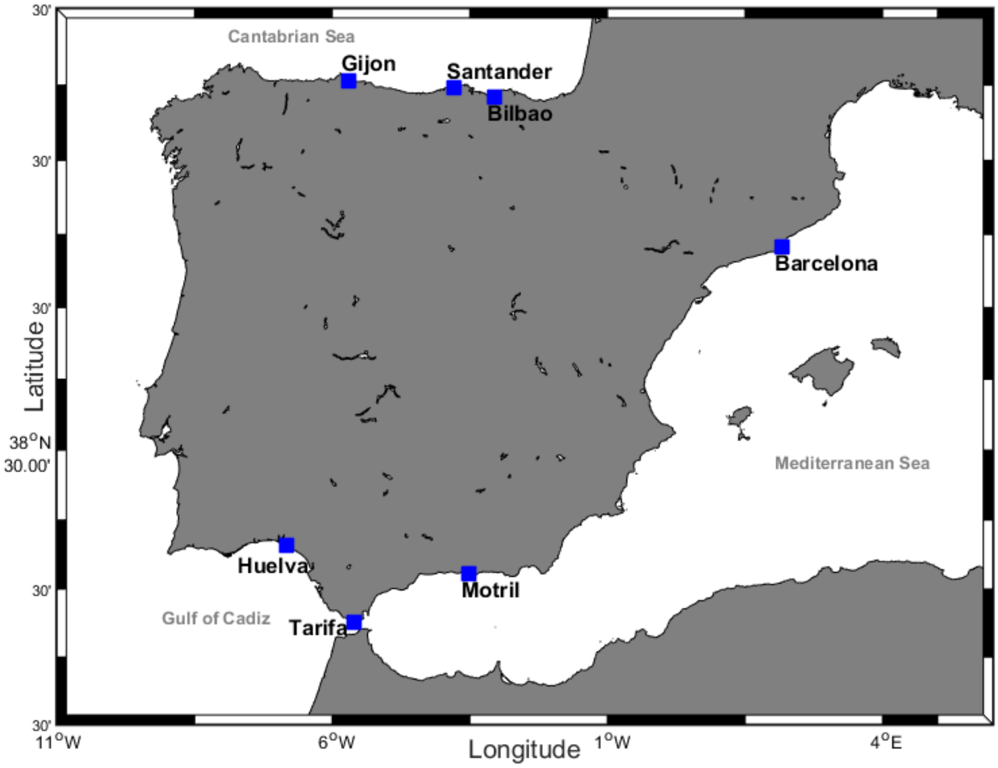

Figure 2.1. Map of the Iberian Peninsula where all the study areas are located (solid blue squares).

2.1. The Gulf of Cadiz

The Gulf of Cadiz (GoC, hereinafter), located in the southwest of the Iberian Peninsula, is the sub-basin that connects the Atlantic Ocean and the Mediterranean Sea (Figure 2.2). In this region, tides are mesotidal, with amplitudes above 1 m. Cape Santa Maria divides the GoC continental shelf in two, i.e., the eastern and western shelf, each of them with different circulation characteristics (Criado-Aldeanueva et al., 2009; Garcia-Lafuente et al., 2006). This thesis focuses on the eastern shelf, delimited by the 100 m isobath and characterised by a width of ~50 km (Garcia-Lafuente et al., 2006; Garcia-Lafuente and Ruiz, 2007).

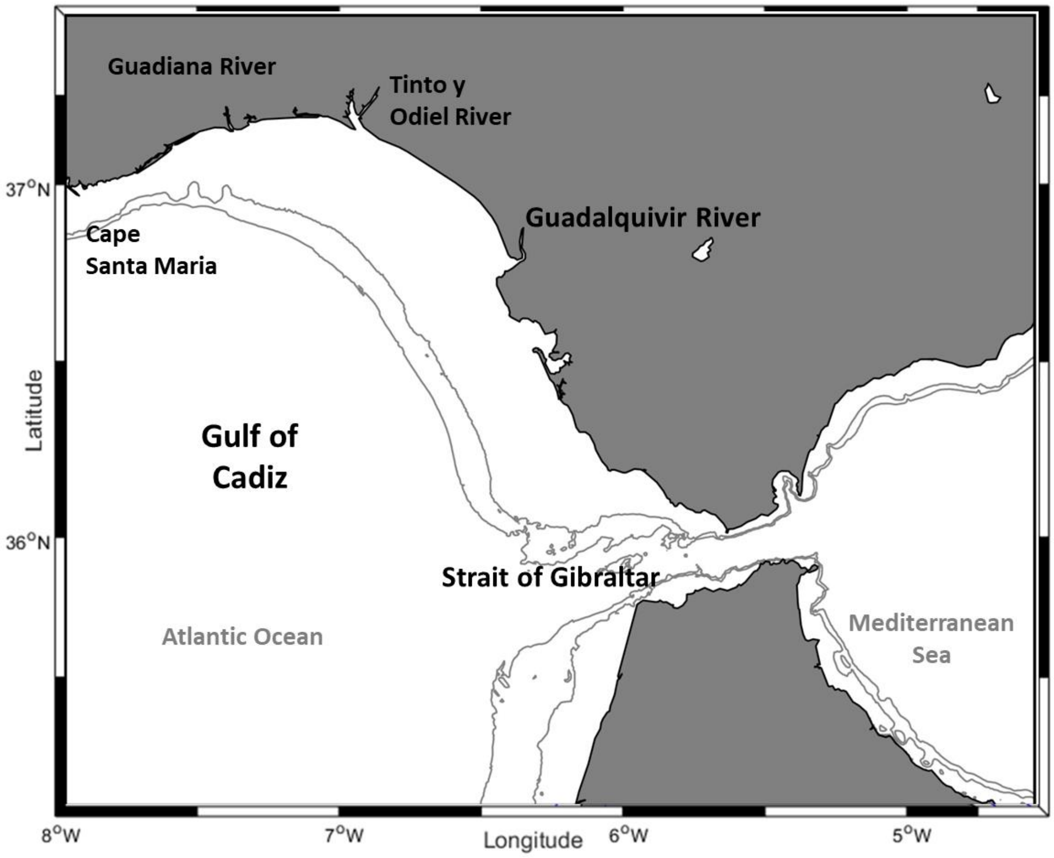

Figure 2.2. Map showing the eastern part of the Gulf of Cadiz. The 100 m and 200 m bathymetry lines are shown.

The GoC surface circulation is connected to the NE part of the North Atlantic Subtropical Gyre formed by the Azores current and presents the same strong seasonal variability (Garcia-Lafuente and Ruiz, 2007; Laiz et al., 2020). The GoC hydrodynamics is dominated by the exchange of water masses through the Strait of Gibraltar, located in the eastern boundary of the study zone (Jia, 2000; Johnson and Stevens, 2000). The warm and dry climate over the Mediterranean Sea causes strong evaporation and the production of a type of dense saline water that circulates through the Strait at greater depths (Gascard and Richez, 1985). The density contrast between the Mediterranean water and the less dense North Atlantic water forces a bilayer exchange flow through the Strait of Gibraltar (Baringer and Price, 1997, 1999; Ochoa and Bray, 1991). During summer, the surface circulation in the GoC is anticyclonic (Criado-Aldeanueva, et al., 2006; Sánchez and Relvas, 2003) and changes to cyclonic during winter (Criado-Aldeanueva, et al., 2006; Mauritzen et al., 2001). Moreover, some authors proposed the existence of a coastal countercurrent (CCC) in the northern fringe (Relvas and Barton, 2002; Stevenson, 1977) that, according to

Garcia-Lafuente et al. (2006) and Peliz et al. (2007), is part of the mesoscale cyclonic cell located over the eastern continental shelf between Cape Santa Maria and the mouth of the Guadalquivir estuary during spring–summer. In fact, according to García-Lafuente et al. (2006), the Guadalquivir River (Section 2.2) plays an important role in the eastern GoC surface circulation. Furthermore, Criado-Aldeanueva et al. (2009) concluded that this countercurrent is generally replaced by an eastward flowing current during autumn and winter. However, more recent studies using long time series of in situ currents measurement suggest that the onset of this countercurrent is a common feature over the year and does not show a seasonal behaviour (Garel et al., 2016). In any case, the strong seasonality of the GoC surface circulation is reflected in the sea level, whose seasonal cycle is mainly composed of the response to atmospheric pressure and the steric changes of the water column (Criado-Aldeanueva et al., 2008; García-Lafuente et al., 2004; Gómez-Enri et al., 2012; Laiz et al., 2013; 2016; Tsimplis and Josey, 2001). However, part of the sea level variability near the coast remains unexplained and may be related to the winds and the Guadalquivir River discharges (Laiz et al., 2016). In this sense, sporadic but heavy freshwater discharges might contribute to the sea level at different timescales (Gómez-Enri et al., 2016b, 2018; Laiz et al., 2013, 2016).

In addition to the Guadalquivir River discharges, the GoC used to receive considerable freshwater inflows from other rivers that flow into the basin (Ambar and Howe, 1979), such as the Guadiana, and the Tinto and Odiel system; however, the input of Tinto and Odiel has decreased significantly since 2005 (Laiz et al., 2020). The estuarine discharges and the effect of the tidal flow give the coastal waters some special thermal and biochemical properties: the presence of warm water masses (García-Lafuente et al., 2006), with a high nutrient concentration (Ruiz et al., 2006), and primary production (Navarro and Ruiz, 2006) during spring and autumn. These conditions make the GoC an area of great ecological interest and important wealth of marine living resources (Baldó et al., 2006; García-Lafuente and Ruiz, 2007; Navarro et al., 2006; Sobrino et al., 1994).

2.2. The Guadalquivir River estuary

The Guadalquivir River, with a length of 650 km, is the largest river in Andalucía (Spain) and is also the only navigable one. As mentioned before, the Guadalquivir is the main contributor of freshwater in the eastern GoC (Figure 2.3) and, for this reason, it plays an important role in the surface circulation (Garcia-Lafuente et al., 2006).

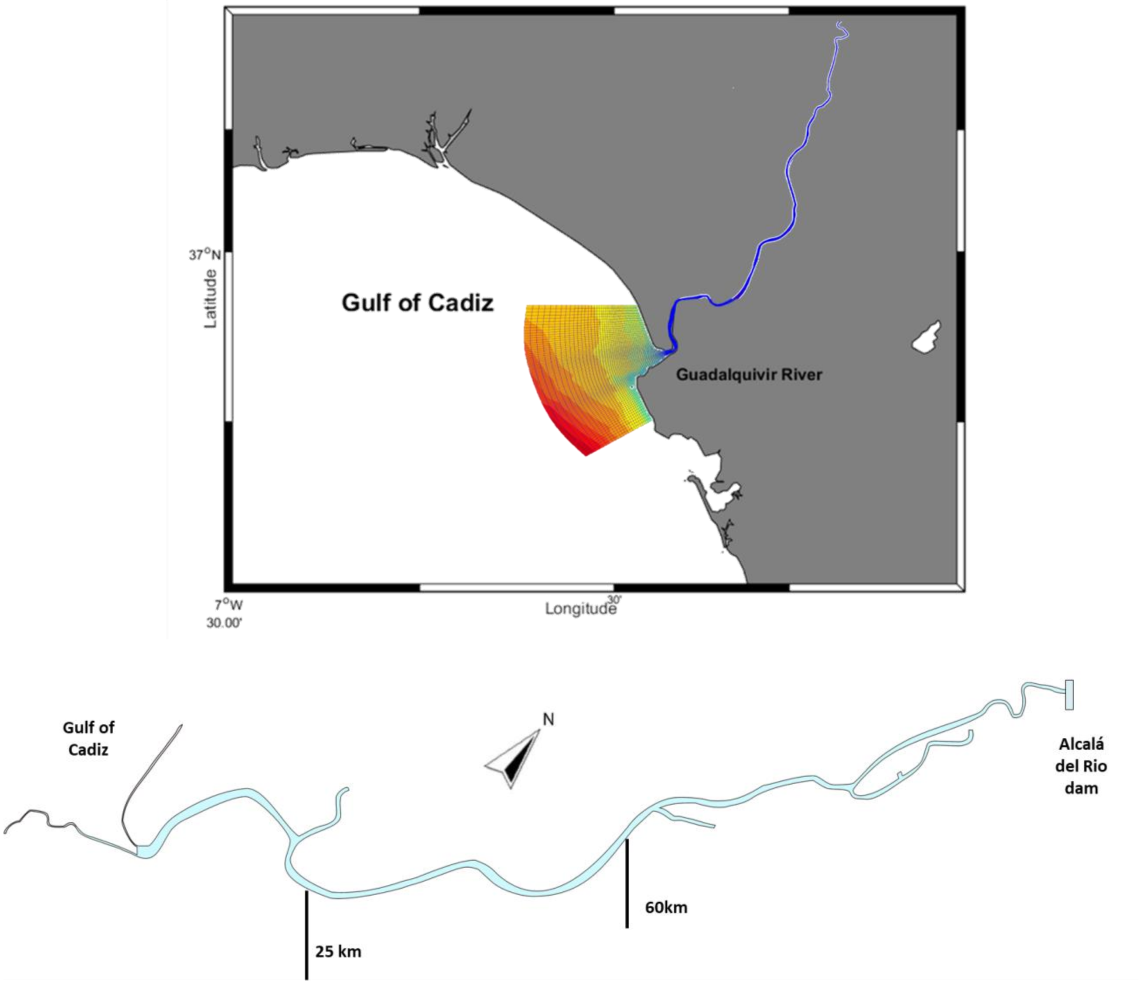

Figure 2.3. (a) Location of the Guadalquivir River estuary in the main study zone and area covered by the model grid implemented (Chapter 5), (b) sections along the river estuary (modified from Díez-Minguito et al., 2012).

The Guadalquivir River is characterised by a high sedimentation rate, which makes it difficult to ensure a minimum navigable depth. For this reason, the Guadalquivir River Estuary's (GRE, hereinafter) natural course has been modified anthropogenically since the 18th century. Currently, the GRE is limited by the Seville's port lock, located in a secondary channel (Figure 2.3). The tidal wave reaches the lock, establishing the head of the estuary 89 km upstream from the river mouth. This anthropogenic construction was built to eliminate the tidal effect in the port of Seville. Then, the depth of the main channel was modified annually or biannually from the mouth up to the port to enable a navigable access and to ensure a minimum navigational depth of 6.5 m below mean sea level (Díez-Minguito, 2012; Ruiz et al. 2015). Due to this, the depth of the main channel is quite uniform along the entire course; however, the width varies from 800 m at the mouth to 150 m at the head. The estuary is convergent, with cross-sections of 4525 m^2 at the outer part and 580 m^2 at the inner section (Díez-Minguito et al., 2012; Losada et al., 2017).

The GRE hydrodynamics is regulated upstream by the Alcalá del Rio dam, located 110 km from the estuary mouth (Contreras and Polo, 2012) (upstream boundary). The discharges from the dam constitute approximately 80% of the freshwater discharges in the estuary (Díez-Minguito, 2012; Navarro et al., 2012). Larger than average discharge rates (100–1000 $m^3\,s^{-1}$) may happen in winter as a result of heavy rainfall, or during spring and summer (100 $m^3\,s^{-1}$) at irrigation times (Contreras and Polo, 2012). According to Laiz et al (2020), the current mean daily river flow is less than 100 $m^3{\cdot}s^{-1}$, with a strong interannual variability, although during normal or low conditions the discharges can be as low as 40 $m^3{\cdot}s^{-1}$ or even less. During low discharge events the salinity intrusion in the estuary reaches the 70 km upstream mark, and occasionally the Port of Seville (Díez-Minguito et al., 2014). Under these conditions, the GRE is tidally dominated, vertically homogeneous, and well-mixed, with the estuary number (N) <0.1 according to the classification of Hansen and Rattray (1966). The flow discharge velocities vary between 1 and 5 $cm{\cdot}s^{-1}$, a negligible value in comparison to the 1 $m{\cdot}s^{-1}$ tidal velocities (Navarro et al., 2012). This situation is reversed during periods of high discharges, when the freshwater inputs can be higher than 400 $m^3{\cdot}s^{-1}$ and the estuary becomes fluvially dominated, with N>>0.1 (Díez-Minguito et al., 2012). In this case, the fluvial currents intensity is similar or higher than the tidal ones (Navarro et al., 2012). Under this scenario, the stratification increases, and a discharge plume can be observed together with a salt-wedge structure at the estuary mouth (Díez-Minguito et al., 2014). During high discharge events the salinity decreases in the estuary and also in the continental shelf, where the plume of less dense water produces an elevation of the water level (Díez- Minguito et al., 2012; Gómez-Enri, et al., 2015; González-Ortegón et al., 2010; González-Ortegón and Drake, 2012; Laiz et al., 2013; 2016; Navarro et al., 2012). This phenomenon can also affect the coastal countercurrent that needs an along-shore pressure gradient as a driver (Criado-Aldeanueva et al., 2009; García-Lafuente et al., 2006; Relvas and Barton, 2002; Stevenson, 1977). This pressure gradient could be related to the warm water accumulated in the Guadalquivir River mouth and the Cadiz Bay during spring and autumn (Navarro 2004); therefore, the countercurrent loses the buoyancy input during winter (García-Lafuente et al., 2006).

After a high discharge period, the estuary needs time to recover and return to its normal conditions. The recovery time depends on the characteristics (oceanographic and atmospheric conditions, the maximum discharge volume, the spring-neap tidal cycle, etc.) and the duration of the event (Díez-Minguito et al., 2012). Exceptionally extreme conditions in the estuary, with flows higher than 3000 $m^3 \cdot s^{-1}$ have also been reported by Díez-Minguito et al. (2012). Following Laiz et al. (2020), those extreme conditions were linked to negative winter NAO values and have not been observed since 2011.

In the GoC and also into the estuary the tide is mesotidal and semidiurnal, which means that the semidiurnal constituents M2, S2, and N2 are the most energetic, with amplitudes of around 1 m in the case of M2 (Álvarez et al. 2001). The ratio between diurnal and semidiurnal constituents (O1+K1)/(M2+S2) is approximately 0.1 (Losada et al., 2017).

Under normal discharge conditions, the estuary can be sectioned into three (Díez-Minguito et al., 2012): section 1, from the estuary mouth (0 km) to 25 km upstream; section 2, between 25-60 km; and section 3, from the 60 km mark to the Alcalá del Rio dam (see Figure 2.3). The first section presents a diffusive behaviour, i.e., the friction dominates and is higher than the inertial acceleration. The amplitude of the semidiurnal and diurnal tidal constituents decreases as a consequence of a rapid exchange in the mouth of the estuary and the presence of important meanders, among others (Díez-Minguito et al., 2012). In the middle section (25-60 km) the channel convergence and friction in the estuary are in balance, so the water level amplitude does not substantially change. The amplitude of the M2 and S2 constituents is amplified along the estuary due to a resonance phenomenon linked to anthropogenic modifications (Álvarez et al., 2001). It must be pointed out that the S2 period is close to the resonance period. Finally, in the last section the tide is affected by the Alcalá del Rio dam reflection, a process that can also influence the bed morphology (Díez-Minguito et al., 2012; Losada et al., 2017).

The state-of-the art presented in this chapter has been taken into consideration for the correct implementation of the model in the GRE (Chapter 5).

2.3. Other study areas for the altimetry validation

In the case of the altimetry studies addressed in this thesis, the study areas were selected based on the availability of radar tide gauge data in the regions where both ascending and descending tracks passed close to the in-situ instruments' locations. The validation of the altimetry sea level data was made in Huelva, located in the GoC (more details in Section 2.1), and in other coastal zones of the Iberian Peninsula. The altimetry study areas can be divided in three coastal environments with different tidal and hydrodynamic conditions: Bilbao, Santander and Gijon in the Cantabrian Sea; Huelva and Tarifa in the Atlantic Ocean; and Motril and Barcelona in the Mediterranean Sea (Figures 2.1).

2.3.1. Bilbao

Bilbao is situated in an embayment within the eastern North Atlantic Ocean, in the Bay of Biscay. The Spanish shelf in this area is narrow (30–40 km) in comparison with the French shelf (Mason et al., 2005). The Bay of Biscay is a region of large tidal amplitudes, between 1 and 4 m, of mesotidal type (Irabar and Ibáñez, 1979), and a strong thermohaline forcing (Pairaud et al., 2003). The circulation system is dominated by a weak anticyclonic circulation in spring and summer (Charria et al., 2013), a slope current, the input of freshwaters by various rivers, coastal upwellings, the northward flow of Mediterranean water, the transport along the submarine canyons (OSPAR, 2000), and the presence of mesoscale features, such as cyclonic and anticyclonic eddies. These features affect the exchange between the abyssal plain and the shelf (Charria et al., 2013; Ferrer and Caballero, 2011; Pingree et al., 1999).

Rivers in the Cantabrian shelf are short due to the proximity of the mountains to the sea, and their total run-off represents a third of the sum of the Loire and Gironde rivers, in the French margin. The maximum flow rates are mainly in spring and the minimum rates at the end of summer (Ferrer et al., 2009). Density currents are observed in the vicinity of estuaries due to the river freshwater discharges; these induce a poleward circulation as a result of the balance between the Coriolis force and the across-shore pressure gradient, modulated by wind (Froidefond et al., 1998; Hermida et al., 1998). The offshore extension of the overelevation caused by river discharge storm events depends on the watershed size and the river's discharge rate, being confined to the river mouth for small rivers (e.g., Nervión River, in Bilbao) and extending up to approximately 28-33 km offshore in the case of large rivers (e.g., Adour and Gironde Rivers, in the French coast), before turning northward to flow along the coast as a density current (Laiz et al, 2014). The main wind direction in the Bay of Biscay shifts from south-westerly to north-westerly (Pingree and Le, 1990).

2.3.2. Santander

Santander Bay is a large semi-closed water body located on the Cantabrian Coast, in the North Atlantic Ocean, belonging to the Bay of Biscay. This area is generally dominated by high energetic waves that propagate from the NW (humid) and other smaller waves from the NNE (cold and dry winds) (Cendrero, 1975; Mendoza et al., 2014). Tides are semidiurnal and mesotidal, with a mean range of 3 m and a spring tidal range of 5 m (Medellin et al., 2008). The area presents a narrow strip along the coast, characterized by the presence of different ecosystems: beaches, dunes, cliffs, marshes or tidal flats, which delimit the coastline (Cendrero, 1975). The total extension of the Santander Bay is of 22.5 km^2, and the 65% correspond to intertidal areas (López et al., 2013).

2.3.3. Gijon

The coastal region of Gijon is a well-mixed system located in the western coast of the Cantabrian Sea, within the Bay of Biscay (Gómez et al., 2014). The coastal shelf is narrow and is bordered mainly by steep cliffs (Flor-Blanco et al., 2015). Tides in this region are mesotidal with a mean tidal range of 2.8 m and a maximum of 4.8 m during spring (Gómez et al., 2014). There are two dominant winds in this area, the E-ENE in summer (weak winds) associated with a synoptic situation of high pressures, good conditions, and the W-WSW (strong winds) in winter (García et al., 2010; González-Marco et al., 2008). The main forcing responsible for coastal dynamic in the region is the wave, together with tides and river discharges (Flor-Blanco et al., 2015). For this reason, the estuaries in the Cantabrian shelf are mainly wave-dominated.

2.3.4. Tarifa

Tarifa is located in the central part of the Strait of Gibraltar (Figure 2.2), that connects the Atlantic Ocean and the Mediterranean Sea. The Tarifa Narrows comprise the narrowest area of the Strait of Gibraltar, with 15 km of width (Farmer and Armi, 1998; Sannino et al., 2002). This area has associated a complex hydrodynamic regime with different scales of variability (Lacombe and Richez, 1982). Winds in this area are zonal with alternative easterlies and westerlies that influence along and across coastal dynamics (Stanichny et al., 2005). Tides are semidiurnal, but with diurnal contributions (Candela, 1990; Mañanes et al., 1998; Tejedor et al., 1999). The tidal current is intensifying near the coastal margin between Tarifa and Gibraltar (Sánchez-Román et al., 2008). The Strait of Gibraltar constitutes a tidal transition area from the mesotidal regime of the GoC and the microtidal of the Alboran Sea. Therefore, is an area characterised by abrupt changes in the spatial structure of tides (González et al., 2019). For this reason, tides are the main forcing mechanism in the region, together with winds (quite persistent) and atmospheric pressure (Vázquez et al., 2008).

2.3.5. Motril

The coast of Motril is located in the northern margin of the Alboran Sea, western Mediterranean Sea. The tides in this area are also semidiurnal, and micro-tidal with an astronomical tidal range of 0.6 m (Bergillos et al., 2017). The tidal propagation and the current patterns are determined by the entrance of Atlantic waters through the Strait of Gibraltar Strait (Barcenas et al., 2011; Parrilla and Kinder, 1987). From a hydrodynamic point of view, the Alboran coasts are mainly dominated by low-energy waves from the W-SW and E-SE, with weak tidal currents (Ortega-Sánchez et al., 2017). According to the Spanish Puertos del Estado (www.puertos.es), easterly and westerly winds alternate in this region.

The littoral dynamics in Motril is complex due to the coastal morphology and the meteorological conditions (Barcenas, 2013; Ercilla et al., 2019; Lobo et al., 2014). This area is characterised by an abrupt coastal physiography due to the proximity of the Betic Mountains to the coast (Barcenas et al., 2011). One of the most important rivers in this region is the Guadalfeo (Viaña-Borja et al., 2019), which is delimited by the Salobreña rock in the west and the Motril Port in the east (Bergillos et al., 2016). The complexity of the coastal morphology is partly due to the submarine canyon system located in front of the coast of Motril that is composed of three main canyons: Almuñecar/Salobreña, Motril and Calahonda (Würtz, 2012). The canyons' system acts like a channel for currents, sediments, and nutrients. Therefore they are areas characterised by complex hydrodynamics and high biological productivity. In Motril in particular, the head of the canyons are located near the coast, at depths of less than 10 m according to Würtz (2012), hence affecting the coastal dynamics.

2.3.6. Barcelona

Barcelona is located in the northeastern part of the Iberian Peninsula, within the western Mediterranean Sea. The range of tidal amplitudes in the Mediterranean Sea is smaller than 1 m (i.e., microtidal). The surface circulation in the northwestern part of the Mediterranean Sea is generally cyclonic and thermohaline (Font et al., 1988). The current in this zone (Liguro-Provençal Current) follows a south-southwest direction. This current is determined by the Coriolis force and the pressure gradient established between the less salty waters (shelf waters) and the denser water masses (continental slope) (Arnau et al., 2004). The coastal hydrodynamics is mainly controlled by the local meteorology, oceanography, and the submarine physiography. The main river tributaries are the Rhone and the Ebro, which are two of the largest Mediterranean rivers (Canals et al., 2004).

CHAPTER 3

Validation of Sentinel-3A SRAL coastal sea level data at high posting rate: 80 Hz

---

The recent launch of the Sentinel-3 space missions requires an effort of the scientific community to determine the accuracy of the altimetric data generated. In this sense, this study will be added to international initiatives, such as the 'Sentinel-3 Validation Team', which are working to validate the products generated by these missions. The Sentinel-3 data will allow the generation of altimetric databases with a sufficient level of quality, both in the open sea and near the coast that can later be scientifically exploited.

The results obtained by validating time series of SLA from the Sentinel-3A SAR Radar ALtimeter (S3A) close to the coast, is described in this chapter. The validation was done using in situ TG measurements along three locations of the Spanish coast. This chapter is organized as follows. A brief introduction is presented in Section 3.1, then data and methodology in sections 3.2 and 3.3, respectively. Section 3.4 shows the results and Section 3.5 the discussion. Finally, Section 3.6 presents the main conclusions of this study.

This chapter was published during the development of this thesis: Aldarias, A., Gómez-Enri, J., Laiz, I., Tejedor, B., Vignudelli, S., & Cipollini, P. (2020). Validation of Sentinel-3A SRAL coastal sea level data at high posting rate: 80 Hz. *IEEE Transactions on Geoscience and Remote Sensing*, *58*(6), 3809-3821, doi: 10.1109/TGRS.2019.2957649.

3.1. Introduction

Satellite radar altimetry, over more than 25 years of its existence, has fully demonstrated its value to monitor global sea level (Cazenave et al., 2018). A great challenge being faced by the altimetry community is to improve the quality of data in coastal areas (Vignudelli et al., 2011) leading to reliable estimates of regional and local sea levels. The coastal altimetry community has faced two problems near the shore. On the one hand, there is a high level of uncertainty associated with the estimation of the geophysical parameters (retracked range, significant wave height (SWH), and wind speed at the sea surface) derived from processing the radar return signal (retracking), which is mainly due to the land contamination of the radar waveforms (Gommenginger et al., 2011). On the other hand, the quality of some range and geophysical corrections used to estimate the sea level [mainly wet tropospheric, tidal, and sea state bias (SSB) corrections] needs improvement (Andersen and Scharroo, 2011; Brown, 2010, 2013; Cipollini et al., 2017; Dinardo et al., 2018; Fenoglio-Marc et al., 2015; Fernandes et al., 2010; Fernandes and Lazaro, 2016; Gómez-Enri et al., 2016b, 2018; Passaro et al., 2016, 2018; Pires et al., 2016; Tran et al., 2010). While products from pulse-limited altimetry have traditionally been provided and used at a posting rate of 1 Hz (which corresponds to an along-track spatial resolution of 7 km between two consecutive measurements), higher rate products (10, 18, 20, or 40 Hz depending on the particular mission, equivalent to 700, 388, 350, and 175 m of along track spatial resolution, respectively) are also available. Some authors compared products at different resolutions in coastal areas for assessing the quality of these data. A validation study of sea level anomaly (SLA) was performed in the closest 30 km to the north-western coast of the Mediterranean Sea using in situ tide gauge (TG) measurements (Birol and Delebecque, 2014). They compared different altimetry products such as Topex/Poseidon at 1 and 10 Hz and Jason-1 and Jason-2 at 1 and 20 Hz. In the case of Jason-1, the correlation coefficients (r) were 0.70–0.76 and 0.73–0.80 at 1- and 20-Hz posting rates, respectively. For Jason-2, the r values were 0.69–0.79 (1 Hz) and 0.72–0.82 (20 Hz). The results indicated an increase in the quality and number of data available at 20 Hz in coastal areas. Then the pulse-limited satellite SARAL/AltiKa, designed to analyse mesoscale processes, was launched in 2013. This operates in the Ka-band with the advantage of a smaller footprint (Bonnefond et al., 2018; Verron et al., 2015). SARAL/AltiKa SLA data at 20 Hz were validated in Huelva (HU) (Gulf of Cadiz, GoC) and it was observed that the root mean square error (rmse) values increased toward the coast when compared with in situ data (Gómez-Enri et al., 2018). For example, the

authors obtained rmse values of 5.3 cm at 10 km, increasing to 35.4 cm at 5 km and to 57 cm at 1 km. This clearly highlights the need for improving the quality of coastal altimetry data. In a previous study, SARAL/AltiKa SLA time series at 40 Hz in the Strait of Gibraltar had been compared with in situ measurements obtaining along-track rmse values between 8 and 10 cm at 7 km from the coast (Gómez-Enri et al., 2016a).
Further advances in coastal altimetry are due to the synthetic aperture radar (SAR) mode of CryoSat-2. The improvements are due to a smaller uncertainty associated with the estimation of the geophysical parameters. SAR-mode altimetry has a smaller footprint in the along-track direction with respect to the pulse-limited footprints, which improves the along track spatial resolution, reduces the noise, and might decrease the land contamination of the radar waveforms (Fenoglio-Marc et al., 2015; Passaro et al., 2016). Therefore, it allows the study of shorter-scale ocean features and processes. Another advantage is a higher quality of the parameters derived from the altimeter measurements (Dinardo et al., 2018; Fenoglio-Marc et al., 2015; Gommenginger et al. 2013). CryoSat-2 SLA data at 20 Hz were validated using TGs in the German Bight and West Baltic Sea, for the 0–10 km segment from the coast (Dinardo et al. 2018). The study evidenced improvements from the SAR mode with respect to the pseudo low resolution mode (PLRM) within the coastal zone. The authors calculated the standard deviation of the difference (stdd) and the correlation coefficient, obtaining average values of 4.4 cm and 0.96, respectively. A similar study (Gómez-Enri et al., 2018) was carried out in Huelva for the 5–20 km segment, obtaining rmse values of 6.4 cm at 20 km, increasing to 8.5 cm at 5 km and to 29.3 cm at 1 km.

The objective of this chapter is to validate time series of SLA from Sentinel-3A SAR Radar ALtimeter (S3A, hereinafter) close to the coast, using in-situ TG measurements along three locations of the Spanish coast: *Huelva* (HU), *Barcelona* (BA) and *Bilbao* (BI). What makes this study novel is that S3A sea level data is analysed at the highest posting rate available, 80 Hz, equivalent to a distance between two consecutive along-track measurements of about 85 m. The number of valid data (VD) near the coast at the three locations, the orientation of the satellite tracks with respect to the land intersection, and the land contamination of the radar waveforms in the 0–5 km track segments are also analysed.

3.2. Data

3.2.1. Altimetry Data

S3A is part of the Sentinels constellation of the Copernicus program. This program is developed by the European Commission (EC) in collaboration with the European Space Agency (ESA) and the European Organisation for the Exploitation of Meteorological Satellites (EUMETSAT) (Dolon et al., 2012). Data from S3A were provided by the ESA Grid Processing On Demand (GPOD) SAR versatile altimetric toolkit for ocean research and exploitation (SARvatore) service, available at: https://gpod.eo.esa.int/. SARvatore-GPOD is based on the processing of S3A data from Level 1a data or full bit rate (FBR), up to Level 2. The SARvatore-GPOD service allows the user to configure the data processing at two processing levels: Level 1b, in which the multilooked radar waveforms are built, and Level 2 allow for the retrieval of the geophysical parameters. The S3A data processing was restricted to the study areas using a GPOD processing baseline tailored for coastal zones. The GPOD options selected for processing the data for this study at Level 1b were: hamming weighting, window in azimuth, approximated Doppler beam steering (beam-forming), Fast Fourier Transformation (FFT) zero-padding, and wider stack subsetting to give a final radar receiving window size of 512 samples. At Level 2, the options were: restricting the retracking to specific surface in all passes and applying a point target response (PTR) width alpha parameter obtained from a look-up table. The retracking method was SAR Altimetry MOde Studies and Applications (SAMOSA+), which is the SAMOSA 2 tailored for application in the open ocean, coastal zone and ice (Ray et al., 2015). Dinardo (2013) provided a complete description of this processing, and its impact on the data output.

S3A is in orbit since February 2016 with a track revisit time of 27 days. Data at GPOD are available since June 2016. Six ascending/descending tracks have been analysed (Table 3.1). The time period selected spanned from June/July 2016 (cycle 5 or 6, depending on the track) to October 2018 (cycle 36 or 37). A total of 32 cycles were retrieved in all cases. The along-track sampling rate selected was the highest of this altimeter in SAR mode: 80 Hz.

.

Table 3.1. Information about the number of track, location, latitude and longitude of the TGs, minimum distance between each TG and the tracks of S3A-SRAL in this zone, transition: OL or LO, time of over passing, and the smaller angle of the track with respect to the coast.

Track nb.	**#114**	**#322**	**#356**	**#008**	**#051**	**#071**
Location	Huelva (HU)		Barcelona (BA)		Bilbao (BI)	
TG position	37.13º N - 6.83º W		41.34º N - 2.17º E		43.35º N – 3.05ºW	
Min. distance TG-S3A SRAL	16.2 km	14.9 km	4.0 km	32.4 km	0.9 km	7.7 km
Type of transition	OL	LO	OL	LO	OL	LO
Track direction	Ascending	Descending	Ascending	Descending	Descending	Ascending
Time of over passing	22:00	10:54	21:21	10:23	10:45	21:40
Angle respect to the coast	46º	75º	39º	61º	74º	88º

3.2.2. Tide Gauge Data

Water levels from the Spanish Puertos del Estado tide gauges' network (http://www.puertos.es) were used in this thesis. This network is part of the Red de Mareógrafos (REDMAR), which is integrated into the Permanent Service for Mean Sea Level (PSMSL) and the Global Sea Level Observing System (GLOSS). The instruments are located at the ports of *Huelva*, *Bilbao*, and *Barcelona* (Figure 3.1). They all are radars, measuring with a frequency of 2 Hz. Although the real-time product is available at a 1-min interval, Puertos del Estado also provides a 5-min delayed product that has passed a standard quality control (Pérez et al., 2013). In addition, the information of amplitude and phase for the main tidal constituents, also provided by Spanish Puertos del Estado, was used for the tidal model assessment.

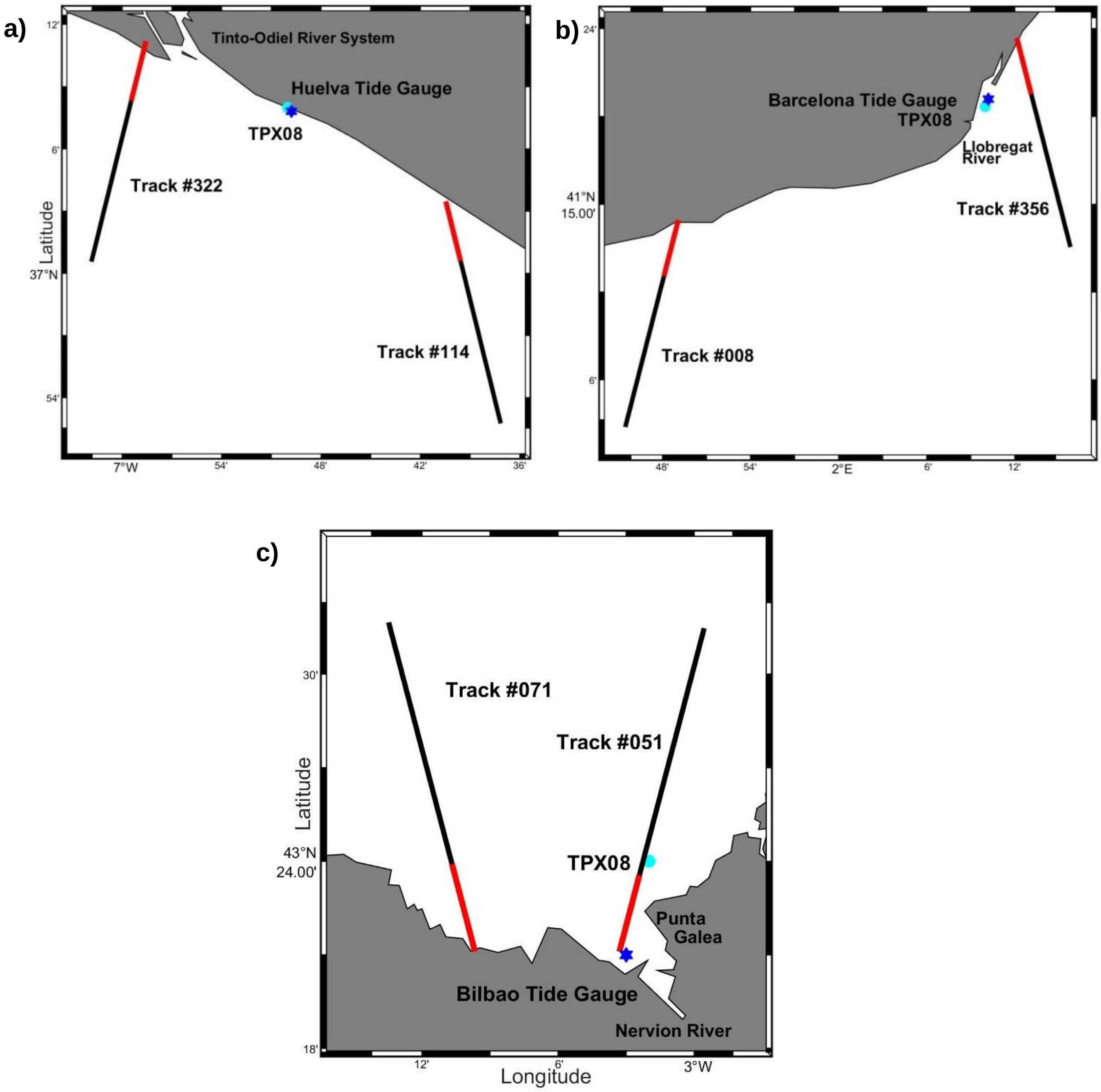

Figure 3.1. Study areas: (a) Huelva, (b) Barcelona, and (c) Bilbao. Track segments of the S3A orbits analysed. Black line: 5–20 km segment. Red line: 0–5 km segment. Blue star: TG positions. Blue point: closest points of the tidal model to the TGs.

3.2.3. Wave Data

Hourly wave height and period data were provided by Puertos del Estado, already corrected using their standard quality control procedures (Puertos del Estado, 2012, 2015a, 2015b). The wave buoys used in this article were: the GoC deep buoy, located at 69 km from HU_TG, the *Barcelona* coastal buoy, located at 4 km from BA_TG, and the *Bilbao-Vizcaya* deep buoy, located at 32 km of BI_TG.

3.2.4. TPXO8 tidal model Data

TPXO is a series of ocean tide global models, which fits the Laplace Tidal Equations and altimetry data. Each version of the model in the TPXO series is based upon an updated bathymetry and assimilates more data compared to previous versions. All TPXO models were obtained with OTIS (https://www.tpxo.net/otis) (Egbert et al. 1994, Egbert and Erofeeva, 2002). The version TPXO8_v1 tidal model (TPXO8) was used in this study.

3.2.5. Land Topography Data

Land topography was obtained from the Shuttle Radar Topography Mission (SRTM). The product used here was available at http://srtm.csi.cgiar.org/. This is version 4 of the 90 m spatial resolution product (Jarvis et al., 2008). The product from CGIAR-CSI (Consortium for Spatial Information) is based on the finished-grade 3 arc-second SRTM data processed by NASA.

3.3. Methodology

3.3.1. Altimetry

A total of 32 cycles of six different S3A tracks were used in this study (Figure 3.1). The along-track sampling rate selected was the highest of this altimeter in SAR mode: 80 Hz, equivalent to a distance between two consecutive along-track measurements of about 85 m. The time series at 80-Hz posting rate was built in four steps: (1) the latitude–longitude positions of the intersection of the tracks with the coast were obtained using the Google Earth's kmz files available in GPOD; (2) the 0–20 km track segments were selected using the positions obtained in the first step; (3) the distance between two consecutive radar measurements was checked within each cycle to ensure that it remained constant (~85 m); and (4) the time series was constructed using the 32 cycles along the closest tracks to the TGs. The maximum distance between the track segments and the TGs was 32.4 km (Table 3.1). The SLA (Figure 1.1) time series can be calculated using the following equation:

$$\text{S3A\_SLA} = \text{Orbit} - \text{Range} - \text{Range corrections} - \text{Geophysical corrections} - \text{Mean Sea Surface} \qquad \text{(Eq. 3.1)}$$

where Orbit (or Altitude) is the distance between the satellite's center of mass and the reference surface (ellipsoid WGS84). Range is the retracked distance between the instrument and the mean-reflected surface (Fenoglio-Marc et al., 2015; Ray et. al 2015), and it was obtained using the SAMOSA+ retracker (Ray et al. 2015). Range corrections include the dry and wet tropospheric effects from the European Centre for Medium-range Weather Forecasts (ECMWFs) models and the ionospheric correction from the Global Ionospheric Maps (GIMs) of the Jet Propulsion Laboratory. Although there are various alternatives for the wet tropospheric correction (Andersen and Scharroo, 2011; Cipollini et al., 2017; Handoko et al., 2017), GPOD only provides the one based on the ECMWF model. The geophysical corrections include the ocean equilibrium tide, the ocean long period, the ocean load tide, the solid Earth tide, and the pole tide. The atmospheric effects included in the dynamic atmospheric correction (DAC) were not applied to (Eq. 3.1). The tidal correction was obtained from the TPXO8 (Topex Poseidon Global Inverse Solution version 8) tide model (Egbert and Erofeeva, 2002), whose accuracy is analysed in Section 3.4.1. The sea state bias (SSB) correction is not available in the GPOD service at the posting rate used here (80 Hz). Therefore Section 3.4.2 is devoted to the analysis of a solution to overcome the lack of this correction, based on the SWH available in the product. The mean sea surface (MSS) used was DTU15 (Andersen, 2010; Andersen and Knudsen; 2009), the only one available in GPOD at the time of downloading the data.

3.3.2. Tide Gauges

The 5-min delayed tide gauges data were used in this study. The time series was built using the time of the closest measurements to the time of the altimeter data. The temporal difference between altimeter and TG data was below 2.5 min. The Sea Levels were obtained in the following equation:

$$\text{TG\_SeaLevel} = \text{Water Level} - \text{Tide Prediction} \qquad \text{(Eq. 3.2)}$$

where Water Level is the sea level measurement and the Tide Prediction was calculated from the TGs data with a classical harmonic analysis (Pawlowicz et al., 2002).

3.3.3. Comparison between Time Series

The temporal mean of the time series was eliminated to obtain the anomalies: S3A_SLA and TG_SLA, for the altimeter and TG data, respectively. Previously, a data screening was used to remove outliers: (1) the values outside the range: [−1.5, 1.5] m and (2) the values outside the median ± 3 standard deviation (std). Finally, an extra outlier detector was applied to the time series of altimeter measurements based on the along track SWH (available at 80 Hz along-the-track segments). All the measurements outside the range: [0–8] m were considered as an invalid measurement for the computation of the SSB and, thus, discarded. About 5% of the along-track SWH was negative and about 1% bigger than 8 m. The selection of 8 m was made based on the analysis of the wave height roses from the closest buoys to the TG stations for the period 2016–2018 (see Figure 3.2). As shown in Figure 3.2, SWH > 8 m are not observed in the study areas along the analysed time period.

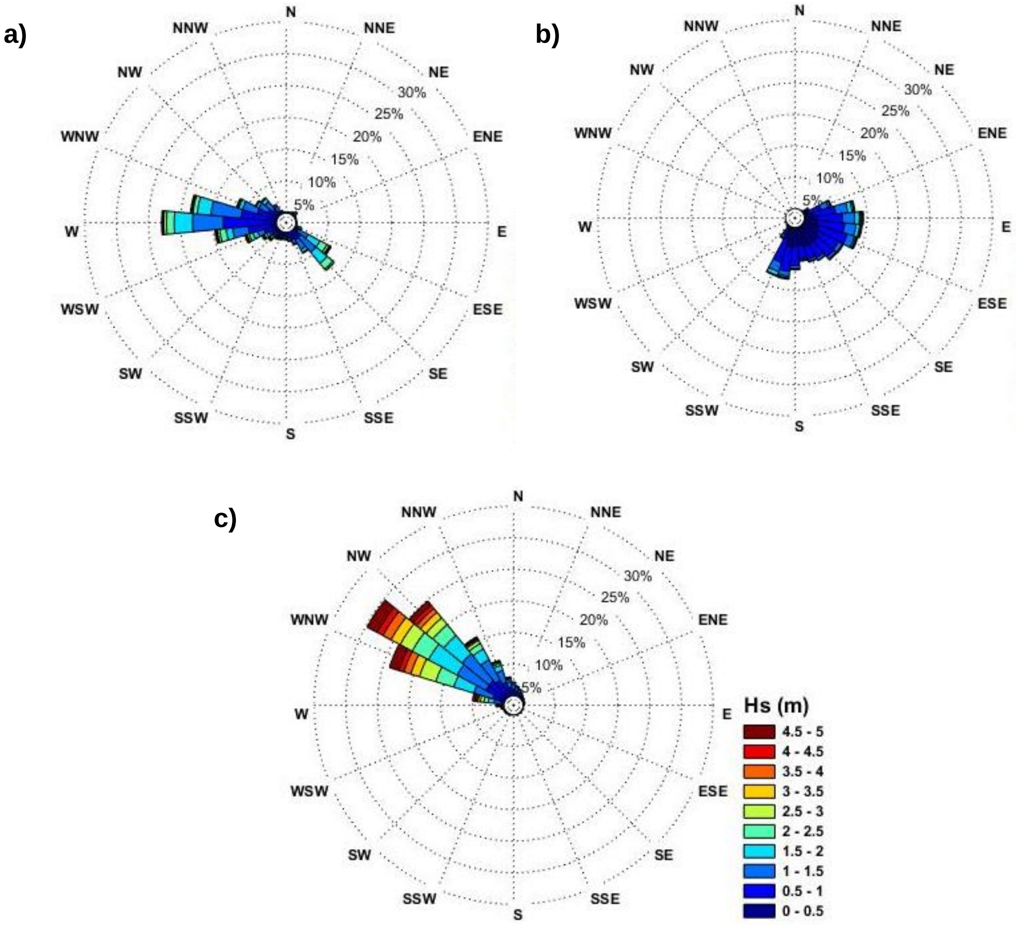

Figure 3.2. Wave roses for the period 2016–2018 from (a) Gulf of Cadiz, (b) Barcelona, and (c) Bilbao-Vizcaya buoys.

Only those tracks with at least 20% of valid cycles, i.e., cycles that successfully passed these screening, were considered for the validation. The S3A_SRAL time series was validated with the TG_SLA ones using two statistical parameters, namely, the Pearson correlation coefficient (r) and the rmse, as in (Birol and Delebecque, 2014; Dinardo et al., 2018; Fenoglio-Marc et al., 2015; Gómez-Enri et al., 2016b, 2018; Passaro et al., 2016). The validation focused on the along-track segment located between 0 and 20 km, with 0 km corresponding to the point where the track intersects the coast.

3.4. Results

3.4.1. Tidal Model Assessment: TPXO8

The TPX08 tide model generates a basic global solution for the main harmonic constituents with 1/30° resolution in the majority of the coastal areas (and 1/6° resolution in the rest of the ocean). The tide model was assessed by comparing the constituents available in the model with the constituents obtained from the TG data analysis. The comparison was made with the closest tidal points to the TGs (Figure 3.1). The amplitudes and phases of the nine constituents available in the global model were compared with those obtained with the TGs and are shown in Table 3.2.

Table 3.2. Amplitudes (cm) and phases (º) of the main tidal constituents in Huelva (HU), Barcelona (BA) and Bilbao (BI). Data from Puertos del Estado TG and the global tidal model TPXO8.

Tidal constituents			**M2**	**S2**	**N2**	**K2**	**K1**	**O1**	**Q1**	**P1**	**M4**
HU	**Amp (cm)**	**TG**	104.0	37.8	22.2	10.6	6.6	5.8	1.7	2.3	2.8
		TPXO8	102.1	37.2	21.7	10.3	6.6	6.0	1.8	2.0	1.7
	Pha(º)	**TG**	57.4	84.1	41.3	81.1	48.1	311.1	228.0	41.9	170.2
		TPXO8	57.1	83.1	41.1	79.3	50.5	308.2	257.5	45.0	156.4
BA	**Amp (cm)**	**TG**	4.6	1.7	1.0	0.5	3.7	2.4	0.3	1.2	0.5
		TPXO8	4.5	1.5	1.0	0.5	3.6	2.2	0.3	1.2	0.4
	Pha(º)	**TG**	213.5	230.7	201.5	228.6	167.8	102.9	51.3	160.4	346.8
		TPXO8	220.5	238.4	204.0	233.1	167.1	108.4	71.6	155.6	356.3
BI	**Amp (cm)**	**TG**	131.1	45.9	27.8	13.0	6.4	7.0	2.2	2.0	2.7
		TPXO8	133.7	46.5	27.9	13.1	6.6	6.6	2.2	2.1	2.5
	Pha(º)	**TG**	92.4	124.9	72.8	121.8	58.9	321.3	274.2	57.0	324.4
		TPXO8	95.3	127.2	85.7	125.0	74.3	323.6	275.2	64.6	306.9

The assessment was performed by estimating the root mean squares (rms) and the root sum of squares (rss) between the tidal model constituents and the TGs data (Oreiro et al., 2014). A summary of the results is shown in Table 3.3. The rms is smaller than 2 cm for all the constituents and locations with the exception of the M2 at *Bilbao* (4.99 cm). The rss is below 2 cm at *Huelva* and *Barcelona*, and up to 5 cm at *Bilbao*. This could be due to the fact that the tidal point used at *Bilbao* is about 6 km away from the TG. The difference in amplitude and phase of the M2 between the model and the TG (Table 3.2) at this location explains the magnitude of the rms and rss, respectively. The results at *Huelva* are in agreement with (Gómez-Enri et al., 2018), where an rss of 2.4 cm was obtained using the outputs of the DTU10 tidal model (Cheng and Andersen, 2011) and the same HU_TG used here. Hence, the TPXO8 model seems to be a good choice to reproduce the tides at the three locations.

Table 3.3. Assessment of the TPXO8 model in the closest point to the tide gauges. Comparison of amplitude and phase of the main tidal constituents using the statistics: room mean squares (rms) and residual sum of squares (rss).

MAIN TIDAL CONSTITUENTS	rms (cm)		
	HUELVA	BARCELONA	BILBAO
M2	1.41	0.40	4.99
S2	0.65	0.17	1.69
N2	0.29	0.03	0.98
K2	0.30	0.03	0.53
K1	0.20	0.08	0.48
O1	0.23	0.19	0.36
P1	0.65	0.08	0.03
Q1	0.23	0.08	0.20
M4	0.86	0.16	0.58
rss (cm)	**1.97**	**0.52**	**5.45**

3.4.2. SSB Correction

As mentioned before, SSB correction is not available in the GPOD service at 80 Hz posting rate. In order to get a first approximation of this correction, a parametric approach was made by estimating the rmse between S3A_SLA and TG_SLA, when SSB values ranging between 0% (no correction) and 10% of the SWH were applied in (Eq. 3.1). The mean rmse for the track segment between 5 and 20 km to the land intersection was estimated. The reason why this track segment was selected is explained later in Section 3.4.3 and 3.4.4. The results are shown in Figure 3.3 for *Huelva* (Figure 3.3a), *Barcelona* (Figure 3.3b), and *Bilbao* (Figure 3.3c), respectively. Overall, the smaller rmse values were observed for SSB corrections ranging between 4% and 7% of the SWH, with very small differences among them of about ±0.01 cm. Hence, an SSB correction of 5% of the SWH was used at all the locations and tracks, in agreement with Fenoglio et al. (2015) and Gómez-Enri et al. (2018).

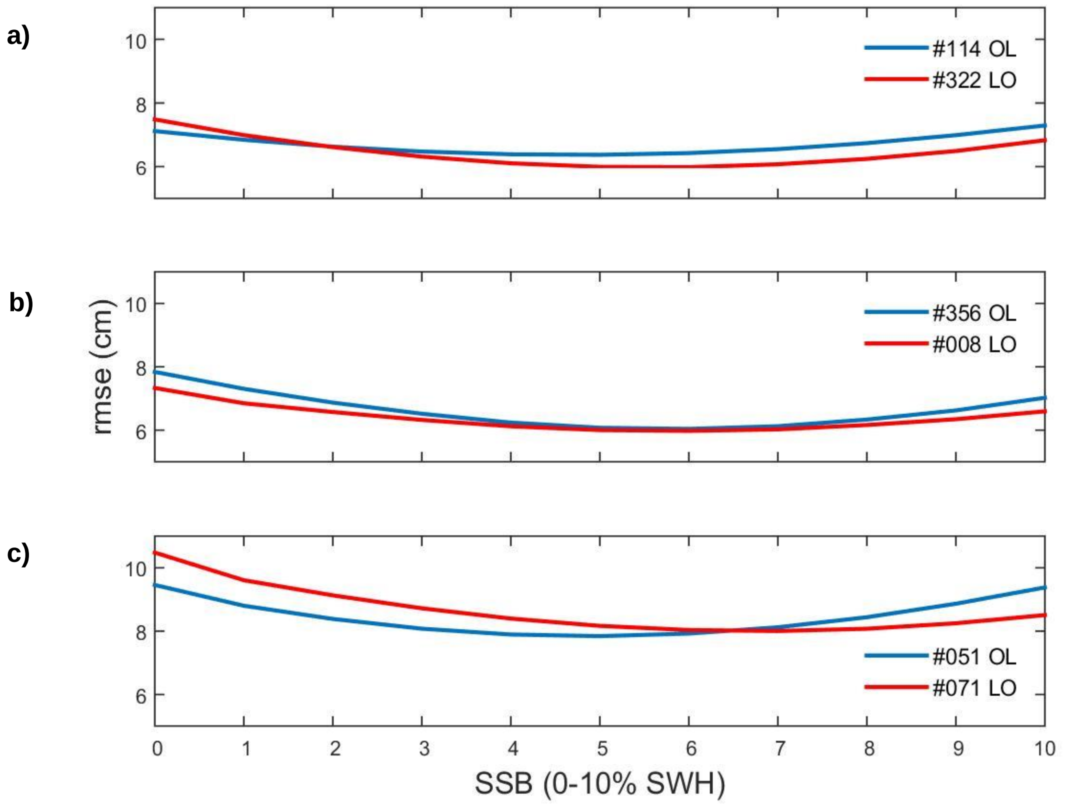

Figure 3.3. Rmse (cm) between S3A_SLA and TG_SLA time series as a function of the percentage of SWH used for the SSB correction at: (a) HU, (b) BA, and (c) BI. Blue line: OL transition. Red line: LO transition.

3.4.3. Availability of Altimetry Data near the Coast

The number of valid data (VD) along-the-track segments are analysed in detail, taking into account their proximity to the coastal crossing, measured as the distance from the intersection of the track with the closest land. Figure 3.4 shows the number of VD along the whole track segment, defined as a distance of 0–20 km to the track's intersection point with the land.

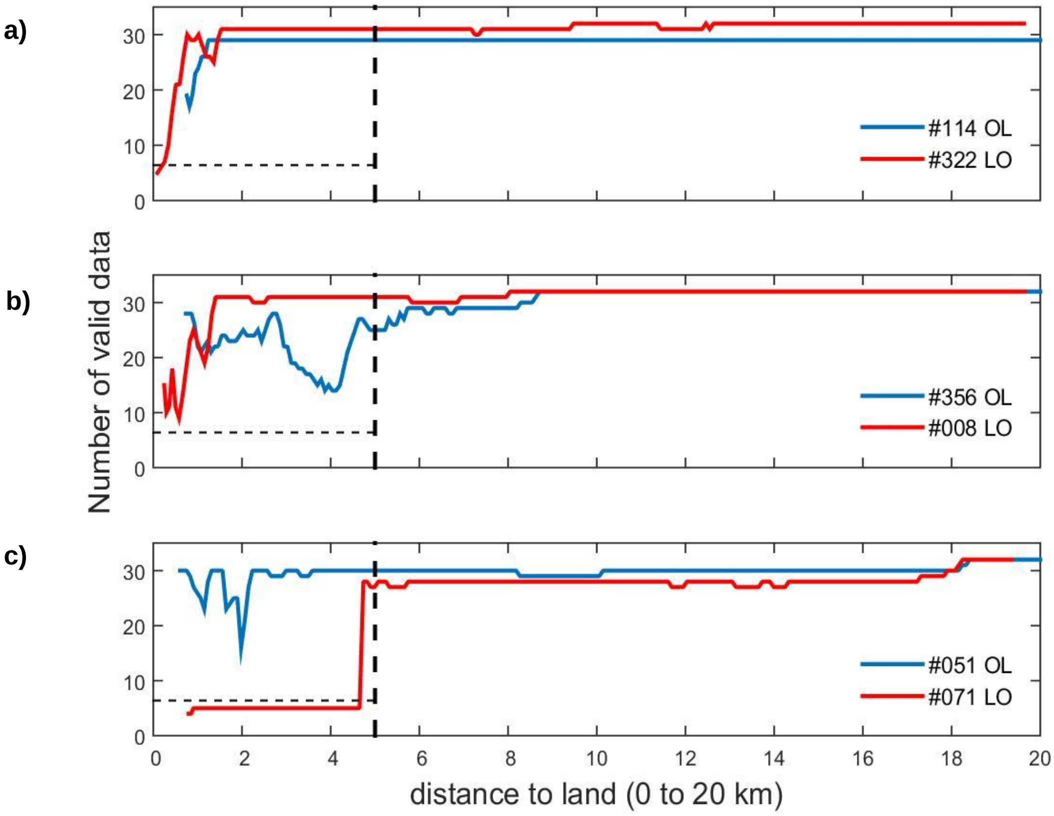

Figure 3.4. Number of valid data in the track segment 0-20 km for (a) HU, (b) BA, and (c) BI. The dashed black line (vertical) indicates the position of the 5 km distance to the coast. The dashed black line (horizontal) gives the limit of 20% of valid data.

The maximum number of VD is 32 (corresponding to 27-day cycles) for all the tracks. Note that three cycles of track #114 (HU) were considered invalid due to the lack of the ocean equilibrium tide correction (OET). The number of VD at *Huelva* is 32 (#322)/29 (#114) up to 2 km to the land intersection (Figure 3.4a). The same is observed for track #008 at *Barcelona* (Figure 3.4b) and #051 at *Bilbao* (Figure 3.4c). Track #356 (BA) shows a strong reduction in the number of VD in the 0–5 segment. Finally, track #071 (BI) shows around 20 valid cycles in the track segment 5–20 km, and a considerably smaller number along the 0–5 km segment.

Table 3.4 summarizes the comparison between the S3A_SLA and TG_SLA time series in the 0–5 km, 5–20 km, and 0–20 km segments at the three locations. The mean rmse, r, confidence level (CL) and percentage of VD were calculated in the three considered track segments. The smaller rmse and larger r values correspond to the 5–20 km segment for all the tracks and locations. The 0–5 km segment, however, shows the largest rmse and smaller r for all the locations and tracks. No valid numbers are shown on track #071 within this segment due to the low percentage of VD (15.6%) obtained. These results reinforce the idea of avoiding using the closest track segments to the coast. A more detailed analysis of the 0–5 km segment is given in Section 3.5.

Table 3.4. Results of the comparison between the altimeter and TG SLA time series in the study areas (HU: Huelva, BA: Bacelona, and BI: Bilbao). Average of rmse (cm), r, CL, and percentage of VD for different portions of the track segments: 0-5 km, 5-20 km, and 0-20 km with respect to the coast.

		0-5 km				**5-20 km**				**0-20 km**			
Zone	**Track**	**rmse (cm)**	**r**	**CL (%)**	**VD (%)**	**rmse (cm)**	**r**	**CL (%)**	**VD (%)**	**rmse (cm)**	**r**	**CL (%)**	**VD (%)**
HU	**#114**	14.2	0.6	95.5	86.0	6.4	0.8	100	90.6	8.0	0.8	99.1	89.9
	#322	16.4	0.6	92.1	87.9	6.0	0.8	100	98.8	8.6	0.7	98.0	96.1
BA	**#356**	29.0	0.2	67.0	68.2	6.1	0.8	100	97.6	11.5	0.6	92.6	90.8
	#008	12.3	0.7	98.5	85.7	6.0	0.8	100	99.1	7.6	0.8	99.6	95.8
BI	**#051**	20.2	0.5	90.5	89.5	7.8	0.8	99.9	94.1	10.9	0.7	97.6	93.0
	#071	---	---	---	15.6	8.2	0.7	99.8	88.5	9.6	0.7	93.5	88.6

3.4.4. Validation of Along-Track S3A Data

Along-track r (Figure 3.5) and rmse (Figure 3.6) values are shown at three locations: *Huelva*, *Barcelona* and *Bilbao*, at 80 Hz posting rate in the 5–20 km segment.

Overall, larger correlations correspond to smaller rmse for all the locations and tracks. The 5–7 km segment shows slightly smaller/bigger r/rmse in some tracks: #322 (HU), #356 (BA), #051, and #071 (BI). Good correlation (>0.8, 95% C.L.) and small rmse (<8 cm) values are obtained along the 7–20 km segment for these tracks and along the 5–20 km segment for tracks: #114 (HU) and #008 (BA). The only exception is observed on track #071 (BI) (Figures 3.5c and 3.6c) at distances between 12 and 17 km to the land intersection. In order to explain this, a more detailed analysis was carried out.

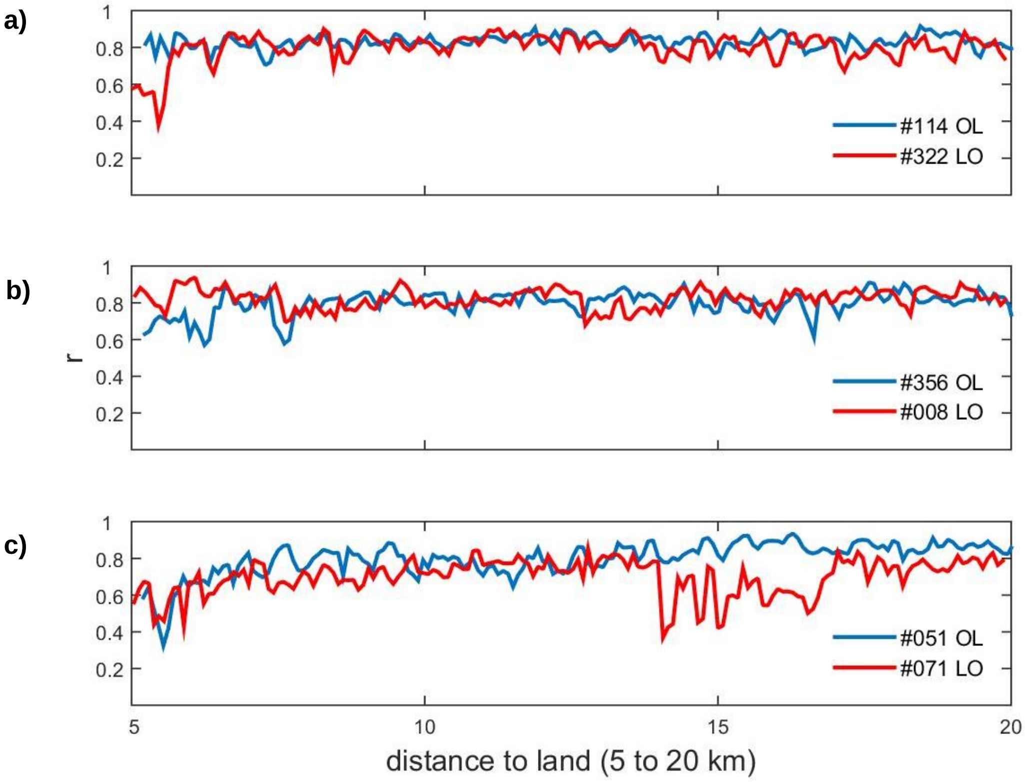

Figure 3.5. Along-track values of r in the 5-20 km track segment at (a) Huelva, (b) Barcelona, and (c) Bilbao.

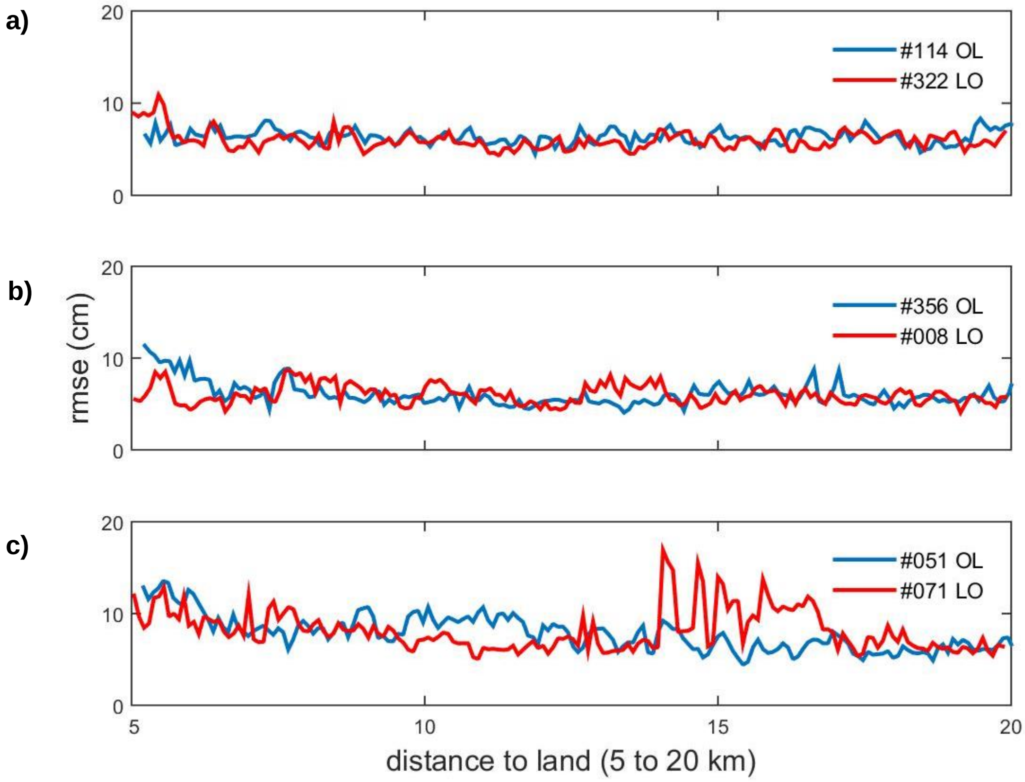

Figure 3.6. Along-track values of rmse (cm) in the 5-20 km track segment at (a) Huelva, (b) Barcelona, and (c) Bilbao.

The cycle-by-cycle along-track S3A_SLA is shown in Figure 3.7a for track #071. Missing data (i.e., non-valid measurements) are observed along most of the track segments in a few cycles as a result of the data-screening process. Cycle 32 (June 5, 2018) shows anomalous (negative) values of SLA in the 12–17 km segment (Figure 3.7b). A deeper investigation of the corrections used in (Eq.3.1) shows that these values correspond to strong negative values in the SSB, which are due to large SWH values. However, the in situ wave buoy time series for that date does not show such high SWH values (Figure 3.2c), the maximum wave heights being about 1.5 m. Thus, retracked high waves could be due to the retracking failing to accurately retrieve the SWH.

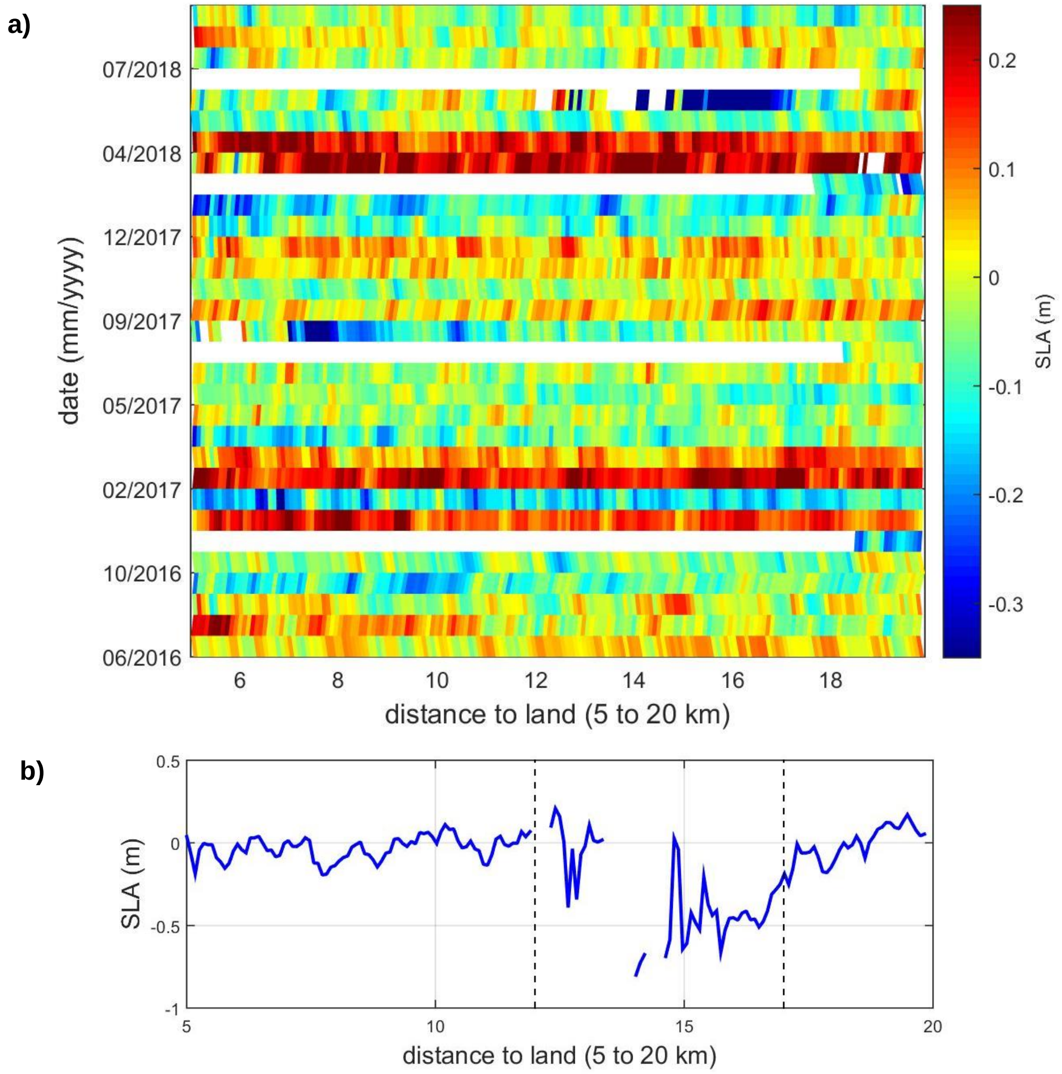

Figure 3.7. (a) Cycle-by-cycle S3A_SLA values in the 5-20 track segment for track #071. (b) S3A_SLA from cycle 032 (June 5, 2018).

Figure 3.8b shows the radargram of the waveforms (cycle 32, track #071). Note that only the power from gates 300 to 400 is shown. High power is observed in the leading edge area at distances from the coast bigger than 17 km, but in the 12 – 17 km segment the power has a much lower level, while higher than average power levels appear in the trailing edge portion of the waveform. A possible explanation for this distribution of power in the waveforms could be the presence of downslope wind gusts in the coastal zone, combined with calmer conditions offshore, with a transition zone in the 12 -17 km distance. Such a distribution of power complicates the retracking of the waveforms and hence the retrieval of accurate geophysical parameters, especially SWH.

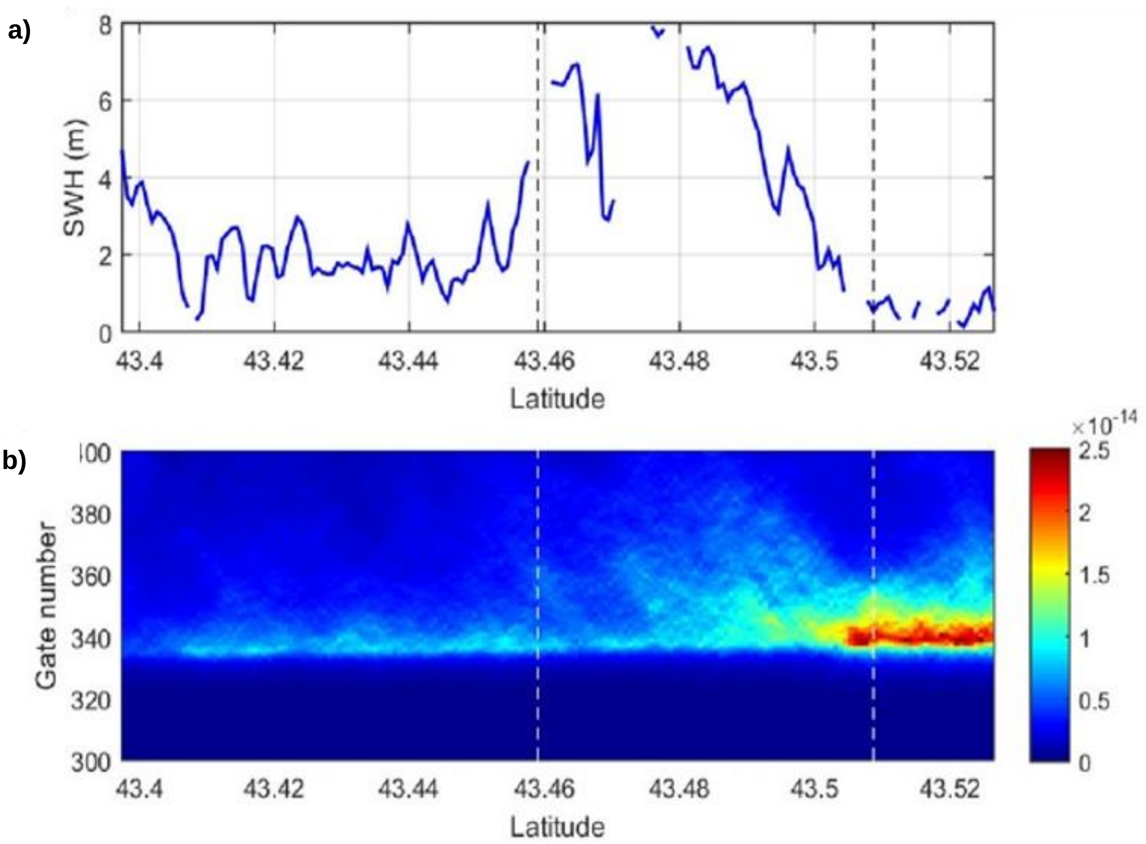

Figure 3.8. (a) Along-track SWH of track #071 (cycle 032) along the 5-20 km track segment (BI). (b) Radargram of the waveforms (only from gate 300 to 400) (power in watts). The positions corresponding to 12 and 17 km to the coast are indicated in black and white dashed lines.

Hence, the same analysis shown in Figures 3.5 and 3.6 was performed for track #071, but excluding cycle 32 from the time series before the comparison with in situ data. The removal of cycle 32 does not affect the along-track values of r (Figure 3.9a) and rmse (Figure 3.9b), with the exception of the 12–17 km segment, where better results are clearly observed. The removal of cycle 32 reduces the average rmse in the 5–20 track segment from 8.2 to 7.3 cm. This example highlights the importance of designing an accurate data screening strategy, supported with in situ data.

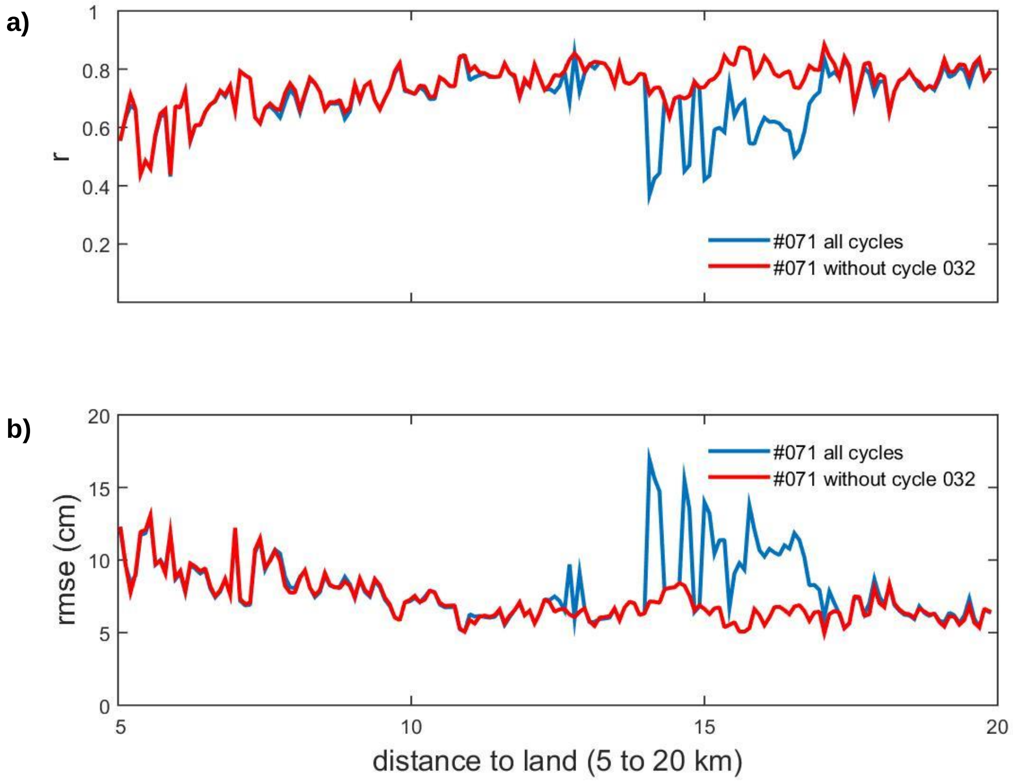

Figure 3.9. Along-track values of (a) r and (b) rmse of track #071 considering all the cycles after data screening (blue line), and removing cycle 32 (red line).

A similar, but significantly weaker behaviour can be found on track #008 (BA) in the 7–14 km segment (Figures 3.5 and 3.6). The analysis of the cycle-by-cycle along-track S3A_SLA (not shown here) presents anomalous values of SLA on cycle 06 (June 29, 2016), also related to high SWH values. The removal of cycle 6 from the S3A_SLA time series presents better results in terms of r (Figure 3.10a) and rmse (Figure 3.10b) along that track segment. When removing cycle 06 from the analysis, the average rmse drops to 5.4 cm in the 5–20 km track segment. Finally, the same problem was observed on track #322 (HU). In this case (not shown here), cycle 11 (December 3, 2016) showed high waves in the 5–6 km track segment not supported by the in situ wave height data. Removing that cycle from the analysis dropped the average rmse to 5.4 cm.

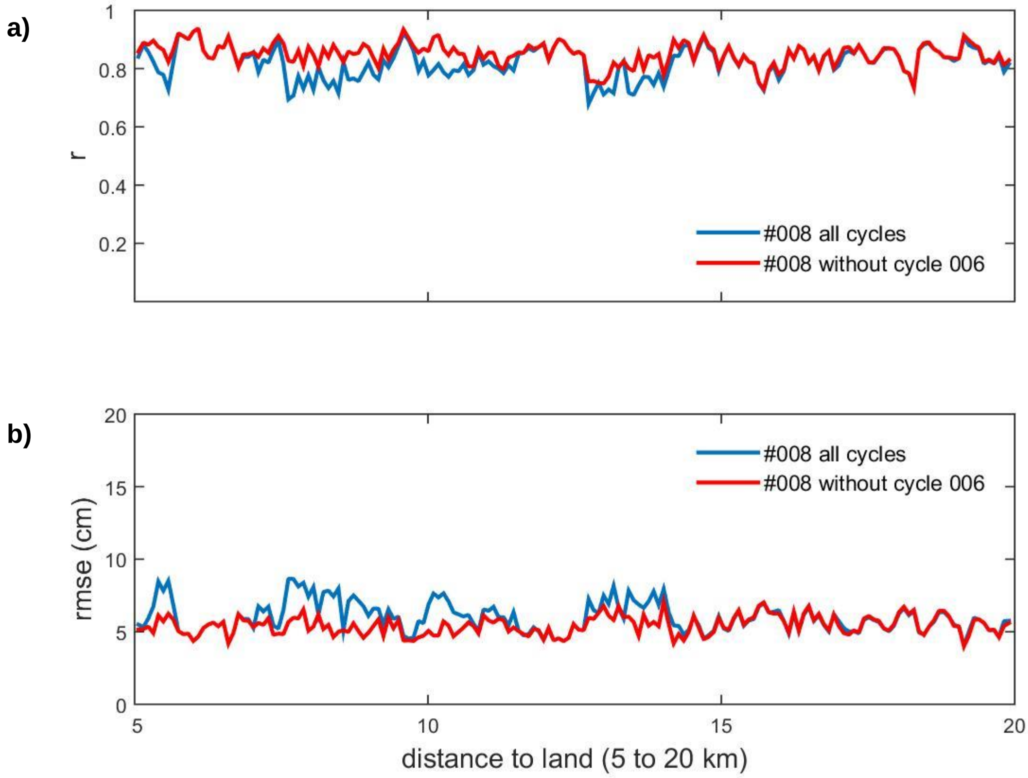

Figure 3.10. Along-track values of (a) r and (b) rmse of track #008 considering all the cycles after data screening (blue line), and removing cycle 06 (red line) .

3.5. Discussion

The coastal altimetry community is focused on the retrieval of accurate measurements near the coast. The results obtained in this chaper demonstrate that the S3A altimeter gives accurate sea level data in the 5–20 km coastal ocean fringe at the highest posting rate available as a standard product, i.e., 80 Hz. The values of r and rmse obtained in this article are between 0.7–0.8 and 6–8 cm, respectively, at all the locations. They are in line with previous validation works using other altimeters in coastal areas. A study in the northwestern Mediterranean Sea obtained correlation coefficients of 0.7–0.8 along the 0–30 km segment for Topex/Poseidon (10 Hz), and Jason 1/2 (20 Hz) (Birol and Delebecque, 2014). Moreover rmse values of 8–10 cm were obtained when comparing SARAL data (40 Hz) with a TG located in the Strait of Gibraltar along two 0–30 km track segments (Gómez-Enri et al., 2016a). In the German Bight and West Baltic Sea, values of average stdd and correlation of 4.4 cm and 0.96 were obtained in the 0–10 km segment (Dinardo et al., 2018). In another study, the use of data from the same TG at *Huelva* used in this chapter and CryoSat-2 data (20 Hz) in the 5–20 km track segment yielded rmse values between 6.4 and 8.5 cm (Gómez-Enri et al., 2018). The validation of time series of sea surface heights from SARAL (40 Hz), Jason-1/2, Envisat and ERS-2 (all at 20 Hz) was also performed along the French Atlantic coast in the southern Bay of Biscay (Vu et al., 2018). The authors analysed the 0–5 km coastal strip and found an rmse ranging between 8 cm (SARAL) and 89 cm (ERS-2). In the Gulf of Finland, a validation study of one year of S3A sea surface heights yielded an rmse of 7 cm with respect to the TGs (Birgiel et al., 2019). A deeper investigation of the 0–5 km segment is presented here. The along-track values of rmse are shown in Figure 3.11 at the three locations.

The two tracks at *Huelva* (Figure 3.11a) show similar rmse values in the 3–5 km segment than in the 5–20 km segment (Figure 3.6a), and increase closer to land. This indicates that good quality data can be obtained (Figure 3.11). Same as Figure 3.6 for the 0–5 km track segment at (a) *Huelva*, (b) *Barcelona*, and (c) *Bilbao* (missing track #071 due to data unavailability within these tracks up to 3 km from the coast). Similarly, accurate S3A data are observed at *Barcelona* over track #008 (3–5 km segment) (Figure 3.11b). On the contrary, a high rmse is observed in the 0–5 km segment at *Barcelona* and *Bilbao* for tracks #356 (Figure 3.11b) and #051 (Figure 3.11c), respectively. As previously mentioned, the 0–5 km segment at *Bilbao* presented less than 20% of VD for track #071 (Figure 3.4c).

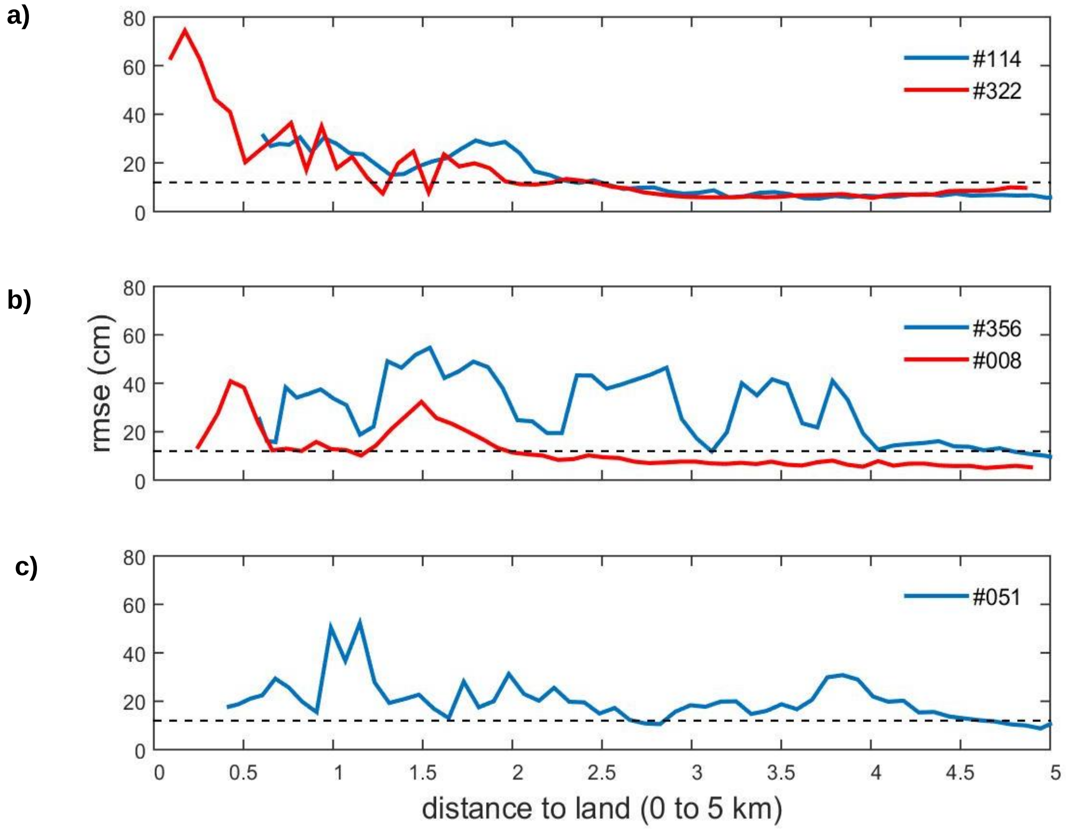

Figure 3.11. Same as Figure 6 for the 0-5 km track segment at (a) HU, (b) BA, and (c) BI. Missing track #071 due to data unavailability.

This evidences that a common track segment with the same level of accuracy cannot be achieved in our study areas. A possible explanation could be the type of transition of the tracks, i.e., ocean-to-land (OL) and land-to-ocean (LO) (Table 3.1). However, this is not the case as good results are found in the LO transitions at *Huelva* (#322) and *Barcelona* (#008) in the 3–5 km segment. A second explanation might be the orientation of the coastline with respect to the track; this could be affecting the retracking of the waveforms due to the land contamination in the SAR altimetry footprint, giving inaccurate retracked Ranges and SWH. The smallest angle between each track and the coastline (θ) has been obtained (Table 3.1). An angle of 90° implies that the track is perpendicular to the coast, so the land contamination on the radar waveforms might be neglected until very close to the coastline. Angles close to zero should complicate the retracking due to land contamination and, hence, the accuracy of the sea level retrievals. Track #114 (HU) is far from being perpendicular to the coast, with ~46° (Figure 3.1a), but shows similar results in terms of rmse to track #322 (Figure 3.11a), which is closer to perpendicular (~75°). In the case of *Barcelona*, track #008 has ~61° and shows much more accurate results with respect to track

#356 (Figure 3.11b), with ~39º. Finally, *Bilbao* does not present accurate values for any of the two tracks in the 0–5 km segment (θ ~74º and 88º for tracks #051 and #071, respectively). Hence, the angle between the tracks and the coastline does not explain the results in terms of rmse at *Huelva* and *Bilbao*. A third possibility is the land topography in the vicinity of the radar measurement footprint area. Figure 3.12 shows the 0–5 km segment of the two tracks at *Huelva*: #114 (Figure 3.12a) and #322 (Figure 3.12b) and *Bilbao*: #051 (Figure 3.12c) and #071 (Figure 3.12d).

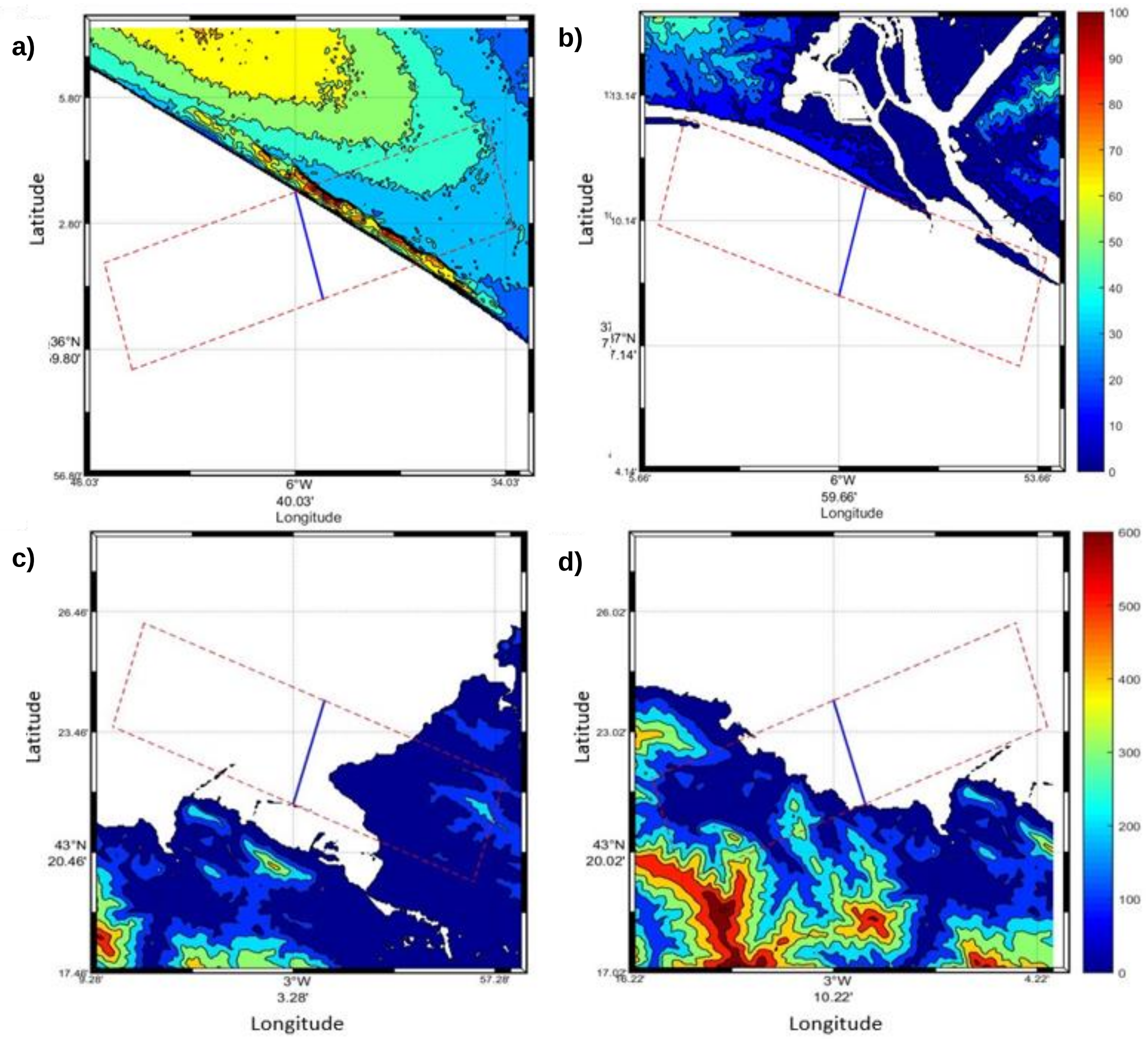

Figure 3.12. Location of 0-5 km track segments at Huelva for tracks (a) #114 and (b) #322, and at Bilbao for tracks (c) #051 and (d) #071. The SRTM land topography (in meters) is also shown. The envelope of the beam-limited footprint in the across-track direction (a radius of about 9.5 km perpendicular to the track) is delimited with a dashed red line.

Cycle 10 was used to show the track position in Figure 3.12. Also included is the land topography obtained from the SRTM data. The focus of this analysis is on the topography of the land located at a maximum perpendicular distance of 9.5 km of either sides of the track segment. This is the approximated beam-limited footprint of the S3A radar altimeter (across-track direction). Considering the distance from the satellite's nadir to land and its height with respect to the sea level at nadir, one might expect the generation of simultaneous echoes with the water at nadir and hence the contamination of the waveforms. Also plotted in Figure 3.12 are the limits of the area inside the beam-limited footprint. Track #114 (Figure 3.12a) shows land areas inside the footprint but the topography is very low and almost flat, so no high land contamination is expected in the vicinity of the leading edge of the waveforms corresponding to the 3–5 km segment. Track #322 (Figure 3.12b) does not show land inside the footprint due to its orientation with respect to the coast, so the small rmse in the 3–5 km segment is well explained. The rmse values observed in the 0–3 km segment might be due to the inaccuracy of some of the range and geophysical corrections applied to estimate S3A_SLA. In the case of track #051 (BI) (Figure 3.12c) is affected by the proximity of Punta Galea in the eastern side of the track segment, which might justify a strong land contamination in the radar waveforms and, hence, inaccurate retrievals of the geophysical parameters. This could explain the rmse observed along the whole 0–5 km segment. Track #071 (Figure 3.12d) shows land areas with a steep topography inside the footprint in the whole segment and thus, a strong land contamination is also expected.

3.6. Conclusions

This chapter presents the results of the validation of six track segments of S3A altimeter near the coasts of Spain. Three TGs located at three areas characterized by coastal environments with different tidal and hydrodynamic conditions were used for comparison: *Huelva*, *Barcelona* and *Bilbao*. The number of VD near the coast at the three locations, the along-track r and rmse of the 0–20 km track segment of each track, the orientation of the satellite tracks respect to the land intersection, and the land contamination of the radar waveforms in the 0–5 km track segments were analysed in detail. From the obtained results, the following conclusions are outlined.

The retrieval of the range and SWH from the S3A waveforms using the SAMOSA+ retracking algorithm and the use of the corrections (Range and Geophysical) available in the SARvatore GPOD service (with the exception of the SSB correction) provide accurate along-track SLA up to very close to the shore (3 km in some cases) at the highest posting rate: 80 Hz. This accuracy was confirmed by comparing the altimeter SLA with the TG data. To our knowledge, this is the first time that S3A sea level data are validated at the highest posting rate available as a standard product. The tidal model available in GPOD (TPXO8) shows a good performance in the three sites. The rss values are in line with other global tidal models: 1.97 cm (*Huelva*), 0.52 cm (*Barcelona*), and 5.45 cm (*Bilbao*). The SSB correction was not available at 80 Hz in GPOD at the time of downloading the data and, hence, a percentage of SWH was applied instead. The use of 5% of SWH as a first approximation seems to be the optimal choice at the three locations to get the best results in terms of smaller rmse and larger r.

Data screening plays a key role in the selection of the altimeter VD. The comparison against TGs spotted anomalous sea level data that were not removed in the standard screening used in this article. Once these data were not considered in the comparison the rmse and r values improved in about 10%. A common distance to the coast with a similar level of accuracy in the SLA from S3A was not achieved in the three locations analysed. At *Huelva* (tracks #114 and #322) and *Barcelona* (track #008), accurate sea level data were observed in the 3–20 km track segment (r = 0.7–0.8 and rmse = 6–8 cm with more that 95% of VD). The same level of accuracy was obtained at *Barcelona* (track #356) and *Bilbao* (tracks #051 and #071) in the 7–20 km track segment. The good results found at *Huelva* in the 3–5 km track segment are explained by the fact that the height of the land topography inside the beam-limited footprint of the altimeter is very low and no bright targets on land seem to affect the retracking. Therefore, negligible land contamination is expected very close to the shore even if the track orientation with respect to the land is not optimal (θ= 48° for track #114). However, the track orientation with respect to the land can explain the different behaviour found at *Barcelona* between track #008 (θ= 61°) and #356 (θ= 39°) because the topography in this region is steeper than in *Huelva*. The abrupt topography observed at *Bilbao* around track #071 and the non-optimal orientation of track #051, explain the poor accuracy found in the 0–5 km track segment. Thus, knowledge of the track orientation with respect to the land and the land topography is needed to explain the results observed by satellite radar altimeters very close to the shore.

Chapter 4

Assessment of Sea Level data of the two-satellite Sentinel-3 mission on coasts around the Iberian Peninsula

---

As mentioned previously, the recent launch of the Sentinel-3 space missions requires an effort from the altimetry community to determine the quality of the data generated, especially in coastal areas. In this sense, this chapter is a continuation of the previous validation work of Sentinel-3A presented in Chapter 3. The work includes an extension of the study areas and the validation of Sentinel-3B (S3B). The results are expected to have the same accuracy in comparison with in-situ tide gauge data, as the radar altimeter on-board S3B is an identical instrument on-board S3A. In addition, GPOD services recently included an updated version of the TPXO tide model used in Chapter 3. Both tidal models were previously validated with in-situ data and then used in the S3 assessment.

This chapter is organized into four sections. Section 4.1 introduces information on both Sentinel-3 mission satellites and previous validation works. Then, Section 4.2 presents the data and methodology used in this study and Section 4.3 shows and discusses the results. Finally, Section 4.4 presents a summary of the main conclusions.

4.1. Introduction

Sentinel-3 is part of the Sentinels constellation of the Copernicus program, developed by the European Commission in collaboration with the ESA and EUMETSAT. The Sentinel-3 main aims are to measure: sea surface topography, sea/land surface colour, and sea/land temperature for environmental and climate studies (Donlon et al. 2012; Mecklenburg et al. 2018). Sentinel-3 is a twin-satellite mission with two satellites already in orbit: Sentinel-3A since February 2016 and Sentinel-3B since April 2018.

Both satellites are identical but the radar altimeter, imaging spectrometer, and other instruments on board could behave slightly differently. This could be misinterpreted as changes in the environment and might influence the data accuracy, especially in the multi-satellite time series. As a result, to compare the performance of the instruments on board, the satellites were positioned in tandem phase between June and October 2018. In the tandem phase, the time-lag between S3A and S3B was 30 seconds, much closer than the nominal position, minimising the uncertainty introduced in the measurements due to the ocean and atmospheric variability (Rieu et al., 2021). Therefore, all measurements are directly comparable (Clerc et al., 2020; Romanazzo et al., 2018), which allows for the assessment of the differences between both satellites, and for the estimation of measurement uncertainties. For the inter-comparison of the Sentinels, a sensitivity analysis was done to observe differences and calculate the covariance of the measurements (Clerc et al. 2020). Moreover, tandem data can also be used to evaluate noise. The results of the tandem phase showed very good consistency between the S3A and S3B instruments. Nevertheless, some uncertainties were detected; for example, a small regional bias on ascending tracks were detected in the comparison between the Delay-Doppler Synthetic Aperture Radar ALtimeter (SRAL) of S3A and the SRAL of S3B (Clerc et al. 2020). Also Mertikas et al. (2020) found a bias difference of +2 cm between S3B and S3A, based only on a few cycles. All of these results highlight the importance and benefits of doing analyses in a tandem position.

After the cross-calibration period, S3B was drifted to the nominal position. Since then, the satellites orbit the Earth at the same time, with a velocity of ~7.4 $km \cdot s^{-1}$, but 140° apart which provides a better global coverage (Clerc et al. 2020). Once both satellites are in their nominal positions in sun-synchronus orbits, the validation and comparison of the S3A and S3B with in-situ or model data are an important tool for understanding and quantifying uncertainties and bias changes (Donlon et al. 2012; Mecklenburg et al. 2018; Nerem et al. 2010; Quartly et al. 2021).

Many authors have already obtained validation results for S3A and S3B altimeters at 20 Hz in SAR mode. Nencioli et al. (2019) validated SWH from S3A in SAR mode and also in PLRM (Pseudo Low Resolution Mode) using buoy in-situ observations off the southwest coast of England. The results showed, on average, better rmse values with SAR mode, 0.46 ± 0.14 m, than with PLRM, 0.84 ± 0.45 m. These results evidenced the advantages of SAR altimetry to obtain accurate data in coastal regions with both satellites. Yang et al. (2019) compared the SWH from S3A and S3B with in-situ buoy data on a global scale. The validation results were quite similar, with rmse values of 0.27 m and 0.31 m for S3A and S3B respectively. Also, Yang et al. (2020) did a validation of the wind speed and SWH using buoy data. The rmse values were around 1 $m \cdot s^{-1}$ for wind speed, and below 0.3 m for SWH, for both S3A and S3B. These studies showed the high accuracy of S3 data (SWH and wind speed) in SAR mode and the similarities between the two S3 satellites. Liibusk et al. (2020) also obtained good validation results (rmse: 0.13-0.15 m) comparing the SSH measurements of S3A and S3B with the Global Navigation Satellite (GNSS) ship measurements in the Gulf of Finland and the Gulf of Riga.

Previously, in Chapter 3, S3A tracks at 80 Hz were validated on three Spanish coasts (more details in Aldarias et al., 2020). Values of 6 cm of rmse in *Huelva* and *Barcelona,* and 8 cm in *Bilbao* were obtained for the track segment 5-20 km from the coast. This chapter is a continuation of this work. The main aim is to validate the SLA time series for the two-satellite Sentinel-3 mission near the coast and analyse possible differences between the satellites. Altimetry data from both satellites at the higher posting rate (80 Hz) are compared with radar tide gauges data on different coasts of the Iberian Peninsula: *Bilbao* (BI), *Santander* (SA), and *Gijon* (GI), in the Cantabrian Sea; *Huelva* (HU) and *Tarifa* (TA), in the Atlantic Sea (Gulf of Cadiz); and *Motril* (MO) and *Barcelona* (BA), in the Mediterranean Sea. In addition, a comparison of the results obtained with two different TPXO tide models (used to correct the tides in the altimeters) was done. The tidal models were previously validated and both were used in the altimetry validation in order to analyse the differences observed in different study areas.

4.2. Data and Methodology

Seven coastal areas of the Iberian Peninsula, previously described in Section 2.3, were selected to validate the altimetry data. These coasts were chosen in order to compare the results in areas with different tidal and oceanographic conditions. Two tracks (one ascending, one descending) were selected for each location from S3A and another two from S3B (Figure 4.1). The proximity of the altimetry tracks to the tide gauge network positions was also taken into account. A summary of the information on the S3A and S3B tracks is shown in Table 4.1, including: the track number, the distance between the track and the tide gauge positions, the track direction (ocean to land or land to ocean) and the orientation (ascending or descending).

Tabla 4.1. S3A and S3B tracks in the study areas: Bilbao (BI), Santander (SA), Gijon (GI), Huelva (HU), Tarifa (TA), Motril (MO), and Barcelona (BA). Number of track (relative orbit), distance between the track and the tide gauge (considering the closest 'ocean' measurement to land) (km), orientation (ascending/descending) and direction of the track (OL: ocean to land, LO: land to ocean).

Study area			**BI**	**SA**	**GI**	**HU**	**TA**	**MO**	**BA**
S3A	**Ascending**	**Track number**	#071	#014	#285	#114	#171	#285	#356
		Dist. S3-TG	8 km	28 km	28 km	14 km	17 km	22 km	5 km
		Direction	LO	LO	LO	OL	OL	OL	OL
	Descending	**Track number**	#051	#379	#265	#322	#051	#165	#008
		Dist. S3-TG	0.7 km	14 km	8 km	16 km	12 km	11 km	32 km
		Direction	OL	OL	OL	LO	LO	LO	LO
S3B	**Ascending**	**Track number**	#128	#071	#342	#114	#171	#342	#356
		Dist. S3-TG	28 km	9 km	10 km	32 km	34 km	20 km	32 km
		Direction	LO	LO	LO	OL	OL	OL	OL
	Descending	**Track number**	#051	#051	#322	#379	#051	#165	#065
		Dist. S3-TG	37 km	26 km	30 km	26 km	30 km	30 km	22 km
		Direction	OL	OL	OL	LO	LO	LO	LO

a)

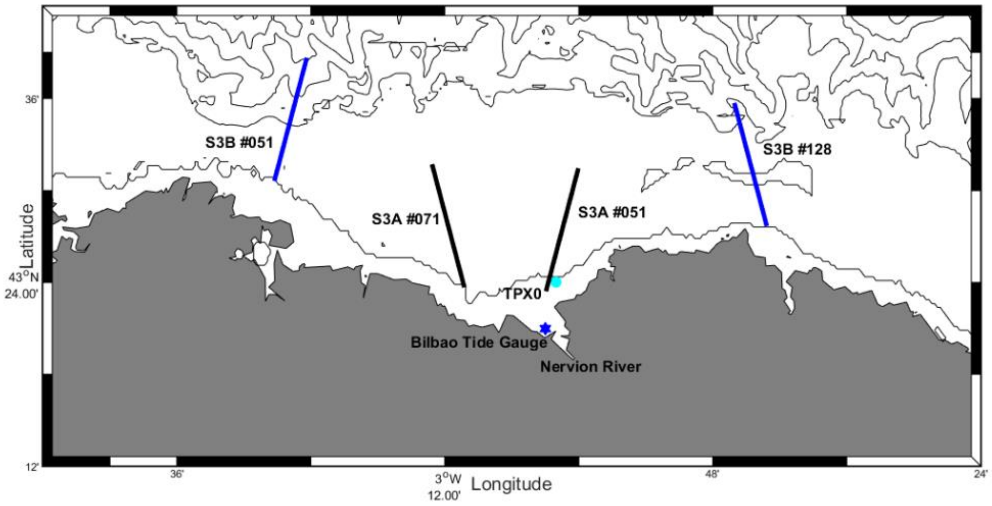
36'
S3B #051
S3B #128
S3A #071
S3A #051
Latitude
43°N
24.00'
TPX0
Bilbao Tide Gauge
Nervion River
12'
36'
3°W
12.00'
Longitude
48'
24'

b)

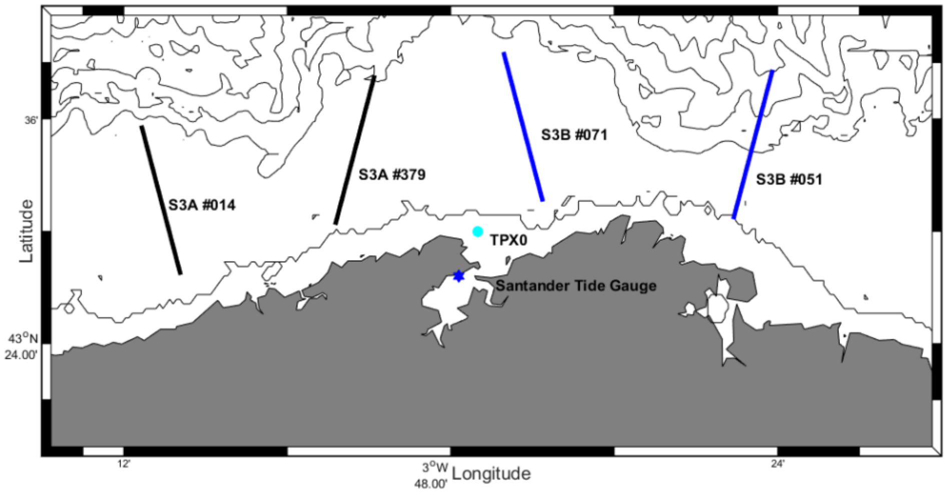
36'
S3B #071
S3A #379
S3B #051
S3A #014
Latitude
TPX0
Santander Tide Gauge
43°N
24.00'
12'
3°W
48.00'
Longitude
24'

c)

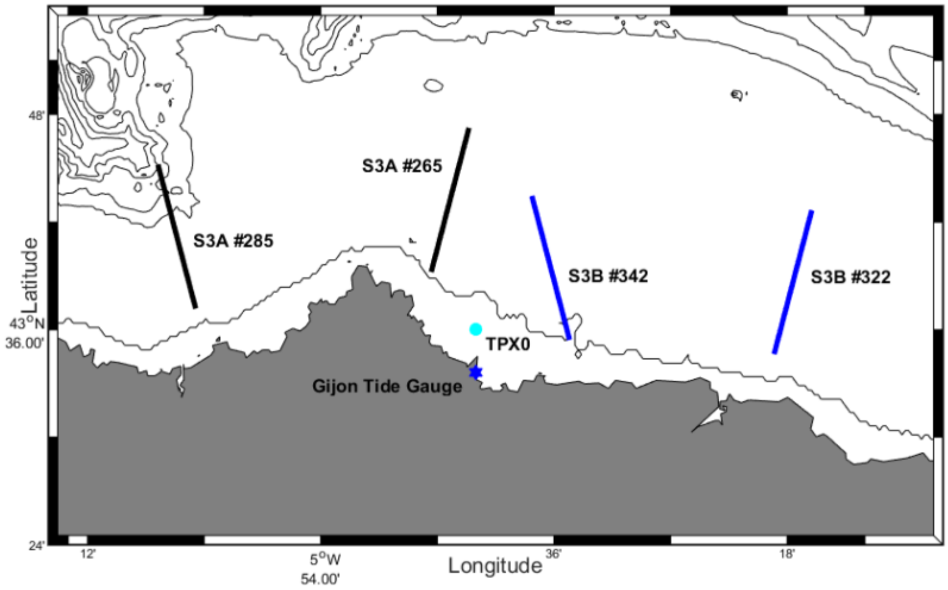
48'
S3A #265
S3A #285
S3B #342
S3B #322
Latitude
43°N
36.00'
TPX0
Gijon Tide Gauge
24'
12'
5°W
54.00'
Longitude
36'
18'

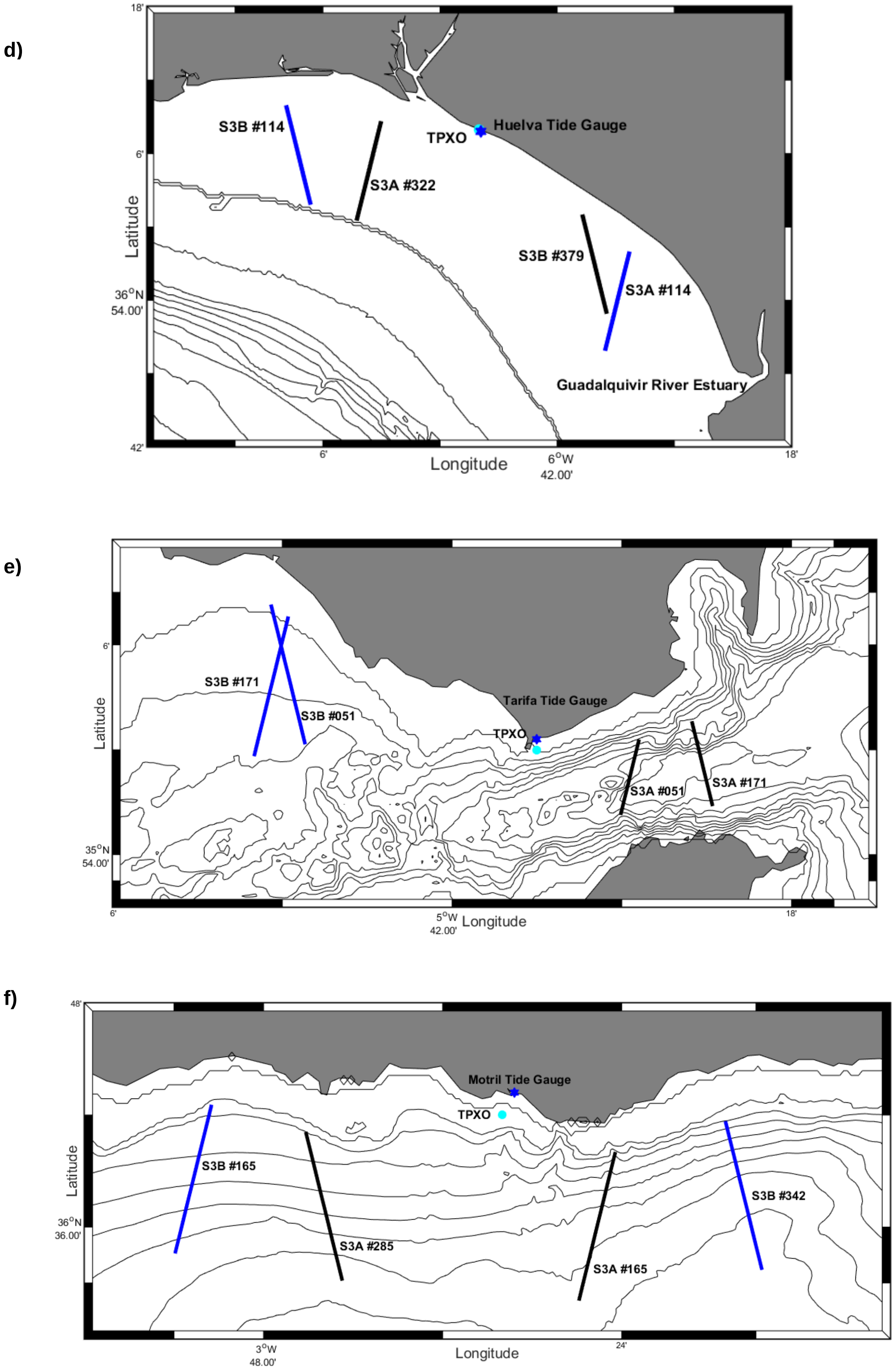
d)
18'
6'
36°N
54.00'
42'
Latitude
Longitude
6°W
42.00'
S3B #114
S3A #322
TPXO
Huelva Tide Gauge
S3B #379
S3A #114
Guadalquivir River Estuary
e)
6'
35°N
54.00'
5°W
42.00'
Latitude
Longitude
S3B #171
S3B #051
Tarifa Tide Gauge
TPXO
S3A #051
S3A #171
f)
48'
36°N
36.00'
3°W
48.00'
24'
Latitude
Longitude
Motril Tide Gauge
TPXO
S3B #165
S3A #285
S3A #165
S3B #342

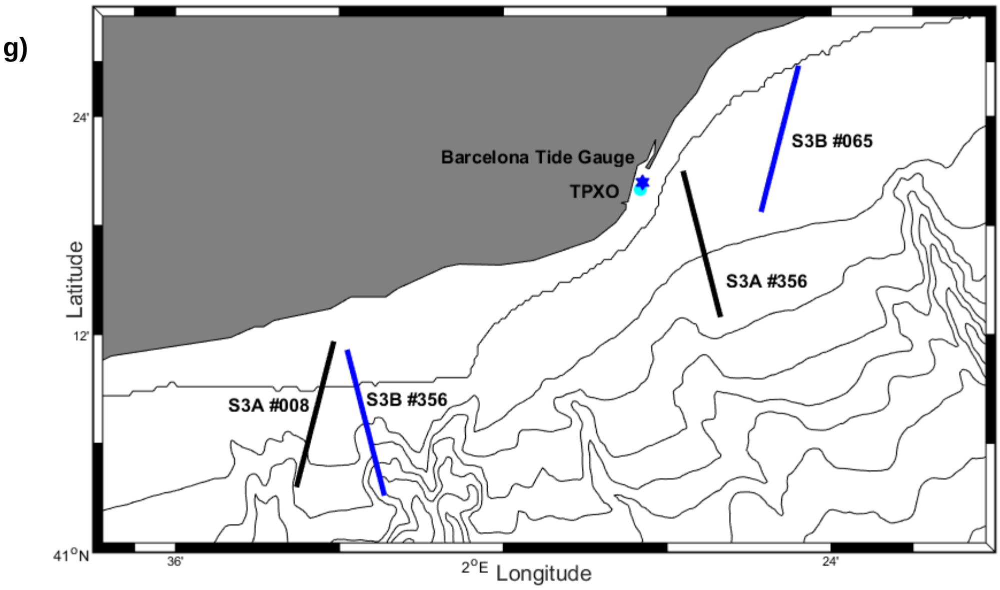

Figure 4.1. Location of the S3A tracks (black line), the S3B tracks (blue line), the radar tide gauges (blue star) and the TPXO points (solid blue dot) used in each study area: (a) Bilbao, (b) Santander, (c) Gijon, (d) Huelva, (e) Tarifa, (f) Motril, and (g) Barcelona.

4.2.1. Altimetry data

S3A and S3B data were provided by the ESA GPOD service. The data processing was done at Level 1b and Level 2 as previously described in Section 3.2.1. Both satellites have a 27-day repeat cycle. In this study, between 21-22 cycles for each track and satellite were selected for the period November-2018 to June-2020. The sea level time series were calculated using Equation 3.1. The only difference was that two datasets for each track were created using different tidal corrections from the TPXO tide model (Topex Poseidon Global Inverse Solution).

4.2.2. TPXO tidal model data

As mentioned in Section 3.2.4, TPXO is a series of ocean tide global models (Egbert et al. 1994, Egbert and Erofeeva, 2002). Each version of the model in the TPXO series is based upon an updated bathymetry and assimilates more data compared to previous versions. For this study, the version TPXO8_v1 and TPXO9_v4 (TPXO8 and TXO9, hereinafter) were used (https://www.tpxo.net/global) with the aim of determining which one provides the best validation results.

The TPXO global models used have a regular grid with a resolution of 1/30 °, and NaN values to represent land positions (bathymetry equal to zero or no bathymetry data). The main difference between both models is an updated bathymetry, and therefore a presumably better representation of the coastline (Svetlana Erofeeva, personal communication). Both models include: the main constituents (M2, S2, N2, K2, K1, O1, Q1 and P1), two long period constituents (Mm and Mf), and three non-linear constituents (M4, MN4, and MS4). Moreover TPXO9 includes the 2N2 and S1 harmonic constituents (currently minor constituents have been included but they are not available in the version used in this work).

4.2.3. Tide gauge data

Water level data from radar tide gauges (TG) located in ports, provided by the Spanish institution Puertos del Estado (http://www.puertos.es/es-es/oceanografia/), were used to validate S3A and S3B. The data were previously described in Section 3.3.2. The TG SLA time series were obtained following Equation 3.2.

Furthermore, the amplitude and phase of the main tidal constituents, also provided by Spanish Puertos del Estado, were used for the tide model's validation. Puertos del Estado performs a harmonic analysis of hourly sea level data (one year of high quality data) using the version of the Foreman analysis and prediction program developed by the University of Hawaii Sea Level Center.

4.2.4. Methodology for the SLA validation along the S3 tracks

The track segment 5 to 20 km was selected for validation, considering the point where each track intersects with the coast. To support the selected segment, a previous analysis of valid data was done in two track segments: 5-20 km and 0-20 km (see Section 4.3.2). A rigorous data screening was applied to remove outliers, and the temporal mean of the time series was removed to obtain the SLA time series: S3A_SLA, S3B_SLA, and TG_SLA, as in Section 3.3.3. After obtaining the SLA time series, the standard deviation of the difference (sdd) was used to compare the altimetry and the tide gauge data (Equation 4.1).

$$sdd = \sqrt{\sum \frac{(S3\_SLA(i) - TG\_SLA) - mean(S3\_SLA\ (i) - TG\_SLA))^2}{(N-1)}} \qquad \text{(Eq. 4.1)}$$

Where N is the number of data points along the time series, S3_SLA is the Sea Level Anomaly for S3A or S3B respectively, i is each instant of time considered in the time series, and TG_SLA is the Sea Level Anomaly from the tide gauge. The calculation is repeated for all the time series of each track. The use of this statistic to compare time series (having removed the time average) is supported by previous studies, e.g. Ablain et al. (2017) and Fenoglio et al. (2015, 2021).

In addition, the normalized sdd (sdd_n, hereinafter) was calculated to obtain a value bounded between 0 and 1 that allows for inter-comparing the results of zones with different variability (Janssen et al., 2007; Krishnan and Bhaskaran, 2020). As the tide amplitudes are different depending on the study area, mesotidal to microtidal (Chapter 2), the range of TG_SLA in each study area was used to adjust the sdd values to a common scale (Eq. 4.2).

$$sdd\_n = \frac{sdd}{\max(TG\_SLA) - \min(TG\_SLA)} \qquad \text{(Eq. 4.2)}$$

4.2.5. Methodology for the TPXO model validation

The validation results for each track were obtained using TPXO8 and TPXO9. To better understand the differences between the tide model versions, a previous validation of both models was done using two statistics: the root mean square (rms) and the root sum of the squares (rss) (Oreiro, 2014). To validate the tide models, the common tidal constituents in TPXO8 and TPXO9 were selected: M2, S2, N2, K2, K1, O1, Q1, P1, M4, MN4, and MS4. Mm and Mf were not included in this analysis (because of their unavailability in the Spanish Puertos del Estado website); nor the O1 constituent in Tarifa. The tide model grid points closest to each tide gauge were used for comparison (Figure 4.1).

4.3. Results and Discussion

4.3.1. TPXO validation results

The results are shown in Table 4.2: the rss of all of the constituents and the rms of M2, which is the main constituent in the study region. In addition, the distance between the TPXO model grid point and the TG was indicated in each case.

Table 4.2. Validation results of TPXO8/9 on each coast: Bilbao (BI), Santander (SA), Gijon (GI), Huelva (HU), Tarifa (TA), Motril (MO), and Barcelona (BA). Distance between the TPXO point and the TG, rms (cm) for the main constituent M2, and rss (cm). In bold the lower rss values.

Tide gauge		BI	SA	GI	HU	TA	MO	BA
Distance TPXO-TG		5.7 km	4.8 km	4.4 km	0.5 km	1.1 km	2.5 km	0.8 km
M2 rms (cm)	TPXO8	4.9	0.7	5.7	1.7	10.9	0.4	0.4
	TPXO9	0.3	3.8	1.4	3.3	6.8	0.4	0.4
rss (cm)	TPXO8	5.5	**1.6**	7.0	**2.6**	12.2	**0.8**	0.6
	TPXO9	**0.8**	4.4	**1.6**	3.9	**7.5**	0.9	**0.5**

The distance between the TPXO-grid point and the TG ranged from 0.5 to 5.7 km (Table 4.2) with the highest distance ocurring in the north of the Iberian Peninsula. Nevertheless, there is not a direct relation between lower distances TPXO-TG and lower rss values. The availability of a TPXO point close to the TG position depends on how precisely the coastline is defined, i.e. it depends on the bathymetry. The longest distance TPXO-TG was found in *Bilbao*, as points closest to the TG were NaN, probably because the model considered these points to be on land. This could be related to the location of the BI_TG in the inner section of the Bilbao port.

Initially, lower rss values were expected with the new model version. However, although TPXO9 use an updated bathymetry which resulted in improvements on average (globally), the results do not necessarily have to improve for all coastal locations (Svetlana Erofeeva, personal communication). The results for *Bilbao*, *Gijon* and *Tarifa* met the initial assumption, but it remains to be seen whether the S3 validation results were also better using TPXO9. On the Mediterranean coasts the results were similar with both models; therefore, no differences were expected in the use of TPXO8 or TPXO9. Nevertheless, in the case of *Huelva* and *Santander* the rss results did not improve with TPXO9 compared to TPXO8 but were in fact worse; hence, lower sdd values were expected when applying TPXO8 tidal corrections for the S3_SLA time series.

Following the validation of the tidal models, the analysis of data availability and the validation of the satellite tracks with both models were performed to study the influence of the tidal model on the S3 validation results.

4.3.2. Availability of S3 data

The results of the percentage of VD (%VD) in the 0-5 km (not shown here) confirmed that in the first km the number of valid data decreased (as in the S3A tracks analysed in Chapter 3), presumably due to the land contamination and the influence of the track orientation with respect to the coast (Aldarias et al., 2020; Cipollini et al. 2009; Gómez-Enri et al. 2018; Gommenginger et al. 2011; Mulero-Martínez et al., 2021; Vignudelli et al., 2011). Therefore, the track segment 5-20 km was selected for this study. In the specific case of S3A tracks in *Tarifa*, the 5-20 km segment has not been used, since *Tarifa* is located in the Strait of Gibraltar between two coasts (Spain and Morocco). Therefore, in order to keep the distance to the coast to 5 km with both coasts, the segments 5-14 km for track #171 and 5-13 km for track #051 were selected (Figure 4.1e).

After removing outliers, the %VD was calculated from the average of the total number of cycles that contained data at each along-track position. The %VD was estimated using the tidal corrections from TPXO8 and TPXO9. The results for the segment 5-20 km are displayed in Figure 4.2. The percentage of VD was above 86% for all tracks with all the tidal models (as in the results shown in Chapter 3).

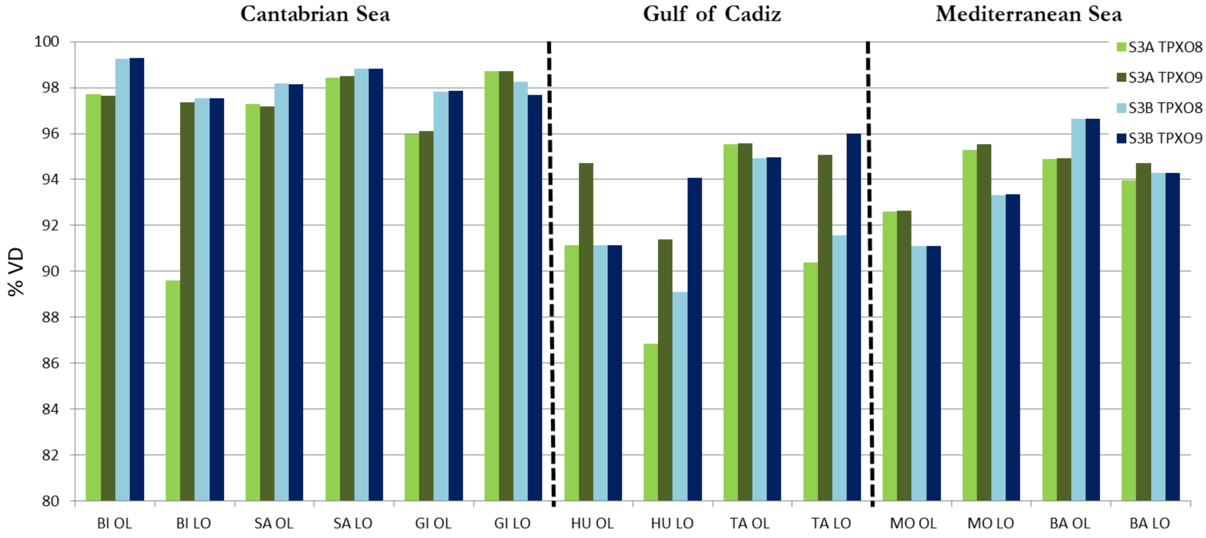

Figure 4.2. Percentage of valid data along the 5-20 km track-segment of S3A (green) and S3B (blue) in each study area, with TPXO8 (light colours) and TPXO9 (dark colours): Bilbao (BI), Santander (SA), Gijon (GI), Huelva (HU), Tarifa (TA),Motril (MO), and Barcelona (BA).

Following Figure 4.2, the results can be analysed in two ways, by comparing: (1) the tidal models and (2) S3A and S3B. Regarding the former, the use of TPXO8 or TPXO9 generally did not change the %VD for the same satellite, as expected. However, there are exceptions. In this sense, differences between 3 and 7 %VD were found when using one model or the other in various tracks (i.e., BI_LO_S3A, HU_OL_S3A, HU_LO_S3A, HU_LO_S3B, TA_LO_S3A, and TA_LO_S3B). In all of the exceptions TPXO9 provided better results (despite the TPXO validation results, Table 4.2). In a deeper analysis of the applied corrections, differences in the availability of Ocean Equilibrium Tide correction (OET) were observed. For all of these tracks the OET was fully NaN for only one or two cycles in the TPXO8 model (as previously shown in Section 3.4.3). The loss of VD was not due to the tidal model or the outliers' detection but could be caused by a failure in the GPOD processing. Therefore, it cannot be ensured that the selection of the tidal model has an impact on the loss of valid data. When comparing S3A and S3B, differences lower than 2% VD were obtained both for the OL and LO tracks, independently of the tidal model used. Hence, the data availability was the same for both S3A and S3B.

Finally, it is relevant to mention that the major data loss was due to the screening of the SWH (Section 3.3.3) which explained between about 1% and 8.5% of the missing data (generally due to negative values of SWH). This highlights the importance of having good quality and specific SSB correction values for S3.

4.3.3. Along-track validation

The results of the along-track validation are shown in Figure 4.3. In general, high accuracy was obtained in the S3 validation with sdd <9cm for most of the tracks in the 5-20 km track-segment. The accuracy of the results is in accordance with previous studies; in Chapter 3, rmse values lower than 8.2 cm were attained for the track segment 5-20 km. Other authors such as Peng and Deng (2020) obtained rmse values between 5 and 20 cm when comparing SLA S3A measurements at 20 Hz in the 0-50 km coastal zone of Australia. Also, Liibusk et al. (2020) achieved rmse values of 13-15 cm when comparing the SSH measurements of S3A and S3B with GNSS measurements in the 2-50 km track segments in the Gulf of Finland and the Gulf of Riga.

Although the validation results showed good accuracy, differences were found with respect to previous analyses. In terms of sdd, the results were lower for the same percentage of

S3A and S3B tracks (Figure 4.3). In both cases the differences between S3A and S3B were independent of the tidal model.

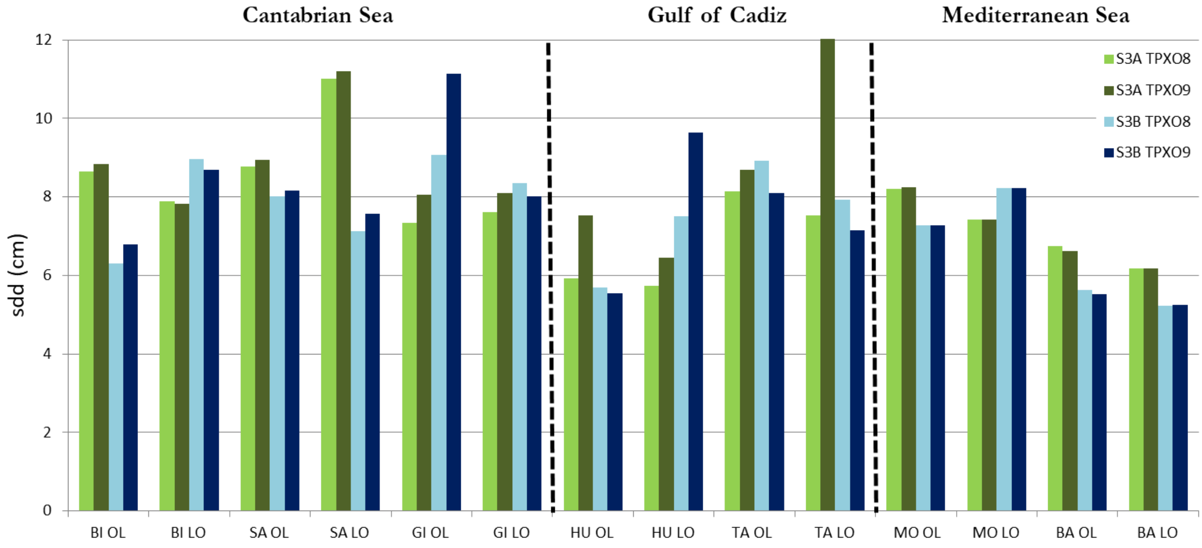

Figure 4.3. Sdd (cm) validation results of S3A (green) and S3B (blue) 5-20 km track-segment with TPXO8 (light colors) and TPXO9 (dark colors) in each study area: Bilbao (BI), Santander (SA), Gijon (GI), Huelva (HU), Tarifa (TA), Motril (MO), and Barcelona (BA).

The differences found between TPXO8 and TPXO9 during the models' validation (Table 4.2) were also observed in the altimetry validation results, as expected (Figure 4.3). In *Santander* and *Huelva* where lower values of rss were obtained with TPXO8, the sdd were also up to 2 cm lower with this model, with the exception of HU_ OL_ S3B were the results were similar (sdd=5.7/5.6 cm using TPXO8/9). In *Tarifa* the tide model validation results show lower rss with TPXO9, although the S3A validation results were better with TPXO8. These results could be a consequence of the distance between the TG (and the TPXO-grid point) and the S3A tracks (Table 4.1, Figure 4.1), and the particularly complex circulation of the study area (Bolado-Penagos et al., 2020; Gómez-Enri et al., 2016a; Laiz et al., 2012). The same ocurrs in *Gijon* where lower sdd values were generally obtained with TPXO8 whilst the use of TPXO9 shows a better adjustment with the TG. For the other study areas, the sdd differences between using TPXO8 or TPXO9 were lower than 0.5 cm, especially in *Motril* and *Barcelona* (differences <0.1 cm).

After analysing the differences between tide models and satellites, the sdd_n statistics were calculated in order to be able to compare the different tracks/study areas. To make this comparison, the best performing tidal model for each track was chosen (Table 4.3) attending to the sdd results (Figure 4.3). On the Mediterranean coasts the differences were negligible, so the latest version was used. Finally 15 tracks were processed with TPXO8, and 13 tracks with TPXO9. In addition Figure 4.4 shows the validation results along the track segments 5-20 km, in terms of sdd_n.

Table 4.3. Tidal model selected for each track in the different study areas: Bilbao (BI), Santander (SA), Gijon (GI), Huelva (HU), Tarifa (TA), Motril (MO), and Barcelona (BA).

Study area		**BI**	**SA**	**GI**	**HU**	**TA**	**MO**	**BA**
S3A	**OL**	TPXO8	TPXO8	TPXO8	TPXO8	TPXO8	TPXO9	TPXO9
	LO	TPXO9						
S3B	**OL**	TPXO8			TPXO9	TPXO9		
	LO	TPXO9			TPXO8			

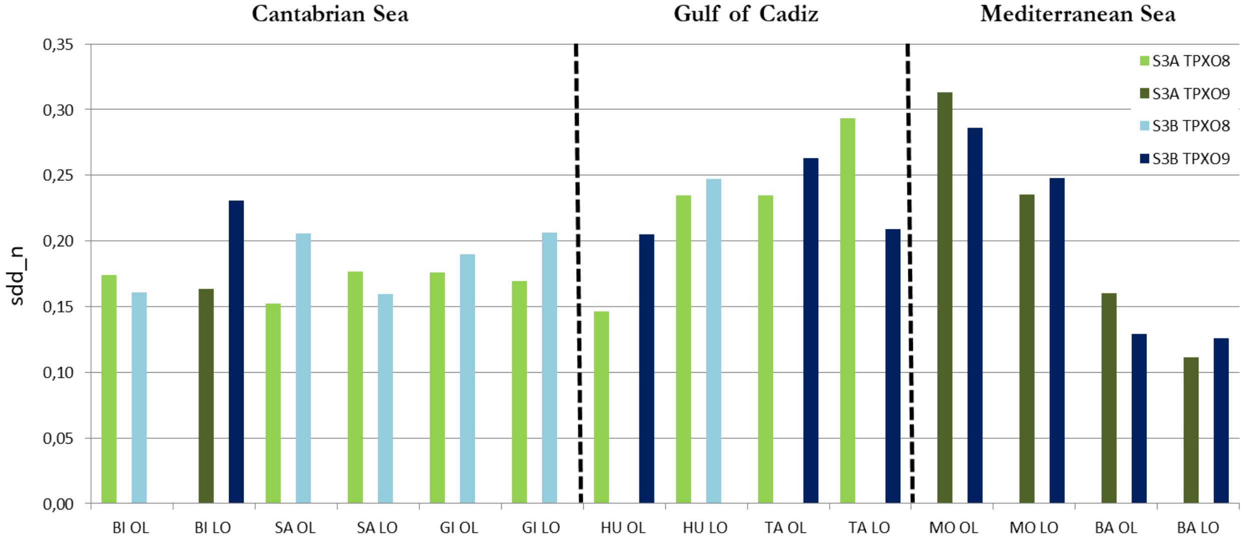

Figure 4.4. Sdd_n results along the track segments 5-20 km for the SLA validation of S3A (pink) and S3B (black) in each study area: Bilbao (BI), Santander (SA), Gijon (GI), Huelva (HU), Tarifa (TA), Motril (MO), and Barcelona (BA) with the best tidal model (Table 4.3).

An influence of the track direction was not observed in the validation results (Figure 4) because the track segment used is far enough away from the coast (5-20 km); i.e. lower sdd_n values were obtained with OL in some coastal areas (e.g. *Bilbao*), and with LO in others (e.g. *Santander*).

In all the cases the differences of sdd_n between S3A and S3B were lower than 0.1. The lowest values of sdd_n were obtained in *Barcelona*, SA_LO_S3A and HU_OL_S3A. *Barcelona* was the coast where the whole set of tracks had the best adjustment with the TG, whereas the largest discrepancies were found in *Motril* and *Tarifa*. The higher sdd_n in *Tarifa* may be due to the hydrodynamic variability in the Strait of Gibraltar, as previously mentioned. The same ocurrs in *Motril*, located in the centre of the Alboran Sea, which is also an area influenced by complex hydrodynamics and geomorphological structures such as submarine canyon systems (Barcenas et al., 2011; Muñoz et al., 2008). A deeper analysis of these results will be necessary to better understand these discrepancies.

4.4. Conclusions

This chapter presents complementary results to the previous chapter (Chapter 3). A total of 28 tracks of S3A and S3B at the high posting rate of 80 Hz were used. Track segments of 5-20 km (with respect to the coast) were validated with TG in-situ measurements around seven different coasts of the Iberian Peninsula. In addition, two tidal models available at GPOD, TPXO8 and TPXO9, were used in this study in order to analyse the differences and find the model with a better performance in each coastal area.

The tidal models showed different results for the same study area during the assessment with in-situ data. A better performance of the updated model, TPXO9 was expected. The rss results indicated a good approximation of TPXO9 in *Bilbao*, *Gijon* and *Tarifa*, and similar rss with both models on the Mediterranean coasts. However, the performance of TPXO8 was better in *Santander* and *Huelva*, with rss of 1.6 and 2.6 cm respectively. In all cases, the best model presented a rss lower than 2 cm, except in *Tarifa* (7.5 cm) probably caused by the area's complex hydrodynamics.

In the analysis of the %VD carried out for the 28 tracks with both tidal models, no differences were found that could be associated with the use of one model or the other. Percentages of VD higher than 86% were obtained for all the tracks. No significant differences were found either between S3A or S3B, both of which showed similar data availability. In the validation of S3A and S3B, good accuracy results were obtained with both altimeters (mean sdd <9cm), in accordance with previous studies (Chapter 3). As in the TPXO model validation, TPXO8 provided better sdd results than the updated version TPXO9 for some coasts. This is the case for example of *Huelva*, located in the Gulf of Cadiz, where more accurate results (improvements of about 2 cm of sdd) were obtained with TPXO8. The same occurred in *Santander*. In both cases a low rss was obtained in the tide model validation and also a low sdd in the S3 validation. Nevertheless this did not happen in all cases. Based on this conclusion, the tide model TPXO8 was chosen for the following chapters to predict or correct tides in the Gulf of Cadiz.

Finally, in order to compare zones with a different level of variability, the normalised sdd was calculated. The poorest validation results were obtained in *Tarifa* and *Motril* which may be due to their complex hydrodynamics, but a deeper analysis will be necessary to confirm this. In any case, the differences of sdd_n between S3A and S3B were lower than 0.1. Therefore, all of these results confirm that the two-satellites are similar and highly accurate in different coastal areas.

CHAPTER 5

Implementation of the Delft3D model in the Guadalquivir River estuary and the Gulf of Cadiz continental shelf

The aim of this study is to provide tools for improving the level of knowledge on sea level variability at different spatial and temporal scales in the Gulf of Cadiz (GoC), as well as on the main forcing mechanisms behind it. In this sense, the working hypothesis is that the discharges from the Guadalquivir River estuary (GRE) affect the GoC continental shelf sea level at different temporal and spatial scales, depending on the volume of freshwater discharged, as well as on the wind and tides regime at the time of discharge. Previous works have analysed this influence using tide gauges and gridded altimetry data (Gómez-Enri et al., 2012; Laiz et al., 2013), but with a limited temporal and/or spatial resolution. To overcome this limitation, the hydrodynamic model Delft3D was implemented in the ~110 km of the GRE and part of the GoC continental shelf. Different scenarios of fluvial discharge were simulated to analyse their effect on the water level along the estuary and the neighbouring continental shelf.

This chapter contains five sections. A brief introduction is presented in Section 5.1. Section 5.2 describes the data used in this study. Section 5.3 focuses on the numerical model and its implementation, and Section 5.4 contains and discusses the most relevant results obtained. Finally, in Section 5.5 a summary and the main conclusions are presented.

Part of the model implementation was carried out during a research internship at the Superior Technical School of Engineering, University of Seville, Spain.

5.1. Introduction

Estuaries are complex systems connecting marine and terrestrial environments, where rivers discharge and tides converge. Transitional environments such as these present high spatiotemporal variability. This variability is due to the tidal-fluvial interactions, atmospheric forcing, salinity and temperature variations, and mixing processes, among others (Del-Rosal-Salido et al., 2019; Martyr- Koller et al., 2017). The natural conditions of estuaries make them important areas for economic activities, such as aquaculture exploitation, farming, navigation, etc. (Mendes et al., 2021; Vousdoukas et al., 2016). For this reason (and many others), approximately 60% of the world's human population lives close to estuaries and coastal areas (Wild-Allen et al., 2013). Numerous works have evidenced the importance of studying the complex physical processes in estuaries under normal and extreme conditions (Baawain et al., 2015; Del-Rosal-Salido et al., 2019; Díez-Minguito et al., 2012; Laiz et al., 2014; Mendes et al., 2021; Sandbach et al., 2018). Traditionally, in-situ data have been used to study these processes, but systematic measurements and long-term time series are rarely available (Del-Rosal-Salido et al., 2019; Díez-Minguito et al., 2013; Losada et al., 2017). This is why the focus is now on numerical models as they can be a useful tool to simulate hydrodynamics (Baawain et al., 2015).
In the case of the Guadalquivir River estuary, there are numerous previous studies which focus on different aspects of its dynamics: tides (Álvarez et al., 2001), tidal-fluvial interactions along the estuary in different scenarios (Díez-Minguito et al., 2012; Losada et al., 2017), turbidity (Contreras and Polo, 2012; Díez-Minguito et al., 2014; Gomiz-Pascual et al., 2021), spatio-temporal variability of water quality parameters (Navarro et al., 2012; Ruiz et al., 2015), salinity intrusion and the mechanisms of salt transport (Contreras and Polo, 2012; Díez-Minguito et al. 2013), contribution of high river discharges to sea level on the Gulf of Cadiz continental shelf (Gómez-Enri et al., 2012; 2015; Laiz et al., 2013; 2016), among others. However, Losada et al. (2017) highlighted the necessity to develop models to help improving the navigability conditions in the GRE main channel, analyse the risk of flooding, control the water quality, and study the physical processes and their relation with chemical and biological processes. To our knowledge, there are no studies with hydrodynamic models that simulate the entire Guadalquivir estuary. Therefore, to respond to this need, this work implemented the Delft3D model in the entire GRE and the neighbouring GoC continental shelf. It must be pointed out that the area covered by the continental shelf was limited to minimize the computational effort.

The hydrodynamic model Delft3D was selected for this study because it is versatile and includes a large number of processes, which means that it can be applied to many different systems and conditions (Lesser el al., 2004). Many authors have successfully implemented this model in estuary areas with different objectives; for example, Zarzuelo et al. (2015) implemented and calibrated the Delft3D model in the Bay of Cadiz to evaluate the hydrodynamic changes induced by human interventions. They calibrated and tested the model for three different variables by comparing the model predictions with in-situ data, obtaining correlation coefficients (r) of 0.99, 0.88, and 0.80, and root mean square errors (rmse) of 0.15 m, 0.13 $m \cdot s^{-1}$, and 0.04 $m \cdot s^{-1}$ for water level, tidal currents, and residual currents, respectively. The authors concluded that the model correctly reproduced the main physical processes in the study area. Sandbach et al. (2018) implemented the Delft3D model in two and three dimensions to study the Tidally-Influenced Fluvial Zone in the Columbia River (North America). The results were similar for both model configurations, with water level rmse values between 0.06 and 0.28 m for the different stations. In addition, similar results were obtained by Elias et al. (2012) for the same estuary. Therefore, Sandbach et al. (2018) concluded that a 2D model was enough to reproduce the hydrodynamic behaviour of the estuary mouth. Another example using the Delft3D model is the study carried out by Des et al. (2019) on the hydrodynamics of intrusion events in the Minho River and Ria de Vigo. The authors calibrated the model in terms of Sea Surface Elevation (SSE), salinity, water temperature, and currents, obtaining good results. In the case of SSE, values of rmse <0.05 m and Skill>0.99 were obtained between the model preditions and the observations. More recently, Mendes et al. (2021) used Delft3D to analyse the interrelation of two estuarine systems, the Mondego estuary and Óbidos Lagoon (Portugal). Highly accurate results were obtained using the model, as can be seen in the comparison between SSE model observations and in-situ measurements (rmse=0.08-0.13 m), as well as in the current velocities (rmse=0.07-0.13 $m \cdot s^{-1}$), evidencing the usefulness of this model. Finally, Martyr-Koller et al. (2017) implemented the Delft3D model in the San Francisco Bay Delta (California) to study the dynamic variations of water levels, river discharges, and salinity. The average water level calibration (and validation) results were: r=0.97 (0.96), bias=0.003 (0.04), rmse=0.14 m (0.18 m) and Skill=0.98 (0.95). The adjustment between model and in-situ data was good for the different sections in spite of the complexity of the study area.

This chapter focusses on the Delft3D model calibration and validation in the GRE and the adjacent continental shelf. With this purpose, the numerical results were compared with time series of observed water level and velocity. During the calibration simulations, most hydrodynamic models in river estuaries only take into consideration the bed roughness parameter. However, in this work the bathymetry was also considered as an adjustment parameter with the aim to minimize the uncertainties of the model results due to errors in the bathymetric data (Garcia et al. 2015; Matte et al. 2017; Yan et al. 2015). Recently, Khanarmueti et al. (2020) implemented the Delft3D model in a micro-tidal estuary using bed roughness and bathymetry to calibrate the model. The authors demonstrated that the model performance was better when calibrating with both variables, especially in terms of water level.

Moreover, in this study, the model results obtained during three different events of high river discharge were qualitatively compared with tracks of CryoSat-2 (CS2) and Sentinel-3A within the GoC continental shelf. A first qualitative comparison between the model and altimetry data is important within the context and final aims of this thesis. Previous works in the GoC that compared gridded altimetry data with in-situ data observed an elevation of the water level on the continental shelf linked to high river discharges (Gómez-Enri et al., 2012; 2015; Laiz et al., 2013; 2016). More specifically, Laiz et al. (2013) indicated that this effect was only observed when the daily average river discharge values were above 300 $m^3 \cdot s^{-1}$ and suggested that its spatial extension was limited to a region close to the estuary mouth. In fact, Gómez-Enri et al. (2015) located the area of influence of the discharge plume up to 20-30 km off the coast by using a new methodology to create high-resolution altimeter products near the coast.

Furthermore, although there are some works comparing model and altimetry data in coastal areas, none are known to have used Delft3D. As an example, Rulent et al. (2020) compared the performance of the regional model Amm15 (Lewis et al., 2019) with S3A and CS2 altimetry data in the United Kingdom Atlantic margin. Total Water Levels were calculated for the model observations and from the altimetry measurements during storm periods. The validation results showed correlation values of 0.98 for both satellites, and average rmse values of 0.28 m and 0.22 m for S3A and CS2, respectively, which increased to 0.40 m and 0.30 m when only considering the measurements from the first 10 km of the coastal strip. Moreover, the authors found an almost constant bias between the model and altimetry data (-0.23 m for S3A and -0.15 m for CS2). They concluded that both models and altimeters have different advantages and disadvantages. As previously discussed in Chapter 1, both tools provide useful information to complement in-situ measurements but their accuracy could be improved close to the coast, especially in the case of altimeters.

5.2. Data

5.2.1. Bathymetry

Four different topography and bathymetry datasets were used to cover the full area of interest:

- Bathymetry data for most of the continental shelf were retrieved from the European Marine Observation and Data Network (EMODnet) (https://www.emodnet-bathymetry.eu/).
- The bathymetry used in the mouth of the estuary and the neighbouring continental shelf was obtained from the Spanish Oceanographic Institute (IEO) ECOCADIZ campaign.
- The river bathymetry was provided by the Research Group 'Dynamics of Environmental Flows' from the University of Seville (Spain).
- The digital terrain model generated by the Instituto de Estadística y Cartografía de Andalucía (Junta de Andalucía, Spain) was used to delimit the land areas (https://www.juntadeandalucia.es/institutodeestadisticaycartografia/prodCartografia/bc/mdt.htm).

5.2.2. TPXO

TPXO is a series of global models of ocean tides, which fits the Laplace Tidal Equations and altimetry data (Egbert et al. 1994; Egbert and Erofeeva, 2002). More details can be found in Section 4.2.2.

The Delft3D model was forced with the TPXO8 main tidal harmonics (amplitude and phase data) which were interpolated to the western boundary limits: M2, S2, N2, K2, K1, O1, P1, Q1, Mf, Mm, M4, MS4, MN4 (https://www.tpxo.net/).

5.2.3. River discharges

Daily average river discharges measured at the Alcalá del Rio dam (37.52º N, 5.98º W) were used to force the Delft3D model. The dam is located 110 km upstream of the Guadalquivir River mouth, being the closest monitoring station to the river mouth. These data were obtained from the Automatic Hydrological Information System (SAIH) of the Guadalquivir Hydrographic Confederation website (https://www.chguadalquivir.es/saih/), managed by the Andalusia Water Agency (Junta de Andalucía, Spain).

5.2.4. Current data

In situ currents time series from Navarro et al. (2012) were used to calibrate and validate the Delft3D model. The authors used a network of Nortek AS Aquadopp Acoustic Doppler Current Profilers (ADCP) operating at a frequency of 1000 kHz, located at six stations along the estuary (Figure 5.1, ADCP1-ADCP6). All of the ADCPs were positioned on the Port of Seville navigational buoys and were set to measure from the free surface water to the bottom. Current profiles were measured with a depth interval of 1 m and a sampling rate of 10 min.

Furthermore, currents time series from three instruments located near the river mouth were also used (Figure 5.1): Data from a Nortek AWAC-AST acoustic Doppler profiler moored to the bottom at 16 m deep (AWAC) were supplied by Navarro et al. (2012), and data from an ADP Sontek (ADP) and an ARGO Sontek (ARGO) located at 15.5 and 14 m depth, respectively, were provided by Díez-Minguito et al. (2012).

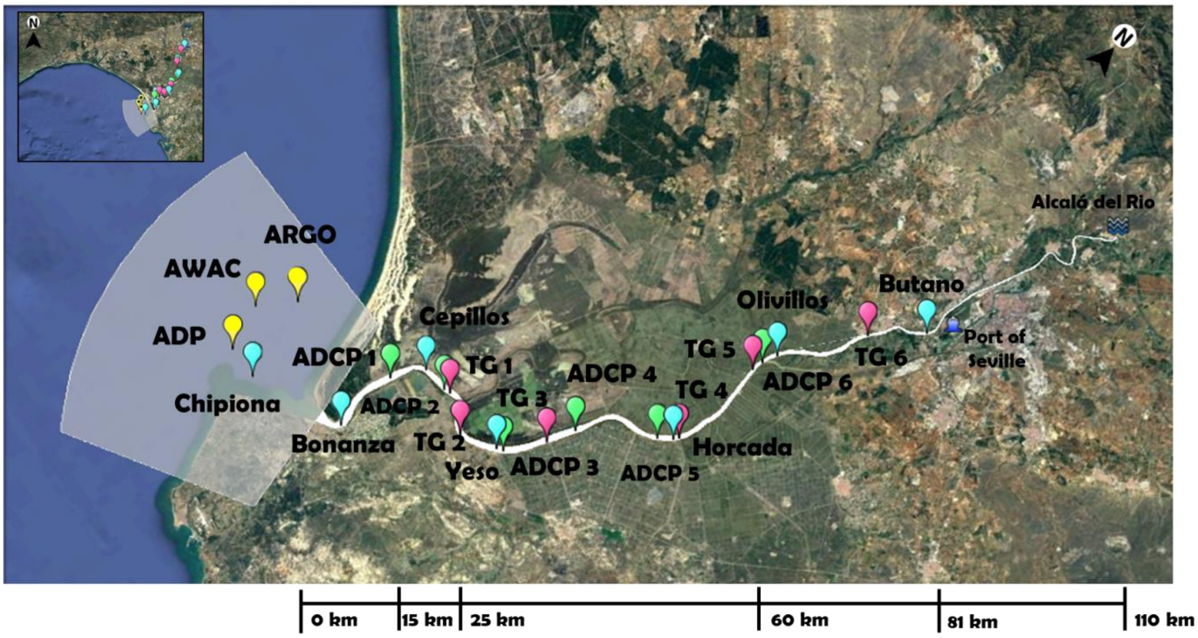

Figure 5.1. Location of the in-situ instruments used in the model calibration and validation. Green balloons: current meters [ADCP1-ADCP6]. Pink balloons: tide gauges, [TG1-TG6]. Blue balloons: tidal gauges [Chipiona, Bonanza, Cepillos, Yeso, Horcada, Olivillos, Butano]. Yellow balloons: current meters in the river mouth [ADP, AWAC, ARGO].

5.2.5. Water level data

Data from seven tide gauges with a sampling rate of 10 min were also obtained from Navarro et al. (2012) and were used to calibrate and validate the water level in the model. The tide gauges, Aqualogger 520PT and NKE-SP2T logger, were located along the river estuary (Figure 5.1, TG1-TG6).

In addition, tidal harmonics provided by Alvarez et al. (2001) were used for the same purpose. The authors had moored seven Aanderaa pressure tide gauges, at seven strategic locations along the estuary (Figure 5.1, Chipiona, Bonanza, Cepillos, Yeso, Horcada, Olivillos, Butano), that were measuring for at least one month with a sampling rate of 10 min. The authors filtered the data with a moving-average Godin filter (Godin, 1972) in order to eliminate fluctuations with a periodicity of less than 1 hour, and then performed a harmonic analysis (Foreman and Henry, 1989) to calculate the amplitude and phase of the four main harmonic constituents (M2, S2, O1, K1) in the study area.

5.2.6. Altimetry data

S3A and CS2 sea level data were used to be qualitatively compared with the model results. Both satellites belong to ESA Missions, S3A to the Copernicus Mission and CS2 to the Earth Explorers Mission. S3A and CS2 have been in orbit since February 2016 and February 2010, respectively. S3A has a 27-day repeat cycle; in the case of CS2, the repeat cycle is 369 days but it has a 30-day sub-cycle.

The altimetry data were provided by the ESA GPOD service. The GPOD options selected to process the data were the same as in Section 3.2.1. The retracking method was SAMOSA+ (Dinardo, 2013; Ray et al., 2015) and the high posting rate of 80 Hz was selected for both satellites.

5.3. Numerical model

5.3.1. Delft3D model

The Delft3D model, developed by the Deltares Institute (https://oss.deltares.nl/web/delft3d), is a model suit composed of several modules: hydrodynamic (FLOW), morphology (MOR), waves (WAVE), water quality (D-WAQ), sediment transport (SED), ecological (ECO), and particle tracking (D-WAQ PAR). All modules together allow for the simulation of hydrodynamic flow (under shallow water assumptions), short wave generation and propagation, heat and salinity transport, sediment transport and morphological changes, ecological processes, and water quality, as well as the interactions among them. Since a large number of processes can be included, Delft3D can be applied to a wide range of systems, including estuaries, rivers, lagoons, and coastal areas, among others.

For this work, FLOW, the central Delft3D module, was used to simulate the hydrodynamics resulting from tidal forcing under different river discharge scenarios. FLOW was developed to model flow phenomena whose horizontal length and time scales are significantly larger than the vertical scales. This module solves the Navier-Stokes equations for an incompressible fluid in two or three dimensions under the shallow-water and Boussinesq assumptions. The system of equations consists of the continuity equation (Equation 5.1), the transport equation solved for temperature and salinity (Equation 5.2), and the horizontal and vertical momentum equations (Equations 5.3 and 5.4). The vertical momentum equation is reduced to the hydrostatic pressure relation, as vertical accelerations are assumed to be small compared to gravitational acceleration and are therefore neglected (Deltares Hydraulics, 2021). The equations are presented in their Cartesian rectangular form:

$$\frac{\partial \xi}{\partial t} + \frac{\partial [h\,\underline{U}]}{\partial x} + \frac{\partial [h\,\underline{V}]}{\partial y} = S \qquad \text{(Eq.5.1)}$$

$$\frac{\partial [hc]}{\partial t} + \frac{\partial [hUc]}{\partial x} + \frac{\partial [hVc]}{\partial y} + \frac{\partial [\omega c]}{\partial \sigma} = h\left[\frac{\partial}{\partial x}\left(D_H \frac{\partial c}{\partial x}\right) + \frac{\partial}{\partial y}\left(D_H \frac{\partial c}{\partial y}\right)\right] + \frac{1}{h}\frac{\partial}{\partial \sigma}\left[D_V \frac{\partial c}{\partial \sigma}\right] + hS \qquad \text{(Eq.5.2)}$$

$$\begin{gathered}\frac{\partial U}{\partial t} + U\frac{\partial U}{\partial x} + \nu\,\frac{\partial U}{\partial y} + \frac{\omega}{h}\,\frac{\partial U}{\partial \sigma} - fV = -\frac{1}{\rho_0}P_x + F_x + M_x + \frac{1}{h^2}\frac{\partial}{\partial \sigma}\left(\nu_V \frac{\partial u}{\partial \sigma}\right)\\ \frac{\partial V}{\partial t} + U\frac{\partial V}{\partial x} + \nu\,\frac{\partial V}{\partial y} + \frac{\omega}{h}\,\frac{\partial V}{\partial \sigma} - fU = -\frac{1}{\rho_0}P_y + F_y + M_y + \frac{1}{h^2}\frac{\partial}{\partial \sigma}\left(\nu_V \frac{\partial v}{\partial \sigma}\right)\end{gathered} \qquad \text{(Eq. 5.3)}$$

$$\frac{\partial P}{\partial \sigma} = -\rho g h \qquad \text{(Eq.5.4)}$$

Where ξ is the free surface elevation relative to a plane (z=0); h is water depth (m), U and V are the depth velocity components ($m \cdot s^{-1}$); S is the contribution due to the discharge or the removal of water, precipitation, and evaporation; c is the mass sediment concentration ($kg \cdot m^{3}$); ω is the vertical velocity component in sigma coordinate system (s^{-1}); σ is the vertical 'sigma' coordinate; D_H and D_V are the horizontal and vertical eddy diffusivity coefficients ($m^2 \cdot s^{-1}$), f is the Coriolis parameter (s^{-1}); Px and Py are the horizontal pressure terms given by Boussinesq approximations; Fx and Fy are the horizontal Reynolds stresses ($m^2 \cdot s^{-2}$); Mx and My represent the contributions due to external sources or sinks of momentum; ρ is the local fluid density ($kg \cdot m^{-3}$); ρ_0 is the reference density of water ($kg \cdot m^{-3}$); u and υ are the Eulerian velocity components in Cartesian coordinates ($m \cdot s^{-1}$); and g is gravity ($m \cdot s^{-2}$). More details can be found in Lesser et al. (2004).

5.3.2. Model implementation

To implement the model in our study area, a grid that includes the Guadalquivir River estuary and the neighbouring continental shelf was defined. The grid is curvilinear and irregular, the cell size varies between 10 m^2 (close to the head) and 300 m^2 (on the continental shelf) and does not include the secondary channels. The model domain is shown in Figure 5.2. A total of 902 grid points were used along the river estuary and the continental shelf, 92 across the continental shelf and 18 across the river. The width along the river estuary is variable following its natural course (the Google Earth tool was used to define the course of the estuary). To compile the bathymetry, four different data sources (previously described in Section 5.2) were used, as none of them covered the grid completely. In fact, in the upper part of the estuary, between 78 km and 110 km from the river mouth, there was no bathymetry data available. Thus, a constant depth value of 5 m was initially assumed which corresponded to the last depth value, but it was modified during the calibration and validation process (Section 5.3.3).

Four boundary conditions were defined (Figure 5.2), three open boundaries on the continental shelf and one closed boundary at the Alcalá del Rio dam. A constant salinity of 36 following Prieto et al. (2009) was used for the open boundaries, and zero for the dam. For the along-shore western boundary ([36.88°,-6.68°], [36.58°, -6.53°]), the Delft3D model was forced with the TPXO tidal harmonics. The amplitude and phase of the 13 tidal constituents were interpolated to the boundary limits (points of intersection with the northern and southern boundaries). For the across-shore northern ([36.88°,-6.68°], [36.89°, -6.41°]) and southern ([36.58°,-6.53°], [36.69°, -6.32°]) boundaries, a Neumann-type flow condition with values of zero was defined. Neumann conditions are applied in cross-shore boundaries in combination with a water level limit in the along-shore boundary (Deltares Hydraulics, 2021) in models with a limited cross-shore extent (where it can be assumed that the along-shore gradient of the water level does not change much in the cross-shore direction). In the river boundary located at the Alcalá del Rio dam, the model was forced with the daily average river discharge values described in Section 5.2. Table 5.1 assembles information on the Delft3D model implementation.

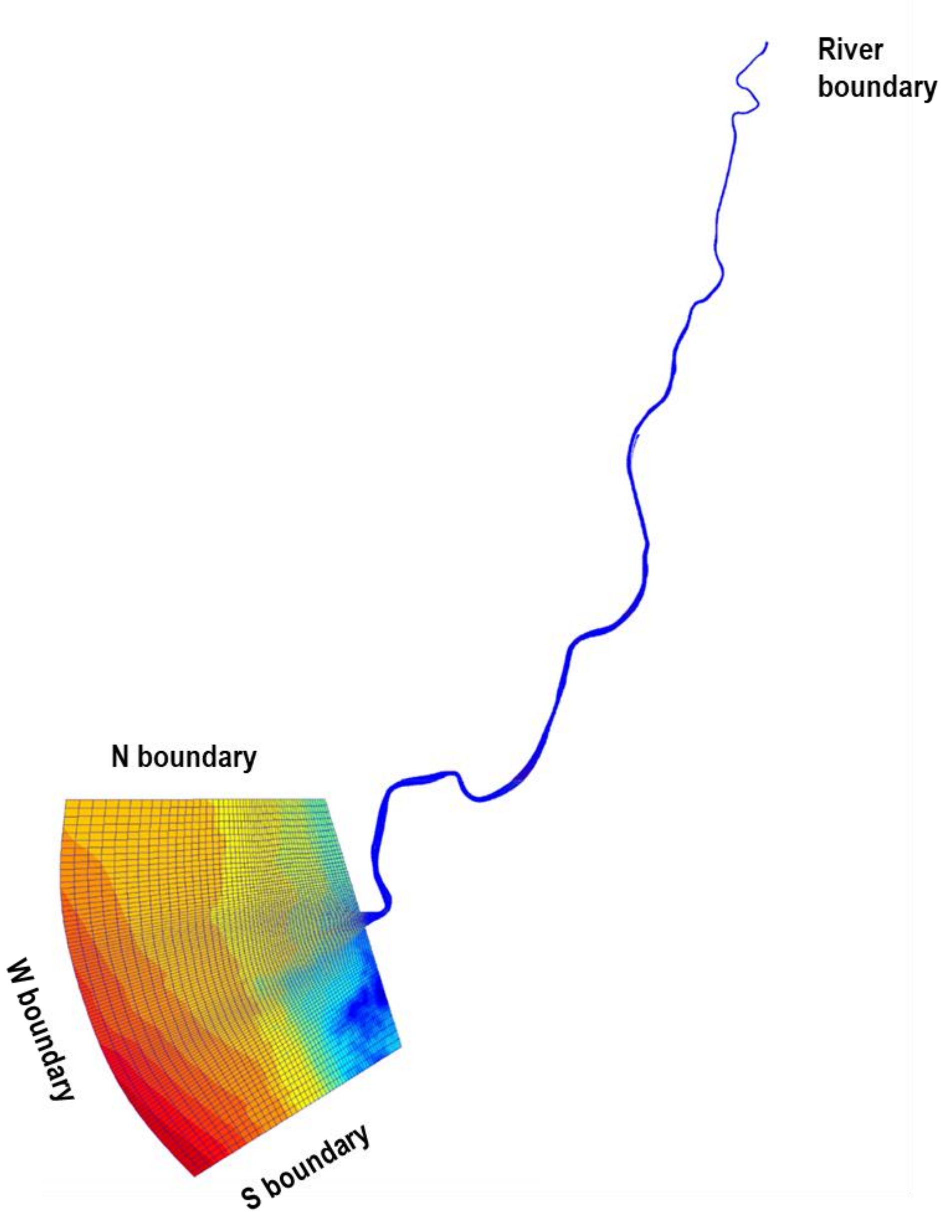

Figure 5.2. Delft3D model grid implemented in the Guadalquivir River estuary and the adjacent Gulf of Cadiz continental shelf. The boundaries location is specified.

Table 5.1. Initial conditions, boundary conditions, and physical and numerical parameters used in the implementation of the Delft3D model.

Grid	Grid points M direction (x axis): 902				
	Grid points N direction (y axis): 92				
	Latitude: 36.7 °				
	Number of layers: 1				
Bathymetry	Non-uniform				
	Values specified at grid cell corners				
Period of simulation	See Table 5.2				
Time step	0.05 s				
Physical processes	Salinity				
Boundary conditions	**Boundary**	West	North	South	River
	Type of border	Water level	Neumann	Neumann	Total discharge
	Type of forcing	Astronomic	Time series	Time series	Time series
Physical parameters	Roughness formula: Chezy (non-uniform). See Table 5.2				
	Horizontal eddy viscosity: 1 $m^2 \cdot s^{-1}$				
	Horizontal eddy diffusivity: 10 $m^2 \cdot s^{-1}$				

To simulate the bottom roughness, different sections with different values of the Chezy coefficient (Equation 5.5) were defined following the zonation proposed by Diez-Minguito et al. (2012) (see Figure 2.3 in Section 2.2). The number of sections and the Chezy values were tested during the model calibration and validation until the best fit with the in-situ data was obtained.

$$C = \frac{H^{\frac{1}{6}}}{\eta} \qquad \text{(Eq. 5.5)}$$

Where C is the Chezy coefficient, H is the water depth and η is the Manning coefficient. As an example, for medium grain size in sand channels a common Manning value is 0.02 $s \cdot m^{-1/3}$ (Arcement and Schneider, 1989), which means that the Chezy values will span between 40 and 100 for the Guadalquivir depth range (min. depth= ~5 m, max. depth= ~12 m).

5.3.3. Model Calibration and Validation

The calibration and validation processes were carried out simultaneously for each case study designed. The different case studies included changes in the bed roughness coefficient (Chezy) and the bathymetry, as explained below, and also the grid resolution. The grid resolution was increased for the meandering section of the GRE, but it did not improve the calibration and validation results. Therefore, this is not shown in this chapter. Table 5.2 summarizes the case studies that will be analysed (see Annex I for the complete list of case studies).

Bathymetry

The bathymetry was a limiting factor in the model implementation for two reasons. Firstly, due to the anthropogenic modifications frequently made to ensure a minimum navigational depth of 6.5 m (Section 2.2). Secondly, errors were included due to the fact that four different datasets, measured at different spatial resolutions and at different dates over a long period of time, were used to compile the model bathymetry.

Initially, in the first case studies, the bathymetry in the upper section of the estuary (between 78 km and 110 km from the river mouth) was defined by using the last depth value available in the datasets (as previously explained in Section 5.3.2). To take into account the bathymetry modifications due to the dredging activities, different case studies were designed with depth values of 5.0 m, 5.5 m, 6.0 m, and 6.5 m in the upper section of the estuary. The corresponding values were considered constant in that section, and were smoothed at the downstream contour (i.e., at the 78 km limit) as well as at the lateral contours. Previous works have also used the bathymetry as a calibration parameter (e.g., Khanarmuei et al., 2020).

Chezy

During the model calibration and validation process, different values of the Chezy coefficient were tested. Initially, three different sections with different Chezy values were defined attending to the zonation established by Diez-Minguito et al. (2012) under a low discharge scenario, and based on morpho-hydrodynamic similarities and dominant tidal processes. The sections (previously described in Section 2.2) were: estuary mouth (0 km) to 25 km (section 1), 25-60 km (section 2), and 60 km to the Alcalá del Rio dam (section 3). The first set of case studies (more than 100 simulations) included different combinations of the Chezy coefficient, with lower values in section 1 and increasing values upstream. The coefficients tested in each section were: [20, 30, 40, and 50] for section 1, [40, 50, 60, 70, and 80] in section 2, and [50, 60, 70, 80, 90, and 100] in section 3 (see Table I, Annex I). Then, a fourth section was created between 15 km and

25 km to better simulate the increasing friction caused by the channel convergence (Figure 5.1), and even a fifth section was added between 18-25 km (see justification in Section 5.4). In all of the case studies, the Chezy coefficients remained the same for the first section (0-25 km) and for the continental shelf (see Table 5.2).

Table 5.2. Case studies shown in this chapter. Dates do not include the set-up time.

Case acronym	Dates	Max. River discharge	Nº Chezy sections [parameter value]	Upstream Depth (m)	Stations studied
Low_50	15/08/2008 to 01/12/2008	91 $m^3 \cdot s^{-1}$	Four [40-60-90-100]	5	River
Low_53	15/08/2008 to 01/12/2008	91 $m^3 \cdot s^{-1}$	Four [40-60-90-100]	6.5	River
Low_55	15/08/2008 to 01/12/2008	91 $m^3 \cdot s^{-1}$	Four [40-60-90-100]	5.5	River
Low_57	15/08/2008 to 01/12/2008	91 $m^3 \cdot s^{-1}$	Four [40-60-90-100]	6	River
Low_59	15/08/2008 to 01/12/2008	91 $m^3 \cdot s^{-1}$	Five [40-60-70-90-100]	6.5	River
High_50	15/12/2008 to 01/04/2009	553 $m^3 \cdot s^{-1}$	Four [40-60-90-100]	5	River
High_53	15/12/2008 to 01/04/2009	553 $m^3 \cdot s^{-1}$	Four [40-60-90-100]	6.5	River
High_55	15/12/2008 to 01/04/2009	553 $m^3 \cdot s^{-1}$	Four [40-60-90-100]	5.5	River
High_57	15/12/2008 to 01/04/2009	553 $m^3 \cdot s^{-1}$	Four [40-60-90-100]	6	River
High_59	15/12/2008 to 01/04/2009	553 $m^3 \cdot s^{-1}$	Five [40-60-70-90-100]	6.5	River
Low_64	10/09/2009 to 01/11/2009	115 $m^3 \cdot s^{-1}$	Five [40-60-70-90-100]	6.5	Continental shelf
Alti_02	07/12/2010 to 17/01/2011	3300 $m^3 \cdot s^{-1}$	Five [40-60-70-90-100]	6.5	Altimetry tracks
Alti_04	05/03/2013 to 20/04/2013	2000 $m^3 \cdot s^{-1}$	Five [40-60-70-90-100]	6.5	Altimetry tracks
Alti_06	09/03/2018 to 21/03/2018	1080 $m^3 \cdot s^{-1}$	Five [40-60-70-90-100]	6.5	Altimetry tracks

For the last set of numerical experiments, changes in the Chezy number and the bathymetry were combined with the aim of improving the results in the last estuary section. More specifically, a constant depth was assumed in the upper section of the estuary using the values included in Table 5.2. For each of those depth values, different configurations of the Chezy number were tested and results were compared (e.g., cases Low_53 and Low_59 in Table 5.2). In addition, different depth values were tested for the same configurations of the Chezy number (e.g., cases Low_50, Low_53, Low_55, and Low_57 in Table 5.2).The results are shown in Section 5.4.

Time series

Observation points were positioned in the same location as the in-situ instruments (but placed in the centre of the channel) to retrieve the model time series. Before comparing the model and in-situ time series, different analyses were done. In the case of the tidal amplitude and phase data from Alvarez et al. (2001), the t-tide tool (Pawlowicz et al., 2002) was used to carry out the tidal prediction with an hourly time interval. No further processing was necessary as the authors had already applied a moving-average Godin filter. In the case of the water levels provided by Navarro et al. (2012), the in-situ data were processed as follows: (1) gaps were identified and filled in with NaN values to construct a continuous time series, (2) a Godin filter $A_nA_nA_{n+1}$ with n=6 for data sampled every 10 min was applied to remove high frequency variations within a period below 1 h (Godin, 1972), (3) the data were interpolated to 1 h, (4) a harmonic analysis with the t-tide tool was done to obtain the amplitude and phase of each constituent, and finally (5) the t-tide tool was used to obtain the tidal prediction.

For the current meter data, the current speed values were used to carry out the comparison with the model results. The processing was as follows: (1) the depth-integrated current velocity components were calculated at each location, (2) gaps were identified and filled in with NaN values, (3) data were interpolated to 1h, (4) data values higher than $\pm 3 \cdot \mathrm{std}$ of the average, were removed in the outlier detection, (5) the time series mean value was removed, (6) a spectral analysis was done to identify the main frequencies and noise, (7) a 4th order Butterworth filter was applied to keep only frequencies between 10 and 25 hours, and finally, (8) the current speeds were calculated. The same processing was performed for the model velocity time series at each location, with the exception of the outlier and gap cleaning, which were not required.

To compare the model and the in-situ time series, the Pearson's correlation coefficient (r), the root mean square error (rmse), and the adjusted determination coefficient (R^2) were used. Furthermore, the error parameters (Table 5.3) proposed by Roelvink et al. (2009) were also used: the Scatter index (SCI), the relative bias (RB), and the Brier skill score (BSS).

Table 5.3. Error parameters [modified from Roelvink et al. (2009)].

Parameter	Formula	Remarks
Scatter index (SCI)	$\frac{rmse_{model-in\_situ}}{max(rms_{in\_situ},\ \lvert< in\_situ >\rvert)}$	SCI indicates the scatter between the model and in-situ data. The statistic is normalized to avoid strange results for data with small mean and large variability.
Relative Bias (RB)	$\frac{< in\_situ - model >}{max(rms_{in\_situ},\ \lvert< in\_situ >\rvert)}$	RB is a relative measure of the bias, normalised in the same way as the SCI.
Brier Skill Score (BSS)	$1 - \frac{Var(in\_situ - model)}{Var\ (in\_situ)}$	BSS relates the variance of the difference between in-situ data and model to the variance of the data. BSS=1 means perfect skill, BSS=0 means no skill.

The comparison was done during events of low river discharge to calibrate the model, and during events of high discharge to validate it. Low discharge events were considered those in which the flow discharged from the Alcalá del Rio dam was lower than 50 $m^3 \cdot s^{-1}$. While during those events the estuary is tidally dominated, during high discharge events (flow higher than 400 $m^3 \cdot s^{-1}$) the estuary is fluvially dominated (Diez-Minguito et al. 2012).

5.3.4. Comparison with altimetry data

A comparison of the model and altimetry water level data during different high discharge events was carried out. One observation point was located at each grid cell along the altimetry track. In all of them the tidal signal was removed from the observed model water level (Equation 5.6):

$$Model\_WL\_corr = Water\ Level - Tidal\ Prediction \qquad \text{(Eq. 5.6)}$$

Where *Water Level* is the water level obtained with the model prediction and the *Tidal Prediction* is calculated from the model data with a classic harmonic analysis (Pawlowicz et al., 2002), based on the ten most important shallow-water constituents with a Signal-to-Noise power Ratio higher than 3.

In the case of the altimeters, the track segment crossing the model grid was selected omitting the closest points to the boundaries. The Absolute Dynamic Topography (ADT), which is the sea level height above the geoid (Figure 1.1), was then calculated along one cycle of S3A and two of CS2 on dates coinciding with the high river discharges (Equation 5.7).

$$ADT\_Alti = Orbit - Range - Range\ corrections - Geophysical\ corrections - Geoid\ correction \quad \text{(Eq. 5.7)}$$

Where:

- *Orbit* is the distance between the satellite's centre of mass and the reference surface (ellipsoid WGS84).
- *Range* is the retracked distance between the instrument and the mean-reflected surface, obtained using the SAMOSA+ retracker (Ray et al., 2015).
- *Range corrections* are modifications of the radar speed and actual scattering surface of the radar pulse; these include the dry and wet tropospheric effects from the European Centre for Medium-range Weather Forecasts (ECMWF) models and the ionospheric correction from the Global Ionospheric Maps (GIMs) of the Jet Propulsion Laboratory.
- *Geophysical corrections* are adjustments to the observed sea surface height, they include: the tidal corrections from the TPXO8 model (Egbert and Erofeeva, 2002), the dynamic atmospheric correction (DAC) of AVISO+ Satellite Altimetry Data from CNES (Centre National d'Études Spatiales, https://www.aviso.altimetry.fr), and the sea state bias (SSB) correction provided by GPOD (Source: Jason2 CLS 2012).
- *Geoid correction* used is the EIGEN (European Improved Gravity model of the Earth by New techniques) 6C4 Geoid Height (Foerste et al., 2014).

The same data screening as in Section 3.3.3 was carried out. Then a moving average filter with a window size of 20 was applied to smooth the *ADT_alti* before comparing it with *Model_WL_corr*. The comparison between model and altimetry was qualitative as the reference levels used by the altimeter and the model are different. In this sense, the *Model_WL_corr* is referred to the model equipotential reference level (Deltares Hydraulics, 2021) and the *ADT_alti* was calculated with respect to the geoid. Therefore, the comparison was done attending to patterns in the spatial variability, i.e., analysing whether the water level close to the river mouth increases in the model observations and if there is correspondence with the observed along-track altimetry data.

5.4. Results and Discussion

Two different simulation periods, with the same length, were selected to calibrate [15/08/2008 to 01/12/2008] and validate [15/12/2008 – 01/04/2009] the model in the estuary. In these periods, the maximum daily river discharge values were 91 $m^3 \cdot s^{-1}$ and 553 $m^3 \cdot s^{-1}$, respectively (Figure 5.3). During the calibration period the freshwater input temporarily exceeded the threshold of 50 $m^3 \cdot s^{-1}$ in cases of low discharge (Díez-Minguito et al., 2012), however this was a one-off peak (91 $m^3 \cdot s^{-1}$) that lasted 4 days, and the average discharge for the full period was 18 $m^3 \cdot s^{-1}$. Therefore, this period was considered suitable for the model calibration.

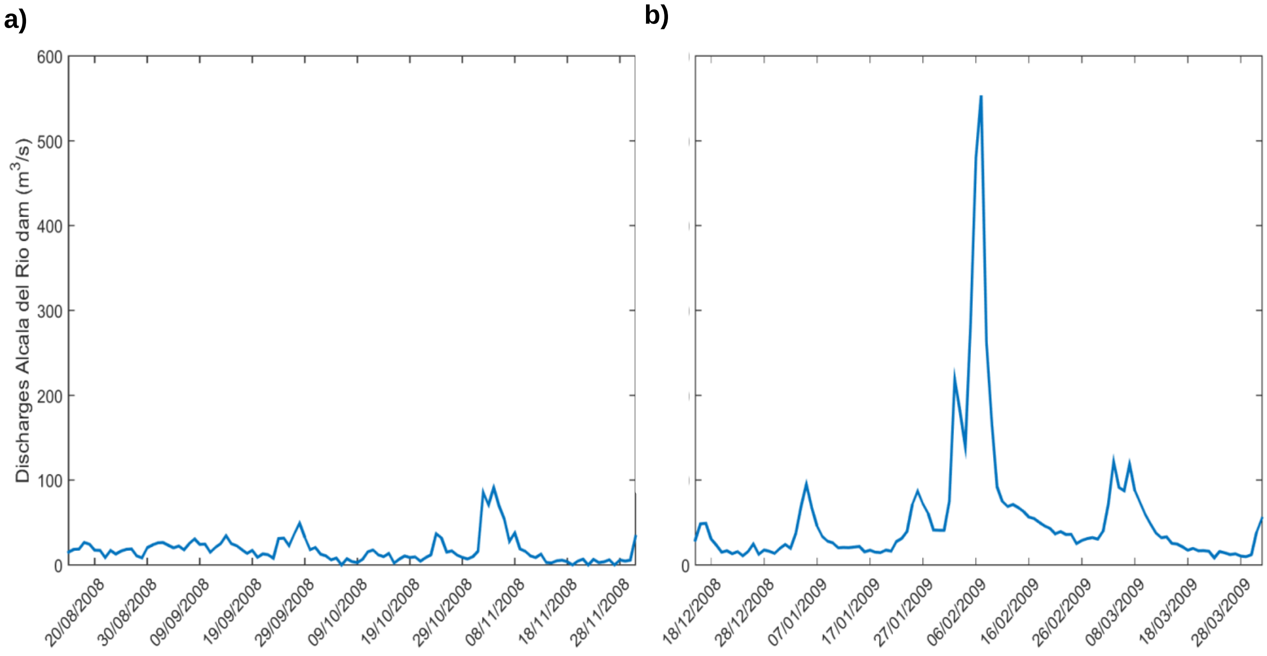

Figure 5.3. Guadalquivir River discharges, measured at the Alcalá del Rio dam, during the calibration (a) and validation (b) study periods.

As mentioned before, the model calibration and validation in the estuary were carried out simultaneously. Different dates were used for the continental shelf calibration points due to in-situ data availability (see Section 5.4.3).

Hereafter, the acronyms in Table 5.2 will be used to refer to the different case studies. In addition, to help with the interpretation of results, the in-situ stations will always be displayed in the upstream direction (mouth-to-head of the estuary, Figure 5.1) in all of the tables and figures of this manuscript.

In addition to the statistical analyses previously described in Section 5.3.3, the Pearson's correlation coefficients displayed in this section were compared using the Fisher transformation (Zar, 2013). The analysis confirmed that all of the r values obtained in the different case studies were significantly different. Moreover, all of the correlation coefficients were obtained with a confidence level (CL) above 95% (p-value<<0.05).

5.4.1. Calibration results for the estuary

Several simulations were carried out to test different configurations of the Chezy coefficient. The best results were obtained using four Chezy sections with the values [40 60 90 100], i.e., the Low_50 case study in Table 5.2. Furthermore, the selected Chezy configuration was used to run three more scenarios using different depth values in the last upstream section (Low_53, Low_55, and Low_57), as mentioned above. Tables 5.4 and 5.5, show the statistical results obtained when comparing the model and in-situ data for these case studies. Our results are in agreement with previous studies performed in similar regions worldwide. For example, Sandbach et al. (2018) demonstrated that a two-dimensional configuration of the Delft3D model was enough to reproduce the Columbia River estuary's hydrodynamics. They obtained rmse values between 6 cm and 28 cm when comparing the model and tide gauge water level data. Their results were poorer in the middle and upper sections of the estuary when this was tidally dominated. Similar results were also obtained by Mendes et al. (2021), who implemented the Delft3D model in the Mondego estuary and obtained rmse values of 7-13 $cm \cdot s^{-1}$ when comparing with ADCP in-situ data.

During low discharge events the estuary is almost totally dominated by tides (Díez-Minguito et al., 2012, Navarro et al., 2012), which simplifies the dynamics, so good calibration results can be anticipated. Under these conditions the water level can be obtained from the superposition of tides and river discharges, with the exception of the outer and middle sections, according to Díez-Minguito et al. (2012). In our case, the worst statistical results were expected upstream where the estuary is influenced by the river discharges. However, the section of the estuary with the worst results was the intermediate one, probably due to the presence of large meanders between kilometres 18 and 40 (Figure 5.1) and other phenomena that will be described below.

Table 5.4. Statistical results of the model calibration in the river estuary: r, rmse (cm, water level; $cm\cdot s^{-1}$, velocities*), and R^2, for the case studies Low_50, Low_53, Low_55 and Low_57. Bold numbers highlight the best results among all case studies. Water level stations (white background). Currents stations (grey shaded background).

	Low_50			**Low_53**			**Low_55**			**Low_57**		
	r	rmse (cm) (cm/s)*	R^2	r	rmse (cm) (cm/s)*	R^2	r	rmse (cm) (cm/s)*	R^2	r	rmse (cm) (cm/s)*	R^2
Chipiona	0.98	17.56	0.95	0.98	17.55	0.95	0.98	17.56	0.96	0.98	17.56	0.95
Bonanza	0.97	16.66	0.95	0.97	16.5	0.95	0.97	16.67	0.95	0.97	16.66	0.95
ADCP1	0.88	8.15*	0.77	0.87	9.17*	0.75	**0.89**	**7.82***	0.79	**0.89**	**7.82***	**0.79**
Cepillos	0.96	16.14	0.93	**0.97**	**15.52**	**0.93**	0.96	16.39	0.93	0.96	16.37	0.93
ADCP2	0.98	20.93*	0.95	0.96	**18.95***	0.92	0.98	20.23*	0.95	0.98	20.28*	0.95
TG1	0.97	15.75	0.93	**0.97**	**12.92**	**0.95**	0.96.	15.66	0.93	0.96	15.7	0.93
TG2	0.96	16.39	0.92	**0.98**	**14.99**	**0.95**	0.96	17.84	0.92	0.96	17.8	0.92
Yeso	**0.91**	**34.35**	**0.82**	0.83	37.3	0.70	0.88	37.31	0.77	0.88	37.13	0.78
ADCP3	0.82	20.74*	0.67	**0.85**	**20.8***	**0.72**	0.81	22.28*	0.67	0.81	22.23*	0.66
TG3	**0.94**	**25.25**	**0.89**	0.88	25.81	0.77	0.91	28.33	0.83	0.92	28.18	0.84
ADCP4	0.91	7.81*	0.83	**0.95**	**5.22***	**0.91**	0.92	8.74*	0.84	0.92	8.73*	0.84
ADCP5	0.81	14.88*	0.66	**0.95**	**20.25***	**0.90**	0.87	14.97*	0.75	0.86	15.04*	0.74
Horcada	0.90	31.17	0.80	**0.91**	**25.51**	**0.82**	0.87	33.2	0.76	0.87	33.14	0.76
TG4	0.95	24.02	0.91	**0.95**	**17.77**	**0.91**	0.93	25.91	0.87	0.94	25.84	0.88
TG5	0.92	30.54	0.85	**0.97**	**19.55**	**0.94**	0.87	32.37	0.76	0.88	32.26	0.77
ADCP6	0.79	12.38*	0.63	**0.94**	**6.23***	**0.89**	0.91	13.54*	0.83	0.91	13.16*	0.82
Olivillos	0.87	33.89	0.76	**0.93**	**23.88**	**0.87**	0.86	33.75	0.73	0.86	33.75	0.74
TG6	0.88	37.73	0.77	**0.95**	**26.09**	**0.90**	0.91	34.81	0.84	0.91	34.86	0.83
Butano	0.90	33.3	0.81	**0.94**	**24.81**	**0.88**	0.93	31.07	0.87	0.93	30.96	0.87

Table 5.5. Statistical results of the model calibration in the river estuary: SCI, RB, and BSS, for the case studies Low_50, Low_53, Low_55, and Low_57. Bold numbers highlight the best results among all case studies. Water level stations (white background). Currents stations (grey shaded background).

	Low_50			**Low_53**			**Low_55**			**Low_57**		
	SCI	RB	BSS	SCI	RB	BSS	SCI	RB	BSS	SCI	RB	BSS
Chipiona	0.22	0.001	0.95	0.22	0.001	0.95	0.22	0.001	0.95	0.22	0.001	0.95
Bonanza	0.23	0.003	0.95	0.23	0.003	0.95	0.23	0.003	0.95	0.23	0.003	0.95
ADCP1	0.23	-0.001	0.74	0.26	0.060	0.70	**0.22**	**-0.008**	**0.76**	0.22	-0.010	0.76
Cepillos	0.27	0.002	0.93	0.26	0.002	0.93	0.27	0.003	0.93	026	0.003	0.93
ADCP2	0.37	-0.330	0.85	0.34	-0.290	0.85	0.36	-0.320	0.86	0.36	-0.32	0.85
TG1	0.30	-0.002	0.91	**0.25**	**-0.003**	**0.94**	0.3	-0.001	0.91	0.30	-0.001	0.95
TG2	0.31	-0.002	0.90	**0.29**	**-0.005**	**0.92**	0.34	-0.001	0.88	0.34	-0.001	0.88
Yeso	**0.57**	**0.005**	**0.68**	0.62	0.003	0.62	0.62	0.005	0.62	0.62	0.005	0.62
ADCP3	0.69	-0.200	0.52	**0.69**	**-0.120**	**0.54**	0.74	-0.320	0.57	0.74	-0.32	0.57
TG3	**0.51**	**-0.002**	**0.74**	0.52	-0.006	0.73	0.58	-0.004	0.67	0.57	-0.003	0.67
ADCP4	0.27	0.150	0.72	**0.18**	**0.080**	**0.86**	0.30	0.190	0.70	0.30	0.19	0.70
ADCP5	0.34	-0.230	0.66	**0.46**	**-0.410**	**0.76**	0.34	-0.260	0.73	0.34	-0.26	0.73
Horcada	0.58	0.001	0.67	**0.47**	**0.001**	**0.78**	0.61	-0.001	0.63	0.61	-0.001	0.63
TG4	0.48	-0.005	0.77	**0.35**	**-0.006**	**0.88**	0.52	-0.008	0.73	0.52	-0.008	0.73
TG5	0.54	-0.007	0.70	**0.35**	**-0.005**	**0.88**	0.58	-0.007	0.67	0.26	-0.007	0.67
ADCP6	0.30	0.030	0.51	**0.15**	**-0.030**	**0.88**	0.33	-0.270	0.81	0.32	-0.26	0.80
Olivillos	0.59	-0.001	0.66	**0.41**	**0.001**	**0.83**	0.58	0.001	0.66	0.58	0.001	0.66
TG6	0.58	-0.004	0.66	**0.4**	**-0.001**	**0.84**	0.54	-0.002	0.71	0.54	-0.002	0.71
Butano	0.52	0.004	0.73	**0.39**	**0.005**	**0.85**	0.49	0.004	0.76	0.48	0.004	0.77

The best statistical results were obtained with the bathymetry configuration of 6.5 m in the last estuary section (Low_53 case study), which coincides with the dredging depth (Díez-Minguito et al., 2012; Ruiz et al. 2015). Figure 5.4 shows the water level comparisons between the model and in-situ data in the following stations: a) Bonanza (close to the estuary mouth), b) TG3 (middle section), and c) TG6 (inner section), for the selected case study (Low_53). Figure 5.5 shows the comparison of velocities for three other stations: a) ADCP1 (outer part of the estuary), b) ADCP3 (middle section), and c) ADCP6 (inner section).

The correlation coefficients for Low_53 ranged between 0.83 and 0.98 in all the stations. In Yeso and TG3, the statistical results obtained in the Low_53 case were poorer in comparison with Low_50 (original bathymetry). In contrast, ADCP1 showed slightly better results in all the statistics with the bathymetry configurations of Low_55 and Low_57. The same pattern was found in the other statistics, with R^2 >0.8, SCI <0.5, and BSS>0.8, indicating that the results were generally good, except in the stations located in the middle of the estuary where the adjustment of the model was poorer (see Tables 5.4 and 5.5). This middle section is still strongly dominated by tides under low discharge conditions; hence, the reason of the discrepancies between the model and in-situ data may be due to the resonance phenomenon created by the anthropogenic modification of the estuary depth which mainly affects the M2 and S2 constituents (Álvarez et al., 2001; Díez-Minguito et al., 2012). As indicated above, the bathymetry is a clear source of error (Section 5.3.3); an increase in depth entails a decrease in friction and thus the damping of the tidal constituents is lower (Álvarez et al., 2001). Therefore, the model underestimations could be related to differences between the bathymetry data used in the model and the real depth during the in-situ sampling. In addition, the stations Yeso and TG3 are located in an area with large meanders (see Figure 5.4); so it is also possible that the model did not correctly simulate the water levels in these complex areas. Another possibility would be that these underestimations are due to the fact that inputs from secondary channels were not taken into consideration (Section 5.3.2). In the case of the bias, the results were more dependent on the instrument itself than on its location along the estuary. While absolute values of RB lower than 0.01 were obtained for the water level stations, indicating a good score between the model and in -situ data, the largest RB values were found in the ADCP stations. A possible explanation for this difference could be the location of the ADCPs on the navigational buoys that are in continuous movement due to the maritime traffic, waves, winds, etc. In fact, the currents vectors showed a certain rotation along the time series, indicating that the buoys were oscillating, which was the reason why we used the speed instead of the velocity components. In addition, it should be taken into account that the model observation points were located in the centre of the estuary while some buoys were located closer to the lateral river boundaries. Finally, the rmse values ranged between 9 cm to 26 cm in the case of water level, even reaching 37 cm in Yeso, and between 5 $cm\cdot s^{-1}$ to 21 $cm\cdot s^{-1}$ for speed. These results were in the range of values obtained in similar studies. For example, Mendes et al. (2021) implemented and calibrated the Delft3D model in two estuarine systems, the Mondego estuary and Óbidos Lagoon (Portugal). They obtained average rmse values of 8-13 cm for SSE and 7-13 $cm\cdot s^{-1}$ for current velocities, when comparing the model with in-situ data. Also, Sandbach et al. (2018), who implemented the Delft3D model in the Columbia River, attained rmse values between 6 and 28 cm during the model calibration. Hence, these results indicate a good fit between model and in-situ data, although there is room for improvement in the middle section of the estuary.

After comparing the four scenarios shown in Tables 5.4 and 5.5, case Low_53 was selected because the model's performance was overall better in the upper section of the river's estuary, while close to the river's mouth all the scenarios presented similar results. Figures 5.4 and 5.5 shown the results with the case Low_53 configuration.

Three different behaviours can be distinguished along the estuary (Figures 5.4 and 5.5), as previously described by Díez-Minguito et al. (2012). Larger water levels were observed at Bonanza, where the estuary is completely dominated by tides. A good match between model and in-situ data was obtained in this station in terms of elevation, with some exceptions (Figure 5.4a). In this sense, the model underestimated the water levels during neap tides and showed a lag every two crests. These asymmetries could be due to a superposition of the M2 and S2 constituents that are the most energetic ones in this estuary, and can create tidal ebb-flood asymmetry in water levels and currents (Guo et al., 2015; Losada et al., 2017). These tidal interactions can also exist between the M2 and M4 constituents (Losada et al. 2017; Parker, 1991). These asymmetries were also identified in the other stations (Figures 5.4b and 5.4c), together with a more notable underestimation in the modelled water elevations. In TG3, the water levels were probably reduced due to bottom friction in the estuary, although convergence and friction are in balance in this section (Díez-Minguito et al., 2012). Other factors that could explain the water level underestimation include errors in the bathymetry, uncertainties in the meanders simulation, and the non-inclusion of secondary channels in the grid design. Nevertheless, a good correlation (0.88) between model and tide gauges was observed at this station. This underestimation in the modelled water levels is also observed in TG6, located at

~77 km upsetream, where no in-situ bathymetry data (78-110 km) was available and it was thus modified during the model calibration (Section 5.2.1). Considering that the largest volume of dredged material removed during anthropogenic interventions takes place at the middle and upper sections of the estuary (Díez-Minguito et al., 2012), bathymetry is the most probable factor explaining the discrepancies observed between the model and in-situ data.

Moreover, TG6 is the closest station to the main secondary channel (Figure 5.1), where the Seville port is located (81 km). Therefore, the in-situ data has an input of water that the model has not taken into account (the secondary channel), which might explain part of the model's underestimation in the water level. The influence of the port channel was even clearer at the Butano station (figure not shown here). As a result of the proximity to the secondary channel, the TG6 station was affected by the resonance phenomena produced by the presence of the port lock (Álvarez et al., 2001). For this reason, higher water levels than in TG3 were observed, less notable in the model data because the secondary channel was not simulated (Figure 5.4c).

The current speed at the ADCP1 location (Figure 5.5a) showed the same order of magnitude for the model and in-situ data, even though the correlation (0.89) and the other statistical results were poorer than expected (Table 5.4 and 5.5). As previously seen in Figure 5.4, the asymmetries due to the superposition of the tidal constituents were identifiable at ADCP1 and all the ADCP stations; less notable at the ADCP3 in-situ time series. At ADCP3, an increase of speed was observed with respect to the other two stations, but it was only notable in the model and not in the in-situ data (Figure 5.5b). ADCP3 was also the ADCP station that showed the poorest statistical results, e.g. rmse of 20.8 $cm \cdot s^{-1}$ and R^2 of 0.72 (see Tables 5.4 and 5.5). As already mentioned, this observation point was located in the middle section of the estuary (Figure 5.1). These differences between model and in-situ data indicated that the model was overestimating the velocities, and it may be that the assumption that convergence and friction are in balance in this section of the estuary (Díez-Minguito et al., 2012) is not being fulfilled in the model. The cause could be that the roughness coefficient was not well adjusted or perhaps due to other factors, such as the uncertainties in the bathymetry, as mentioned above. Finally, the best adjustment was found for ADCP6, located in the last section where the currents were influenced mainly by the reflection in the Alcalá del Rio dam. This indicates a good simulation of the reflection phenomenon by the model.

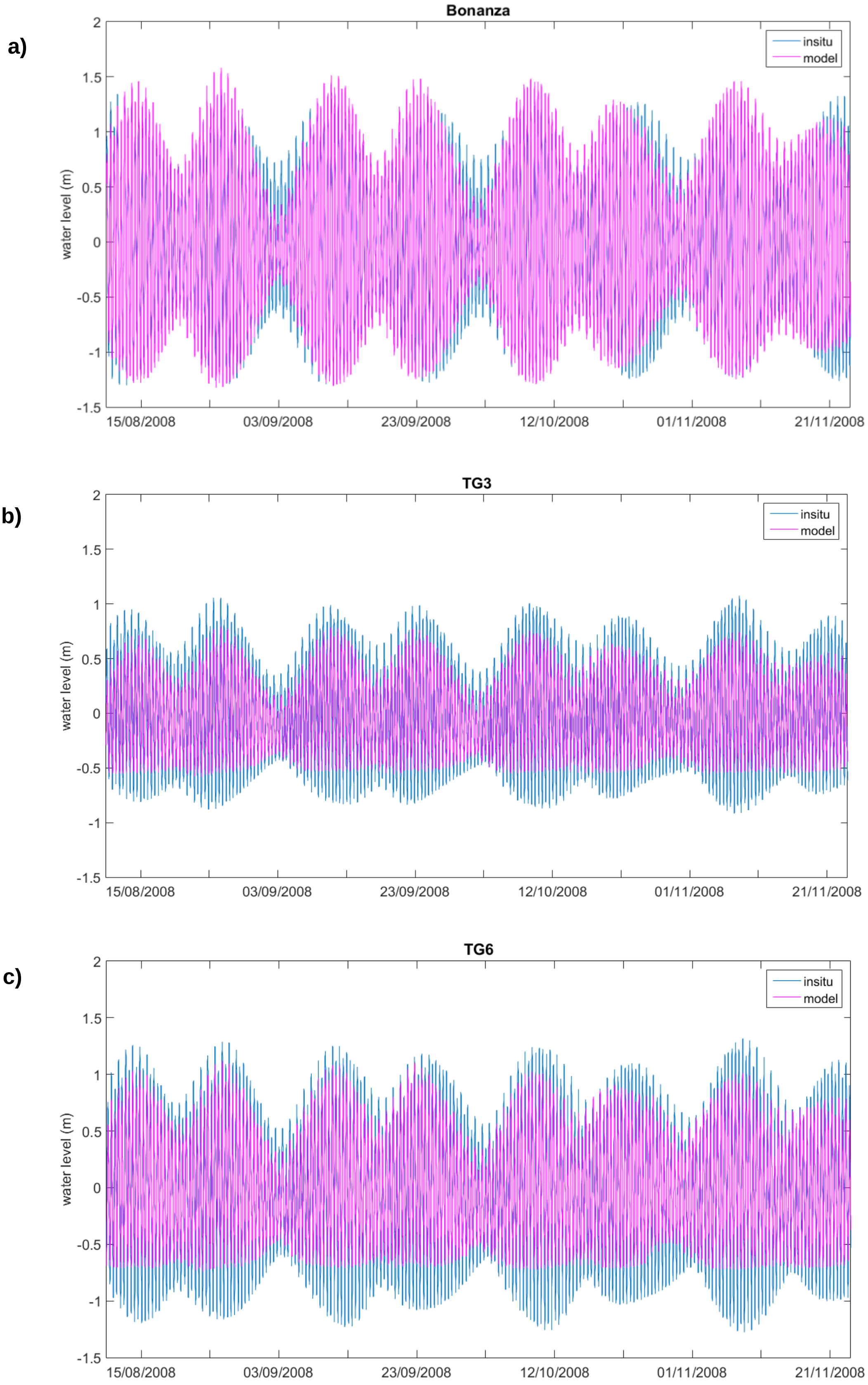

Figure 5.4 Water level comparisons between the model and in-situ data for the stations: Bonanza (a), TG3 (b), and TG6 (c). Case Low_53.

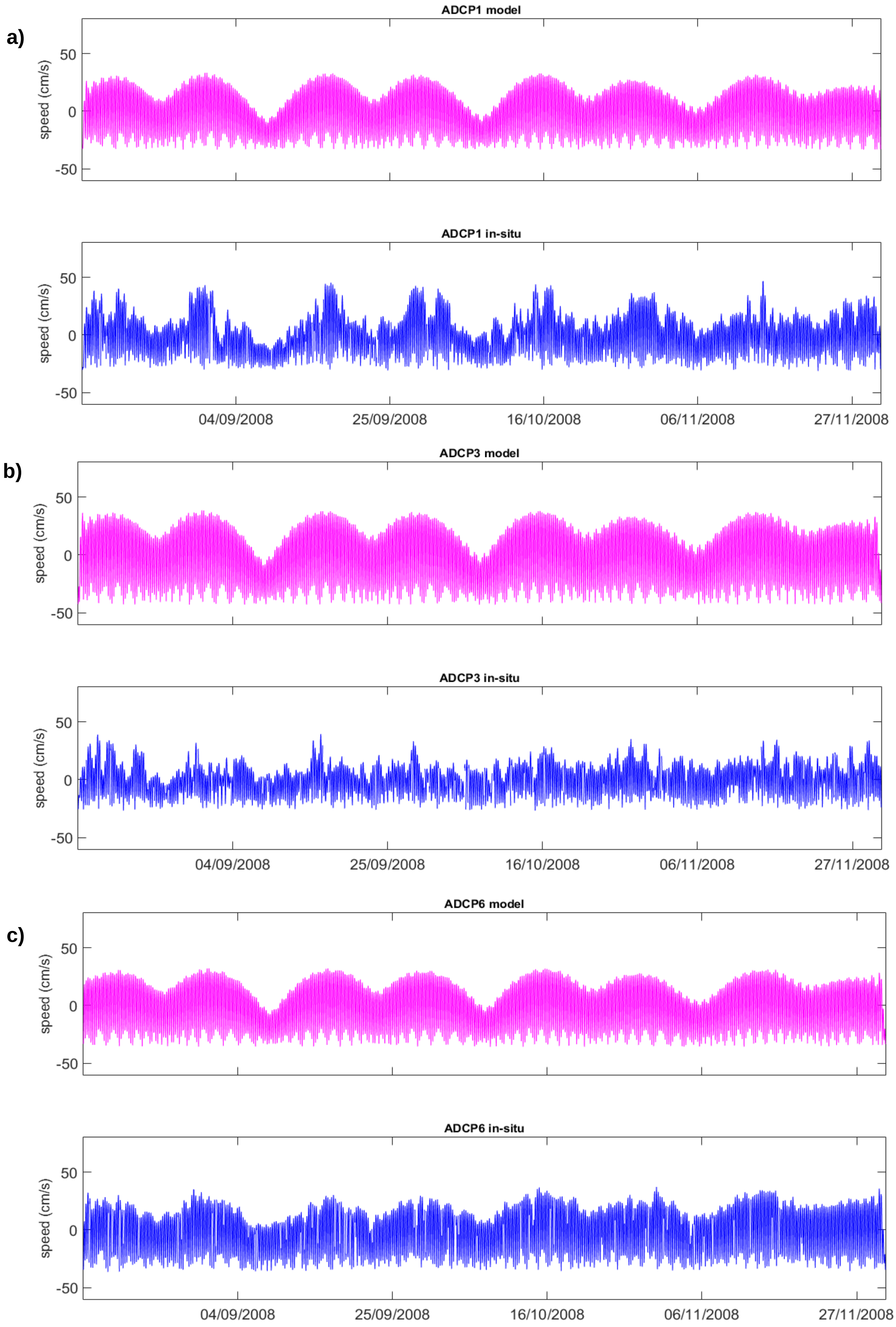

Figure 5.5. Speed (cm·s^{-1}) comparisons between the model (pink) and in-situ (blue) data for the stations ADCP1 (a), ADCP3 (b), and ADCP6 (c). Case Low_53.

Therefore, Figures 5.4 and 5.5 confirm the statistical results, i.e., the model adjustment is generally good, but it could be improved in the middle section where the biggest differences between model and in-situ data were found. Thus, the third Chezy section was divided into two different sections with the aim of improving the results in this zone. As a result, the new sections were defined as follows: section 1 (0-15 km), section 2 (15-25 km), section 3 (25-30 km), section 4 (35-60 km), and section 5 (60-110 km). The chosen Chezy coefficients were 40, 60, 70, 90 and 100, respectively (Low_59 case study, Table 5.2).

Table 5.6 shows the results for Low_59. As expected, an improvement of the statistical results was achieved at the Yeso and TG3 stations. Although in ADPC3 the results were similar or poorer, e.g., the bias was -0.26 in Low_59 and -0.12 in Low_53. Different Chezy values were tested close to the ADCP3 location (see Table I, Annex I), however Low_59 was the final configuration selected because it provided the best results in the middle section without negatively affecting the adjustment in the other sections of the estuary.

Figure 5.6 shows the comparison between the model and in-situ water level time series in Yeso during the calibration period for the Low_50 and Low_59 cases, to analyse the improvement of the adjustment in the middle section. The model underestimated the water level in both cases, although slightly less in the Low_59 case. Maximum differences of 86 cm between water level series were obtained in Low_50 with respect to differences of 69 cm in the Low_59 case study. In the case of TG3 station (figure not shown here), the maximum differences between model and in-situ data were also lower for the Low_59 case (56 cm) than for the Low_50 case (64 cm).

Table 5.6. Statistical results of the model calibration in the river estuary: r, rmse (cm, water level; $cm\cdot s^{-1}$, velocities*), SCI, RB, and BSS, for the case study Low_59. Bold numbers indicate the improvements in the middle section of the estuary. Water level stations (white background). Currents stations (grey shaded background).

Low_59	**r**	**rmse (cm) (cm/s)***	**R^2**	**SCI**	**RB**	**BSS**
Chipiona	0.98	17.55	0.95	0.22	0	0.95
Bonanza	0.97	16.39	0.95	0.23	0.003	0.95
ADCP1	0.87	9.65*	0.76	0.27	0.099	0.68
Cepillos	0.97	15.47	0.93	0.26	0.002	0.93
ADCP2	0.96	17.05*	0.92	0.30	-0.26	0.87
TG1	0.98	11.45	0.95	0.22	-0.003	0.95
TG2	0.98	14.69	0.95	0.28	-0.005	0.92
Yeso	**0.85**	**34.69**	**0.73**	**0.57**	**0.003**	**0.67**
ADCP3	0.85	22.86*	0.72	0.76	-0.26	0.60
TG3	**0.91**	**22.36**	**0.83**	**0.45**	**-0.006**	**0.80**
ADCP4	0.95	5.89*	0.90	0.20	0.11	0.84
ADCP5	0.95	19.02*	0.90	0.44	-0.39	0.78
Horcada	0.91	24.19	0.83	0.44	0.001	0.80
TG4	0.96	16.32	0.92	0.32	-0.006	0.90
TG5	0.97	17.88	0.94	0.32	-0.005	0.90
ADCP6	0.94	6.88*	0.88	0.17	0.015	0.85
Olivillos	0.94	22.64	0.88	0.44	0.001	0.80
TG6	0.95	24.74	0.90	0.38	-0.001	0.86
Butano	0.94	23.73	0.88	0.37	0.06	0.86

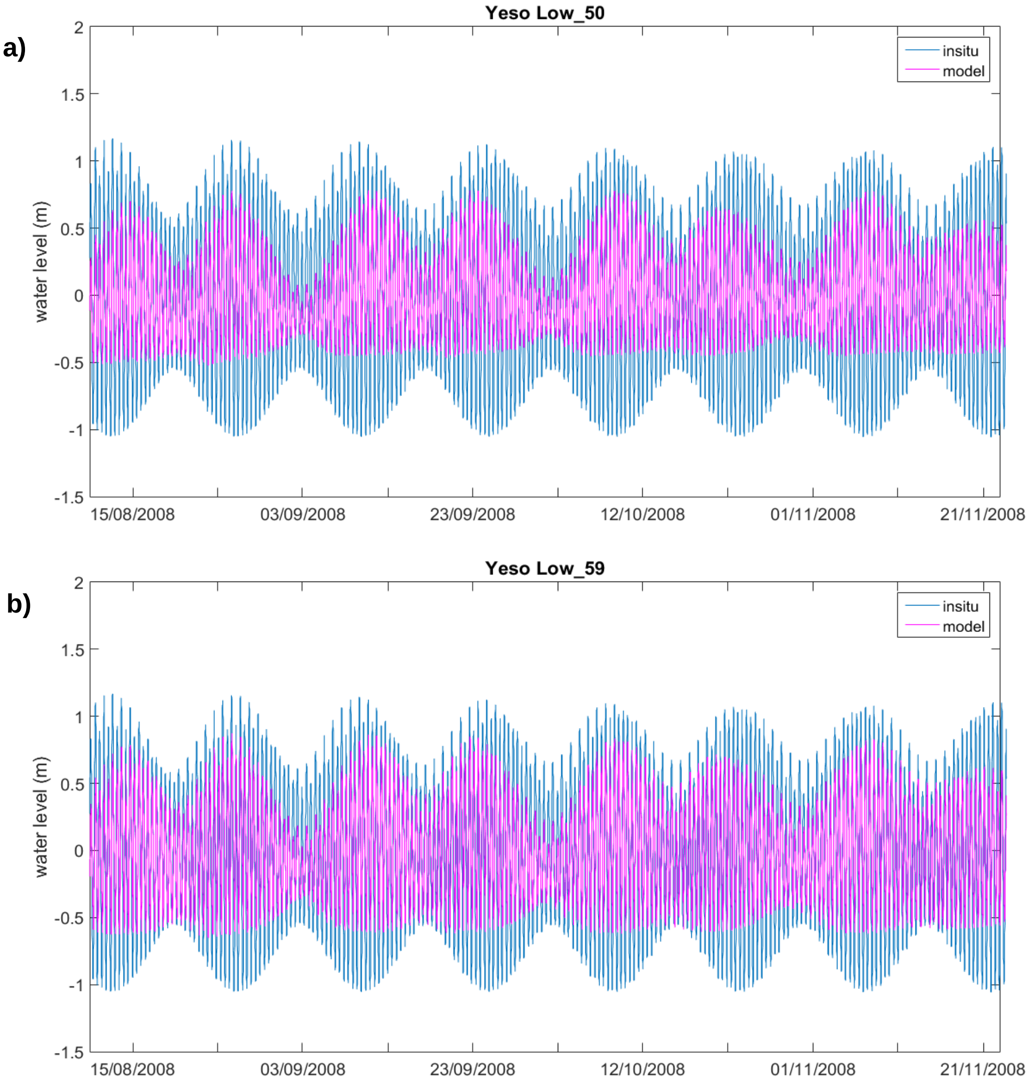

Figure 5.6. Water level comparisons between the model and in-situ data at Yeso, using two different scenarios: Low_50 (a) and Low_59 (b).

5.4.2. Validation results for the estuary

In this section, the validation results along the estuary are analysed, following the same structure as in the previous Section 5.4.1. Table 5.7 and 5.8 show the results obtained from the comparison between the model and in-situ data during the validation period.

Table 5.7. Statistical results of the model validation in the river estuary: r, rmse (cm, water level; cm·s^{-1}, velocities*), and R^2, cases High_50, High_53, High_55 and High_57. Bold numbers indicate the best results among case studies. Water level stations (white background). Currents stations (grey shaded background).

	High_50			High_53			High_55			High_57		
	r	rmse (cm) (cms/s)*	R^2	r	rmse (cm) (cms/s)*	R^2	r	rmse (cm) (cms/s)*	R^2	r	rmse (cm) (cms/s)*	R^2
Chipiona	0.97	18.38	0.95	0.97	18.38	0.95	0.97	18.38	0.95	0.97	18.38	0.95
Bonanza	0.97	17.37	0.94	0.97	17.3	0.94	0.97	17.37	0.94	0.97	17.36	0.94
ADCP1	0.83	12.81*	0.68	0.82	11.73*	0.68	0.83	12.58*	0.69	0.83	12.61*	0.69
Cepillos	0.96	16.57	0.92	0.96	16.34	0.92	0.96	16.87	0.92	0.96	16.8	0.92
ADCP2	0.92	25.99*	0.84	0.92	25.94*	0.86	0.93	27.41*	0.87	0.93	27.46*	0.87
TG1	0.97	14.66	0.94	**0.98**	**12.07**	**0.96**	0.97	14.58	0.94	0.97	14.6	0.94
TG2	0.96	16.65	0.92	**0.97**	**15.67**	**0.94**	0.92	18.16	0.91	0.95	18.06	0.91
Yeso	**0.87**	**35.56**	**0.76**	0.79	38.77	0.63	0.84	38.59	0.70	0.84	38.41	0.71
ADCP3	0.68	17.99*	0.47	**0.71**	**17.93***	**0.50**	0.69	18.83*	0.48	0.69	18.81*	0.48
TG3	**0.89**	**26.74**	**0.79**	0.84	27.34	0.71	0.85	29.66	0.73	0.86	29.49	0.73
ADCP4	0.73	11.29*	0.53	0.74	11.18*	0.56	0.74	11.02*	0.56	0.74	11.02*	0.56
ADCP5	0.78	22.26*	0.61	**0.90**	**28.53***	**0.81**	0.81	22.7*	0.66	0.81	22.76*	0.66
Horcada	0.86	32.46	0.74	**0.88**	**27.07**	**0.78**	0.82	34.47	0.68	0.83	34.39	0.68
TG4	0.91	28.54	0.83	**0.93**	**19.82**	**0.86**	0.89	27.41	0.78	0.89	27.31	0.79
TG5	0.87	31.97	0.77	**0.94**	**21.45**	**0.89**	0.83	33.67	0.69	0.83	33.57	0.70
ADCP6	0.73	15.48*	0.54	**0.84**	**13.36***	**0.71**	0.81	19.82*	0.66	0.81	19.4*	0.65
Olivillos	0.83	35.42	0.69	**0.91**	**25.82**	**0.83**	0.82	35.34	0.67	0.82	35.32	0.67
TG6	0.84	39.33	0.70	**0.91**	**29.2**	**0.83**	0.88	36.26	0.77	0.88	36.32	0.77
Butano	0.86	35.45	0.75	**0.90**	**28.51**	**0.81**	0.90	32.72	0.81	0.90	32.65	0.81

Table 5.8. Statistical results of the model validation in the river estuary: SCI, RB, and BSS, cases High_50, High_53, High_55, and High_57. Bold numbers indicate the best results among all of the case studies. Water level stations (white background). Currents stations (grey shaded background).

	High_50			**High_53**			**High_55**			**High_57**		
	SCI	RB	BSS	SCI	RB	BSS	SCI	RB	BSS	SCI	RB	BSS
Chipiona	0.23	-0.001	0.95	0.23	-0.001	0.95	0.23	-0.001	0.95	0.23	-0.001	0.95
Bonanza	0.24	0.001	0.94	0.24	0.001	0.94	0.24	0.001	0.94	0.24	0.001	0.94
ADCP1	0.30	-0.18	0.67	0.28	-0.12	0.65	0.3	-0.17	0.67	0.30	-0.17	0.67
Cepillos	0.27	0.001	0.92	0.27	0.001	0.93	0.28	0.001	0.92	0.28	0.001	0.92
ADCP2	0.41	-0.36	0.77	0.41	-0.36	0.77	0.44	-0.38	0.77	0.44	-0.39	0.77
TG1	0.28	0.001	0.92	**0.23**	**-0.001**	**0.97**	0.28	0.002	0.92	0.28	0.002	0.92
TG2	0.32	-0.001	0.90	**0.30**	**-0.005**	**0.91**	0.35	-0.001	0.88	0.35	0.001	0.88
Yeso	**0.60**	**0.003**	**0.64**	0.64	0.001	0.59	0.64	0.003	0.59	0.64	0.003	0.59
ADCP3	0.46	0.03	0.20	**0.56**	**0.08**	**0.22**	0.48	0.007	0.24	0.48	0.005	0.24
TG3	**0.55**	**0.001**	**0.70**	0.55	-0.004	0.70	0.61	-0.002	0.63	0.6	-0.002	0.64
ADCP4	0.32	-0.06	0.44	0.31	-0.11	0.50	0.31	-0.02	0.45	0.31	-0.02	0.45
ADCP5	0.43	-0.33	0.59	**0.55**	**-0.48**	**0.63**	0.44	-0.35	0.63	0.44	-0.35	0.62
Horcada	0.60	-0.001	0.64	**0.5**	**0.001**	**0.75**	0.64	-0.002	0.60	0.63	-0.001	0.60
TG4	0.51	-0.001	0.73	**0.40**	**-0.001**	**0.84**	0.55	-0.004	0.70	0.55	-0.004	0.70
TG5	0.57	-0.002	0.67	**0.38**	**-0.001**	**0.85**	0.6	-0.002	0.64	0.60	-0.002	0.64
ADCP6	0.33	-0.08	0.44	**0.28**	**-0.14**	**0.66**	0.42	-0.33	0.65	0.41	-0.32	0.64
Olivillos	0.61	-0.001	0.63	**0.45**	**0.001**	**0.8**	0.61	0.001	0.63	0.61	0.001	0.63
TG6	0.61	0.001	0.63	**0.45**	**0.004**	**0.80**	0.56	0.003	0.69	0.56	0.003	0.69
Butano	0.55	0.005	0.70	**0.44**	**0.006**	**0.8**	0.51	0.005	0.74	0.51	0.005	0.74

All the case studies (High_50, High_53, High_55, and High_57) include four sections with Chezy coefficients [40 60 90 100] but differ in the depth value used in the last upstream section (see Table 5.2). The best adjustment was achieved with the High_53 case, which coincided with that of the calibration (Low_53), i.e., when the depth along the last upstream section was set to 6.5 m. The results of the validation were slightly poorer in comparison with the calibration results. For example, the rmse was ~2 cm larger at the tide gauge stations during validation and about 4-5 $cm \cdot s^{-1}$ larger at the ADCP stations (see Tables 5.5 and 5.7). These differences were also observed by Martyr-Keller et al. (2017), who implemented the Delft3D model in San Francisco Bay and obtained average rmse values of 14 cm and 18 cm for calibration (short period) and validation (large period that includes a wide range of conditions, i.e. flood and drought conditions, pumping rates, and gate operations), respectively, when comparing model and in-situ water levels.

The High_53 configuration improved the validation results mainly at the inner section of the estuary, but not at the middle one. At Yeso and TG3 stations higher values of r and R^2 and lower values of rmse were obtained with High_50 in comparison with High_53 (Tables 5.7 and 5.8). As mentioned before, the Low_53 and High_53 cases were not the best configuration for the intermediate section, but they were for the rest of the estuary. In the outer section, the worst performance was obtained at the ADCP1 position, with an R^2 value of 0.68 and BSS of 0.65. Also, a particularly bad adjustment was found at ADCP3 (as during the calibration) and ADCP4. The low accurate results at the ADCP stations during high discharge events were related with the instrument location on the navigational buoys. In fact, higher biases (RB) were also obtained at all the ADCP stations than at the water level stations (Table 5.7 and 5.8).

During high discharge events the estuary is fluvially dominated (Díez-Minguito et al., 2012). River discharges modifiy the tide's propagation along the estuary and contribute to the tidal energy dissipation (Guo et al., 2015; Jay et al., 2015) and the decrease of wave celerity (Losada et al., 2017). In order to better understand the influence of high discharges, Figures 5.7 and 5.8 show the comparison between the model and in-situ water levels and current speeds at different representative stations (the same stations as shown in Section 5.4.1 were selected for a better comparison). The behaviour along the estuary remained split into the three distinct sections, in the same way as proposed by Díez-Minguito et al. (2012).

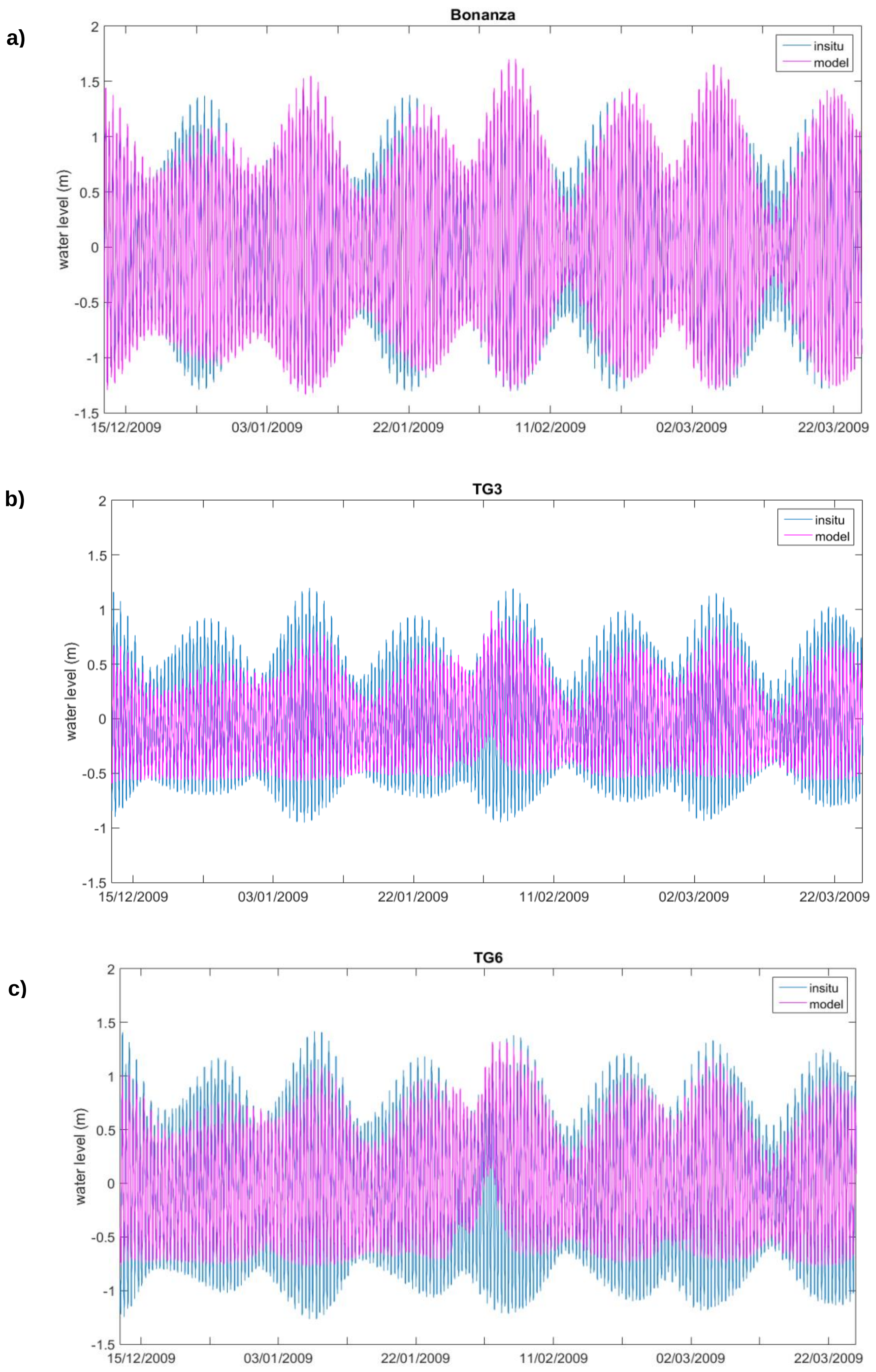

Figure 5.7. Water level comparisons between the model and in-situ data at the stations: Bonanza, TG3, and TG6. Case High_53.

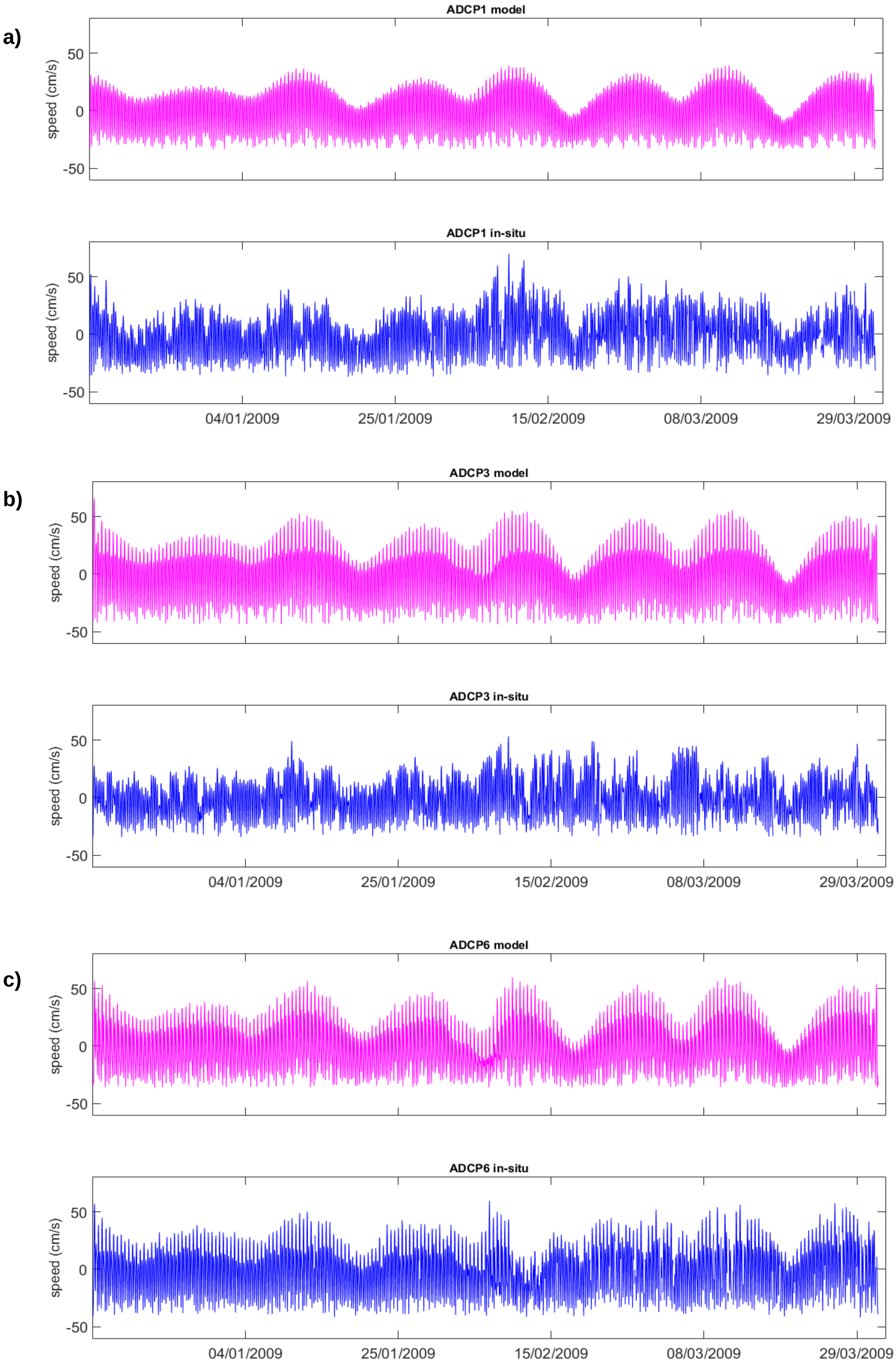

Figure 5.8. Speed (cm·s^{-1}) comparisons between the model (pink) and in-situ (blue) data at the stations ADCP1 (a), ADCP3 (b), and ADCP6 (c). Case High_53.

In Bonanza, water levels of 1-2 m were obtained (Figure 5.7a), which are lower than expected because during high freshwater discharges the water level is not just obtained by the superposition of tides and river discharges (as in normal discharges) (Losada et al., 2017). Furthermore, in Bonanza, close to the river's mouth where the depth increases, the tidal amplitude damping is weaker due to lower friction. In addition, the values obtained are in agreement with the results of Losada et al. (2017) for discharges below 2000 $m^3 \cdot s^{-1}$. They explained that these results were also due to the high ratio between the volume of water on the tidal flat and the volume found in the channel during those discharge conditions.

Figure 5.3b shows that the peak of discharge took place between 02/02/2009 and 09/02/2009, which coincides with a mismatch in the model water levels with respect to the in-situ data for the middle and upper stations (Figures 5.7b and 5.7c). High discharges affect the tidal dynamics, dissipating tidal energy, damping the amplitude (especially for short period constituents, Losada et al., 2017), and altering the phases (Guo et al., 2015). This can be observed especially in the innermost section (TG6, Figure 5.7c) where the damping effect was accentuated, in agreement with Losada et al. (2017). Other noticeable consequence of the high discharge contribution is an upstream reduction of the tidal range between spring and neap tides (comparing Figures 5.7a and 5.7c). This response to freshwater input was well simulated by the model, although it underestimated the water levels. These discrepancies were also observed during the calibration, and the possible reasons were outlined in Section 5.4.1. A similar response was observed in Figure 5.8. At the ADCP3 station, the model overestimated the current speed, and from the time of the maximum discharge, both model and in-situ series were unsynchronised. The same behaviour was found at the ADCP6; after the peak of discharge a lag between model observation and in-situ measurements was observed and the model began to slightly overestimate the current speed (Figure 5.8c).This mismatch between model and in-situ data could be due to uncertainties associated with the model configuration (friction coefficients, bathymetry, etc.), but also to the uncertainties associated with the location of the in-situ instruments, as previously mentioned. In addition, an increase of the current speed was also observed coinciding with the peak of the maximum discharge, which was more notable upstream (Figure 5.8). Losada et al. (2017) demonstrated that this increase in the current speed for discharges of 500-1000 $m^3 \cdot s^{-1}$ was not attributable to the effects of the dam, but rather to the decrease in friction due to high sediment concentrations. The turbidity during high discharge conditions can increase several orders of magnitude in almost the entire estuary according to Díez-Minguito et al. (2014). Another phenomenon that could be observed in the middle and inner stations is that, as a result of the freshwater discharges, the effect of tidal asymmetries disappears or is smoothed out (Figures 5.7 and 5.8).

As in the calibration period, a case study with a fifth Chezy section was simulated (case High_59, Table 5.2) in order to improve the adjustment in the middle section. The validation results are shown in Table 5.9.

Table 5.9. Statistical results of the model validation in the river estuary: r, rmse (cm, water; cm·s^{-1}, velocities*), SCI, RB, and BSS, case High_59. Bold numbers indicate the best results among all of the case studies. Water level stations (white background). Currents stations (grey shaded background).

High_59	**r**	**rmse (cm) (cm/s)***	**R^2**	**SCI**	**RB**	**BSS**
Chipiona	0.97	18.38	0.95	0.23	-0.001	0.95
Bonanza	0.97	17.25	0.94	0.24	0	0.94
ADCP1	0.83	11.22*	0.69	0.26	-0.08	0.64
Cepillos	0.96	16.55	0.92	0.27	0	0.93
ADCP2	0.92	24.04*	0.85	0.38	-0.33	0.79
TG1	0.98	11.09	0.96	0.21	-0	0.96
TG2	0.97	15.4	0.94	0.30	-0.005	0.91
Yeso	**0.82**	**36.22**	**0.68**	**0.60**	**0.002**	**0.64**
ADCP3	**0.71**	19.46*	**0.50**	0.50	**0.007**	**0.27**
TG3	**0.88**	**24.08**	**0.77**	**0.48**	**-0.004**	**0.77**
ADCP4	0.74	10.97*	0.55	0.31	-0.089	0.49
ADCP5	0.90	27.29*	0.81	0.53	-0.46	0.65
Horcada	0.89	25.75	0.79	0.47	0.001	0.78
TG4	0.93	18.45	0.87	0.37	-0	0.87
TG5	0.95	19.86	0.90	0.35	-0	0.88
ADCP6	0.83	13.00*	0.70	0.27	-0.093	0.63
Olivillos	0.91	24.58	0.84	0.42	0	0.82
TG6	0.91	27.99	0.84	0.43	0.004	0.81
Butano	0.91	27.50	0.82	0.43	0.006	0.82

The statistical results at the Yeso and TG3 stations improved for the configuration of case High_59 (Table 5.9) with respect to High_53, as in the low discharge cases, without negatively affecting the other estuary sections. Slight improvements were also obtained at the ADCP3 location (Table 5.9), which did not happen in Low_59. However, some statistics were still better for case High_50 in the middle estuary (Table 5.7 and Table 5.8): R^2 values were 0.76, 0.47, and 0.79 for Yeso, ADCP3, and TG3 in the High_50 case, whilst in High_59 they were 0.68, 0.50, and 0.77, respectively. In any case, Figure 5.9 indicates that the model underestimated the water level more in the High_50 case, justifying the choice of High_59 as the final configuration. Maximum differences of 104 cm between the water level time series were obtained in the High_50 case with respect to the 96 cm obtained in High_59 for Yeso, 105 cm and 88 cm for TG3 in High_50 and High_59 respectively, and smaller differences for ADCP3.

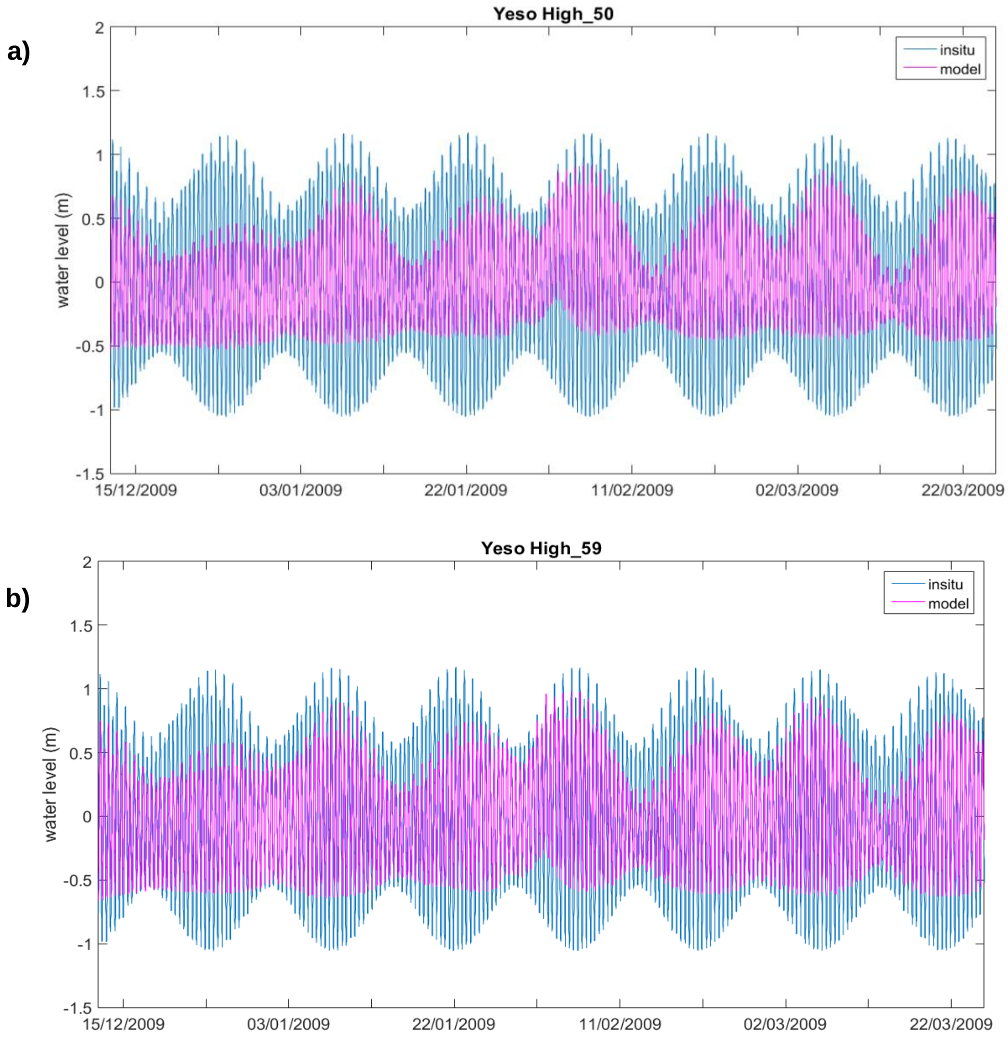

Figure 5.9. Water level comparisons between the model and in-situ data at Yeso, for two different scenarios: High_50 (a), and High_59 (b).

5.4.3. Results for the continental shelf

The in-situ data for the continental shelf were measured in a different period than those for the river. Moreover, there were no data available for high discharge events. For this reason, only a period during low discharges was selected for the model calibration [10/09/2009 to 01/11/2009]. The maximum daily discharge rate during this period was 115.5 $m^3 \cdot s^{-1}$ with an average value of 16.8 $m^3 \cdot s^{-1}$ (Figure 5.10). The calibration results for the continental shelf, Low_64 case study, are shown in Table 5.10.

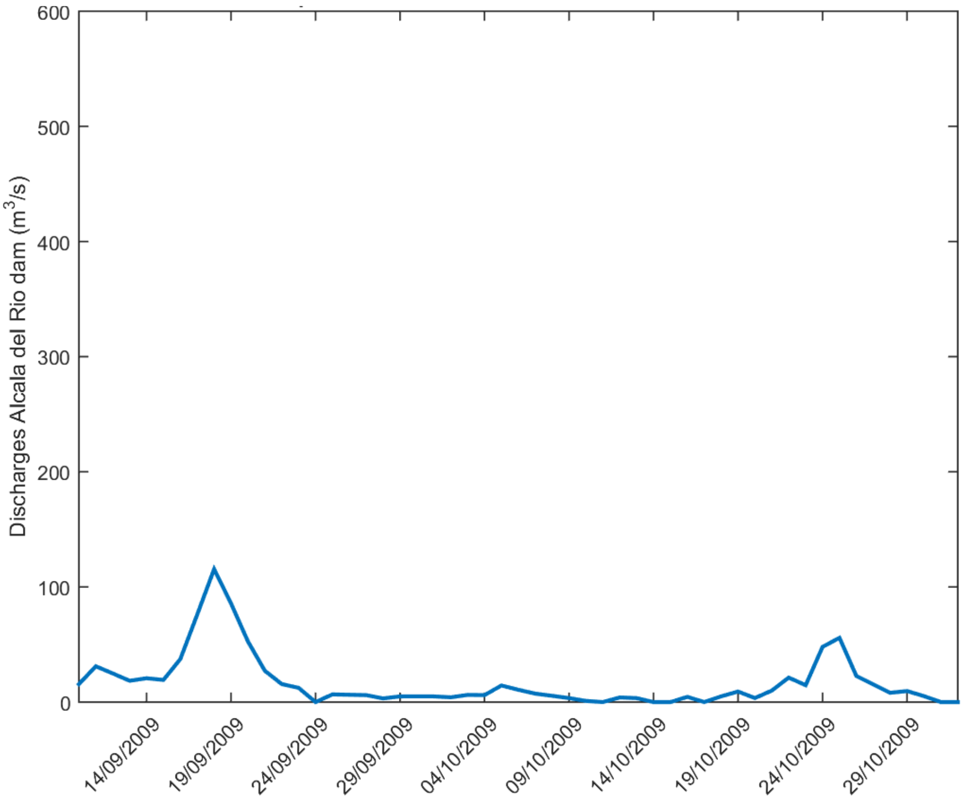

Figure 5.10. Guadalquivir River discharges, measured at the Alcalá del Rio dam, during the calibration period for the continental shelf.

Table 5.10. Calibration results for the continental shelf, case Low_64: r, rmse ($cm \cdot s^{-1}$, current speed), R^2, SCI, RB, and BSS.

Low_64	r	rmse (cm/s)	R^2	SCI	RB	BSS
ADP	0.89	3.9	0.79	0.36	-0.27	0.77
AWAC	0.84	3.5	0.71	0.39	-0.31	0.70
ARGO	0.81	1.8	0.66	0.30	-0.14	0.65

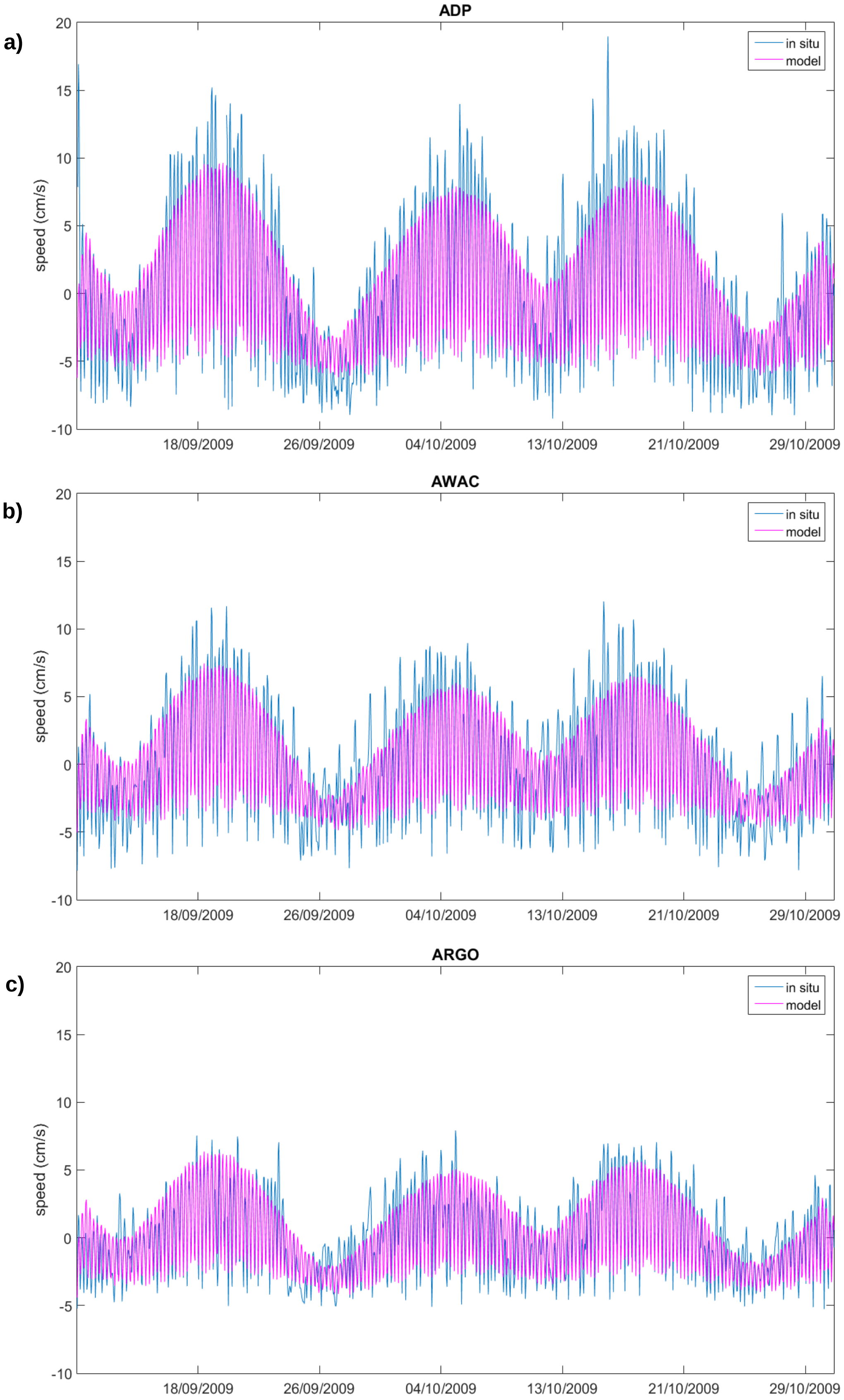

Figure 5.11. Current speed time series at the observation points located on the continental shelf: ADP (a), AWAC (b), and ARGO (c). Low_64 case study.

The calibration for the continental shelf was carried out at three points along the perimeter of the river mouth. The results obtained at the ADP and AWAC stations indicated a good correlation between observed and measured data, r >0.8, and also a good skill, with R^2 and BSS >0.7. The worst R^2 results (0.66) were obtained at the ARGO location, although the rmse (1.8 $cm \cdot s^{-1}$) was the lowest in comparison with ADP and AWAC stations (Table 5.10). This may be because ADCP and AWAC were located right in front of the GRE mouth, while ARGO was located further north with respect to the mouth. In addition, to better understand the statistical results, the current speed time series for the model and in-situ data are shown in Figure 5.11. Overall, the graphics show a good match between the model and in-situ data for the three stations. Both time series show a northward decrease in the current speed, with the largest values observed at the closest station to the river mouth (ADP) and the lowest ones at the farthest location (ARGO). The model underestimated the current speed at the three stations, especially at ADP where differences of up to 10 $cm \cdot s^{-1}$ were found. The adjustment was better at ARGO, with lower differences in the speed and lower rmse values. Considering that this station is the farthest one from the river mouth, it is probably less affected by the river's discharge fluctuations. It is also important to highlight that winds were not included in the model simulations and hence, the dynamics of the river's discharge plume are not fully captured by the model. An attempt to retrieve more in-situ currents was made during an oceanographic cruise that took place in July 2019, covering the river mouth and the surrounding continental shelf. However, no date could be obtained due to technical problems with the vessel's ADCP.

5.4.4. Qualitative comparison between the model and altimetry data

In-situ data were not available for the continental shelf during high discharge periods. However, data from satellite altimetry tracks passing over the study area can be used instead to study the influence of the discharge on the continental shelf. With this purpose, a qualitative comparison between the model simulations and different altimetry data was carried out during three high-discharge events: 07/12/2010 – 17/01/2011 (Alti_02 case), 05/03/2013 – 20/04/2013 (Alti_04 case), 09/03/2018 – 21/03/2018 (Alti_06 case). In the cases Alti_02 and Alti_04, tracks of CS2 were used. The tracks selected passed the study area on the 27/12/2010 at 17:00 (Figure 5.12a) and 28/03/2013 at 00:00 (Figure 5.13a), respectively. The S3A track #114 was used to analyse the results in the Alti_06 case, in particular cycle 029 which corresponds to 19/03/2018 at 22:00 (Figure 5.14a). The maximum daily discharge rates during the periods selected were 3343 $m^3 \cdot s^{-1}$ (Alti_02 case), 2032 $m^3 \cdot s^{-1}$ (Alti_04 case), and 1081 $m^3 \cdot s^{-1}$ (Alti_06 case). Unfortunately, on the days when the satellites passed directly over the study area, the daily discharges at the Alcalá del Rio dam were lower than 1200 $m^3 \cdot s^{-1}$ (see the vertical lines in Figures 5.12a, 5.13a, and 5.14a).

During periods of high discharge rates, the estuary is fluvially dominated, i.e., the fluvial current speed will be similar or higher than the tidal velocities (Navarro et al., 2012). Consequently, the stratification increases, and a salt-wedge structure appears close to the mouth of the estuary (Díez-Minguito et al., 2014). The low-salinity plume propagates along the estuary until it reaches the continental shelf, where it produces an elevation of the water level (Díez- Minguito et al., 2012; Gómez-Enri, et al., 2015; González-Ortegón et al., 2010; González-Ortegón and Drake, 2012; Laiz et al., 2013; 2016; Navarro et al., 2012) that can be detected with the model. When the satellite tracks pass close enough to the river mouth, an increase in the ADT along-track is also expected. Previous studies found SLA values higher than 15 cm in the track positions closest to the GRE during a high discharge event (Gómez-Enri et al., 2015), but only when the satellites crossed the area close to the mouth. For this work, the available tracks were located approximately 23 km (Alti_02), 17 km (Alti_04), and 20 km (Alti_06) from the river mouth. The tracks were not very close to the mouth, but they were within the 20-30 km offshore area, which Gómez-Enri et al. (2015) established as the zone of influence of the discharge plume.

On the shelf, an increase in the water level elevation was observed in the model during three high discharge events (Figures 5.12b, 5.13b, 5.14b). The water level in the model increased at least 20 cm close to the mouth and corresponded to the low-salinity plume as shown on the salinity maps (Figures 5.12c, 5.13c, 5.14c were obtained with the model and were not validated with in-situ salinity data). This over-elevation seems to be limited to an area close to the river mouth, as suggested by previous studies (Laiz et al, 2013). Minimum values of 12 cm from the model_WL_corr (model data along-track, Eq. 5.6) were considered to delimit the plume extension on the continental shelf (see the dotted lines in Figures 5.12b, 5.13b, 5.14b). This value was obtained from the average minimum model_WL_corr of the three case studies simulated.

The event studied in Alti_02 was the second longest, 42 days, and was the event with the highest discharge rates (Figures 5.12a). For this reason, it was expected to be the event where the salinity plume was most noticeable. However, the CS2 track used to compare with the model's results was the furthest from the river mouth and the closest to the model's western boundary. Hence, smaller changes in the water level elevation were observed, both in the model along-track and with the altimeter (Figure 5.12b and 5.12d). In addition, the modelled salinity plume extended to ~20 km on the date the satellite overpassed the study area, and therefore did not reach the track position, located at 23 km from the river mouth (Figure 5.12b and 5.12c). The salinity in the model was zero close to the river mouth and reached a maximum value of 27 at the offshore limit of the salinity plume (Figure 5.12c). The track passed over the study area during flood tides; hence, the direction of tidal propagation was inshore towards the estuary and the extension of the salinity plume was more restricted to the area closest to the mouth. For this reason, the water level elevation in Figure 5.12d was not very noticeable. In any case, both series (ADT_alti and model_WL_corr) presented similar behaviours from a qualitative point of view.

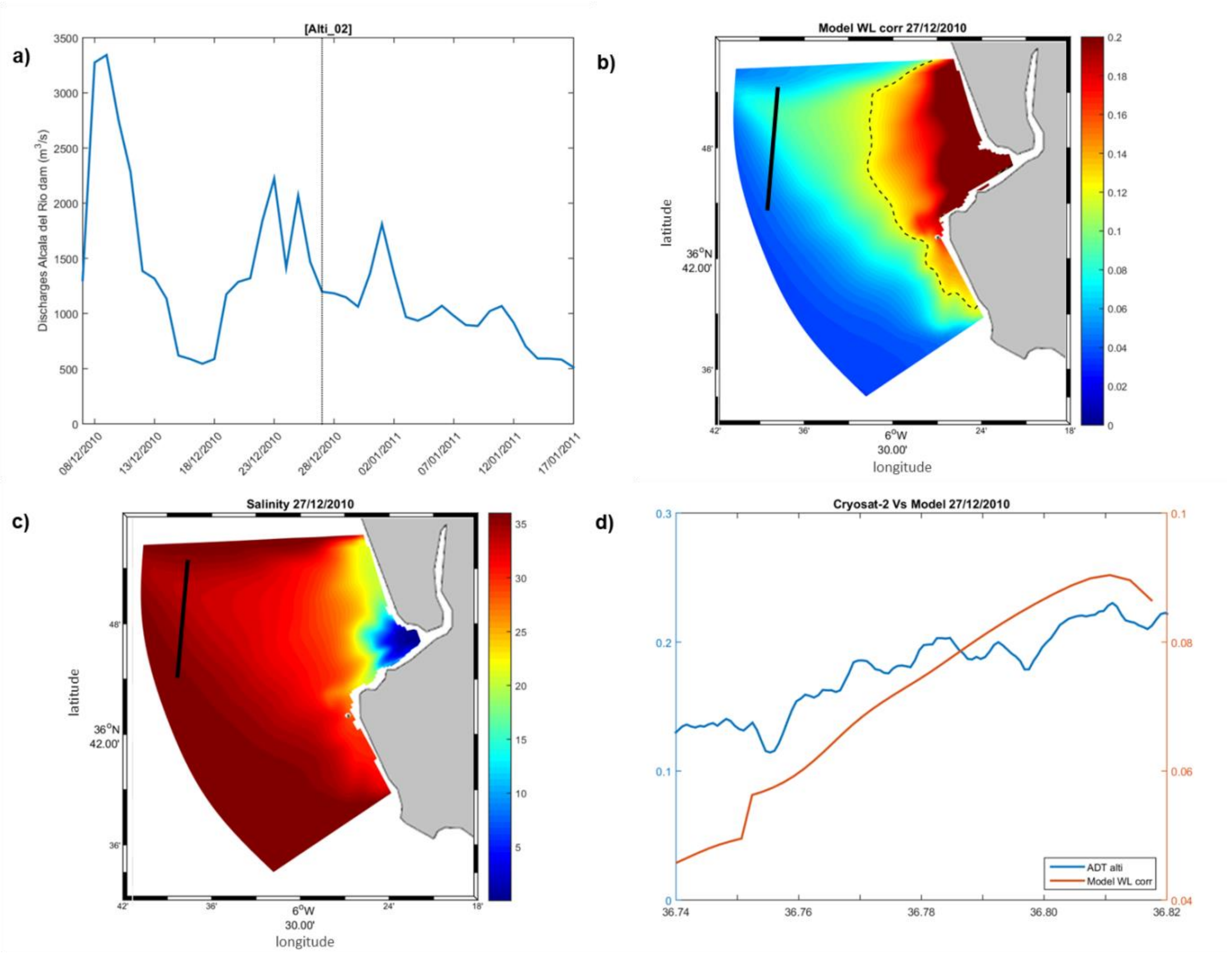

Figure 5.12. Alti_02 case. River daily discharges during the period 07/12/2010 – 17/01/2011 (a). Model_WL_corr at the time that the CS2 track (black line) is available in the study area, the dotted line delimit the plume extension (b). Map of salinity at the time that the CS2 track was available in the study area (c). Comparison between the model_WL_corr (m) and ADT_alti (m) along-track (d).

The longest discharge event studied, with a duration of 47 days, was the one analysed in Alti_04. This case study was the most favourable with respect to the location and orientation of the CS2 track used (Figure 5.13b). Nevertheless, the extension of the salinity plume only reached about 15 km on the date of study (Figure 5.13c), as the tide propagation was again toward the estuary. Even so, the effect of the high river discharge on the continental shelf could be analysed. The model and altimetry data showed the same qualitative increase in the water level in the area affected by the salinity plume. Similar values of salinity than in Alti_02 were observed with the model along the salinity plume, i.e., zero near the mouth and 29 close to the track. In Figure 5.13c, the salinity plume formed a small protuberance on its southernmost edge, separated from the main front that seems to coincide with the two water elevation peaks observed at the ADT_alti and model_WL_corr data (Figure 5.13d).

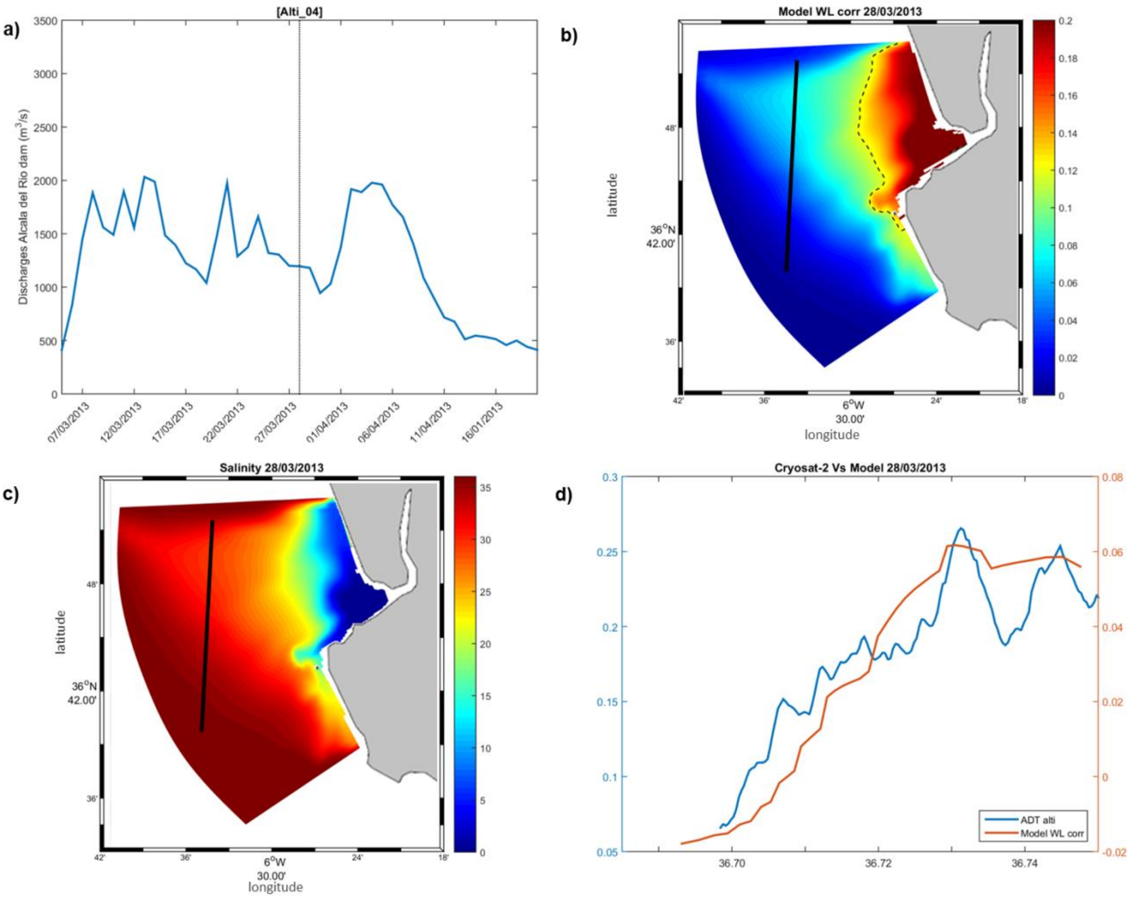

Figure 5.13. Alti_04 case. River daily discharges during the period 05/03/2013 – 20/04/2013 (a). Model_WL_corr at the time that the CS2 track (black line) is available in the study area, the dotted line delimit the plume extension (b). Map of salinity at the time that the CS2 track is available in the study area (c). Comparison between the model_WL_corr (m) and ADT_alti (m) along-track (d).

The last event studied (Alti_06 case) was the shortest and least intense (Figure 5.14a). Therefore, less noticeable changes in the water level elevation on the continental shelf were expected, both in the model and in the altimetry data. Nevertheless, the horizontal extension of the salinity plume was almost 20 km from the mouth (Figure 5.14b) due to the offshore tide propagation (ebb tide). The salinity obtained with the model was zero in the river mouth and 31 close to the track position (Figure 5.14c). In this case, the peak of maximum discharge concurred with the date in which the S3A #114 track passed over the GoC continental shelf. For this reason, an elevation of the water level in the continental shelf was clearly observed in both products (Figure 5.14d).

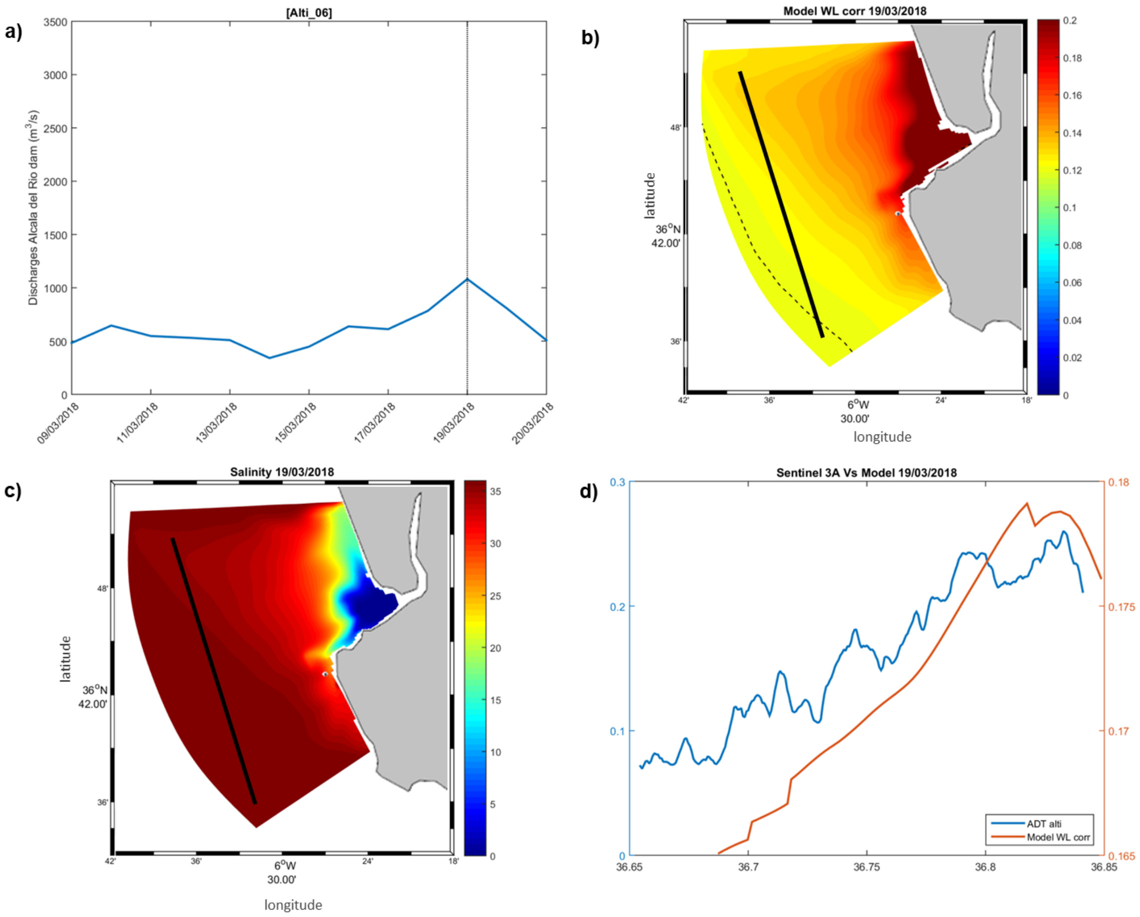

Figure 5.14. Alti_06 case. River daily discharges during the period 09/03/2018 – 21/03/2018 (a). Model_WL_corr at the time that the S3A #114 track (black line) is available in the study area, the dotted line delimit the plume extension (b). Map of salinity at the time that the S3A track is available in the study area (c). Comparison between the model_WL_corr (m) and ADT_alti (m) along-track (d).

5.5. Summary and conclusions

Although there are numerous studies focused on analysing the Guadalquivir River dynamics, mostly with in situ data, this is the first time that the Delft3D model was implemented to simulate the dynamics of the entire estuary and the adjacent Gulf of Cadiz continental shelf. To our knowledge, there is only one previous modelling work on the Guadalquivir River, but it is an idealized model (Siles-Ajamil et al., 2019). This model is useful from the point of view of management, but it has important limitations; i.e. nonlinear effects are not considered, hence it is not able to replicate residual effects on tidal wave propagation or salt transport, tidal-fluvial interaction effects can not be analysed, only low river flow conditions are simulated, etc.

The Delft3D model implemented in this study was successfully calibrated and validated with in-situ data. The calibration was performed under normal discharge conditions, when the estuary was tidally dominated, and the validation was done during a high discharge event, in which the estuary was fluvially dominated. The Chezy coefficient and also the bathymetry were used as adjustment parameters, since important improvements were obtained when the bathymetry was included. From all the model configurations explored, the best results were obtained with the Low_59/High_59 case studies (see Table 5.2). This configuration included five Chezy sections and the depth of the last section of the estuary was set to 6.5 m, which corresponds to the dredging depth. Three different sections were identified in the estuary, in agreement with Díez-Minguito et al. (2012). The poorest model's performance was obtained in the middle section with all the configurations, where the water level was always underestimated. The highest accuracy was obtained at the outer section of the estuary and on the continental shelf. Overall, the statistical results obtained for the Low_59 and High_59 cases were in line with previous works that calibrated the Delft3D model in an estuary, as discussed in Section 5.4. Although the model performed well in both cases, there were differences between the calibration (Tables 5.4 and 5.5) and validation results (Tables 57 and 5.8), which evidenced larger discrepancies between the model and the in-situ data during periods of high discharge.

On the one hand, the results demonstrated that the model was able to reproduce the dynamics in the estuary as well as different phenomena, such as the resonance of the semidiurnal components due to the changes in bathymetry along the estuary, the superposition of the tidal constituents, the Alcalá del Rio dam reflection, the high discharges, the low salinity plume, and the tidal damping phenomena, among others. On the other hand, differences between model and in-situ observations could be attributed to model configuration, including the bottom friction parameter, the lack of turbulent vertical mixing (2D configuration), errors in the bathymetry, or the lack of wind forcing, among others, as mentioned in the first section of this manuscript. For this study, two main sources of uncertainties were identified during the model implementation, the bathymetry and the initial conditions. Regarding the bathymetry, there are many processes strongly affeted by changes in the estuary's depth, e.g., bottom friction. Two sources of errors were expected due to: (1) the fact that four different datasets, measured at different spatial resolutions and at different dates over a long period of time, were used to compile the model bathymetry, and (2) the anthropogenic modifications frequently made to ensure a minimum navigational depth of 6.5 m. In the case of the initial conditions, it is important to take into consideration that the model was only forced with tides from a global model (TPXO8) and with daily averaged river discharge data (not instantaneous data). Besides, a zero-salinity value was assumed for the freshwater discharge, and a constant value of 36 for the continental shelf. The tidal model was validated in the Gulf of Cadiz in Chapter 4, using in-situ data from the tide gauge located in Huelva. Ideally, the model should have been validated with in-situ data along/close to the western boundary. Also, atmospheric forcing was not considered. The model's results close to the river mouth and on the continental shelf could be more accurate if the wind field was included, as it directly influences the extension and orientation of the discharge plume. Furthermore, uncertainties were found in the velocities associated with the in-situ data. In general, currents data from the ADCPs showed higher biases with the model probably due to the location of the instruments on the navigational buoys, which induced vertical and rotational movements in the instruments. Under these conditions it is difficult to accurately analyse the response of the model with respect to the in-situ velocities.

Finally, a qualitative comparison between model and altimetry was carried out. The results proved that high river discharges affect the water level on the continental shelf, in accordance with previous studies (e.g., Gómez-Enri et al., 2017; Laiz et al.,2013; among others). An elevation of the water level on the continental shelf was observed with the model and measured with the altimetry. Moreover, the discharge plume could be observed in the model simulation close to the river mouth, characterised by null salinity values. A quantitative comparison could not be carried out as the reference levels used by the altimeter (geoid) and the model (equipotential reference level) are different. To correct the bias between both datasets, a longer track-segment into the model grid would be necessary, and therefore a larger grid would be required, which implies a larger computational effort.

Despite the current uncertainties and limitations, and the capacity for future improvements (see Chapter 8), the model has shown to be a useful tool for the study of the dynamics of the Guadalquivir estuary and the influence of its discharges on the sea level of the adjacent continental shelf.

CHAPTER 6

Sentinel-3 Fully Focused SAR: precision and accuracy in the Gulf of Cadiz

---

Radar altimetry is an essential component for observing complex ocean circulation. In coastal areas, where 95 % of the socioeconomic activities are located, understanding the physical processes that drive coastal ocean dynamics is a priority (Vignudelli et al., 2011). As mentioned earlier, the coastal altimetry community is actively committed to provide the best product to help those studies. This chapter focuses on finding the best product, in terms of accuracy and precision, to study the Gulf of Cadiz coastal sea level variations. One of the most novel concepts in coastal altimetry is Fully Focussed SAR (FF SAR) processing which introduces an improvement in the along-track resolution. The FF SAR processing in the Gulf of Cadiz was tested in this study using the Sentinel-3A and Sentinel-3B tracks used in previous chapters (Chapter 3 and 4).
This chapter is structured as follows: Section 6.1 is an introduction to the topic. Sections 6.2 and 6.3 show the data and methodology, respectively. In Section 6.4, the results obtained in the precision and accuracy analyses are shown. Then, in Section 6.5 the improvements of the FF SAR products compared to unfocused SAR are discussed. Finally, conclusions can be found in Section 6.6.

The work presented in this chapter was developed during a research internship at the Deutsches Geodätisches Forschungsinstitut of the Technical University of Munich (DGFI-TUM), and with the collaboration of Aresys (Advanced Remote Sensing Systems, spin-off of Polytechnic of Milan) and the Technical University of Delft, who provided S3 FF SAR experimental products.

6.1. Introduction

Previously, Chapter 3 and 4 referred to the great challenge of the altimetry community to improve the quality of data in coastal areas (Vignudelli et al., 2011). The coastal altimetry community is actively working to reach this objective. In the last few years, improvements in different aspects of altimetry have been carried out. One of the most important was the development of SAR altimetry. The main difference between conventional altimetry (pulse limited or low resolution mode, PLRM) and the SAR mode is the Pulse Repetition Frequency (PRF) which is higher for SAR. The high PRF allows for the Delay-Doppler (DD) concept to be applied (Dinardo et al., 2021). DD produces a beam-limited footprint along-track and a pulse-limited footprint across-track in SAR products (Raney, 1998), while traditional radar altimetry has pulse-limited footprints in both directions (Figure 6.1). This means high resolution along-track and lower noise when retrieving the geophysical parameters (Vignudelli et al., 2011); these advantages of SAR have been demonstrated by many authors (Bonnefond et al., 2018; Boy et al., 2012; Cipollini et al., 2017; Dinardo et al., 2018, 2021; Fenoglio-Marc et al., 2015; Gómez-Enri et al., 2018; Gommenginger et al., 2013; Mulero-Martínez et al., 2021; Peng and Deng, 2020; Raynal et al., 2018).

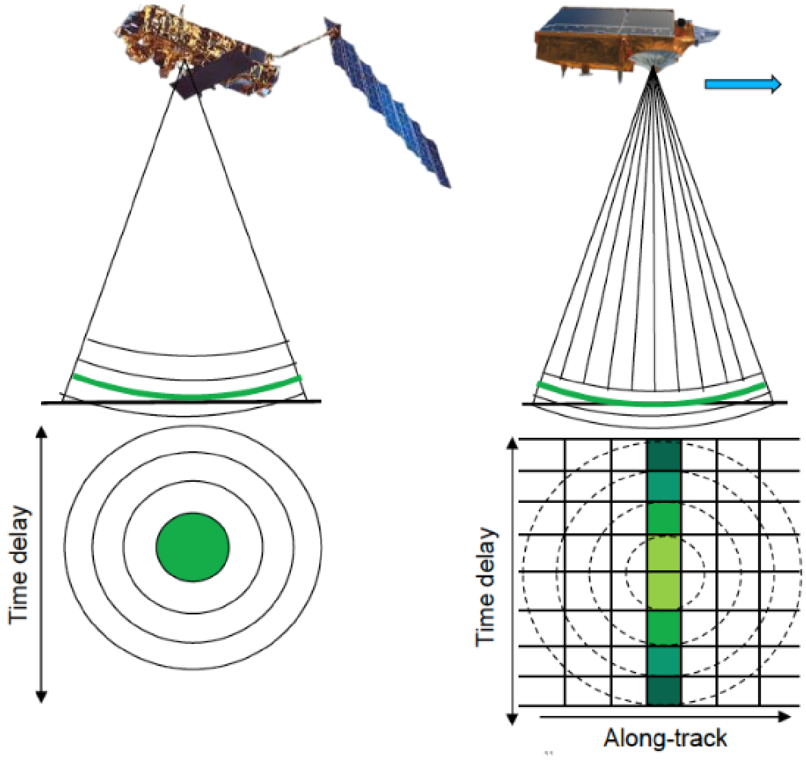

Figure 6.1. Comparison between conventional (left-hand side) and SAR (right-hand side) Altimetry. Green represents the footprint area. (Source: ESA).

Fully Focused SAR (FF SAR) is a novel product that introduces improvements to SAR (also known as unfocused SAR) in along-track resolution. For this reason FF SAR is especially useful in heterogeneous environments: coastal areas, inland waters or sea ice. The main difference in the FF processing is the increase of the along-track resolution up to the theoretical limit, which is equal to half the antenna length (~0.5 m), in contrast to the ~300 m unfocused SAR along-track resolution (Egido and Smith 2017; Guccione et al., 2018). Hence, the FF SAR footprint is SAR focused along-track and continues to be pulse-limited across-track. The FF SAR waveforms result from the combination of radar echoes, for each single look a new waveform that is independent of the previously calculated one is obtained. The shape of the FF SAR waveform is similar to the SAR one, which simplifies the retracking process (Egido and Smith 2017). The number of statistically independent looks obtained is higher than in unfocused SAR which means an improvement in the effective number of looks (ENL) and better geophysical parameters estimation (Egido and Smith 2017; Raney, 2011). The main inconvenience of FF SAR is the high computational effort, and the challenge is to determine whether this effort is worthwhile, in terms of precision and accuracy. Some researchers are already working to reduce the computational time without losing accuracy (Guccione et al., 2018).

As a consequence of a small footprint along-track, the influence of land contamination in coastal areas is reduced (Jensen and Raney, 1998). Moreover, SAR products are available with a high posting rate: 20, 40, and 80 Hz, in contrast to the traditional 1 Hz products. High posting rate products allow the study of coastal processes with better precision and accuracy.

Improvements in SAR coastal altimetry are also due to the developments in dedicated coastal waveform retrackers. Waveform retracking consists of fitting a model response to the real waveform, and converting waveforms into geophysical parameters (Gommenginger et al., 2011; Vignudelli et al., 2011). In coastal areas, mainly in the first 0-10 km, the waveform's shape changes with respect to that expected, and the residual noise can make the retrieval of the parameters more difficult (Passaro et al., 2014). For this reason, studying the coastal waveforms and classifying them was essential before developing coastal retrackers (e.g., Andersen et al., 2010; Berry et al., 2010; Deng et al., 2002). Many empirical and physical retrackers were tested in recent years (Vignudelli et al., 2011). In this study, different retrackers (threshold retracker, SAMOSA, SAMOSA+, and

ALES+ SAR) were used in order to determine the best product for the study area. More details about them can be found in Section 6.2.

Another relevant development in coastal altimetry is related to the quality of the range and geophysical corrections used to estimate sea level. Some corrections are more difficult to model than others, depending on their spatial-temporal variability and how they are affected by the presence of land (Vieira et al., 2019; Vignudelli et al., 2011), such as the wet tropospheric correction (Fernandes et al. 2014) or the SSB correction, the latter being the main source of uncertainty even today (Rieu et al., 2021). No further details are given as the aim of this chapter is not to test new range and geophysical corrections.

In this chapter, two different FF SAR algorithms were applied to Sentinel-3A (S3A) and Sentinel-3B (S3B) tracks in the Gulf of Cadiz (Spain). S3 SLA measurements were validated by comparing them to radar tide gauges. Both products used, the FF SAR Back Projection (BP), developed by Egido and Smith (2017), and the FF SAR Omega-Kappa (WK) algorithm, implemented by Guccione et al. (2018), were validated over a transponder for CryoSat-2 with good results. Moreover, a validation with in-situ data in inland waters was done by Kleinherenbrink et al. (2020) using CryoSat-2 FF SAR WK. The authors obtained values of standard deviation between 2 cm and 21.5 cm in different river segments. Due to the increase in the along-track resolution of S3 FF SAR with respect to to S3 unfocused SAR, a similar or even better accuracy and precision is expected. However, no publications have been found dedicated to the S3 FF SAR validation.

This chapter has two main objectives: (1) to validate S3 FF SAR in the Gulf of Cadiz in terms of its accuracy and precision and (2) to analyse whether FF SAR allows for obtaining good quality data closer to the coast than unfocused SAR.

6.2. Data

6.2.1. Altimetry data

As mentioned before, S3A and S3B have been in orbit since February 2016 and April 2018. The time period selected for S3A covers from September 2016 (cycle 8 or 9, depending on the track selected) to December 2019 (cycle 52 or 53), with a total of 45 cycles per track. In the case of S3B, the time period chosen is November/December 2018 (cycle 19) to December 2019 (cycle 33), with 15 cycles per track. The along-track sampling rate selected was the highest available for this altimeter in SAR mode: 80 Hz for the whole dataset, as in previous chapters.

Four tracks were used in the Gulf of Cadiz, two of S3A and two of S3B (Table 6.1, Figure 4.1.), as well as the six different datasets described below (Table 6.2). Data were obtained from GPOD or from personal communications (Table 6.2).

Table 6.1. Information about the S3 tracks used in this study. Number of tracks (relative orbit), distance between the track and tide gauge at the closest point to the coast (km), type of transition (OL: ocean to land, LO: land to ocean), track direction (ascending/descending), and angle with respect to the coast.

	S3A #114	**S3A #322**	**S3B #114**	**S3B #379**
Distance S3-TG	16 km	15 km	32 km	26 km
Transition	OL	LO	OL	LO
Track direction	Ascending	Descending	Ascending	Descending
Time of over passing	22:00	10:54	22:05	10:55
Angle respect to the coast	46º	75º	84º	69º

Table 6.2. Summary of datasets. Information about nomenclature, retracker used and processing.

	Retracker	**Processing**
SAM+ SAR	SAMOSA+	Unfocused SAR (GPOD)
ALES+ SAR	ALES+ SAR	
FF SAR BP	SAMOSA	FF SAR Back projection provided by F. Ehlers[1] and F. Schlembach[2]
FF SAR BP ALES+	ALES+ SAR	FF SAR BP reprocessing by M. Passaro[2]
FF SAR WK	Threshold set to 60%	FF SAR Omega –Kappa provided by Aresys[3]
FF SAR WK ALES+	ALES+ SAR	FF SAR WK reprocessing by M. Passaro[2]

(1) Technical University of Delft. (2) DGFI-Tecnhical University of Munich. (3) Spin-off University of Milan.

Up to four different retrackers were used to obtain the different products or datasets: (1) SAMOSA (SAR Altimetry Mode Studies and Applications) is a physical retracker, which is a previous version of SAMOSA+, the retracker used in previous chapters (Dinardo et al., 2018). (2) SAMOSA+, which is SAMOSA tailored for application in the open ocean, coastal zone and ice (Ray et al., 2015). (3) A thereshold retracker (Davis, 1993) that it is an empirical retracker based on the statistical properties of the waveform data and, more specifically, a threshold retracker set to 60% to determine the objective gate and improve the range estimation. (4) In order to standarize, all the products were retracked with the Adaptive Leading Edge Subwaveform (ALES) retracker. ALES is a retracker applicable in coastal areas and open ocean with the same accuracy and that only uses one algorithm (Passaro et al., 2014). ALES+ SAR is the version for Delay-Doppler waveforms and is based on a simplified version of the Brown-Hayne functional form to track the leading edge of the waveform (see Passaro et al. (2020) for a full description). Only a subwaveform with a specific width, according to the SWH, is retracked by ALES+ SAR, avoiding the typical signal perturbations of coastal areas. In addition, a SSB correction is provided with the ALES+ retracking, but has not been used in this study in order to make the different datasets as comparable as possible with each other. ALES+ SAR retracker was included in this work because numerous coastal altimetry studies demonstrated that it provided better validation results. For example, one of the most recent studies, Mostafavi et al. (2021), compared standard retrackers (Ocean and MLE4) and ALES+ in S3A and Jason 3 and obtained accuracy improvements of 0.5-1 cm in the sea surface height. Furthermore, the authors concluded that the closest coastal limit usable with high quality results is between 2 km to 3 km for S3A ALES+, and 7-10 km in the case of Jason 3 ALES+.

SAM+ SAR:

Data from S3 were provided by the ESA GPOD SARvatore service, available at: https://gpod.eo.esa.int/. The configuration is the same as the one used in Section 3.1.1 for coastal areas.

ALES+ SAR:

The same GPOD configuration as in SAM+ SAR was used in this dataset, with the exception of the ALES+ SAR retracker, that was applied instead of SAMOSA.

FF SAR BP:

A description of the proceedings to obtain the FF SAR BP data can be found in Egido and Smith (2017). The technique is based on SAR imaging BP algorithms adapted to the altimeter nadir-looking geometry. A coherent integration of the echoes along the entire illumination time was performed to obtain the FF SAR waveforms. For S3 data, a prototype version of Kleinherenbrink et al. (2020) was provided by F. Ehlers and F. Schlembach. The retracking was done using the SAMOSA model.

FF SAR BP ALES+:

This dataset was created using the FF SAR BP waveforms which were retracked using ALES+ SAR.

FF SAR WK:

A detailed description of the proceeding to obtain the FF SAR WK data can be found in Guccione et al. (2018). In essence, the Fully Focused principle is the same as in FF SAR BP; however, the WK algorithm was applied with the aim to optimize the computational time. Data were provided by Aresys (https://www.aresys.it/) with the same configuration used in FF SAR BP. To retrack, a threshold retracker (Davis, 1993) set to 60% was used.

FF SAR WK ALES+:

The difference in this dataset with respect to the FF SAR WK is that the ALES+ SAR retracker was applied instead of the Threshold retracker.

6.2.2. Tide gauge data

In-situ water level data from radar tide gauges (TG) located in ports, provided by the Spanish institution Puertos del Estado, were used to validate S3A and S3B. The same dataset was previously described in Section 3.2.2.

6.2.3. Land Topography data

Land topography was obtained from the SRTM Digital Elevation Database. The product (http://srtm.csi.cgiar.org/) was previously described in Section 3.2.4.

6.3. Methodology

6.3.1. Altimetry time series

The sea level anomaly S3 time series at 80-Hz posting rate (S3_SLA) were created following the methodology detailed in Section 4.3.1. The only change made was to the geophysical corrections. In particular, the sea state bias (SSB) correction recently updated in GPOD was applied (Source: Jason 2 CLS 2012, https://www.cls.fr). All the corrections selected to calculate the SLA for the FF datasets were kept the same as in unfocused SAR, taken from GPOD and interpolated to the latitude-longitude positions.

6.3.2. Tide gauge time series

For comparison with the altimetry data, the TG measurements were selected at the time closest to the satellite's passing time. The TG sea level time series (TG_SL) was obtained following the methodology previously described in Section 4.3.2.

6.3.3. Precision analysis

To evaluate the precision of each track, and to compare between the different datasets, the noise was calculated along the track segment 0-20 km for a better estimation. For each cycle of a track, the SLA difference between two consecutive measurements was calculated. These differences were considered a good estimation of noise, since SLA is not expected to change significantly in 85 m, which is the distance between consecutive measurements. Subsequently, using the average of these differences, the noise over a single cycle was obtained. Finally, the track noise was determined by averaging the noise over all cycles.

6.3.4. Accuracy analysis

The validation of the S3 time series in the segment 0-5 km using TG data was done to analyse the accuracy of each track and dataset. The Percentages of Cycles for High Correlation (PCHC, hereinafter) were calculated for three thresholds, correlation >0.9, >0.8, and >0.7. The statistic was obtained from a function that estimates the Pearson correlation coefficient and, if the correlation was below the established threshold, the cycle with the largest differences between TG and S3 was removed. This calculation was successively done until the correlation was higher than the threshold; the PCHC was then calculated (Passaro et al., 2015). Moreover, a second condition was added in which the p-value had to be lower than 0.05 (95% confident level). The PCHC was independent of the outlier detection, as it was done before. Therefore, the results of the different datasets were directly comparable.

Subsequently, a rigorous data screening was applied in two steps to remove outliers. In the first data screening, values higher than 1.5 m and lower to -1.5 m were excluded in S3_SLA. In the second screening, values higher than the average of ± 3 times the scaled median absolute deviation (Equation 6.1), were also discarded.

$$\text{MAD scaled (X)} = \text{factor} \bullet \text{median}\,(\,|X - \text{median}(X)\,|) \qquad \text{(Eq. 6.1)}$$

Where X is the S3_SLA time series, and the factor applied was 1.4286 to obtain the scaled MAD. The scaled MAD using this factor is approximately equal to the standard deviation (std) for a normal distribution (Passaro et al., 2015). According to Alvera-Azcárate et al. (2012) statistics based on the median are more robust and suitable for outlier detection and should be applied to satellite data. The scaled MAD is calculated for all the time series of each track.

Finally, the temporal mean of the S3_SLA and TG_SLA time series' was removed. For comparison, the standard deviation of the difference (sdd) was used (Equation 4.1).

6.4. Results

6.4.1. Datasets comparison

A first comparison of the datasets was done to analyse differences. Figure 6.2 shows an example of the comparison of SLA time series for one single cycle of ocean-to-land tracks.

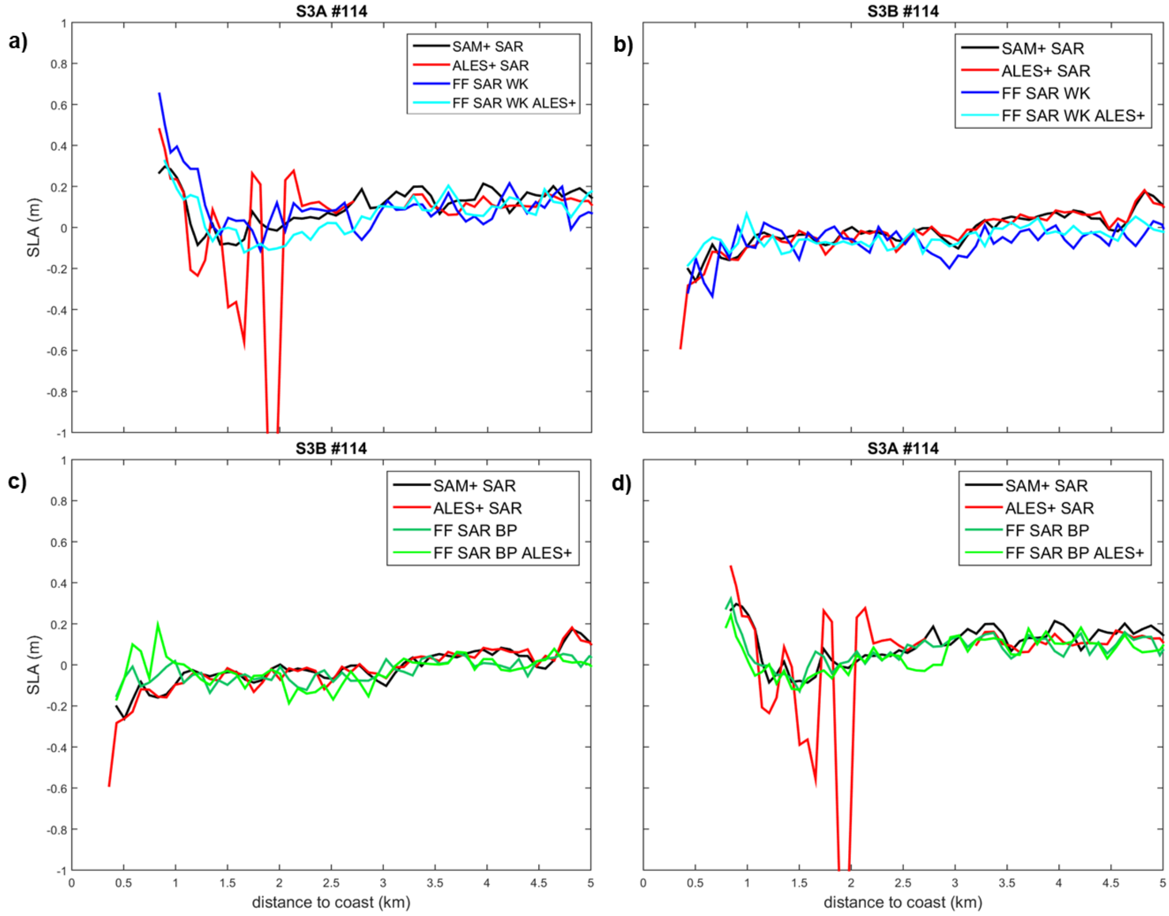

Figure 6.2. SLA (m) in the track segment 0-to-5 km. Comparison between unfocused SAR datasets and: (a) FF SAR Omega-Kappa in track S3A #114 and (b) S3B #114, (c) FF SAR Back Projection in track S3A #114 and (d) S3B #114.

Although some discrepancies were observed between datasets, the behaviour was similar for all series (this also applies to the tracks not show here). In the case of ALES+ SAR in S3A #114 (Figure 6.2a and 6.2c) NaN SLA values were obtained in the track segment 0-3 km due to anomalous values of the range detected in the outlier screening. Therefore, the ALES+ retracker failed in the fitting, which usually happens when the waveforms are very strange (Marcello Passaro, personal communication). Moreover, NaN values of the range for the track S3B #379 were observed in the 0-1.5 km segment (not shown here). S3A #114 and S3B #379 were the least perpendicular tracks with respect to the coast (Table

6.1). For this reason, the waveform could be more affected by the land contamination than other track waveforms (Figure 6.3), as explained in Chapter 3. The ALES+ SAR dataset was demonstrated to be more affected by land contamination in the footprint than the SAM+ SAR or FF SAR datasets (with ALES+ SAR or other retrackers).

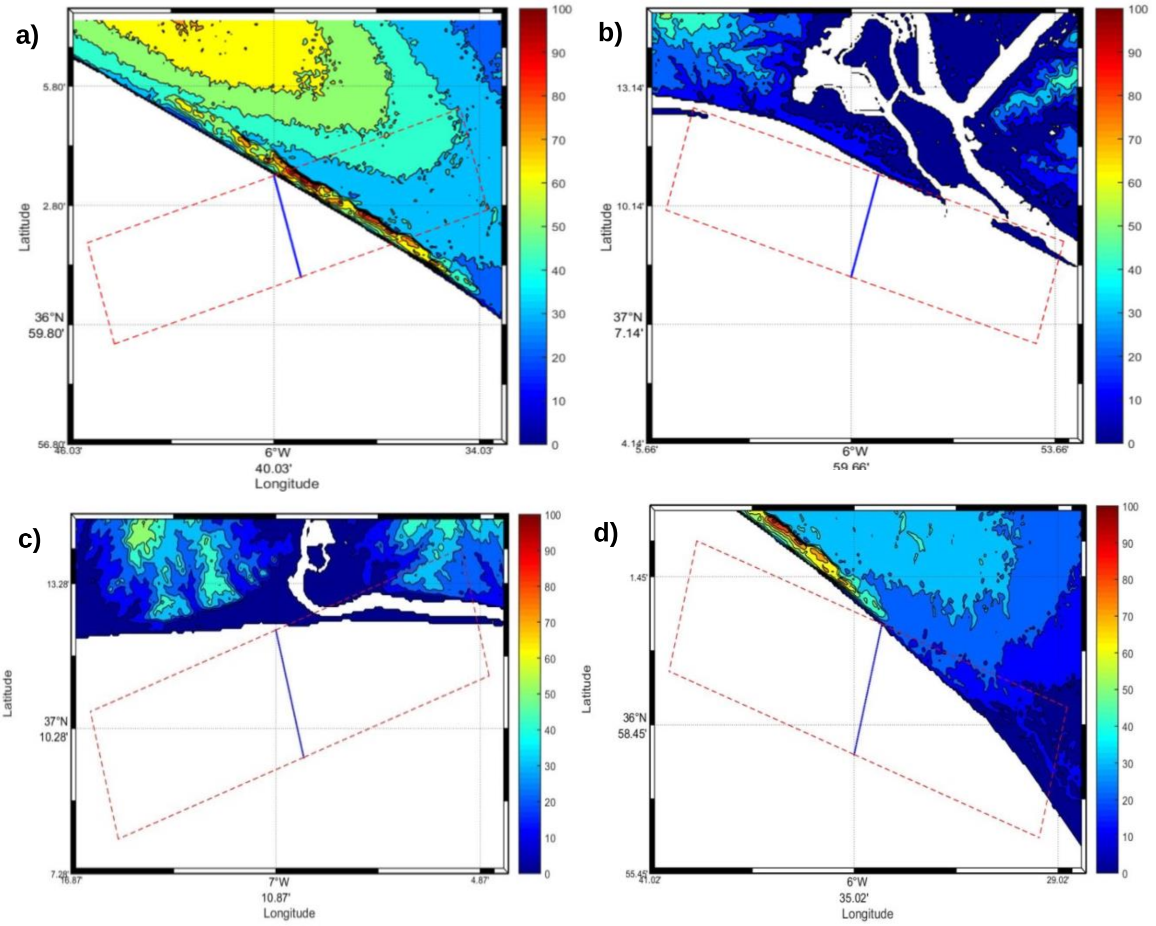

Figure 6.3. Location of 0-5 km track segments for tracks (a) #114 and (b) #322 of S3A and (c) #114 and (d) #379 of S3B. The SRTM land topography (m) is also shown. The envelope of the beam-limited footprint in the across-track direction (a radius of about 9.5 km perpendicular to the track) is delimited with a dashed red line.

6.4.2. Precision analysis: [0 – 20] km

The precision analysis was done on a longer track segment [0- 20] km, using the differences between consecutive SLA measurements along-track to estimate the noise. In Figure 6.4 the noise of each track and dataset are represented in a box and whisker plot for comparison.

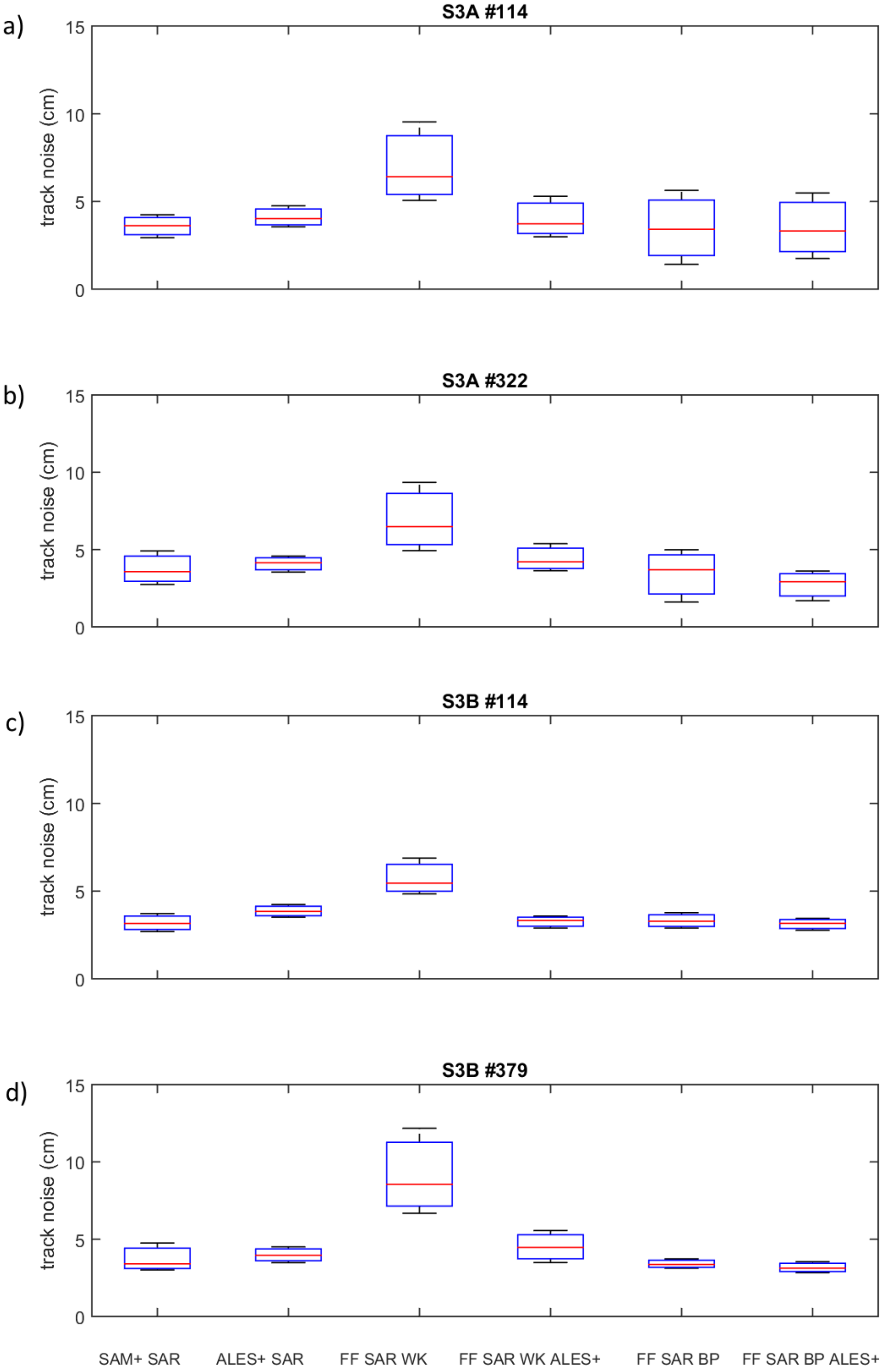

Figure 6.4. Summary of noise along track segment 0-20 km for S3A #114(a), S3A #322(b), S3B #114 (c) and S3B #379 (d).

Similar noise was obtained in unfocused SAR with both retrackers (Figure 6.3). For the FF SAR datasets, the noise decreased in all cases using the ALES+ retracker; highlighting improvements of up to 4 cm in the case of the WK dataset. The lowest noise values were found in the FF SAR BP ALES+ (2.9 -3.3 cm). Comparing the products with ALES+ retracker, the FF SAR BP ALES+ noise was lower in all the tracks than in ALES+ SAR. Hence, in terms of precision, the extra computational effort of FF BP is worthwhile against FF WK algorithm processing.

In S3B tracks the range of noise variation was smaller, but this may be due to the difference in the number of cycles used: 45 cycles for S3A and only 15 cycles for S3B. It should be noted that the statistics are less robust with a lower number of cycles.

6.4.3. Accuracy analysis: [0 – 5] km

As part of the accuracy analysis, the PCHC were calculated with p-values < 0.05 and r values higher than 0.9, 0.8 and 0.7. The results of the three correlation thresholds for the different datasets are shown in Table 6.4. The PCHC analysis was done before the outlier detection, therefore all of the cycles were included and the different datasets may be directly compared. As expected, lower percentages were obtained with higher r thresholds.

Table 6.3. PCHC results for the four tracks and the different datasets at three correlation thresholds. (The best results for each track are in **bold**).

[0-5] km	S3A #114			S3A #322			S3B #114			S3B #379		
r threshold	0.9	0.8	0.7	0.9	0.8	0.7	0.9	0.8	0.7	0.9	0.8	0.7
SAM+ SAR	35%	55%	61%	3%	5%	24%	28%	43%	59%	29%	52%	69%
ALES+ SAR	29%	41%	44%	32%	64%	70%	**31%**	46%	57%	23%	40%	58%
FF SAR WK	34%	59%	66%	30%	62%	78%	25%	43%	59%	13%	23%	34%
FF SAR WK ALES+	41%	59%	66%	34%	64%	**79%**	27%	**49%**	**67%**	18%	29%	42%
FF SAR BP	42%	**63%**	**72%**	**49%**	**71%**	77%	14%	23%	31%	**44%**	**66%**	**82%**
FF SAR BP ALES+	**48%**	60%	66%	43%	59%	60%	27%	41%	54%	17%	37%	60%

For all of the tracks, higher PCHC were obtained with FF SAR than with unfocused SAR with the largest differences between datasets being for S3A #322. In general, PCHC values above 50 % with the 0.7 threshold were obtained for all tracks, which indicates a good correlation with the in-situ data along the track segment analysed (0-5 km). However, higher PCHC values were expected, at least with Fully-Focused products.

To continue with the accuracy analysis, the validation with TG was carried out. The sdd mean value along the track segment 0 to 5 km and the std associated are shown in the Table 6.5. The mean results were almost always lower with the FF SAR products, similar in S3B #114, although variations can be found using the different retrackers. In general, improvements were observed using the ALES+ retracker in FF SAR products, except for the S3A #114 track as previously shown in Figure 6.2. However, in unfocused products SAMOSA+ resulted to be the most accurate retracker.

Table 6.4. Summary of sdd (cm) ± std (cm) mean values along the track segment [0-5] km for the different datasets.

sdd (cm)	S3A #114	S3A #322	S3B #114	S3B #379
SAM+ SAR	9.9 ± 3.5 cm	8.3 ± 4.5 cm	7.8 ± 4.6 cm	10.4 ± 4.0 cm
ALES+ SAR	10.0 ± 4.2 cm	9.3 ± 5.0 cm	7.9 ± 3.3 cm	11.3 ± 9.2 cm
FF SAR WK	11.2 ± 4.8 cm	10.1 ± 5.6 cm	9.7 ± 6.4 cm	16.8 ± 7.2 cm
FF SAR WK ALES+	12.0 ± 6.2 cm	10.5 ± 8.3 cm	7.9 ± 4.5 cm	11.3 ± 4.6 cm
FF SAR BP	**9.8** **± 4.5 cm**	9.8 ± 5.5 cm	9.8 ± 4.7 cm	10.8 ± 1.4 cm
FF SAR BP ALES+	11.0 ± 5.8 cm	**6.6** **± 1.4 cm**	7.9 ± 5.4 cm	**9.0** **± 2.1 cm**

To make a precise comparison of the datasets, the only products that were really comparable with each other were those retracked with the same retracker: ALES+ SAR, FF SAR WK ALES+ and FF SAR BP ALES+. So, hereinafter the comparison will be only shown with the ALES+ datasets, as they presented the largest improvements.

Comparing only these datasets in Table 6.5, better results were obtained in FF SAR than in unfocused SAR, and the BP product showed similar or better accuracy than the WK algorithm products. In this analysis the worst results were obtained with the tracks that presented a lower angle with respect to the coast (Table 6.1). For a deeper analysis, the sdd results along-track for the ALES+ datasets are shown in the next figures: Figure 6.5 for track S3A #114, Figure 6.6 for track S3A #322, Figure 6.7 for track S3B #114 and Figure 6.8 for track #379. The sdd was not calculated when the number of cycles different to NaN was below 5, and therefore are absent in the figures.

Besides the mean sdd values being better with FF SAR, lower values of sdd along-track were also obtained with respect to unfocused SAR, especially with FF SAR BP ALES+, so the improvement affected the whole of the track segment. Although track S3B #379 was the exception, the high data loss in the first few kilometres of the ALES+ SAR datasets (Figure 6.8) should be taken into consideration. As expected, the values of sdd obtained close to the coast were higher than for the rest of the segment, although the decrease did not always occur at the same distance. The optimal track segment, or how close to the coast accurate data can be obtained, was calculated. For this, the closest point to the coast after which the sdd did not rise above 10 cm was detected. In Figures 6.5-to-6.8, these points are marked with a blue asterisk for unfocused SAR datasets and a red asterisk for FF SAR datasets. The results showed that the optimum km points were located closest to zero in the FF SAR datasets than in unfocused SAR, which is a significant improvement for users. The only exception found was in S3B #114 where the FF SAR WK ALES+ was worse than with unfocused SAR, but lower sdd values were obtained with respect to ALES+ SAR in previous positions 1-3 km (Figure 6.7). Comparing the different FF SAR products, a large optimum track segment was obtained with FF SAR BP ALES+ for all the tracks. However, lower sdd values were not always obtained for FF SAR BP ALES+ than for FF SAR WK ALES+ close to the coast (see for example Figure 6.5). The best approximation to the coast was obtained in track S3A #322 (Figure 6.6), which was the track with the footprint least contaminated by land (see Table 6.1 and Figure 6.3).

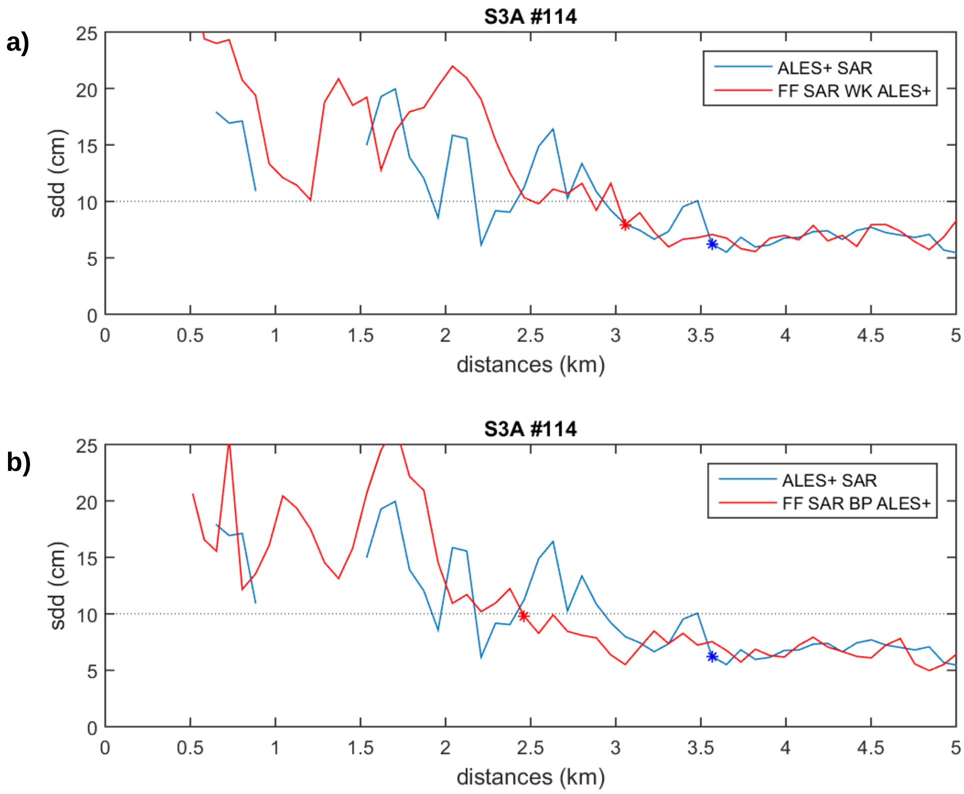

Figure 6.5. Results of sdd along the 0-5 km track segment for track S3A #114. Comparison between unfocused SAR (ALES+ SAR) and FF SAR WK ALES+ (a) and FF SAR BP ALES+ (b).

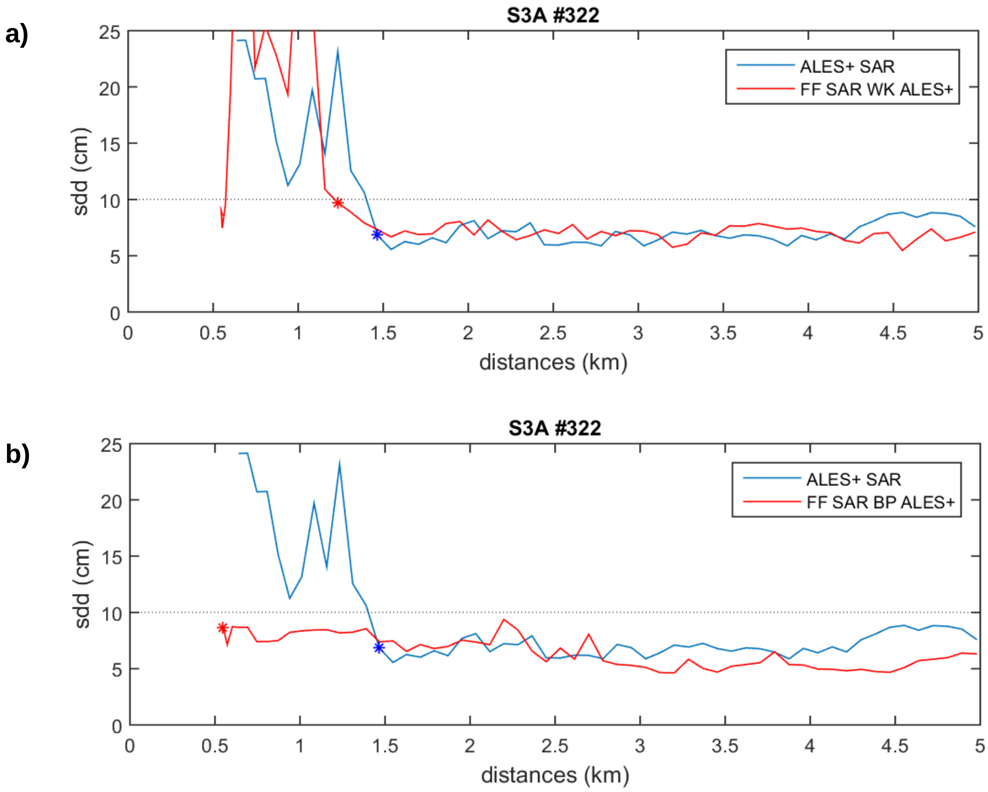

Figure 6.6. Results of sdd along the 0-5 km track segment for track S3A #322. Comparison between unfocused SAR (ALES+ SAR) and FF SAR WK ALES+ (a) and FF SAR BP ALES+ (b).

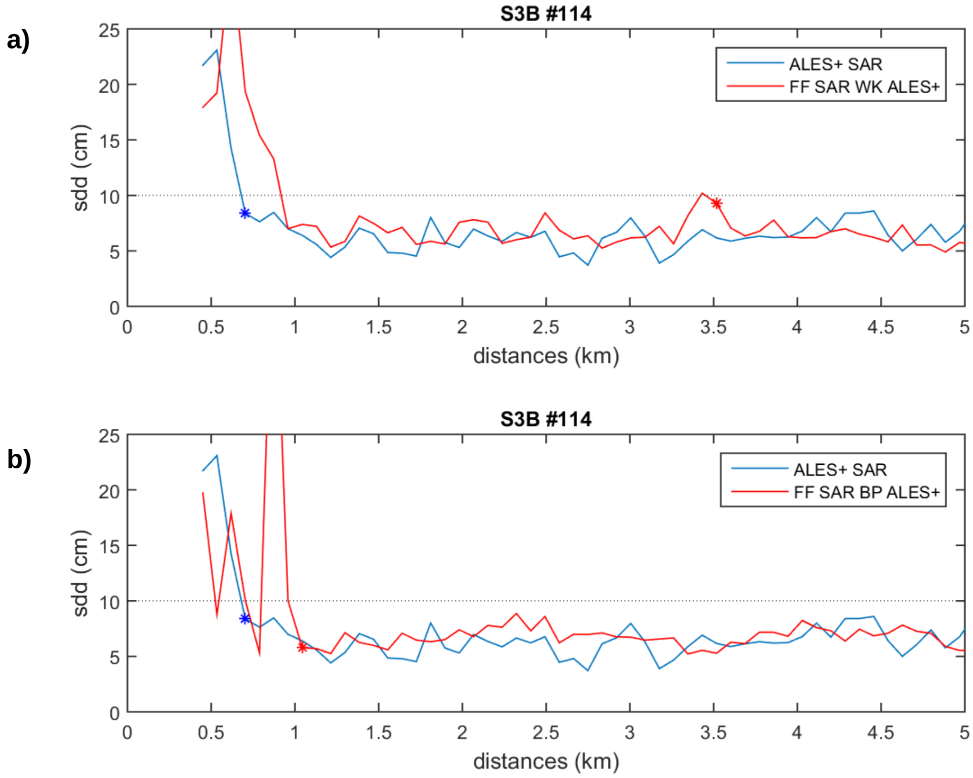

Figure 6.7. Results of sdd along the 0-5 km track segment for track S3B #114. Comparison between unfocused SAR (ALES+ SAR) and FF SAR WK ALES+ (a) and FF SAR BP ALES+ (b).

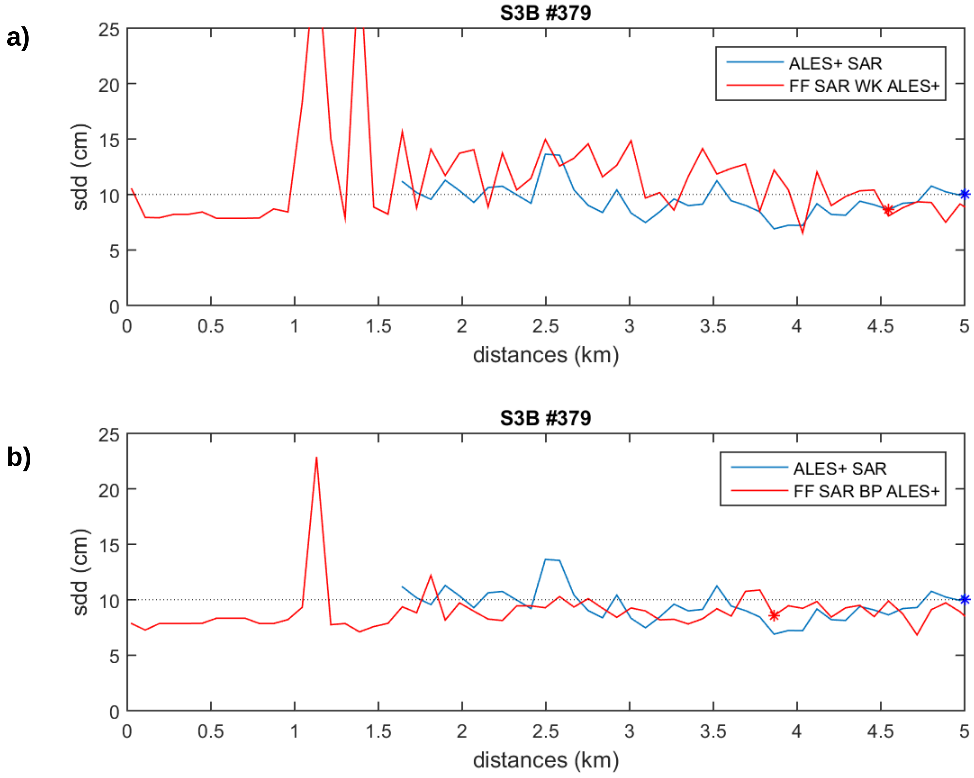

Figure 6.8. Results of sdd along the 0-5 km track segment for track S3B #379. Comparison between unfocused SAR (ALES+ SAR) and FF SAR WK ALES+ (a) and FF SAR BP ALES+ (b).

6.5. Discussion

The coastal altimetry community has the responsibility to provide the best available product for studying and understanding the physical processes that drive coastal ocean dynamics (Vignudelli et al., 2011). To this end, one of the clearest aims is to obtain high quality data as close to the coast as possible, and FF products were developed with this objective (among others) (Egido and Smith, 2017). For users of these products (applications), the most interesting aspect is that the data in proximity to the coast improves without losing precision and accuracy, compared to unfocused SAR. For agencies or developers, it would also be desirable to obtain a product with a reduced computational effort (Guccione et al. 2018).

The results obtained demonstrate that the FF SAR provides accurate and precise sea level data in the Gulf of Cadiz. No publications dedicated to the validation of these products in coastal areas have been found. There are however, various studies focused in inland water (Egido and Smith, 2018, Kleinherenbrink et al. 2020; Yuan, 2019) and sea ice (communications at conferences). Therefore, in this study the discussion was elaborated in comparison to the unfocused SAR results. Regarding the precision, the values obtained in unfocused SAR (3.2-4 cm) along-track SLA 80 Hz measurements were according with the 1-4 cm of noise obtained by Peng and Deng (2020) for the [0-20] km track segment, although they used SLA 1 and 4 Hz measurements. Comparing the datasets used in this chapter, lower noise was obtained for all the tracks in the case of FF SAR BP ALES+, with improvements of up to 1.5 cm. In terms of accuracy, the PCHC analysis demonstrated a clear advantage of the FF over unfocused products in the [0 – 5] km track segment. Moreover, a decrease of up to 4-5 cm in terms of sdd was obtained for FF SAR as well as better optimum track segments.

A common segment for all tracks is difficult to obtain, even in the same study area (see Figures 6.5 to 6.8) as there are many factors, such as the orientation of the coast, the land topography, the direction of the tracks, or the distance between the tracks and the TG, which can have an influence on the data's quality (see Chapter 3). To compare between tracks, the optimum track segment (optimum km-to-5 km) and the sdd in this optimum segment (sdd*) were calculated (Table 6.6). In general, accurate data can be obtained up to 2 km closer in the case of FF SAR than unfocused SAR, similar in S3B #114.

Table 6.5. Information on how close to the coast accurate data can be obtained: mean sdd (cm) ± std (cm) for each track and dataset, optimum km point where the sdd is below 10 cm (and does not increase), mean sdd* (cm) in the optimum track segment (km point identified to 5 km). In parenthesis, the number of points used to calculate the statistics in each case, being 60 the maximum number of points along-track.

Dataset	**Tracks:**	**S3A #114**	**S3A #322**	**S3B #114**	**S3B #379**
ALES+ SAR	sdd	10.0 ± 4.2 cm (60)	9.3 ± 5.0 cm (60)	7.9 ± 3.3 cm (60)	11.3 ± 9.2 cm (60)
	km point	3.6 km	1.3 km	**0.9 km**	4.9 km
	sdd*	6.8 cm ± 0.7 cm(23)	7.0 cm ± 0.9 cm (43)	**6.4 cm** **± 1.2 cm (55)**	9.9 cm ± 0.9 cm (1)
FF SAR WK ALES+	sdd	12.0 ± 6.2 cm (60)	10.5 ± 8.3 cm(60)	7.9 ± 4.5 cm (60)	11.3 ± 4.6 cm (60)
	km point	3.1 km	1.1 km	3.5 km	4.4 km
	sdd*	7.1 cm ± 0.9 cm (30)	7.1 cm ± 0.8 cm (46)	6.4 cm ± 1.0 cm (25)	8.6 cm ± 0.7 cm (7)
FF SAR BP ALES+	sdd	11.0 ± 5.8 cm (60)	6.6 ± 1.4 cm (60)	7.9 ± 5.4 cm(60)	9.0 ± 2.1 cm (60)
	km point	**2.4 km**	**0.6 km**	**1.0 km**	**3.7 km**
	sdd*	**7.0 cm** **± 1.1 cm** (36)	**6.6 cm** **± 1.4 cm** (60)	**6.7 cm** **± 0.9 cm** (54)	**8.9 cm** **± 0.8 cm** (25)

Different behaviours depending on the direction of the tracks (OL/LO) were not found. In fact the best approximation to the coast was obtained in the LO track S3A #322 (Figure 6.6), contrary to what might have been initially thought (see Chapter 3). Nevertheless, the orientation of the tracks did have an influence. Shorter optimum track segments were obtained in tracks less perpendicular with respect to the coast: S3A #114 and S3B #379 (Table 6.1 and 6.6), i.e., a reduced approach to the coast. In the case of S3A #114, poorer accuracy and precision were obtained close to the coast due to the fact that one side of the track is entirely within land in the 0-5 km segment (Figure 6.3); however, this is less noticeable in the FF SAR validation results than in unfocused (Table 6.6). In S3B #379, a similar precision was obtained in the cases of FF SAR BP ALES+ and ALES+ SAR in comparison with tracks with a more perpendicular angle, but the validation results were poorer. The angle has an influence on accuracy and precision (Vignudelli et al., 2011; 2019), however these results could also be due to the distance between the S3 track and the TG and the differences in the hydrodynamic characteristics of both areas measured by these instruments (Gómez-Enri et al., 2018). A more in depth study with a longer time series will be necessary, but one hypothesis that may explain these differences could be that the S3B #379 track is the closest track to the mouth of the GRE (22 km). As analysed in Chapter 6, the Guadalquivir River discharges have a strong influence in the surface circulation. In addition, the onset of the coastal countercurrent (previously mentioned in Chapter 2) is frequent in this area (Garcia-Lafuente et al., 2006) and its distance from the coast is variable and not well determined. Therefore, the high-precision FF SAR product could be useful to study these coastal processes and structures (Egido and Smith, 2017).

6.6. Conclusions

This chapter presents the results obtained for the validation of the new Sentinel-3 SAR products in four track segments of the Gulf of Cadiz. Six different S3 datasets were used: two unfocused products, two products of FF SAR WK, and another two of FF SAR BP; one dataset of each pair was reprocessed with the same retracker, ALES+ SAR. The validation was done in terms of precision, along the track segment 0-20 km, and accuracy, comparing the SLA altimetry measurements in the 0-5 km track segment with the in-situ TG data.

As a conclusion of the precision analysis, the noise values were similar between the unfocused datasets and improved using ALES+ retracker in the case of FF datasets. Comparing the products retracker with ALES+, a noise of 3-4 cm was obtained for all of the datasets, being the most precise the FF SAR BP ALES+ for all of the tracks. Highly accurate SLA measurements were also obtained with FF SAR. For the PCHC analysis, better percentages were obtained also with FF SAR in comparison with unfocused SAR, but not always with ALES+ retracking. FF SAR BP ALES+ and FF SAR WK ALES+ showed similar values of PCHC. Nevertheless, differences between FF products were found in terms of sdd, the sdd values were similar or lower in FF SAR BP ALES+ than in FF SAR WK ALES+. Moreover, FF BP algorithm achieved more precise results. Hence, the computational time reduction in FF SAR WK did not result in an improvement with respect to FF SAR BP whose results were more accurate and precise.

The greatest advantage of FF SAR is that it produces good quality data closer to the coast than unfocused SAR. However, a common track segment for the four tracks was not found, even in the same study area, mainly due to the differences in the tracks' orientation (θ). Accurate results were obtained with FF SAR BP ALES+ from the 0.6 km point for the S3A #322 track (θ = 75º), and an improvement up to 2 km for the S3B #114 track (θ= 84º) with respect to unfocused ALES+ SAR. Shorter track segments were obtained for tracks S3A #114 (θ= 46º) and S3B #379 (θ= 69º) which are more affected by land contamination in the satellite footprint. For S3B #379, the differences of accuracy could also be related to changes in the surface circulation that should be studied more in depth (coastal countercurrent, GRE discharges, etc.).

To conclude, the FF SAR processing of the S3 tracks in the Gulf of Cadiz provide high quality sea level data close to the coast. Nevertheless, a larger number of tracks and study areas with different hydrodynamic conditions will be necessary to prove the advantages of FF SAR.

CHAPTER 7

General Conclusions

In this dissertation, different tools and products were used in order to generate high quality products that could be used to improve the knowledge on sea level variation in coastal areas, with a focus on the Gulf of Cadiz. The main general scientific contributions of this work are summarised below:

1. The methodology proposed for the Sentinel-3 validation in coastal areas proved to be useful and replicable for other studies. Improvements were included during the development of this thesis, incorporating new available corrections, and changes in the design of accurate data screening.

2. The validation of S3A SLA data, from the GPOD service, at 80 Hz was done using in-situ tide gauge measurements. The results demonstrated that the same or higher levels of accuracy can be obtained with high rate products in the coastal track segment 5-20 km.

3. For some tracks, accurate results were achieved from 3 km with respect to the coast. However, a common distance with respect to the coast was not found due to land contamination influenced by the angle of the track with the coast, the topography of the coast and, and to a lesser degree, by the direction of the track.

4. The validation results of S3A and S3B on seven different coasts of Spain indicated the same data availability and quality for both altimeters.

5. TPXO8 and TPXO9 tidal models were validated around the Iberian Peninsula. Contrary to expectations, a more current version of the tide model did not always lead to improvements for all of the coasts studied. In the case of Huelva, in the Gulf of Cadiz, better results were obtained in the validation of TPXO8, and a better accuracy of the altimetry data was also obtained when using the TPXO8 tidal correction available in GPOD.

6. The Delft3D model demonstrates to be a useful tool to study the hydrodynamics in the Guadalquivir River estuary. The simulations adequately reproduced the tides and the freshwater inputs in normal and high discharge conditions.

7. Improvements in the model calibration and validation results were obtained when the bathymetry was included as an adjustment parameter, in addition to roughness. Nevertheless, the bathymetry remains a major source of uncertainty in the model.

8. The model calibration and validation results were good along the estuary and on the continental shelf. However, better accuracy could be obtained in the estuary middle section with a more refined grid in the meander areas, high quality bathymetry data or taking into account the flow input of the secondary channels.

9. In the qualitative comparison between the model and the altimetry tracks, the same behaviour was found. Both products were able to represent the effect of freshwater discharges from the Guadalquivir estuary on the elevation of the sea level on the Gulf of Cadiz continental shelf. Future model configurations should include wind forcing as well as realistic initial and boundary conditions for temperature, salinity, and currents.

10. The novel Fully Focused SAR processing technique used in S3A and S3B tracks provided similar or higher degree of precision and accuracy data than unfocused SAR in the Gulf of Cadiz.

11. Advantages in the use of SAMOSA+ or ALES+ in S3 unfocused products were not found. However, in the case of the S3 FF SAR product, better results were obtained when the applying ALES+ SAR retracker.

12. A better approximation to the coast (0.6 – 2.3 km) was obtained with FF SAR Back Projection products when retracked with ALES+ SAR. However, a common track segment for the four tracks was not found, as occurred with the unfocused products.

13. The combination of hydrodynamic models and coastal altimetry could be a powerful and accurate tool for the study of sea level variability in coastal areas.

CHAPTER 8

Future work

8.1. Altimetry

8.1.1. Improvements and extension of the study

The precision and accuracy analysis carried out in Chapter 6 demonstrated the advantages of the Fully Focused processing. It was concluded that Sentinel-3 tracks FF SAR can provide high quality sea level data close to the coast in the Gulf of Cadiz. Nevertheless, a larger number of tracks and study areas will be necessary to confirm these advantages. The purpose is to extend this work to the coastal areas used for the Sentinel-3A and 3B validation in Chapter 4.

Furthermore, the FF SAR products used in this study are prototypes. For the development of this work, a working group was created with researchers from Aresys, Technical University of Delft, Deutsches Geodätisches Forschungsinstitut of the Technical University of Munich and the University of Cadiz. The intention of this team is to continue working on product improvement and validation.

8.1.2. Fully Focused SAR applications

In addition, regarding FF SAR, in order to assess the potential of the different algorithms and retrackers for their use in coastal oceanographic applications, across-track surface current velocities, derived from the different SLA retrievals, will be compared with high-frequency radar (HFR) data. The final aim is to improve our knowledge of coastal processes such as the coastal countercurrent observed in the Gulf of Cadiz (its origin is still in debate), taking advantage of the good quality data available closer to the coast (1-2 km) compared to unfocused SAR (up to 3 km) (Mulero-Martinez et al., 2021; Aldarias et al., 2020).

8.2. Numerical model

8.2.1. Model improvements

As mention in Section 5.5, the model provided good quality results but they can still be improved. The following are some of the proposals for improving the accuracy of the model's output:

- WIND. Wind forcing was not analysed in this work. Some test simulations were done including unidirectional easterly, westerly, southerly, and northerly winds. However, the wind forcing numerical experiments could not be included in this thesis due to time constraints. Nevertheless, this task will be further pursued with the aim of accurately studying the spatial extension and propagation of the salinity plume on the continental shelf.

- WAVES. A considerable improvement, mainly in versatility, would be the coupling of the Delft3D-WAVE module. However, modelling waves propagation is computationally intensive, and, in some cases, waves may not have a substantial impact on water levels along the estuary (Del-Rosal-Salido et al., 2019).

- BATHYMETRY. It was one of the great limiting factors in this study. An updated bathymetry that covers the total study area will be useful to improve the model results, not only in calibration and validation.

- GRID. The design of the grid for the numerical model was performed taking into account the computational time and processes to be modelled. In this case, the chosen grid size was enough to study the hydrodynamics in the Guadalquivir River estuary and the closestmost continental shelf. However, in order to study the salinity plume and the CCC, or to carry out better comparisons with altimetry data, it is necessary to enlarge the grid in the continental shelf. A comparison with S3 FF SAR products could then be done to analyse the performance of the model close to the coast.

- ALTIMETRY. To solve the problem caused by the differences between the model and altimetry data reference levels is a work in progress. However, it will be necessary to increase the grid coverage on the continental shelf, in order to have more altimetry measurements available within the model grid. In addition, a good opportunity could be to obtain gridded maps of altimetry data (as in Gómez-Enri et al., 2015) to have a better spatial and time resolution and allow for the comparison with the model during periods of high freshwater discharge. Moreover, the recent advances in altimetry allow for measurements to be obtained for a river with a width of around 200 m (Scheineder et al., 2018). This data could strengthen the calibration and validation results.

8.2.2. Model applications

Previous studies such as Fernandez-Delgado et al. (2007) and Guerreiro et al. (2013) highlighted the important role of river discharges to increase the spawning, nursery and feeding grounds of small pelagic fishes. In this sense, the author of this thesis is collaborating in two research projects, InBlue and EcoInvadiz, whose main researcher is Enrique González-Ortegón (Annex II). The projects started in 2020 and will be active until 2023. One of the main objectives is to study the spatial distribution and impact of invasive species in the Guadalquivir River Estuary. In particular, the model implemented will be used to study the larval spread of three non-native species in the area.

References

Ablain, M., Legeais, J. F., Prandi, P., Marcos, M., Fenoglio-Marc, L., Dieng, H. B.,... & Cazenave, A. (2017). Satellite altimetry-based sea level at global and regional scales. Surveys in Geophysics, 38(1), 7-31. doi: 10.1007/s10712-016-9389-8

Aldarias, A., Gómez-Enri, J., Laiz, I., Tejedor, B., Vignudelli, S., & Cipollini, P. (2020). Validation of Sentinel-3A SRAL coastal sea level data at high posting rate: 80 Hz. IEEE Transactions on Geoscience and Remote Sensing, 58(6), 3809-3821. doi: 10.1109/TGRS.2019.2957649

Allen, J. I., Somerfield, P. J., & Gilbert, F. J. (2007). Quantifying uncertainty in high-resolution coupled hydrodynamic-ecosystem models. Journal of Marine Systems, 64(1-4), 3-14. doi: 10.1016/j.jmarsys.2006.02.010

Alvarez, O., Tejedor, B., & Vidal, J. (2001). La dinámica de marea en el estuario del Guadalquivir: un caso peculiar de 'resonancia antrópica'. Física de la Tierra, 13, 11-24. doi: 10.5209/rev_FITE.2001.n13.12748

Alvera-Azcárate, A., Sirjacobs, D., Barth, A., & Beckers, J. M. (2012). Outlier detection in satellite data using spatial coherence. Remote Sensing of Environment, 119, 84-91. doi: 10.1016/j.rse.2011.12.009

Ambar, I., & Howe, M. R. (1979). Observations of the Mediterranean outflow—II The deep circulation in the vicinity of the Gulf of Cadiz. Deep Sea Research Part A. Oceanographic Research Papers, 26(5), 555-568. doi: 10.1016/0198-0149(79)90096-7

Andersen, O. B. (2010). The DTU10 Global Gravity field and mean sea surface–improvements in the Arctic. In 2nd IGFS meeting.

Andersen, O. B., & Knudsen, P. (2009). The DNSC08 mean sea surface and mean dynamic topography. J. Geophys. Res., (114), C11. doi:10.1029/2008JC005179

Andersen, O. B., & Scharroo, R. (2011). Range and geophysical corrections in coastal regions: and implications for mean sea surface determination. In Coastal altimetry (pp. 103-145). Springer, Berlin, Heidelberg. doi: 10.1007/978-3-642-12796-0_5

Arcement, G. J., & Schneider, V. R. (1989). Guide for selecting Manning's roughness coefficients for natural channels and flood plains. doi: 10.3133/wsp2339

Arnau, P., Liquete, C., & Canals, M. (2004). River mouth plume events and their dispersal in the Northwestern Mediterranean Sea. Oceanography-Washington DC-Oceanography Society, 17, 22-31.

Baawain, M., Choudri, B. S., Ahmed, M., & Purnama, A. (2015). Recent progress in desalination, environmental and marine outfall systems. Basel, Switzerland: Springer International Publishing. doi: 10.1007/978-3-319-19123-2

Baldó, F., García-Isarch, E., Jiménez, M. P., Romero, Z., Sánchez-Lamadrid, A., & Catalán, I. A. (2006). Spatial and temporal distribution of the early life stages of three commercial fish species in the northeastern shelf of the Gulf of Cádiz. Deep Sea Research Part II: Topical Studies in Oceanography, 53(11-13), 1391-1401. doi: 10.1016/j.dsr2.2006.04.004

Bárcenas, P. (2011). Spatial variability of surficial sediments on the northern shelf of the Alboran Sea: the effects of hydrodynamic forcing and supply of sediment by rivers. Journal of Iberian Geology, 37(2), 195-214. doi: 10.5209/rev_JIGE.2011.v37.n2.8

Bárcenas Gascón, P. (2013). Procesos morfogenéticos y evolución reciente de los depósitos prodeltaicos del sureste de la Península Ibérica: aplicaciones de modelos matemáticos. PhD Thesis. University of Málaga.

Baringer, M. O. N., & Price, J. F. (1997). Mixing and spreading of the Mediterranean outflow. Journal of Physical Oceanography, 27(8), 1654-1677. doi: 10.1175/1520-0485(1997)027<1654:MASOTM

Baringer, M. O. N., & Price, J. F. (1999). A review of the physical oceanography of the Mediterranean outflow. Marine Geology, 155(1-2), 63-82. doi: 10.1016/S0025-3227(98)00141-8

Bellafiore, D., & Umgiesser, G. (2010). Hydrodynamic coastal processes in the North Adriatic investigated with a 3D finite element model. Ocean Dynamics, 60(2), 255-273. doi:10.1007/s10236-009-0254-x

Benveniste, J., Cazenave, A., Vignudelli, S., Fenoglio-Marc, L., Shah, R., Almar, R., ... & Wöppelmann, G. (2019). Requirements for a coastal hazards observing system. Frontiers in Marine Science, 6, 348. doi: 10.3389/fmars.2019.00348/full

Bergillos, R. J., Masselink, G., & Ortega-Sánchez, M. (2017). Coupling cross-shore and longshore sediment transport to model storm response along a mixed sand-gravel coast under varying wave directions. Coastal Engineering, 129, 93-104. doi: 10.1016/j.coastaleng.2017.09.009

Bergillos, R. J., Rodriguez-Delgado, C., & Iglesias, G. (2019). Wave farm impacts on coastal flooding under sea-level rise: a case study in southern Spain. Science of the total environment, 653, 1522-1531. doi: 10.1016/j.scitotenv.2018.10.422

Berry, P. A. M., Garlick, J. D., Freeman, J. A., & Mathers, E. L. (2005). Global inland water monitoring from multi-mission altimetry. Geophysical Research Letters, 32(16). doi: 10.1029/2005GL022814

Berry, P. A. M., Freeman, J. A., & Smith, R. G. (2010). An enhanced ocean and coastal zone retracking technique for gravity field computation. In Gravity, geoid and Earth observation (pp. 213-220). Springer, Berlin, Heidelberg. doi: 10.1007/978-3-642-10634-7_28

Birgiel, E., Ellmann, A., & Delpeche-Ellmann, N. (2019). Performance of Sentinel-3A SAR altimetry retrackers: The SAMOSA coastal sea surface heights for the Baltic Sea. In Fiducial Reference Measurements for Altimetry (pp. 23-32). Springer. doi: 10.1007/1345_2019_59.

Birol, F., & Delebecque, C. (2014). Using high sampling rate (10/20 Hz) altimeter data for the observation of coastal surface currents: A case study over the northwestern Mediterranean Sea. Journal of Marine Systems, 129, 318-333. doi: 10.1016/j.jmarsys.2013.07.009

Bolado-Penagos, M., González, C. J., Chioua, J., Sala, I., Gomiz-Pascual, J. J., Vázquez, Á., & Bruno, M. (2020). Submesoscale processes in the coastal margins of the Strait of Gibraltar. The Trafalgar–Alboran connection. Progress in Oceanography, 181, 102219. doi: 10.1016/j.pocean.2019.102219

Bonnefond, P., Verron, J., Aublanc, J., Babu, K. N., Berge-Nguyen, M., Cancet, M., ... & Watson, C. (2018). The benefits of the Ka-band as evidenced from the SARAL/AltiKa altimetric mission: Quality assessment and unique characteristics of AltiKa data. Remote Sensing, 10(1), 83. doi:10.3390/rs10010083

Bos, K. J., Roelvink, J. A., & Dingemans, M. W. (1997). Modelling the impact of detached breakwaters on the coast. In Coastal Engineering 1996 (pp. 2022-2035). doi: 10.1061/9780784402429.157

Boy, F., J. D. Desjonqueres, N. Picot, T. Moreau, S. Labroue, J. C. Poisson, & P. Thibaut (2012), CryoSat processing prototype: LRM and SAR processing on CNES side, oral presentation, in the 2012 OSTST meeting, Venice-Lido, Italy. [Available at http://www.aviso.altimetry.fr/fileadmin/documents/OSTST/2012/oral/02_friday_28/02_instr_processing_II/02_IP2_Boy.pdf]

Brêda, J. P. L. F., Paiva, R. C. D., Bravo, J. M., Passaia, O. A., & Moreira, D. M. (2019). Assimilation of satellite altimetry data for effective river bathymetry. Water Resources Research, 55(9), 7441-7463. doi: 10.1029/2018WR024010

Brown, S. (2010). A novel near-land radiometer wet path-delay retrieval algorithm: Application to the Jason-2/OSTM advanced microwave radiometer. IEEE Transactions on Geoscience and Remote Sensing, 48(4), 1986-1992. doi: 10.1109/TGRS.2009.2037220

Brown, S. (2013). Maintaining the long-term calibration of the Jason-2/OSTM advanced microwave radiometer through intersatellite calibration. IEEE Transactions on Geoscience and Remote Sensing, 51(3), 1531-1543. doi: 10.1109/TGRS.2012.2213262

Calmant, S., Seyler, F., & Cretaux, J. F. (2008). Monitoring continental surface waters by satellite altimetry. Surveys in geophysics, 29(4), 247-269. doi: 10.1007/s10712-008-9051-1

Canals, M., Arnau, P., Liquete, C., Colas, S., & Casamor, J. L. (2004). Catalogue and data set on river systems from Mediterranean watersheds of the Iberian Peninsula. Univ. Barcelona, 220 p.

Candela, J. (1990). The barotropic tide in the Strait of Gibraltar. In The Physical Oceanography of Sea Straits (pp. 457-475). Springer, Dordrecht. doi: 10.1007/978-94-009-0677-8_22

Castaing, P., & Allen, G. P. (1981). Mechanisms controlling seaward escape of suspended sediment from the Gironde: a macrotidal estuary in France. Marine Geology, 40(1-2), 101-118. doi: 10.1016/0025-3227(81)90045-1

Cazenave, A., Meyssignac, B., Ablain, M., Balmaseda, M., Bamber, J., Barletta, V., ... & Wouters, B. (2018). Global sea-level budget 1993-present. Earth System Science Data, 10(3), 1551-1590. doi: 10.5194/essd-10-1551-2018

Cendrero, A. (1975). Environmental geology of the santander bay area, northern Spain. Environmental Geology, 1(2), 97-114. doi: 10.1007/BF02415536

Chao, S. Y., & Boicourt, W. C. (1986). Onset of estuarine plumes. Journal of Physical Oceanography, 16(12), 2137-2149. doi: 10.1175/1520-0485(1986)016<2137:OOEP>2.0.CO;2

Charria, G., Lazure, P., Le Cann, B., Serpette, A., Reverdin, G., Louazel, S., ... & Morel, Y. (2013). Surface layer circulation derived from Lagrangian drifters in the Bay of Biscay. Journal of Marine Systems, 109, S60-S76. doi: 10.1016/j.jmarsys.2011.09.015

Cheng, Y., & Andersen, O. B. (2011). Multimission empirical ocean tide modeling for shallow waters and polar seas. Journal of Geophysical Research: Oceans, 116(C11). doi:10.1029/2011JC007172.

Cipollini, P., Benveniste, J., Birol, F., Fernandes, M. J., Obligis, E., Passaro, M., ... & Wilkin, J. (2017). Satellite altimetry in coastal regions. In Satellite altimetry over oceans and land surfaces (pp. 343-380). CRC Press. ISBN: 978-1-4987-4345-7

Cipollini, P., Benveniste, J., Bouffard, J., Emery, W., Gommenginger, C., Griffin, D., ... & Zavala-Garay, J. (2010). The role of altimetry in coastal observing systems. Proceedings of OceanObs, 9, 181-191.

Clerc, S., Donlon, C., Borde, F., Lamquin, N., Hunt, S. E., Smith, D., ... & Guérou, A. (2020). Benefits and lessons learned from the Sentinel-3 tandem phase. Remote Sensing, 12(17), 2668. doi: 10.3390/RS12172668

Creel, L. (2003). Ripple effects: population and coastal regions (pp. 1-7). Washington, DC: Population reference bureau. [Available at: https://pdf.usaid.gov/pdf_docs/Pnadd169.pdf]

Criado-Aldeanueva, F., García-Lafuente, J., Navarro, G., & Ruiz, J. (2009). Seasonal and interannual variability of the surface circulation in the eastern Gulf of Cadiz (SW Iberia). Journal of Geophysical Research: Oceans, 114(C1). doi:10.1029/2008JC005069

Criado-Aldeanueva, F., J. García-Lafuente, J. M. Vargas, J. Del Río, A. Vázquez, A. Reul, & A. Sánchez (2006), Distribution and circulation of water masses in the Gulf of Cadiz from in situ observations, Deep Sea Res., Part II, 53, 1144–1160, doi:10.1016/j.dsr2.2006.04.012.

Criado-Aldeanueva, F., Vera, J. D. R., & García-Lafuente, J. (2008). Steric and mass-induced Mediterranean sea level trends from 14 years of altimetry data. Global and Planetary Change, 60(3-4), 563-575. doi: 10.1016/j.gloplacha.2007.07.003

Contreras, E., & Polo, M. J. (2012). Measurement frequency and sampling spatial domains required to characterize turbidity and salinity events in the Guadalquivir estuary (Spain). Natural Hazards and Earth System Sciences, 12(8), 2581-2589. doi: 10.5194/nhess-12-2581-2012

Cugier, P., & Le Hir, P. (2002). Development of a 3D hydrodynamic model for coastal ecosystem modelling. Application to the plume of the Seine River (France). Estuarine, Coastal and Shelf Science, 55(5), 673-695. doi: 10.1006/ecss.2001.0875

Davis, C. H. (1993). A surface and volume scattering retracking algorithm for ice sheet satellite altimetry. IEEE Transactions on Geoscience and Remote Sensing, 31(4), 811-818, doi: 10.1109/36.239903

De Vriend, H.J., Zyserman, J., Nicholson, J., Roelvink, J.A., Pechon, P., & Southgate, H.N. (1993). Medium-term 2DH coastal area modelling. Coastal Engineering 21 (1–3), 193–224. doi: 10.1016/0378-3839(93)90051-9

Deltares Hydraulics. (2021). Delft3D-FLOW User Manual. Simulation of multi-dimensional hydrodynamic flows and transport phenomena, including sediments. (https://oss.deltares.nl/web/delft3d/manuals)

Del-Rosal-Salido, J., Folgueras, P., Ortega-Sanchez, M., & Losada, M. A. (2019). Beyond flood probability assessment: An integrated approach for characterizing extreme water levels along transitional environments. Coastal Engineering, 152, 103512. doi: 10.1016/j.coastaleng.2019.103512

Deng, X., Featherstone, W. E., Hwang, C. W., & Berry, P. A. M. (2002). Estimation of contamination of ERS-2 and POSEIDON satellite radar altimetry close to the coasts of Australia. Marine Geodesy, 25(4), 249-271. doi: 10.1080/01490410214990

Des, M., DeCastro, M., Sousa, M. C., Dias, J. M., & Gómez-Gesteira, M. (2019). Hydrodynamics of river plume intrusion into an adjacent estuary: The Minho River and Ria de Vigo. Journal of Marine Systems, 189, 87-97. doi: 10.1016/j.jmarsys.2018.10.003

Dhote, P. R., Thakur, P. K., Domeneghetti, A., Chouksey, A., Garg, V., Aggarwal, S. P., & Chauhan, P. (2021). The use of SARAL/AltiKa altimeter measurements for multi-site hydrodynamic model validation and rating curves estimation: An application to Brahmaputra River. Advances in Space Research, 68(2), 691-702. doi: 10.1016/j.asr.2020.05.012

Díez-Minguito, M., Baquerizo, A., Ortega-Sánchez, M., Navarro, G., & Losada, M. A. (2012). Tide transformation in the Guadalquivir estuary (SW Spain) and process-based zonation. Journal of Geophysical Research: Oceans, 117(C3). doi: 10.1029/2011JC007344

Díez-Minguito, M., Contreras, E., Polo, M. J., & Losada, M. A. (2013). Spatio-temporal distribution, along-channel transport, and post-riverflood recovery of salinity in the Guadalquivir estuary (SW Spain). Journal of Geophysical Research: Oceans, 118(5), 2267-2278. doi: 10.1002/jgrc.20172

Díez-Minguito, M., Baquerizo, A., De Swart, H. E., & Losada, M. A. (2014). Structure of the turbidity field in the G uadalquivir estuary: Analysis of observations and a box model approach. Journal of Geophysical Research: Oceans, 119(10), 7190-7204. doi: 10.1002/2014JC010210

Dinardo, S. (2013). Guidelines for the SAR (delay-Doppler) L1b processing. ESA document. Reference: XCRY-GSEG-EOPS-TN-14-0042.

Dinardo, S., Fenoglio-Marc, L., Becker, M., Scharroo, R., Fernandes, M. J., Staneva, J., ... & Benveniste, J. (2021). A RIP-based SAR retracker and its application in North East Atlantic with Sentinel-3. Advances in Space Research, 68(2), 892-929. doi: 10.1016/j.asr.2020.06.004 0273-1177

Dinardo, S., Fenoglio-Marc, L., Buchhaupt, C., Becker, M., Scharroo, R., Fernandes, M. J., & Benveniste, J. (2018). Coastal SAR and PLMR altimetry in German bight and west Baltic sea. Advances in Space Research, 62(6), 1371-1404. doi: 10.1016/j.asr.2017.12.018

Domeneghetti, A., Castellarin, A., Tarpanelli, A., & Moramarco, T. (2015). Investigating the uncertainty of satellite altimetry products for hydrodynamic modelling. Hydrological Processes, 29(23), 4908-4918. doi: 10.1002/hyp.10507

Donlon, C., Berruti, B., Buongiorno, A., Ferreira, M. H., Féménias, P., Frerick, J., ... & Sciarra, R. (2012). The global monitoring for environment and security (GMES) sentinel-3 mission. Remote Sensing of Environment, 120, 37-57. doi: 10.1016/j.rse.2011.07.024

Egbert, G. D., Bennett, A. F., & Foreman, M. G. (1994). TOPEX/POSEIDON tides estimated using a global inverse model. Journal of Geophysical Research: Oceans, 99(C12), 24821-24852. doi: 10.1029/94JC01894

Egbert, G. D., & Erofeeva, S. Y. (2002). Efficient inverse modeling of barotropic ocean tides. Journal of Atmospheric and Oceanic technology, 19(2), 183-204. doi: 10.1175/1520-0426(2002)019%3C0183

Egido, A., & Smith, W. H. (2017). Fully focused SAR altimetry: theory and applications. IEEE Transactions on Geoscience and Remote Sensing, 55(1), 392-406, doi: 10.1109/TGRS.2016.2607122

Elias, E. P., Gelfenbaum, G., & Van der Westhuysen, A. J. (2012). Validation of a coupled wave-flow model in a high-energy setting: The mouth of the Columbia River. Journal of Geophysical Research: Oceans, 117(C9). doi: 10.1029/2012JC008105

Ercilla, G., Juan, C., Periáñez, R., Alonso, B., Abril, J. M., Estrada, F., ... & Valencia, J. (2019). Influence of alongslope processes on modern turbidite systems and canyons in the Alboran Sea (southwestern Mediterranean). Deep Sea Research Part I: Oceanographic Research Papers, 144, 1-16. doi: 10.1016/j.dsr.2018.12.002

Farmer, D. M., & Armi, L. (1988). The flow of Atlantic water through the Strait of Gibraltar. Progress in Oceanography, 21(1), 1-103. doi: 10.1016/0079-6611(88)90055-9

Fenoglio-Marc, L., Dinardo, S., Scharroo, R., Roland, A., Sikiric, M. D., Lucas, B., ... & Weiss, R. (2015). The German Bight: A validation of CryoSat-2 altimeter data in SAR mode. Advances in Space Research, 55(11), 2641-2656. doi: 10.1016/j.asr.2015.02.014

Fenoglio, L., Dinardo, S., Uebbing, B., Buchhaupt, C., Gärtner, M., Staneva, J., ... & Kusche, J. (2021). Advances in NE-atlantic coastal sea level change monitoring by Delay Doppler altimetry. Advances in Space Research, 68(2), 571-592. doi: 10.1016/j.asr.2020.10.041

Fernandes, M. J., & Lázaro, C. (2016). GPD+ wet tropospheric corrections for CryoSat-2 and GFO altimetry missions. Remote Sensing, 8(10), 851. doi:10.3390/rs8100851

Fernandes, M. J., Lázaro, C., Nunes, A. L., Pires, N., Bastos, L., & Mendes, V. B. (2010). GNSS-derived path delay: An approach to compute the wet tropospheric correction for coastal altimetry. IEEE Geoscience and Remote Sensing Letters, 7(3), 596-600. doi: 10.1109/LGRS.2010.2042425

Fernandes, M. J., Lázaro, C., Nunes, A. L., & Scharroo, R. (2014). Atmospheric corrections for altimetry studies over inland water. Remote Sensing, 6(6), 4952-4997. doi:.3390/rs6064952

Fernandes, M. J., Nunes, A. L., & Lázaro, C. (2013). Analysis and inter-calibration of wet path delay datasets to compute the wet tropospheric correction for CryoSat-2 over ocean. Remote Sensing, 5(10), 4977-5005. doi:10.3390/rs5104977

Fernández-Delgado, C., Baldó, F., Vilas, C., García-González, D., Cuesta, J. A., González-Ortegón, E., & Drake, P. (2007). Effects of the river discharge management on the nursery function of the Guadalquivir river estuary (SW Spain). Hydrobiologia, 587(1), 125-136. doi: 10.1007/s10750-007-0691-9

Ferrer, L., & Caballero, A. (2011). Eddies in the Bay of Biscay: A numerical approximation. Journal of Marine Systems, 87(2), 133-144. doi :10.1016/j.jmarsys.2011.03.008

Ferrer, L., Fontán, A., Mader, J., Chust, G., González, M., Valencia, V., ... & Collins, M. B. (2009). Low-salinity plumes in the oceanic region of the Basque Country. Continental Shelf Research, 29(8), 970-984. doi: 10.1016/j.csr.2008.12.014

Flor-Blanco, G. (2015). Hydrodynamic controls of morpho-sedimentary evolution in a rock-bounded mesotidal estuary. Tina Menor (N Spain). Journal of Iberian Geology, 41(3), 315-332. doi: 10.5209/rev_JIGE.2015.v41.n3.50313

Foerste, Ch., Bruinsma, S. L., Abrikosov, O., Lemoine, J. M., Schaller, T., Götze, H. J., ... & Biancale, R. (2014). EIGEN-6C4: The latest combined global gravity field model including GOCE data up to degree and order 2190 of GFZ Potsdam and GRGS Toulouse. GFZ Data Services. doi: 10.5880/icgem.2015.1

Font, J., Salat, J., & Tintoré, J. (1988). Permanent features of the circulation in the Catalan Sea. Oceanologica Acta, Special issue.

Foreman, M. G. G., & Henry, R. F. (1989). The harmonic analysis of tidal model time series. Advances in Water Resources, 12(3), 109-120. doi: 10.1016/0309-1708(89)90017-1

Froidefond, J. M., Jegou, A. M., Hermida, J., Lazure, P., & Castaing, P. (1998). Variabilité du panache turbide de la Gironde par télédétection. Effets des facteurs climatiques. Oceanologica acta, 21(2), 191-207.

García, A., Sámano, M. L., Juanes, J. A., Medina, R., Revilla, J. A., & Álvarez, C. (2010). Assessment of the effects of a port expansion on algae appearance in a costal bay through mathematical modelling. Application to San Lorenzo Bay (North Spain). Ecological Modelling, 221(10), 1413-1426. doi: 10.1016/j.ecolmodel.2010.02.002

Garcia, M., Ramirez, I., Verlaan, M., & Castillo, J. (2015). Application of a three-dimensional hydrodynamic model for San Quintin Bay, BC, Mexico. Validation and calibration using OpenDA. Journal of Computational and Applied Mathematics, 273, 428-437. doi: 10.1016/j.cam.2014.05.003

García-Lafuente, J., Delgado, J., Criado-Aldeanueva, F., Bruno, M., del Río, J., & Vargas, J. M. (2006). Water mass circulation on the continental shelf of the Gulf of Cadiz. Deep Sea Research Part II: Topical Studies in Oceanography, 53(11-13), 1182-1197. doi:10.1016/j.dsr2.2006.04.011

García-Lafuente, J., Del Río, J., Alvarez Fanjul, E., Gomis, D., & Delgado, J. (2004). Some aspects of the seasonal sea level variations around Spain. Journal of Geophysical Research: Oceans, 109(C9). doi: 10.1029/2003JC002070

García-Lafuente, J., & Ruiz, J. (2007). The Gulf of Cádiz pelagic ecosystem: a review. Progress in Oceanography, 74(2-3), 228-251. doi: 10.1016/j.pocean.2007.04.001

Garel, E., Laiz, I., Drago, T., & Relvas, P. (2016). Characterisation of coastal counter-currents on the inner shelf of the Gulf of Cadiz. Journal of Marine Systems, 155, 19-34. doi:10.1016/j.jmarsys.2015.11.001

Gascard, J. C., & Richez, C. (1985). Water masses and circulation in the Western Alboran Sea and in the Straits of Gibraltar. Progress in Oceanography, 15(3), 157-216.doi: 10.1016/0079-6611(85)90031-X

Gessler, D., Hall, B., Spasojevic, M., Holly, F., Pourtaheri, H., & Raphelt, N. (1999). Application of 3D mobile bed, hydrodynamic model. Journal of Hydraulic Engineering, 125(7), 737-749. doi: 10.1061/(ASCE)0733-9429(1999)125:7(737)

Godin, G., 1972. The Analysis of Tides. (No. 551.4708 G6). University of Toronto Press, Toronto, 264pp.

Gómez, A. G., Juanes, J. A., Ondiviela, B., & Revilla, J. A. (2014). Assessment of susceptibility to pollution in littoral waters using the concept of recovery time. Marine pollution bulletin, 81(1), 140-148. doi: 10.1016/j.marpolbul.2014.02.004

Gómez-Enri, J., Aboitiz, A., Tejedor, B., & Villares, P. (2012). Seasonal and interannual variability in the Gulf of Cadiz: Validation of gridded altimeter products. Estuarine, Coastal and Shelf Science, 96, 114-121. doi: 10.1016/j.ecss.2011.10.013

Gómez-Enri, J., Escudier, R., Pascual, A., & Mañanes, R. (2015). Heavy Guadalquivir River discharge detection with satellite altimetry: The case of the eastern continental shelf of the Gulf of Cadiz (Iberian Peninsula). Advances in Space Research, 55(6), 1590-1603. doi: 10.1016/j.asr.2014.12.039

Gomez-Enri, J., Cipollini, P., Passaro, M., Vignudelli, S., Tejedor, B., & Coca, J. (2016a). Coastal altimetry products in the strait of Gibraltar. IEEE Transactions on Geoscience and Remote Sensing, 54(9), 5455-5466. doi: 10.1109/TGRS.2016.2565472

Gómez-Enri, J., Scozzari, A., Soldovieri, F., Coca, J., & Vignudelli, S. (2016b). Detection and characterization of ship targets using CryoSat-2 altimeter waveforms. Remote Sensing, 8(3), 193. doi:10.3390/rs8030193

Gómez-Enri, J., Vignudelli, S., Cipollini, P., Coca, J., & González, C. J. (2018). Validation of CryoSat-2 SIRAL sea level data in the eastern continental shelf of the Gulf of Cadiz (Spain). Advances in Space Research, 62(6), 1405-1420. doi: 10.1016/j.asr.2017.10.042

Gómez-Enri, J., Villares, P., Tejedor, B., Aboitiz, A., Laiz, I., Coca, J., ... & Torres, J. R. (2014). From ENVISAT RA-2 to CRYOSAT SIRAL: validation of altimeter products near the coast (the ALCOVA Project). In Remote Sensing of the Ocean, Sea Ice, Coastal Waters, and Large Water Regions 2014, Vol. 9240, p. 92400P. International Society for Optics and Photonics. doi: 10.1117/12.2067501

Gomiz-Pascual, J. J., Bolado-Penagos, M., Gonzalez, C. J., Vazquez, A., Buonocore, C., Romero-Cozar, J., ... & Bruno, M. (2021). The fate of Guadalquivir River discharges in the coastal strip of the Gulf of Cádiz. A study based on the linking of watershed catchment and hydrodynamic models. Science of the Total Environment, 795, 148740. doi: 10.1016/j.scitotenv.2021.148740

Gommenginger, C., Martin-Puig, C., Amarouche, L., & Raney, R. K. (2013). Review of state of knowledge for SAR altimetry over ocean. Report of the EUMETSAT JASON-CS SAR mode error budget study: EUM/RSP/REP/14/749304

Gommenginger, C., Thibaut, P., Fenoglio-Marc, L., Quartly, G., Deng, X., Gómez-Enri, J., ... & Gao, Y. (2011). Retracking altimeter waveforms near the coasts. In Coastal altimetry (pp. 61-101). Springer, Berlin, Heidelberg. doi: 0.1007/978-3-642-12796-0_4

González, C. J., Reyes, E., Álvarez, Ó., Izquierdo, A., Bruno, M., & Mañanes, R. (2019). Surface currents and transport processes in the Strait of Gibraltar: Implications for modeling and management of pollutant spills. Ocean & Coastal Management, 179, 104869. doi: 10.1016/j.ocecoaman.2019.104869

González-Marco, D., Sierra, J. P., de Ybarra, O. F., & Sánchez-Arcilla, A. (2008). Implications of long waves in harbor management: the Gijón port case study. Ocean & Coastal Management, 51(2), 180-201. doi: 10.1016/j.ocecoaman.2007.04.001

González-Ortegón, E., Subida, M. D., Cuesta, J. A., Arias, A. M., Fernández-Delgado, C., & Drake, P. (2010). The impact of extreme turbidity events on the nursery function of a temperate European estuary with regulated freshwater inflow. Estuarine, Coastal and Shelf Science, 87(2), 311-324. doi: 10.1016/j.ecss.2010.01.013

González-Ortegón, E., & Drake, P. (2012). Effects of freshwater inputs on the lower trophic levels of a temperate estuary: physical, physiological or trophic forcing?. Aquatic Sciences, 74(3), 455-469. doi: 10.1007/s00027-011-0240-5

Guccione, P., Scagliola, M., & Giudici, D. (2018). 2D Frequency domain fully focused SAR processing for high PRF radar altimeters. Remote Sensing, 10(12), 1943, doi: 10.3390/rs10121943

Guerreiro, C., Macías, D., Peliz, A., Prieto, L., & Ruiz, J. (2013). The role of estuarine discharges on the biogeochemical characteristics of the nearby continental shelf ecosystem. The Guadalquivir-Gulf of Cádiz case study. In EGU General Assembly Conference Abstracts EGU2013-8361.

Guo, L., van der Wegen, M., Jay, D. A., Matte, P., Wang, Z. B., Roelvink, D., & He, Q. (2015). River-tide dynamics: Exploration of nonstationary and nonlinear tidal behavior in the Y angtze R iver estuary. Journal of Geophysical Research: Oceans, 120(5), 3499-3521. doi: 10.1002/2014JC010491

Handoko, E. Y., Fernandes, M. J., & Lázaro, C. (2017). Assessment of altimetric range and geophysical corrections and mean sea surface models—Impacts on sea level variability around the Indonesian seas. Remote Sensing, 9(2), 102. doi:10.3390/rs9020102

Hansen, D. V., & Rattray Jr, M. (1966). New dimensions in estuary classification 1. Limnology and oceanography, 11(3), 319-326. doi: 10.4319/lo.1966.11.3.0319

Hermida, J., Lazure, P., Froidefond, J. M., Jegou, A. M., & Castaing, P. (1998). La dispersion des apports de la Gironde sur le plateau continental. Données in situ, satellitales et numériques. Oceanologica acta, 21(2), 209-221.

Hoegh-Guldberg, O., Cai, R., Poloczanska, E. S., Brewer, P. G., Sundby, S., Hilmi, K., ... & McKinnell, S. M. (2014). The ocean. Climate Change 2014: Impacts, Adaptation, and Vulnerability, Part B: Regional Aspects, Chapter 30. Cambridge University Press, Cambridge, pp. 1655-1731.

Iribar, X., & Ibáñez, M. (1979). Subdivisión de la zona intermareal de San Sebastián en función de los datos obtenidos con mareógrafo. In Acta 1º Simposio Ibérico de Estudio del Bentos Marino (pp. 521-524).

Janssen, P. A., Abdalla, S., Hersbach, H., & Bidlot, J. R. (2007). Error estimation of buoy, satellite, and model wave height data. Journal of Atmospheric and Oceanic Technology, 24(9), 1665-1677. doi: 10.1175/JTECH2069.1

Jarihani, A. A., Callow, J. N., Johansen, K., & Gouweleeuw, B. (2013). Evaluation of multiple satellite altimetry data for studying inland water bodies and river floods. Journal of Hydrology, 505, 78-90. doi: 10.1016/j.jhydrol.2013.09.010

Jarvis, A. (2008). Hole-field seamless SRTM data, International Centre for Tropical Agriculture (CIAT). [Available at: http://srtm.csi.cgiar.org]

Jay, D. A., Leffler, K., Diefenderfer, H. L., & Borde, A. B. (2015). Tidal-fluvial and estuarine processes in the lower Columbia River: I. Along-channel water level variations, Pacific Ocean to Bonneville Dam. Estuaries and Coasts, 38(2), 415-433. doi: 10.1007/s12237-014-9819-0

Jensen, J. R., & Raney, R. K. (1998). Delay/Doppler radar altimeter: Better measurement precision. In IGARSS'98. Sensing and Managing the Environment. 1998 IEEE International Geoscience and Remote Sensing. Symposium Proceedings. (Cat. No. 98CH36174),Vol. 4, pp. 2011-2013. doi: 10.1109/IGARSS.1998.703724

Jia, Y. (2000). Formation of an Azores Current due to Mediterranean overflow in a modeling study of the North Atlantic. Journal of Physical Oceanography, 30(9), 2342-2358. doi: 10.1175/1520-0485(2000)030<2342

Jiang, L., Madsen, H., & Bauer-Gottwein, P. (2019). Simultaneous calibration of multiple hydrodynamic model parameters using satellite altimetry observations of water surface elevation in the Songhua River. Remote sensing of environment, 225, 229-247. doi: 10.1016/j.rse.2019.03.014

Johnson, J., & Stevens, I. (2000). A fine resolution model of the eastern North Atlantic between the Azores, the Canary Islands and the Gibraltar Strait. Deep Sea Research Part I: Oceanographic Research Papers, 47(5), 875-899. doi: 10.1016/S0967-0637(99)00073-4

Khanarmuei, M., Suara, K., Sumihar, J., & Brown, R. J. (2020). Hydrodynamic modelling and model sensitivities to bed roughness and bathymetry offset in a micro-tidal estuary. Journal of Hydroinformatics, 22(6), 1536-1553. doi: 10.2166/hydro.2020.102

Kleinherenbrink, M., Naeije, M., Slobbe, C., Egido, A., & Smith, W. (2020). The performance of CryoSat-2 fully-focussed SAR for inland water-level estimation. Remote Sensing of Environment, 237, 111589. doi: 10.1016/j.rse.2019.111589

Krishnan, A., & Bhaskaran, P. K. (2020). Performance of CMIP5 wind speed from global climate models for the Bay of Bengal region. International Journal of Climatology, 40(7), 3398-3416. doi: 10.1002/joc.6404

Lacombe, H., & Richez, C. (1982). The regime of the Strait of Gibraltar. In Elsevier oceanography series (3), 13-73. Elsevier. doi: 10.1016/S0422-9894(08)71237-6

Laiz, I., Ferrer, L., Plomaritis, T. A., & Charria, G. (2014). Effect of river runoff on sea level from in-situ measurements and numerical models in the Bay of Biscay. Deep Sea Research Part II: Topical Studies in Oceanography, 106, 49-67. doi: 10.1016/j.dsr2.2013.12.013

Laiz, I., Gómez-Enri, J., Tejedor, B., Aboitiz, A., & Villares, P. (2013). Seasonal sea level variations in the gulf of Cadiz continental shelf from in-situ measurements and satellite altimetry. Continental Shelf Research, 53, 77-88. doi: /10.1016/j.csr.2012.12.008

Laiz, I., Tejedor, B., Gomez-Enri, J., Aboitiz, A., & Villares, P. (2016). Contributions to the sea level seasonal cycle within the Gulf of Cadiz (Southwestern Iberian Peninsula). Journal of Marine Systems, 159, 55-66. doi: 10.1016/j.jmarsys.2016.03.006

Laiz, I., Pelegrí, J. L., Machín, F., Sangrà, P., Hernández-Guerra, A., Marrero-Díaz, A., & Rodríguez-Santana, A. (2012). Eastern boundary drainage of the North Atlantic subtropical gyre. Ocean Dynamics, 62(9), 1287-1310. doi: 10.1007/s10236-012-0560-6

Laiz, I., Plecha, S., Teles-Machado, A., González-Ortegón, E., Sánchez-Quiles, D., Cobelo-García, A., ... & Tovar-Sánchez, A. (2020). The role of the Gulf of Cadiz circulation in the redistribution of trace metals between the Atlantic Ocean and the Mediterranean Sea. Science of the Total Environment, 719, 134964. doi: 10.1016/j.scitotenv.2019.134964

Lavin, A., Valdes, L., Sanchez, F., Abaunza, P., Forest, A., Boucher, J., …& Jegou, A.M. . (2004). The Bay of Biscay: the encountering of the Ocean and the Shelf (18b, E). In The Global Coastal Ocean—Interdisciplinary Regional Studies and Syntheses, vol. 14. Cambridge, MA, USA: Harvard Univ. Press, 2004, pp. 933–1001.

Lazure, P., & Dumas, F. (2008). An external–internal mode coupling for a 3D hydrodynamical model for applications at regional scale (MARS). Advances in water resources, 31(2), 233-250. doi: 10.1016/j.advwatres.2007.06.010

Lazure, P., Garnier, V., Dumas, F., Herry, C., & Chifflet, M. (2009). Development of a hydrodynamic model of the Bay of Biscay. Validation of hydrology. Continental Shelf Research, 29(8), 985-997. doi: 10.1016/j.csr.2008.12.017

Lesser, G.R., (2009). An approach to medium-term coastal morphological modelling. PhD Thesis, UNESCO-IHE & Delft Technical University, Delft. CRC Press/Balkema. ISBN 978-0-415-55668-2. [Available at: http://resolver.tudelft.nl/uuid:27a1ffa0-580e-4eae-907b-ce6f901e652e]

Lesser, G. R., & Roelvink, J. A. a., van Kester, J. a. TM, Stelling, GS, 2004. Development and validation of a three-dimensional morphological model. Coastal Engineering, 51(8-9), 883-915. doi: 10.1016/j.coastaleng.2004.07.014

Lewis, H. W., Castillo Sanchez, J. M., Siddorn, J., King, R. R., Tonani, M., Saulter, A., ... & Bricheno, L. (2019). Can wave coupling improve operational regional ocean forecasts for the north-west European Shelf?. Ocean Science, 15(3), 669-690. doi: 10.5194/os-15-669-2019

Liibusk, A., Kall, T., Rikka, S., Uiboupin, R., Suursaar, Ü., & Tseng, K. H. (2020). Validation of copernicus sea level altimetry products in the baltic sea and estonian lakes. Remote Sensing, 12(24), 4062. doi: 10.3390/rs12244062

List, J. H., Jaffe, B. E., Sallenger Jr, A. H., & Hansen, M. E. (1997). Bathymetric comparisons adjacent to the Louisiana barrier islands: processes of large-scale change. Journal of Coastal Research, ISNN: 0749-0208. 670-678.

Liu, Y., Kerkering, H., & Weisberg, R. H. (2015). Introduction to coastal ocean observing systems. In Coastal Ocean Observing Systems (pp. 1-10). Academic Press. doi: 10.1016/B978-0-12-802022-7.00001-8

Liu, Y., & Gupta, H. V. (2007). Uncertainty in hydrologic modeling: Toward an integrated data assimilation framework. Water resources research, 43(7). doi: 10.1029/2006WR005756

Lobo, F. J., Le Roy, P., Mendes, I., & Sahabi, M. (2014). The Gulf of Cádiz continental shelves. Geological Society, London, Memoirs, 41(1), 109-130. doi: 10.1144/M41.9

López, I., Álvarez, C., Gil, J. L., García, A., Bárcena, J. F., & Revilla, J. A. (2013). A method for the source apportionment in bathing waters through the modelling of wastewater discharges: development of an indicator and application to an urban beach in Santander (Northern Spain). Ecological indicators, 24, 334-343. doi: 10.1016/j.ecolind.2012.07.003

Losada, M. A., Díez-Minguito, M., & Reyes-Merlo, M. Á. (2017). Tidal-fluvial interaction in the Guadalquivir River Estuary: Spatial and frequency-dependent response of currents and water levels. Journal of Geophysical Research: Oceans, 122(2), 847-865. doi: 10.1002/2016JC011984

Loucks, D. P., & Van Beek, E. (2017). Water resource systems planning and management: An introduction to methods, models, and applications. Springer. doi: 10.1007/978-3-319-44234-1

Mañanes, R., Bruno, M., Alonso, J., Fraguela, B., & Tejedor, L. (1998). Non-linear interaction between tidal and subinertial barotropic flows in the Strait of Gibraltar. Oceanologica Acta, 21(1), 33-46. doi: 10.1016/S0399-1784(98)80047-9

Martyr-Koller, R. C., Kernkamp, H. W. J., Van Dam, A., van der Wegen, M., Lucas, L. V., Knowles, N., ... & Fregoso, T. A. (2017). Application of an unstructured 3D finite volume numerical model to flows and salinity dynamics in the San Francisco Bay-Delta. Estuarine. Coastal and Shelf Science, 192, 86-107. doi: 10.1016/j.ecss.2017.04.024

Mason, E., Coombs, S. H., & Oliveira, P. B. (2005). An overview of the literature concerning the oceanography of the eastern North Atlantic region. Relatórios Científicos e Técnicos IPIMAR Serie Digital, 33, 59. ISNN: 1645-863X

Matte, P., Secretan, Y., & Morin, J. (2017). Hydrodynamic modeling of the St. Lawrence fluvial estuary. I: Model setup, calibration, and validation. Journal of Waterway, Port, Coastal, and Ocean Engineering, 143(5), 04017010. doi: 10.1061/(ASCE)WW.1943-5460.0000397

Mauritzen, C., Morel, Y., & Paillet, J. (2001). On the influence of Mediterranean water on the central waters of the North Atlantic Ocean. Deep Sea Research Part I: Oceanographic Research Papers, 48(2), 347-381. doi: 10.1016/S0967-0637(00)00043-1

Mecklenburg, S., Dransfeld, S., Gascon, F., Nieke, J., Donlon, C., Drusch, M., ... & Berruti, B. (2018). ESA's Sentinel-3 Mission-Status and Performance. In IGARSS 2018-2018 IEEE International Geoscience and Remote Sensing Symposium, 3917-3919. doi: 10.1109/IGARSS.2018.8518877

Medellín, G., Medina, R., Falqués, A., & González, M. (2008). Coastline sand waves on a low-energy beach at “El Puntal” spit, Spain. Marine Geology, 250(3-4), 143-156. doi: 10.1016/j.margeo.2007.11.011

Mendes, J., Ruela, R., Picado, A., Pinheiro, J. P., Ribeiro, A. S., Pereira, H., & Dias, J. M. (2021). Modeling Dynamic Processes of Mondego Estuary and Óbidos Lagoon Using Delft3D. Journal of Marine Science and Engineering, 9(1), 91. doi: 10.3390/jmse9010091

Mendoza, E., Silva, R., Zanuttigh, B., Angelelli, E., Andersen, T. L., Martinelli, L., ... & Ruol, P. (2014). Beach response to wave energy converter farms acting as coastal defence. Coastal Engineering, 87, 97-111. doi: 10.1016/j.coastaleng.2013.10.018

Mertes, L. A. (2002). Remote sensing of riverine landscapes. Freshwater biology, 47(4), 799-816. doi: 10.1046/j.1365-2427.2002.00909.x

Mertikas, S., Tripolitsiotis, A., Donlon, C., Mavrocordatos, C., Féménias, P., Borde, F., ... & Cullen, R. (2020). The ESA Permanent Facility for altimetry calibration: Monitoring performance of radar altimeters for Sentinel-3A, Sentinel-3B and Jason-3 using transponder and sea-surface calibrations with FRM standards. Remote Sensing, 12(16), 2642. doi: 10.3390/RS12162642

Mostafavi, M., Delpeche-Ellmann, N., & Ellmann, A. (2021). Accurate Sea Surface heights from Sentinel-3A and Jason-3 retrackers by incorporating High-Resolution Marine Geoid and Hydrodynamic Models. Journal of Geodetic Science, 11(1), 58-74. doi: 10.1515/jogs-2020-0120

Mulero-Martínez, R., Gómez-Enri, J., Mañanes, R., & Bruno, M. (2021). Assessment of near-shore currents from CryoSat-2 satellite in the Gulf of Cádiz using HF radar-derived current observations. Remote Sensing of Environment, 256, 112310. doi: 10.1016/j.rse.2021.112310

Muñoz, A., Ballesteros, M., Montoya, I., Rivera, J., Acosta, J., & Uchupi, E. (2008). Alborán Basin, southern Spain—part I: geomorphology. Marine and Petroleum Geology, 25(1), 59-73. doi: 10.1016/j.marpetgeo.2007.05.003

Navarro, G. (2004). Escalas de variabilidad espacio-temporal de procesos pelágicos en el Golfo de Cádiz. PhD Thesis. University of Cadiz.

Navarro, G., Huertas, I. E., Costas, E., Flecha, S., Díez-Minguito, M., Caballero, I., ... & Ruiz, J. (2012). Use of a real-time remote monitoring network (RTRM) to characterize the Guadalquivir estuary (Spain). Sensors, 12(2), 1398-1421. doi: 10.3390/s120201398

Navarro, G., & Ruiz, J. (2006). Spatial and temporal variability of phytoplankton in the Gulf of Cádiz through remote sensing images. Deep Sea Research Part II: topical studies in oceanography, 53(11-13), 1241-1260. doi: 10.1016/j.dsr2.2006.04.014

Nencioli, F., & Quartly, G. D. (2019). Evaluation of Sentinel-3A wave height observations near the coast of southwest England. Remote Sensing, 11(24), 2998. doi: 10.3390/rs11242998

Nerem, R. S., Chambers, D. P., Choe, C., & Mitchum, G. T. (2010). Estimating mean sea level change from the TOPEX and Jason altimeter missions. Marine Geodesy, 33(S1), 435-446. doi: 10.1080/01490419.2010.491031

Nicholson, J., Broker, I., Roelvink, J. A., Price, D., Tanguy, J. M., & Moreno, L. (1997). Intercomparison of coastal area morphodynamic models. Coastal Engineering, 31(1-4), 97-123. doi: 10.1016/S0378-3839(96)00054-3

Ochoa, J., & Bray, N. A. (1991). Water mass exchange in the Gulf of Cadiz. Deep Sea Research Part A. Oceanographic Research Papers, 38, S465-S503. doi: 10.1016/S0198-0149(12)80021-5

Oreiro, F. A., D'Onofrio, E., Grismeyer, W., Fiore, M., & Saraceno, M. (2014). Comparison of tide model outputs for the northern region of the Antarctic Peninsula using satellite altimeters and tide gauge data. Polar Science, 8(1), 10-23. doi: 10.1016/j.polar.2013.12.001

Ortega-Sánchez, M., Bergillos, R. J., López-Ruiz, A., & Losada, M. A. (2017). Morphodynamics of Mediterranean mixed sand and gravel coasts. Springer International Publishing. doi: 10.1007/978-3-319-52440-5

OSPAR Commission for the Protection of the Marine Environment of the North-East Atlantic. (2000). Quality Status Report 2000: Region IV: Bay of Biscay and Iberian Coast. OSPAR Commission for the Protection of the Marine Environment of the North-East Atlantic.

Pairaud, I., Marsaleix, P., & Auclair, F. (2003). Tidal and thermohaline circulation in the Bay of Biscay. In EGS-AGU-EUG Joint Assembly (p. 7058).

Paiva, R. D., Collischonn, W., Bonnet, M. P., De Goncalves, L. G. G., Calmant, S., Getirana, A., & Santos da Silva, J. (2013). Assimilating in situ and radar altimetry data into a large-scale hydrologic-hydrodynamic model for streamflow forecast in the Amazon. Hydrology and Earth System Sciences, 17(7), 2929-2946. doi: 10.5194/hess-17-2929-2013

Parker, B. B. (1991). The relative importance of the various nonlinear mechanisms in a wide range of tidal interactions. Tidal hydrodynamics, 237-268.

Parrilla, G., & Kinder, T. H. (1987). The Physical Oceanography of the Alboran Sea. Naval Ocean Research and Development Activity NSTL Station MS.

Passaro, M., Cipollini, P., Vignudelli, S., Quartly, G. D., & Snaith, H. M. (2014). ALES: A multi-mission adaptive subwaveform retracker for coastal and open ocean altimetry. Remote Sensing of Environment, 145, 173-189. doi: 10.1016/j.rse.2014.02.008

Passaro, M., Dinardo, S., Quartly, G. D., Snaith, H. M., Benveniste, J., Cipollini, P., & Lucas, B. (2016). Cross-calibrating ALES Envisat and CryoSat-2 Delay–Doppler: a coastal altimetry study in the Indonesian Seas. Advances in Space Research, 58(3), 289-303. doi: 10.1016/j.asr.2016.04.011

Passaro, M., Fenoglio-Marc, L., & Cipollini, P. (2015). Validation of significant wave height from improved satellite altimetry in the German Bight. IEEE Transactions on Geoscience and Remote Sensing, 53(4), 2146-2156, doi: 10.1109/TGRS.2014.2356331

Passaro, M., Müller, F. L., Oelsmann, J., Rautiainen, L., Dettmering, D., Hart-Davis, M. G., ... & Benveniste, J. (2021). Absolute Baltic Sea Level Trends in the Satellite Altimetry Era: A Revisit. Frontiers in Marine Science. doi: 10.3389/fmars.2021.647607

Passaro, M., Nadzir, Z. A., & Quartly, G. D. (2018). Improving the precision of sea level data from satellite altimetry with high-frequency and regional sea state bias corrections. Remote Sensing of Environment, 218, 245-254. doi: 10.1016/j.rse.2018.09.007

Passaro, M., Restano, M., Sabatino, G., Orrú, C., & Benveniste, J. (2020). The ALES+ SAR Service for Cryosat-2 and Sentinel-3 at ESA GPOD. In OSTST 2020.

Pawlowicz, R., Beardsley, B., & Lentz, S. (2002). Classical tidal harmonic analysis including error estimates in MATLAB using T_TIDE. Computers & Geosciences, 28(8), 929-937. doi: 10.1016/S0098-3004(02)00013-4

Peliz, A., Dubert, J., Marchesiello, P., & Teles-Machado, A. (2007). Surface circulation in the Gulf of Cadiz: Model and mean flow structure. Journal of Geophysical Research: Oceans, 112(C11). doi:10.1029/2007JC004159

Peng, F., & Deng, X. (2018). Validation of improved significant wave heights from the Brown-Peaky (BP) retracker along the east coast of Australia. Remote Sensing, 10(7), 1072. doi: 10.3390/rs10071072

Peng, F., & Deng, X. (2020). Validation of Sentinel-3A SAR mode sea level anomalies around the Australian coastal region. Remote Sensing of Environment, 237, 111548. doi: 10.1016/j.rse.2019.111548

Pérez, B., Álvarez Fanjul, E., Pérez, S., de Alfonso, M., & Vela, J. (2013). Use of tide gauge data in operational oceanography and sea level hazard warning systems. Journal of Operational Oceanography, 6(2), 1-18. doi: 10.1080/1755876X.2013.11020147

Pingree, R. D., & Le Cann, B. (1990). Structure, strength and seasonality of the slope currents in the Bay of Biscay region. Journal of the Marine Biological Association of the United Kingdom, 70(4), 857-885.

Pingree, R. D., Sinha, B., & Griffiths, C. R. (1999). Seasonality of the European slope current (Goban Spur) and ocean margin exchange. Continental Shelf Research, 19(7), 929-975.

Pires, N., Fernandes, M. J., Gommenginger, C., & Scharroo, R. (2016). A conceptually simple modeling approach for Jason-1 sea state bias correction based on 3 parameters exclusively derived from altimetric information. Remote Sensing, 8(7), 576. doi:10.3390/rs8070576

Pratama, M. B., Venugopal, V., Ajiwibowo, H., Ginting, J. W., & Novico, F. (2020). Modelling Tidal Flow Hydrodynamics of Sunda Strait, Indonesia. ILMU KELAUTAN: Indonesian Journal of Marine Sciences, 25(4), 165-172. doi: 10.14710/ik.ijms.25.4.165-172

Puertos del Estado. (2012). Red Costera de Boyas. Informe de datos de la boya de Barcelona. Accessed: Nov. 2012. [Available at: https://www.puertos.es/es-es/oceanografia/Paginas/portus.aspx]

Puertos del Estado. (2015a). Red de Boyas de Aguas Profundas. Informe de Datos de la Boya de Golfo de Cádiz. Accessed: Nov. 2015. [Available at: https://www.puertos.es/es-es/oceanografia/Paginas/portus.aspx]

Puestos del Estado. (2015b). Red de Boyas de Aguas Profundas. Informe de Datos de la Boya de Bilbao. Accessed: Nov. 2015. [Available at: https://www.puertos.es/es-es/oceanografia/Paginas/portus.aspx]

Raney, R. K. (1998). The delay/Doppler radar altimeter. IEEE Transactions on Geoscience and Remote Sensing, 36(5), 1578-1588. doi: 10.1109/36.718861

Raney, R. K. (2011). CryoSat SAR-mode looks revisited. IEEE Geoscience and Remote Sensing Letters, 9(3), 393-397. doi: 10.1109/LGRS.2011.2170052

Ray, C., Martin-Puig, C., Clarizia, M. P., Ruffini, G., Dinardo, S., Gommenginger, C., & Benveniste, J. (2015). SAR altimeter backscattered waveform model. IEEE Transactions on Geoscience and Remote Sensing, 53(2), 911-919. doi: 10.1109/TGRS.2014.2330423

Raynal, M., Labroue, S., Moreau, T., Boy, F., & Picot, N. (2018). From conventional to Delay Doppler altimetry: A demonstration of continuity and improvements with the Cryosat-2 mission. Advances in Space Research, 62(6), 1564-1575. doi: 10.1016/j.asr.2018.01.006

Reffray, G., Fraunié, P., & Marsaleix, P. (2004). Secondary flows induced by wind forcing in the Rhône region of freshwater influence. Ocean Dynamics, 54(2), 179-196. doi: 10.1007/s10236-003-0079-y

Relvas, P., & Barton, E. D. (2002). Mesoscale patterns in the Cape Sao Vicente (Iberian peninsula) upwelling region. Journal of Geophysical Research: Oceans, 107(C10), 28-1. doi: 10.1029/2000JC000456

Rieu, P., Moreau, T., Cadier, E., Raynal, M., Clerc, S., Donlon, C., ... & Maraldi, C. (2021). Exploiting the Sentinel-3 tandem phase dataset and azimuth oversampling to better characterize the sensitivity of SAR altimeter sea surface height to long ocean waves. Advances in Space Research, 67(1), 253-265. doi: 10.1016/j.asr.2020.09.037

Roelvink, J. A., Jeuken, M. C. J. L., Van Holland, G., Aarninkhof, S. G. J., & Stam, J. M. T. (2001). Long-term, process-based modelling of complex areas. In Coastal Dynamics' 01, 383-392. doi: 10.1061/40566(260)39

Roelvink, D., Reniers, A., Van Dongeren, A. P., De Vries, J. V. T., McCall, R., & Lescinski, J. (2009). Modelling storm impacts on beaches, dunes and barrier islands. Coastal engineering, 56(11-12), 1133-1152. doi: 10.1016/j.coastaleng.2009.08.006

Romanazzo, M., Morales-Santiago, J. M., Jauregui, L., & Emanuelli, P. P. (2018). Tandem operations preparation for Sentinel-3 A/B: paving the way for C/D models. In 2018 SpaceOps Conference (p. 2520). doi: 10.2514/6.2018-2520

Ruiz, J., Polo, M. J., Díez-Minguito, M., Navarro, G., Morris, E. P., Huertas, E., ... & Losada, M. A. (2015). The Guadalquivir estuary: a hot spot for environmental and human conflicts. In Environmental management and governance (pp. 199-232). Springer, Cham. doi: 10.1007/978-3-319-06305-8_8

Ruiz-Reina, A., & López-Ruiz, A. (2021). Short-term river mouth bar development during extreme river discharge events: The role of the phase difference between the peak discharge and the tidal level. Coastal Engineering, 170, 103982. doi: 10.1016/j.coastaleng.2021.103982

Rulent, J., Mir Calafat, F., Banks, C. J., Bricheno, L., Gommenginger, C., Green, M., ... & Martin, A. (2020). Comparing Water Level Estimation In Coastal And Shelf Seas From Satellite Altimetry And Numerical Models. Frontiers in Marine Science, 7, 919. doi: 10.3389/fmars.2020.549467

Sánchez-Román, A., Criado-Aldeanueva, F., García-Lafuente, J., & Sánchez, J. C. (2008). Vertical structure of tidal currents over Espartel and Camarinal sills, Strait of

Gibraltar. Journal of Marine Systems, 74(1-2), 120-133. doi: 10.1016/j.jmarsys.2007.11.007

Sánchez, R. F., & Relvas, P. (2003). Spring–summer climatological circulation in the upper layer in the region of Cape St. Vincent, Southwest Portugal. ICES Journal of Marine Science, 60(6), 1232-1250. doi: 10.1016/S1054-3139(03)00137-1

Sandbach, S. D., Nicholas, A. P., Ashworth, P. J., Best, J. L., Keevil, C. E., Parsons, D. R., ... & Simpson, C. J. (2018). Hydrodynamic modelling of tidal-fluvial flows in a large river estuary. Estuarine, Coastal and Shelf Science, 212, 176-188. doi: 10.1016/j.ecss.2018.06.023

Sannino, G., Bargagli, A., & Artale, V. (2002). Numerical modeling of the mean exchange through the Strait of Gibraltar. Journal of Geophysical Research: Oceans, 107(C8), 9-1. doi: 10.1029/2001JC000929

Schneider, R., Tarpanelli, A., Nielsen, K., Madsen, H., & Bauer-Gottwein, P. (2018). Evaluation of multi-mode CryoSat-2 altimetry data over the Po River against in situ data and a hydrodynamic model. Advances in water resources, 112, 17-26. doi: 10.1016/j.advwatres.2017.11.027

Schumann, G. J. (2015). Preface: Remote sensing in flood monitoring and management. Remote Sensing, 7(12), 17013-17015. doi: 10.1029/2008RG000274

Shchepetkin, A. F., & McWilliams, J. C. (2005). The regional oceanic modeling system (ROMS): a split-explicit, free-surface, topography-following-coordinate oceanic model. Ocean modelling, 9(4), 347-404. doi: 10.1016/j.ocemod.2004.08.002

Shen, Y., Liu, D., Jiang, L., Yin, J., Nielsen, K., Bauer-Gottwein, P., ... & Wang, J. (2020). On the Contribution of Satellite Altimetry-Derived Water Surface Elevation to Hydrodynamic Model Calibration in the Han River. Remote Sensing, 12(24), 4087. doi: 10.3390/rs12244087

Siles-Ajamil, R., Díez-Minguito, M., & Losada, M. Á. (2019). Tide propagation and salinity distribution response to changes in water depth and channel network in the Guadalquivir River Estuary: An exploratory model approach. Ocean & Coastal Management, 174, 92-107. doi: 10.1016/j.ocecoaman.2019.03.015

Sobrino, I., Gómez, M. P. J., Modrego, F. R., & Domínguez, J. B. (1994). Descripción de las pesquerías demersales de la región suratlántica española. Informes Técnicos Instituto Español de Oceanografía, ISSN 0212-1565 (151), 3-79.

Stanichny, S., Tigny, V., Stanichnaya, R., & Djenidi, S. (2005). Wind driven upwelling along the African coast of the Strait of Gibraltar. Geophysical research letters, 32(4). doi: 10.1029/2004GL021760

Steijn, R., Roelvink, D., Rakhorst, D., Ribberink, J., & van Overeem, J. (1999). North-Coast of Texel: a comparison between reality and prediction. In Coastal Engineering 1998 (pp. 2281-2293). doi: 10.1061/9780784404119.171

Stevenson, R. E. (1977). Huelva Front and Malaga, Spain, eddy chain as defined by satellite and oceanographic data.. Deutsche Hydrografische Zeitschrift, 30(2), 51-53.

Straatsma, M., & Huthoff, F. (2011). Uncertainty in 2D hydrodynamic models from errors in roughness parameterization based on aerial images. Physics and Chemistry of the Earth, Parts A/B/C, 36(7-8), 324-334. doi: 10.1016/j.pce.2011.02.009

Sutherland, J., Walstra, D. J. R., Chesher, T. J., Van Rijn, L. C., & Southgate, H. N. (2004). Evaluation of coastal area modelling systems at an estuary mouth. Coastal Engineering, 51(2), 119-142. doi: 10.1016/j.coastaleng.2003.12.003

Struiksma, N. (1985). Prediction of 2-D bed topography in rivers. Journal of hydraulic Engineering, 111(8), 1169-1182. doi: 10.1061/(ASCE)0733-9429(1985)111:8(1169)

Tejedor, L., Izquierdo, A., Kagan, B. A., & Sein, D. V. (1999). Simulation of the semidiurnal tides in the Strait of Gibraltar. Journal of Geophysical Research: Oceans, 104(C6), 13541-13557. doi: 10.1029/1998JC900102

Thompson, A., Guo, Y., & Moin, S. (2008). Uncertainty analysis of a two-dimensional hydrodynamic model. Journal of Great Lakes Research, 34(3), 472-484. doi: 10.3394/0380-1330(2008)34[472:UAOATH]2.0.CO;2

Tsimplis, M. N., & Josey, S. A. (2001). Forcing of the Mediterranean Sea by atmospheric oscillations over the North Atlantic. Geophysical Research Letters, 28(5), 803-806. doi: 10.1029/2000GL012098

Tsimplis, M. N., Proctor, R., & Flather, R. A. (1995). A two-dimensional tidal model for the Mediterranean Sea. Journal of Geophysical Research: Oceans, 100(C8), 16223-16239. doi: 10.1029/95JC01671

Tran, N., Vandemark, D., Labroue, S., Feng, H., Chapron, B., Tolman, H. L., ... & Picot, N. (2010). Sea state bias in altimeter sea level estimates determined by combining wave model and satellite data. Journal of Geophysical Research: Oceans, 115(C3). doi: 10.1029/2009JC005534

Vázquez, Á., Bruno, M., Izquierdo, A., Macías, D., & Ruiz, A. (2008). Meteorologically forced subinertial flows and internal wave generation at the main sill of the Strait of Gibraltar. doi: 10.1016/j.dsr.2008.05.008

Verron, J., Sengenes, P., Lambin, J., Noubel, J., Steunou, N., Guillot, A., ... & Gupta, P. K. (2015). The SARAL/AltiKa altimetry satellite mission. Marine Geodesy, 38(sup1), 2-21. doi: 10.1080/01490419.2014.1000471

Viaña-Borja, S. P., & Ortega-Sánchez, M. (2019). Automatic methodology to detect the coastline from Landsat images with a new water index assessed on three different Spanish Mediterranean deltas. Remote Sensing, 11(18), 2186. doi: 10.3390/rs11182186

Vieira, E., Lázaro, C., & Fernandes, M. J. (2019). Spatio-temporal variability of the wet component of the troposphere–Application to Satellite Altimetry. Advances in Space Research, 63(5), 1737-1753. doi: 10.1016/j.asr.2018.11.015

Vignudelli, S., Birol, F., Benveniste, J., Fu, L. L., Picot, N., Raynal, M., & Roinard, H. (2019). Satellite altimetry measurements of sea level in the coastal zone. Surveys in geophysics, 40(6), 1319-1349. doi: 10.1007/s10712-019-09569-1

Vignudelli, S., Cipollini, P., Roblou, L., Lyard, F., Gasparini, G. P., Manzella, G., & Astraldi, M. (2005). Improved satellite altimetry in coastal systems: Case study of the Corsica Channel (Mediterranean Sea). Geophysical Research Letters, 32(7). doi: 10.1029/2005GL022602

Vignudelli, S., Kostianoy, A. G., Cipollini, P., & Benveniste, J. (2011). Coastal altimetry. Springer Science & Business Media. ISBN: 978-3-642-12796-0. doi: 10.1007/978-3-642-12796-0

Vousdoukas, M. I., Voukouvalas, E., Mentaschi, L., Dottori, F., Giardino, A., Bouziotas, D., ... & Feyen, L. (2016). Developments in large-scale coastal flood hazard mapping. Natural Hazards and Earth System Sciences, 16(8), 1841-1853. doi: 10.5194/nhess-16-1841-2016

Vu, P. L., Frappart, F., Darrozes, J., Marieu, V., Blarel, F., Ramillien, G., ... & Birol, F. (2018). Multi-satellite altimeter validation along the French Atlantic coast in the southern bay of Biscay from ERS-2 to SARAL. Remote Sensing, 10(1), 93. doi:10.3390/rs10010093

Watanabe, A., Maruyama, K., Shimizu, T., & Sakakiyama, T. (1986). Numerical prediction model of three-dimensional beach deformation around a structure. Coastal Engineering in Japan, 29(1), 179-194. doi: 10.1080/05785634.1986.11924437

Wild-Allen, K., Skerratt, J., Whitehead, J., Rizwi, F., & Parslow, J. (2013). Mechanisms driving estuarine water quality: a 3D biogeochemical model for informed management. Estuarine, Coastal and Shelf Science, 135, 33-45. doi: 10.1016/j.ecss.2013.04.009

Wollast, R. (1998). Evaluation and comparison of the global carbon cycle in the coastal zone and in the open ocean. p. The Sea, Vol. 10, 213-252.

Würtz, M. (2012). Mediterranean submarine canyons: Ecology and governance. IUCN.

Yan, K., Tarpanelli, A., Balint, G., Moramarco, T., & Baldassarre, G. D. (2015). Exploring the potential of SRTM topography and radar altimetry to support flood propagation modeling: Danube case study. Journal of Hydrologic Engineering, 20(2), 04014048. doi: 10.1061/(ASCE)HE.1943-5584.0001018

Yang, J., & Zhang, J. (2019). Validation of Sentinel-3A/3B satellite altimetry wave heights with buoy and Jason-3 data. Sensors, 19(13), 2914. doi: 10.3390/s19132914

Yang, J., Zhang, J., Jia, Y., Fan, C., & Cui, W. (2020). Validation of sentinel-3A/3B and Jason-3 altimeter wind speeds and significant wave heights using buoy and ASCAT data. Remote Sensing, 12(13), 2079. doi: 10.3390/rs12132079

Yuan, Y. (2019). Estimation of River Width with Fully-Focused SAR Altimetry Data. [Available at: http://resolver.tudelft.nl/uuid:1c056849-d54e-46fc-857c-86dcb89f007f]

Zar, J. H. (2013). Biostatistical analysis. Pearson. ISBN: 0-13-082390-2.

Zarzuelo, C., Díez-Minguito, M., Ortega-Sánchez, M., López-Ruiz, A., & Losada, M. Á. (2015). Hydrodynamics response to planned human interventions in a highly altered embayment: The example of the Bay of Cádiz (Spain). Estuarine, Coastal and Shelf Science, 167, 75-85.

Annexes

ANEX I. Model simulations

Summary of main simulations carried out during the model calibration and validation, and the qualitative comparison with altimetry data. Information about: case acronym (Low_: events of low or normal discharges, High_: events of high discharges), simulation dates (without include the model set-up time) maximum river discharge during the simulation period, number of Chezy section and parameter value in each section, upstream depth value (section 78-110 km), and stations studied in each simulation. In Table I the study cases show in the thesis document are highlighted.

Table I. Summary of model simulations.

Case acronym	Dates	Max. River discharge	Nº Chezy sections [parameter value]	Upstream Depth (m)	Stations studied
Low_01	15/08/2008 to 01/12/2008	91 $m^3 \cdot s^{-1}$	Three [40-50-50]	5	River
Low_02	15/08/2008 to 01/12/2008	91 $m^3 \cdot s^{-1}$	Three [40-50-60]	5	River
Low_03	15/08/2008 to 01/12/2008	91 $m^3 \cdot s^{-1}$	Three [30-50-60]	5	River
Low_04	15/08/2008 to 01/12/2008	91 $m^3 \cdot s^{-1}$	Three [20-50-60]	5	River
Low_05	15/08/2008 to 01/12/2008	91 $m^3 \cdot s^{-1}$	Three [50-50-60]	5	River
Low_06	15/08/2008 to 01/12/2008	91 $m^3 \cdot s^{-1}$	Three [40-40-60]	5	River
Low_07	15/08/2008 to 01/12/2008	91 $m^3 \cdot s^{-1}$	Three [40-60-60]	5	River
Low_08	15/08/2008 to 01/12/2008	91 $m^3 \cdot s^{-1}$	Three [40-70-60]	5	River
Low_09	15/08/2008 to 01/12/2008	91 $m^3 \cdot s^{-1}$	Three [40-80-60]	5	River
Low_10	15/08/2008 to 01/12/2008	91 $m^3 \cdot s^{-1}$	Three [40-60-50]	5	River
Low_11	15/08/2008 to 01/12/2008	91 $m^3 \cdot s^{-1}$	Three [40-60-70]	5	River
Low_12	15/08/2008 to 01/12/2008	91 $m^3 \cdot s^{-1}$	Three [40-60-80]	5	River
Low_13	15/08/2008 to 01/12/2008	91 $m^3 \cdot s^{-1}$	Three [40-60-90]	5	River
Low_14	15/08/2008 to 01/12/2008	91 $m^3 \cdot s^{-1}$	Three [40-60-100]	5	River
Low_15	15/08/2008 to 01/12/2008	91 $m^3 \cdot s^{-1}$	Three [40-50-100]	5	River
Low_16	15/08/2008 to 01/12/2008	91 $m^3 \cdot s^{-1}$	Three [40-70-100]	5	River
Low_17	15/08/2008 to 01/12/2008	91 $m^3 \cdot s^{-1}$	Three [40-80-100]	5	River

Low_18	15/08/2008 to 01/12/2008	91 $m^3 \cdot s^{-1}$	Three [40-50-90]	5	River
Low_19	15/08/2008 to 01/12/2008	91 $m^3 \cdot s^{-1}$	Three [40-50-80]	5	River
Low_20	15/08/2008 to 01/12/2008	91 $m^3 \cdot s^{-1}$	Three [40-50-70]	5	River
Low_21	15/08/2008 to 01/12/2008	91 $m^3 \cdot s^{-1}$	Three [30-60-90]	5	River
Low_22	15/08/2008 to 01/12/2008	91 $m^3 \cdot s^{-1}$	Three [30-50-90]	5	River
Low_23	15/08/2008 to 01/12/2008	91 $m^3 \cdot s^{-1}$	Three [30-70-90]	5	River
Low_24	15/08/2008 to 01/12/2008	91 $m^3 \cdot s^{-1}$	Three [30-80-90]	5	River
Low_25	15/08/2008 to 01/12/2008	91 $m^3 \cdot s^{-1}$	Three [20-60-90]	5	River
Low_26	15/08/2008 to 01/12/2008	91 $m^3 \cdot s^{-1}$	Three [20-50-90]	5	River
Low_27	15/08/2008 to 01/12/2008	91 $m^3 \cdot s^{-1}$	Three [20-70-90]	5	River
Low_28	15/08/2008 to 01/12/2008	91 $m^3 \cdot s^{-1}$	Three [20-80-90]	5	River
Low_29	15/08/2008 to 01/12/2008	91 $m^3 \cdot s^{-1}$	Three [30-60-100]	5	River
Low_30	15/08/2008 to 01/12/2008	91 $m^3 \cdot s^{-1}$	Three [30-50-100]	5	River
Low_31	15/08/2008 to 01/12/2008	91 $m^3 \cdot s^{-1}$	Three [30-70-100]	5	River
Low_32	15/08/2008 to 01/12/2008	91 $m^3 \cdot s^{-1}$	Three [30-80-100]	5	River
Low_33	15/08/2008 to 01/12/2008	91 $m^3 \cdot s^{-1}$	Three [20-60-100]	5	River
Low_34	15/08/2008 to 01/12/2008	91 $m^3 \cdot s^{-1}$	Three [20-50-100]	5	River
Low_35	15/08/2008 to 01/12/2008	91 $m^3 \cdot s^{-1}$	Three [20-70-100]	5	River
Low_36	15/08/2008 to 01/12/2008	91 $m^3 \cdot s^{-1}$	Three [20-80-100]	5	River
Low_37	15/08/2008 to 01/12/2008	91 $m^3 \cdot s^{-1}$	Four [40-50-70-90]	5	River
Low_38	15/08/2008 to 01/12/2008	91 $m^3 \cdot s^{-1}$	Four [40-50-70-100]	5	River
Low_39	15/08/2008 to 01/12/2008	91 $m^3 \cdot s^{-1}$	Four [40-50-80-90]	5	River
Low_40	15/08/2008 to 01/12/2008	91 $m^3 \cdot s^{-1}$	Four [40-50-80-100]	5	River
Low_41	15/08/2008 to 01/12/2008	91 $m^3 \cdot s^{-1}$	Four [40-60-70-90]	5	River

Low_42	15/08/2008 to 01/12/2008	91 $m^{3}\cdot s^{-1}$	Four [40-60-70-100]	5	River
Low_43	15/08/2008 to 01/12/2008	91 $m^{3}\cdot s^{-1}$	Four [40-60-80-90]	5	River
Low_44	15/08/2008 to 01/12/2008	91 $m^{3}\cdot s^{-1}$	Four [40-60-80-100]	5	River
Low_45	15/08/2008 to 01/12/2008	91 $m^{3}\cdot s^{-1}$	Four [30-60-70-90]	5	River
Low_46	15/08/2008 to 01/12/2008	91 $m^{3}\cdot s^{-1}$	Four [30-60-70-100]	5	River
Low_47	15/08/2008 to 01/12/2008	91 $m^{3}\cdot s^{-1}$	Four [30-60-80-90]	5	River
Low_48	15/08/2008 to 01/12/2008	91 $m^{3}\cdot s^{-1}$	Four [30-60-80-100]	5	River
Low_49	15/08/2008 to 01/12/2008	91 $m^{3}\cdot s^{-1}$	Four [40-60-90-90]	5	River
Low_50	15/08/2008 to 01/12/2008	91 $m^{3}\cdot s^{-1}$	Four [40-60-90-100]	5	River
Low_51	15/08/2008 to 01/12/2008	91 $m^{3}\cdot s^{-1}$	Four [40-50-90-90]	5	River
Low_52	15/08/2008 to 01/12/2008	91 $m^{3}\cdot s^{-1}$	Four [40-50-90-100]	5	River
Low_53	15/08/2008 to 01/12/2008	91 $m^{3}\cdot s^{-1}$	Four [40-60-90-100]	6.5	River
Low_54	15/08/2008 to 01/12/2008	91 $m^{3}\cdot s^{-1}$	Four [40-50-90-100]	6.5	River
Low_55	15/08/2008 to 01/12/2008	91 $m^{3}\cdot s^{-1}$	Four [40-60-90-100]	6	River
Low_56	15/08/2008 to 01/12/2008	91 $m^{3}\cdot s^{-1}$	Four [40-50-90-100]	6	River
Low_57	15/08/2008 to 01/12/2008	91 $m^{3}\cdot s^{-1}$	Four [40-60-90-100]	5.5	River
Low_58	15/08/2008 to 01/12/2008	91 $m^{3}\cdot s^{-1}$	Four [40-50-90-100]	5.5	River
Low_59	15/08/2008 to 01/12/2008	91 $m^{3}\cdot s^{-1}$	Five [40-60-70-90-100]	6.5	River
Low_60	15/08/2008 to 01/12/2008	91 $m^{3}\cdot s^{-1}$	Five [40-60-80-90-100]	6.5	River
Low_61	15/08/2008 to 01/12/2008	91 $m^{3}\cdot s^{-1}$	Five [40-50-70-90-100]	6.5	River
Low_62	15/08/2008 to 01/12/2008	91 $m^{3}\cdot s^{-1}$	Five [40-50-80-90-100]	6.5	River
High_01	15/12/2008 to 01/04/2009	553 $m^{3}\cdot s^{-1}$	Three [40-50-50]	5	River
High_02	15/12/2008 to 01/04/2009	553 $m^{3}\cdot s^{-1}$	Three [40-50-60]	5	River

High_03	15/12/2008 to 01/04/2009	553 $m^3 \cdot s^{-1}$	Three [30-50-60]	5	River
High_04	15/12/2008 to 01/04/2009	553 $m^3 \cdot s^{-1}$	Three [20-50-60]	5	River
High_05	15/12/2008 to 01/04/2009	553 $m^3 \cdot s^{-1}$	Three [50-50-60]	5	River
High_06	15/12/2008 to 01/04/2009	553 $m^3 \cdot s^{-1}$	Three [40-40-60]	5	River
High_07	15/12/2008 to 01/04/2009	553 $m^3 \cdot s^{-1}$	Three [40-60-60]	5	River
High_08	15/12/2008 to 01/04/2009	553 $m^3 \cdot s^{-1}$	Three [40-70-60]	5	River
High_09	15/12/2008 to 01/04/2009	553 $m^3 \cdot s^{-1}$	Three [40-80-60]	5	River
High_10	15/12/2008 to 01/04/2009	553 $m^3 \cdot s^{-1}$	Three [40-60-50]	5	River
High_11	15/12/2008 to 01/04/2009	553 $m^3 \cdot s^{-1}$	Three [40-60-70]	5	River
High_12	15/12/2008 to 01/04/2009	553 $m^3 \cdot s^{-1}$	Three [40-60-80]	5	River
High_13	15/12/2008 to 01/04/2009	553 $m^3 \cdot s^{-1}$	Three [40-60-90]	5	River
High_14	15/12/2008 to 01/04/2009	553 $m^3 \cdot s^{-1}$	Three [40-60-100]	5	River
High_15	15/12/2008 to 01/04/2009	553 $m^3 \cdot s^{-1}$	Three [40-50-100]	5	River
High_16	15/12/2008 to 01/04/2009	553 $m^3 \cdot s^{-1}$	Three [40-70-100]	5	River
High_17	15/12/2008 to 01/04/2009	553 $m^3 \cdot s^{-1}$	Three [40-80-100]	5	River
High_18	15/12/2008 to 01/04/2009	553 $m^3 \cdot s^{-1}$	Three [40-50-90]	5	River
High_19	15/12/2008 to 01/04/2009	553 $m^3 \cdot s^{-1}$	Three [40-50-80]	5	River
High_20	15/12/2008 to 01/04/2009	553 $m^3 \cdot s^{-1}$	Three [40-50-70]	5	River
High_21	15/12/2008 to 01/04/2009	553 $m^3 \cdot s^{-1}$	Three [30-60-90]	5	River
High_22	15/12/2008 to 01/04/2009	553 $m^3 \cdot s^{-1}$	Three [30-50-90]	5	River
High_23	15/12/2008 to 01/04/2009	553 $m^3 \cdot s^{-1}$	Three [30-70-90]	5	River
High_24	15/12/2008 to 01/04/2009	553 $m^3 \cdot s^{-1}$	Three [30-80-90]	5	River
High_25	15/12/2008 to 01/04/2009	553 $m^3 \cdot s^{-1}$	Three [20-60-90]	5	River

High_26	15/12/2008 to 01/04/2009	553 $m^{3}\cdot s^{-1}$	Three [20-50-90]	5	River
High_27	15/12/2008 to 01/04/2009	553 $m^{3}\cdot s^{-1}$	Three [20-70-90]	5	River
High_28	15/12/2008 to 01/04/2009	553 $m^{3}\cdot s^{-1}$	Three [20-80-90]	5	River
High_29	15/12/2008 to 01/04/2009	553 $m^{3}\cdot s^{-1}$	Three [30-60-100]	5	River
High_30	15/12/2008 to 01/04/2009	553 $m^{3}\cdot s^{-1}$	Three [30-50-100]	5	River
High_31	15/12/2008 to 01/04/2009	553 $m^{3}\cdot s^{-1}$	Three [30-70-100]	5	River
High_32	15/12/2008 to 01/04/2009	553 $m^{3}\cdot s^{-1}$	Three [30-80-100]	5	River
High_33	15/12/2008 to 01/04/2009	553 $m^{3}\cdot s^{-1}$	Three [20-60-100]	5	River
High_34	15/12/2008 to 01/04/2009	553 $m^{3}\cdot s^{-1}$	Three [20-50-100]	5	River
High_35	15/12/2008 to 01/04/2009	553 $m^{3}\cdot s^{-1}$	Three [20-70-100]	5	River
High_36	15/12/2008 to 01/04/2009	553 $m^{3}\cdot s^{-1}$	Three [20-80-100]	5	River
High_37	15/12/2008 to 01/04/2009	553 $m^{3}\cdot s^{-1}$	Four [40-50-70-90]	5	River
High_38	15/12/2008 to 01/04/2009	553 $m^{3}\cdot s^{-1}$	Four [40-50-70-100]	5	River
High_39	15/12/2008 to 01/04/2009	553 $m^{3}\cdot s^{-1}$	Four [40-50-80-90]	5	River
High_40	15/12/2008 to 01/04/2009	553 $m^{3}\cdot s^{-1}$	Four [40-50-80-100]	5	River
High_41	15/12/2008 to 01/04/2009	553 $m^{3}\cdot s^{-1}$	Four [40-60-70-90]	5	River
High_42	15/12/2008 to 01/04/2009	553 $m^{3}\cdot s^{-1}$	Four [40-60-70-100]	5	River
High_43	15/12/2008 to 01/04/2009	553 $m^{3}\cdot s^{-1}$	Four [40-60-80-90]	5	River
High_44	15/12/2008 to 01/04/2009	553 $m^{3}\cdot s^{-1}$	Four [40-60-80-100]	5	River
High_45	15/12/2008 to 01/04/2009	553 $m^{3}\cdot s^{-1}$	Four [30-60-70-90]	5	River
High_46	15/12/2008 to 01/04/2009	553 $m^{3}\cdot s^{-1}$	Four [30-60-70-100]	5	River
High_47	15/12/2008 to 01/04/2009	553 $m^{3}\cdot s^{-1}$	Four [30-60-80-90]	5	River
High_48	15/12/2008 to 01/04/2009	553 $m^{3}\cdot s^{-1}$	Four [30-60-80-100]	5	River

High_49	15/12/2008 to 01/04/2009	553 $m^3 \cdot s^{-1}$	Four [40-60-90-90]	5	River
High_50	15/12/2008 to 01/04/2009	553 $m^3 \cdot s^{-1}$	Four [40-60-90-100]	5	River
High_51	15/12/2008 to 01/04/2009	553 $m^3 \cdot s^{-1}$	Four [40-50-90-90]	5	River
High_52	15/12/2008 to 01/04/2009	553 $m^3 \cdot s^{-1}$	Four [40-50-90-100]	5	River
High_53	15/12/2008 to 01/04/2009	553 $m^3 \cdot s^{-1}$	Four [40-60-90-100]	6.5	River
High_54	15/12/2008 to 01/04/2009	553 $m^3 \cdot s^{-1}$	Four [40-50-90-100]	6.5	River
High_55	15/12/2008 to 01/04/2009	553 $m^3 \cdot s^{-1}$	Four [40-60-90-100]	6	River
High_56	15/12/2008 to 01/04/2009	553 $m^3 \cdot s^{-1}$	Four [40-50-90-100]	6	River
High_57	15/12/2008 to 01/04/2009	553 $m^3 \cdot s^{-1}$	Four [40-60-90-100]	5.5	River
High_58	15/12/2008 to 01/04/2009	553 $m^3 \cdot s^{-1}$	Four [40-50-90-100]	5.5	River
High_59	15/12/2008 to 01/04/2009	553 $m^3 \cdot s^{-1}$	Five [40-60-70-90-100]	6.5	River
High_60	15/12/2008 to 01/04/2009	553 $m^3 \cdot s^{-1}$	Five [40-60-80-90-100]	6.5	River
High_61	15/12/2008 to 01/04/2009	553 $m^3 \cdot s^{-1}$	Five [40-50-70-90-100]	6.5	River
High_62	15/12/2008 to 01/04/2009	553 $m^3 \cdot s^{-1}$	Five [40-50-80-90-100]	6.5	River
Low_63	10/09/2009 to 01/11/2009	115 $m^3 \cdot s^{-1}$	Four [40-60-90-100]	6.5	Continental shelf
Low_64	10/09/2009 to 01/11/2009	115 $m^3 \cdot s^{-1}$	Five [40-60-70-90-100]	6.5	Continental shelf
Alti_01	07/12/2010 to 17/01/2011	3300 $m^3 \cdot s^{-1}$	Four [40-60-90-100]	6.5	Altimetry tracks
Alti_02	07/12/2010 to 17/01/2011	3300 $m^3 \cdot s^{-1}$	Five [40-60-70-90-100]	6.5	Altimetry tracks
Alti_03	05/03/2013 to 20/04/2013	2000 $m^3 \cdot s^{-1}$	Four [40-60-90-100]	6.5	Altimetry tracks
Alti_04	05/03/2013 to 20/04/2013	2000 $m^3 \cdot s^{-1}$	Five [40-60-70-90-100]*	6.5	Altimetry tracks
Alti_05	09/03/2018 to 21/03/2018	1080 $m^3 \cdot s^{-1}$	Four [40-60-90-100]	6.5	Altimetry tracks
Alti_06	09/03/2018 to 21/03/2018	1080 $m^3 \cdot s^{-1}$	Five [40-60-70-90-100]	6.5	Altimetry tracks

ANEX II. Summary of Scientific Activities

Publications in International Journals

Aldarias, A., Gómez-Enri, J., Laiz, I., Tejedor, B., Aboitiz, A., Vignudelli, S., & Cipollini, P. 2020. Validation of Sentinel-3A SRAL Coastal Sea Level Data at High Posting Rate: 80 Hz. IEEE Transactions on Geoscience and Remote Sensing, 58(6), 3809-3821.doi: 10.1109/TGRS.2019.2957649.

Aldarias, A., Gómez-Enri, J., Laiz, I., & Vignudelli, S. 2022. Assessment of Sea Level data of the two-satellite Sentinel-3 mission on coasts around the Iberian Peninsula. *In preparation.*

Aldarias, A. et al. *2022*. Sentinel-3 Fully Focused SAR: precision and accuracy in the Gulf of Cadiz. *In preparation.*

International Conferences

Aldarias, A., Gómez-Enri, J., Laiz, I., Tejedor, B., Vignudelli, S., Cipollini, P. 2018. Validation of coastal sea level altimetry data at high posting rate: 80 Hz, from Sentinel-3a SRAL. 25 Years of Progress in Radar Altimetry Symposium. Ponta Delgada, Azores, Portugal. (p.211). Poster.

Gómez-Enri, J., Aldarias, A., Vignudelli, S., Cipollini, P., Laiz, I., Passaro M., Tejedor, B. 2018. Lessons learned after 10 years of validation of coastal altimetry products in the Gulf of Cadiz and the Strait of Gibraltar. 25 Years of Progress in Radar Altimetry Symposium. Ponta Delgada, Azores. (p. 211). Poster.

Aldarias, A., Gómez-Enri, J., Laiz, I., Tejedor, A., Vignudelli, S., Cipollini, P. 2020.Assesing the quality of Sentinel-3A SRAL sea level data around Spanish coasts. CAW12 Final Report (p.25-26). Oral communication.

Gómez-Enri, J., Aldarias, A., Vignudelli, S., Cipollini, P. Sentinel 3A approaching the coast: effect of track orientation and coastal topography. CAW12 Final Report (p.30). Poster.

Bolado-Penagos, M., Aldarias, A., Plomaritis, T.A., Laiz, I. 2021. Introduction to physical oceanography for high ability students. Proceedings of INTED2021 Conference (p.1706-1715).

Aldarias, A., Laiz, I., Gómez Enri, J., López Ruiz, A., Plomaritis, T., Díez-Minguito, M. "Comparing sea level values in the Guadalquivir River Estuary and the Gulf of Cadiz continental shelf from a numerical model, satellite altimetry and in-situ data.". International congress of Water and Coastal Management. Book of Abstracts WACOMA 2021, pp. 39-42. Oral communication.

Aldarias, A., Passaro, M., Gómez-Enri, J., Mulero-Martínez, R., Laiz, I., Ehlers, F., Schlembach, F., Scagliola, M. 2022. Analysis of Fully Focused and unfocused SAR data in the [0 - 5] km of the coastal strip. Ocean Surface Topography Science Team. Oral communication (accepted).

Aldarias, A., Passaro, M., Gómez-Enri, J., Mulero-Martínez, R., Laiz, I., Ehlers, F., Schlembach, F., Scagliola, M. 2022. Accuracy and precision assessment of Sentinel-3 Fully-Focused SAR in the Gulf of Cadiz (Spain). Benefits for oceanographic applications. Living Planet Symposium. Oral communication (pending approval).

National Conferences

Aldarias, A., Gómez-Enri, J., Laiz, I. 2018. Validation of coastal altimetric products in the Gulf of Cadiz from Sentinel-3A SRAL (Original title: Validación de productos altimétricos costeros en el golfo de Cádiz, procedentes de Sentinel-3A SRAL). IV Scientific Symposium of Students. Faculty of Marine and Environmental Sciences, University of Cadiz, Spain. (p.19). Oral communication.

Aldarias, A., Gómez-Enri, J., Laiz, I., Tejedor, B., B., Aboitiz, Vignudelli, S., Cipollini, P. 2018. Assessment of delay-doppler altimeter data in the Spanish coast: Barcelona, Bilbao and Huelva. V Encounter of Physical Oceanography (EOF). Vigo, Spain. (p. 150). Poster.

Aldarias, A., Gómez-Enri, J., Laiz, I., Tejedor, A., Vignudelli, S., Cipollini, P. 2018. Assessment of delay-doppler altimeter data in the Spanish Coast: Barcelona, Bilbao and Huelva. I Congress of Young Marine Researchers. Cadiz, Spain. ISBN:978-84-09-05170-0. (p.55-56). Oral communication.

Aldarias, A., Gómez-Enri, J., Laiz, I. 2019. The first 5 km of the coastal fridge with Sentinel-3a satellite. (Original title: Los primeros 5 km de franja costera vistos desde el satélite Sentinel-3a). V Scientific Symposium of Students. Faculty of Marine and Environmental Sciences, University of Cadiz, Spain. (In press). Oral communication.

Aldarias, A., Gómez-Enri, J., Laiz, I., Tejedor, A., Vignudelli, S., Cipollini, P. 2019. Sentinel-3a: an avance for coastal altimetry. (Original title: Sentinel-3a SRAL: un avance para la altimetría costera.Validación en las costas de la península ibérica). Teledetección: Hacia una vision global del cambio climático. 2019. Ediciones Universidad de Valladolid. ISBN: 978-84-1320-038-5, (391-394). Oral communication.

Ana Aldarias, Irene Laiz, Jesús Gómez Enri, Alejandro López Ruiz, Theoharis Plomaritis, Manuel Díez-Minguito. 2021. Implementation of the Delft3D model in the Guadalquivir River Estuary and the Gulf of Cadiz continental shelf. (Original title: Implementación del modelo delft3D en el estuario del rio Guadalquivir y la plataforma costera del Golfo de Cádiz). III Congress of Young Marine Researchers. Motril, Spain.2021 ISBN: 978-84-09-36126-7 (pp.234-235). Oral communication.

Internship abroad

The author did a national research internship within the Research Group 'Dynamic of Environmental Flows' at the Engineer Technic Superior School (University of Seville, Spain) from 24th June to 31st July 2019 and 1st October to 30th November 2019, under the supervision of Dr. Alejandro López Ruiz. The activities carried out were the Delft3D model implementation in the Gualdalquivir River Estuary and the adjacent continental shelf.

The author did an international research internship in the Deutsche Geodätische Forschungsinstitut at the Technical University of Munich (DGFI-TUM, Germany) from 13th September to 12th December 2021, under the supervision of Dr. Marcello Passaro. The activities carried out were the validation of Sentinel-3 Fully Focused products in the Gulf of Cadiz.

Scientific courses and complementary activities

2018. Oral communication techniques at the university classroom (25 hours). Teaching Innovation Program. University of Cadiz.

2018. Create presentations and posters as a professional: graphic design for researchers and lecturers (25 hours). University of Cadiz, Spain.

2018. How to increase the visibility of our publications using profiles and social networks for researchers (25 hours). Teaching Innovation Program. University of Cadiz

2018. Indexes and Impact Factor and Quality Indications in academic publications for accreditation (25 hours). Teaching Innovation Program. University of Cadiz

2019. Bibliographic reference managers: Mendeley (15 hours). Teaching Innovation Program. University of Cadiz.

2019. IV International Summer School on Dynamics of Estuarine and Nearshore Systems (60 hours). Organizer by the Institute for Marine and Atmospheric Research of the Utrecht University (Netherlands) and the Environmental Fluid Dynamics Group of the University of Granada (Spain).

2019. MATLAB Applied to Marine Sciences (20 hours). University of Cadiz Doctorate School (EDUCA).

2019. Oceanography and Programming oriented to objects with Python (20 hours). University of Cadiz Doctorate School (EDUCA).

2019. Advanced Ocean Synergy Training Course (40 hours). European Space Agency (ESA). Chania, Greece.

2020. Coastal Altimetry Training Course (10 hours). European Space Agency (ESA). ESRIN, Frascati, Italy.

2020. Search, management and communication of scientific information (35 hours). University of Cadiz Doctorate School (EDUCA).

2020. English for STEM. University of Ferrara (10h).
2020. English C1.1 Certificated Course (90 hours). Modern Language Centre (CSLM). University of Cadiz.

2021. English C1.2 Certificated Course (90 hours). Modern Language Center (CSLM). University of Cadiz.

2021. Remote Sensing as a global tool (25 hours). International University of Menendez Pelayo (UIMP Valladolid).

2021. Intensive English course. English Level C1 (108 hours). Educational First. St. Julian's International Languages Center, Malta.

Project collaboration

Project collaborator. 2020. Original title: El cangrejo invasor Callinectes sapidus en el golfo de Cádiz: Distribución, impacto en las comunidades nativas y estrategias de gestión (InvBlue) (PID2019-105978RA-I00). Lead researcher: Enrique González Ortegón. Financed by the Ministry of Science and Innovation (01/06/2020-31/05/2023).

Project collaborator. 2020. Original title: Ecología de las especies no nativas corvinata real, cangrejo azul y camarón pistola en la zona costera del Golfo de Cádiz (EcoInvadiz) (P18-RT-5010). Lead researcher: Enrique González Ortegón. Financed by the Economic Transformation, Industry, Knowledge and Universities Council, Andalusia Regional Goverment (01/01/2020 - 31/12/2023)

Project collaborator. 2020. Sentinel-3 and Cryosat SAR/SARIN radar Altimetry ffor coastal zone and inland water. Entity: SatOc Ltd. Lead researcher: Jesús Gómez Enri (University of Cadiz). Financed by the European Space Agency (01/02/2020-01/02/2022).

Teaching experience

Internship supervisor and tutor for the Final Degree Project. 2019/20. Original title: Puesta en Valor del Ecosistema de la salina de San José (El Puerto de Santa María).

Internship supervisor and tutor for the Final Degree Project. 2019/20. Original title: La Laguna del Gallo (El Puerto de Santa María): Bases para su conservación y restauración ecológica.

Teaching collaboration in Marine Sciences Degree. 2020/21. Subject SIG and Remote Sensing, Applied Physics Department, University of Cadiz (30 h).

Teaching collaboration in Environmental Sciences Degree. 2020/21. Subject SIG and Remote Sensing, Applied Physics Department, University of Cadiz (30 h).

Teaching collaboration in Environmental Sciences Degree. 2021/22. Subject SIG and Remote Sensing, Applied Physics Department, University of Cadiz (15 h).

Participation in the annual workshop ‘Introduction to Physical Oceanography: the ocean is a large natural laboratory’, as part of the Extracurricular Enrichment Program for Students with High Capabilities from the University of Cadiz and the Territorial Delegation of Education in Cadiz. Applied Physics Department, University of Cadiz, Spain. 2018-2022.